Boundary Element Methods for Inductive Hardening

Dissertation

zur Erlangung des Grades eines Doktors
der Naturwissenschaften
der Fakultät für Physik
der Eberhard-Karls-Universität zu Tübingen

vorgelegt von

Jörg Ostrowski

aus Sindelfingen

2003

Tag der mündlichen Prüfung: 19.12.2002

Dekan: Prof. Dr. H. Müther

1. Berichterstatter: Prof. Dr. H. Ruder

2. Berichterstatter: Prof. Dr. R. Hiptmair

Abstract

This study deals with the simulation of inductive hardening of conducting workpieces made of steel. The aim is to calculate the propagation of heat in the workpiece. Based on this knowledge, the hardened zone can be predicted with sufficient precision. Since the simulation is to be applied in industry, workpieces and inductors are supposed to have a complex three dimensional shape. The electromagnetic calculations are based on the *quasi-static approximation of Maxwell's equations in frequency domain*, and the non-linear heat conduction equation is used to evaluate the temperature distribution.

The focus of this treatise is on the computation of the electromagnetic fields, especially on the *boundary element methods* (BEM) applied in order to master the unbounded exterior of the conductors. In the interior of the conductors, the skin effect plays an important role and the electromagnetic fields show a rapid decay. If the numerical solution is to resolve this effect, the mesh must be very fine at the surface, whereas this is not necessary elsewhere. To save storage, the mesh is *refined adaptively* in the interior, with the aid of a residual based error estimator. The equations for the conducting region are solved using a *finite element method* (FEM). A hierarchical system of three models is presented for the coupling of the BEM equations for the exterior with the FEM equations for the interior. The *eddy current approach* is the model with the most convenient properties. The *FEM/BEM coupling* is strong and symmetric, the equations have a unique solution, and the convergence of an iterative solver can be guaranteed. There is also a quasi-optimal a priori error etimate for a conforming Garlerkin discretization based on *edge elements* and *Raviart-Thomas elements*. However in terms of implementation the eddy current approach is also the most complicated one. The *impedance model* can be used as an approximation. It is based on the same equations for the two regions but in this model the coupling is realized only weakly by imposing so-called impedance boundary conditions on the surface of the conductors. The weak coupling has the advantage that the BEM and FEM parts can be solved independently. In order to get a first rough estimate of the electromagnetic fields, the *magnetostatic approach* is developed. As far as the BEM computations are concerned it assumes the negligible penetration depth of a perfect conductor and the FEM/BEM parts are coupled only uni-directionally. A kind of scalar magnetic potential is used in all three models, and in regions with nontrivial topology they are multivalued. In that case, the jumps of the magnetic potentials at suitable cutting surfaces or cutting cycles are associated with the total currents in the conductors, these surfaces or cycles must be added to the meshes. For this purpose, an *algorithm for the automatic construction and classification of generators of* $H_1(\Gamma_h, \mathbb{Z})$ for triangulated surfaces is introduced. Unlike the FEM matrices, the BEM matrices are dense and cannot be stored completely. A H^2-*Matrix Approximation* is applied on the four utilized kernels of elaborate structure. *Analytical solutions* are developed to verify the electromagnetic computations.

The non-linear heat problem is solved with an implicit Euler method. Measurements of the surface temperature during the process are made for the validation of these calculations. Comparisons of the predicted hardened zone in the simulation with real hardened items are most important for the program's verification.

Zusammenfassung

Diese Arbeit behandelt die numerische Simulation des induktiven Härtens leitender Werkstücke aus Stahl. Ziel ist die transiente Berechnung der Temperaturverteilung im Werkstück, deren Kenntnis eine ausreichend genaue Vorhersage der Härtezone erlaubt. Die Form der Werkstücke und Induktoren muß als allgemein dreidimensional angenommen werden, da die Simulation in der Industrie angewandt werden soll. Die elektromagnetischen Berechnungen basieren auf der *quasistatischen Näherung* der *Maxwell Gleichungen* im Frequenzbereich. Zur Temperaturberechnung wird die nichtlineare Wärmeleitungsgleichung benutzt.

Das Hauptaugenmerk dieser Dissertation liegt auf der Berechnung der elektromagnetischen Felder, insbesondere auf den *Randelementmethoden* (BEM), die zur Behandlung des unbeschränkten Außenraums eingeführt werden. Im Leiterinnern spielt der *Skin Effekt* eine wichtige Rolle, aufgrund dessen die Felder nach innen schnell abfallen. Soll dieser Effekt in der Simulation aufgelöst werden, so muß das Mesh an der Leiteroberfläche sehr fein sein. Um Speicher zu sparen, wird das Mesh im Leiterinnern mit Hilfe eines *Residuen basierten Fehlerschätzers adaptiv verfeinert*. Die Gleichungen werden mit einer *finiten Elementmethode* (FEM) gelöst. Für die Kopplung der BEM-Gleichungen des Äußeren mit den FEM-Gleichungen des Inneren wird ein hierarchisches System aus drei Modellen vorgestellt. Der *Wirbelstromansatz* ist das Model mit den besten Eigenschaften. Die *FEM/BEM-Kopplung* ist stark und symmetrisch, die Gleichungen sind eindeutig lösbar, und die Konvergenz eines iterativen Lösers kann garantiert werden. Für eine konforme Garlerkin Diskretisierung mit *Kantenelementen* und *Raviart-Thomas Elementen* existiert außerdem ein *quasi optimaler a priori Fehlerschätzer*. Allerdings ist der Wirbelstromansatz auch am schwierigsten zu implementieren. Das *Impedanzmodel* kann als Näherung benutzt werden. Es basiert auf denselben Gleichungen für Außen- und Innenraum, die hier aber, unter Anwendung von Impedanz-Randbedingungen, nur schwach gekoppelt sind. Der *magnetostatische Ansatz* wurde entwickelt, um einen ersten groben Eindruck der elektromagnetischen Felder zu erhalten. Hier geht man im BEM-Teil von der vernachlässigbaren Eindringtiefe eines perfekten Leiters aus, wobei der FEM-Teil nur einseitig angekoppelt wird. In allen drei Modellen wird eine Art skalares magnetisches Potential benutzt. Dabei wird man mit dem typischen Problem der Unstetigkeit in nicht einfach wegzusammenhängenden Gebieten konfrontiert. Die Sprünge des Potentials an frei wählbaren Schnittflächen bzw. Oberflächenpfaden sind mit den Gesamtströmen in den Leitern verknüpft. Zu diesem Zweck wurde ein *Algorithmus zur automatischen Konstruktion und Klassifizierung von Generatoren von* $H_1(\Gamma_h, \mathbb{Z})$ *auf triangulierten Oberflächen* entwickelt. Die BEM-Matrizen sind im Gegensatz zu den FEM-Matrizen nicht dünn besetzt und können deshalb nicht komplett gespeichert werden. Eine H^2*-Matrix Approximationsmethode* wurde deshalb auf die vier auftretenden komplizierte Kerne angewandt. Zur Verifikation der elektrodynamischen Berechnungen wurden *analytische Lösungen* entwickelt.

Das nichtlineare Wärmeleitungsproblem wird mit Hilfe einer impliziten Euler Methode gelöst. Messungen der Oberflächentemperatur während des Prozesses wurden zum Zwecke der Validierung dieser Rechenergebnisse durchgeführt. Vergleiche zwischen der berechneten Härtezone mit realen gehärteten Teilen sind die wichtigste Möglichkeit zur Verifikation des Programms.

The devil is a squirrel, and I know him well...

Contents

Chapter 1

Introduction

The hardening of steel is an old, established procedure. First mentioned 2800 years ago in Homer's epic poems, hardening was described as the work of a smith, who heated the steel until it was glowing and then hardened the part by ducking it into cold water. Pioneer work for the explanation of the process was done by Max von Laue, a German physicist who found in 1912 with the aid of Röntgen's X-rays that atoms have a periodic configuration in crystals. It is clear that the properties of a metal are determined by this configuration, and the hardening is nothing else but a phase transition, i.e., a change in the configuration of the atoms. So what Homer's smith did was to initiate two phase transitions: If steel is heated up to a temperature of 720^oC it firstly changes into austenite. Ducking the item into water causes a fast cooling, and the atoms of the lattice congeal into a new hard phase, the martensite.

Of course, heating and fast cooling must still be done nowadays if steel is to be hardened, but heating techniques have changed since Homer's days. Depending on the desired outcome, the most promising heating strategy is employed. Martensite is hard but also brittle, thus some workpieces have to be hardened only in a precisely defined region in order to avoid cracks during use. Examples are the driveshaft of a car with its joints. They should remain flexible in the interior and abraison resistent on the surface. A fast and precisely localized heating strategy which is restricted to regions close to the surface must be applied. Induction heating, the subject of this examination, accomplishes these demands. It has become a standard procedure when it comes to handling metals as part of a manufacturing process [Ben90]. Hardly any other non-intrusive technology can compete with induction heating in terms of speed, controllability and heating power. Cooling of the hot workpieces is still done by pouring water on it.

Controlling the inductive hardening process, however, entails a detailed quantitative insight into the spatial conversion of electric energy into heat, and how the heat propagates through the material. This is the topic of the present study. The insights are to be gained by a numerical simulation. In the future, this simulation is meant to constitute the kernel of a program to be applied in the industry, thus it must be able to deal with parts of arbitrary geometry. This restricts the involved algorithms to a much smaller class than would be the case if the program were used by its developers only. So in addition to electrodynamics and heat propagation, a further goal consists in finding a numerical scheme able to deal with all geometries automatically.

During induction heating, a rotating conducting *workpiece* is exposed to a time-dependent elec-

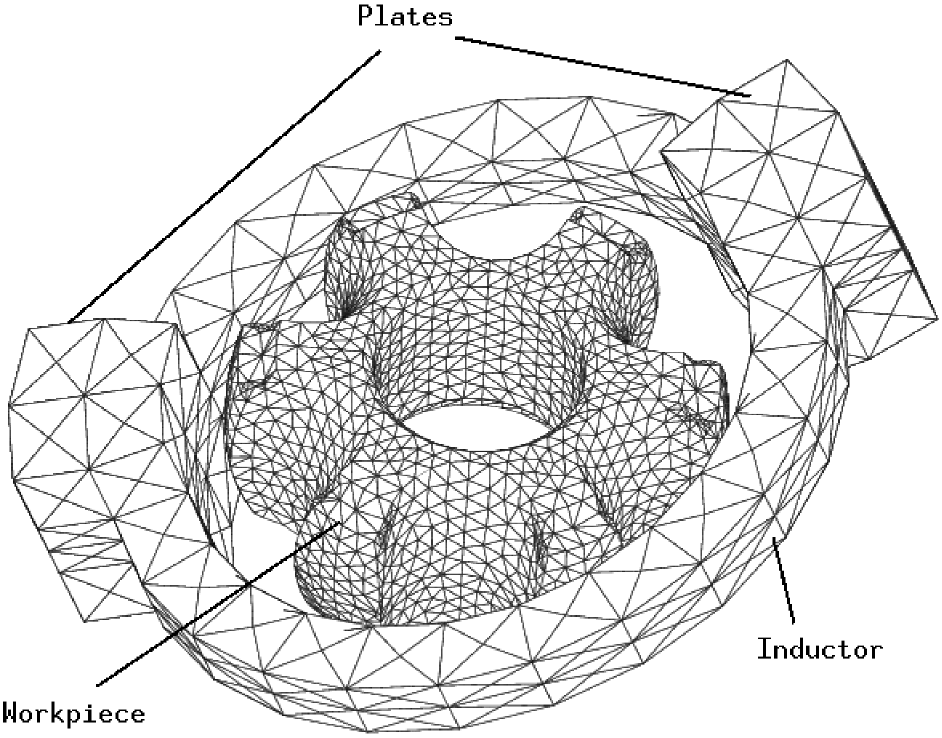

Figure 1.1: Typical setting for induction hardening

tromagnetic field generated by an alternating current in an *inductor*, usually some coil. The field penetrates the conductor and, according to Faraday's law, triggers *eddy currents*. It is the Ohmic losses due to the eddy currents which, eventually, heat the conductor. The dominant skin effect causes the workpiece to be heated chiefly in a thin layer at the surface. The induced eddy currents can be located exactly if the right inductor is chosen. Thus, the hardened zone in the workpiece depends heavily on the shape of the inductor. The program to be developed assists in finding an adequate one. This is the reason why the project could also be called *computer-aided inductor design*. The shape can as well be found by empirical experiments, but numerical simulations promise to find it faster, more comprehensively, and cheaper.

Much work has been done on developing codes for the numerical simulation of induction heating. Some approaches resort to semianalytic methods [HGU94, GHZU95], but these are confined to very simple geometries. Other settings feature cylindrical symmetry and have been tackled by codes based on essentially two-dimensional models [RS96, SR97]. A survey of techniques which can be applied to genuinely three-dimensional induction heating problems is given in [MML94]. There, the authors stick to vector-valued surface currents as principal unknowns in the boundary element method.

In this work, an unsymmetric 'real life' situation is considered as depicted in Figure 1.1. The conductor may be some technical item like a bolt, an axle, or a screw and may feature a rather complex topology with a few holes drilled into it. The inductor has the topolgy of a torus and may neither intersect nor touch the conductor. It might be a copper pipe bent into a coil carrying some coolant inside. The item to be heated circulates slowly with approximately $50Hz$ in order to achieve even heating. Chunks of highly permeable non-conducting materials are placed close to the inductor to deflect the magnetic fields. All the shapes are usually available in the form of CAD data, their surfaces composed of smooth facets.

The inductor is fed with a sinusoidal alternating current of 10 to $40kA$ at medium-range frequencies of 5 to $30kHz$. The size of the items is a few centimeters, and the whole process takes only a couple of seconds. It is important to realize that the two main physical effects, electromagnetic induction and heat conduction, occur on vastly different time-scales. This means that there is hardly any change in the temperature of the conductor within one cycle of the electromagnetic fields. Thus, a partial decoupling can be employed and the simulation can be done by carrying out the following two steps in turns [PKU97, CGC$^+$94]:

1. Compute eddy currents and Ohmic losses based on material parameters that are determined by a stationary temperature distribution.

2. Update the temperature distribution by taking into account the heat generation computed in the first step.

The mentioned phase transition into austenite takes place at the temperature of 720^oC. The hardened phase martensite originates when the workpiece is quenched under a shower. The aim of the simulation is not the high precision calculation of the phase transitions. The thermodynamic processes are taken into account only in a rough way. It is assumed that the workpiece is hardened in the zone with temperatures above 830^oC because the dynamic of the process predicts the respective regions will completely be transformed into austenite, which is essential for the desired phase change into martensite under the shower. Chapter 2 gives more insight into the phase transitions and explains how the heat propagation is calculated numerically.

This study mainly pays attention to the electromagnetic aspects of the problem. Frequencies, dimensions and material parameters justify the use of the *quasi-static approximation of Maxwell's equation in frequency domain*.

The dominant *skin effect* commands attention in the interior of the conductors: It denotes the rapid decay of the electromagnetic fields away from the surface of a conductor. Roughly speaking, the fields are present only up to a certain *skin depth* δ below the surface of the conductor. This strongly local behavior enforces adaptive techniques in the interior if the storage is to stay manageable. An *adaptive finite element method* (FEM) based on *linear edge elements* is used for solving Maxwell's equations inside the conductors.

If the right completion conditions are chosen, this seems to be a feasible scheme for the unbounded exterior of the conductors as well. The rotation of the workpiece is an obstacle, however. One could argue that even for rotating workpieces it is possible to restrict oneself exclusively to FEM methods if two grids are used for workpiece and inductor, that have a grinding connection. But this argumentation no longer holds if the arbitrary geometry of both parts has to be taken into accout autonomously by the program. An auspicious alternative is the use of a *boundary element method* (BEM) on a *Lagrangian mesh*. It automatically fulfils two purposes: The unbounded exterior is included without any approximations, and the rotation is not a difficulty for a Lagrangian mesh. These are the main arguments why this method is used here. The focus of this dissertation is on the BEM part and on all the ingredients essential for its implementation.

The FEM part of the interior and the BEM part of the exterior domain must be coupled. In Chapter 3, a hierarchical system of three models is developed for the coupling. All three models disregard the induction by the movement of the workpiece, for the following reason: It rotates only with a frequency of approximately $50Hz$, which can be neglected compared with the frequency of some kHz of the alternating exciting current in the inductor.

The *eddy current approach* from Section 3.1 establishes a strong and symmetric coupling of the two parts. The equations are uniquely solvable, and due to their symmetry, the convergence of a fast iterative solver can be guaranteed. A *quasi-optimal a priori error estimate* exists for a *conforming Garlerkin discretization*, i.e., the error between the numerical solution and the continuous solution of the quasi-static approximation vanishes for decreasing meshwidths. These are nice properties, but the implementation of this model takes a lot of effort because everything is coupled strongly.

A possibility for a partial decoupling of the FEM part and the BEM part is the *impedance model* of Section 3.2. The FEM part in the equations of the eddy current approach can be split off by applying *impedance boundary conditions*. This is a good approximation if the item is relatively 'flat'. Thus one expects problems at edges and corners. The impedance model has the advantage that FEM and BEM parts can be implemented separately, and that all occuring operators are also needed in the eddy current approach. So if the impedance model is step one of an implementation, nearly everything is prepared for the eddy current approach.

Since both models are based on a formulation including some kind of scalar magnetic potentials, one is faced with the typical *topological problems*. The potential is multivalued if the conductors are not simply connected and it has discontinuities at some *cutting surfaces*. As far as the BEM part is concerned, the traces of these cuts are *cycles* on the surface, and they are needed in both models. An algorithm for the automatical construction of those paths is presented in Section 4.4.

As already stated above, the mesh must be refined adaptively in the interior of the conductors in order to resolve the skin effect. This is done with the aid of a *residual based error estimator*, explained in simple terms in Section 5.1. The additional elements are mainly located at the surface of the conductors and they do not cause great difficulties for the sparse FEM operators, but for the dense BEM operators they are a problem. A *compression technique* must be applied that is presented in Section 5.3.

The material parameters of steel C45, the material used for all realistic simulations, are shown in Section 5.1.1. Each of the coefficients depends on the temperature. As already mentioned, the timescales of electromagnetics and thermodynamics are different, and for the electrodynamic part it is sufficient to update the coefficients after a certain timespan. Additionally, the magnetic permeability μ_r depends on the strength of the magnetic field. This *ferromagnetic behavior* causes the electromagnetic models to be *non-linear*, and in frequency domain one has to cope with this problem by using *time-averages of the permeability* and by applying a *relaxation scheme*. Both is explained in Section 5.1.1. The complete algorithms of the eddy current approach and the impedance model work according to Figure 1.2 and Figure 1.3.

```
program EDDY CURRENT MODEL
Input: $(I_{Exciting}\,,\omega_{Exciting}\,,\omega_{Rotation}\,,\epsilon_{Refine}\,,N_{Steps}\,,Heatingtime\,,N_{Rotation})$
{
  read Meshes;
  read Material Parameters;
  set $T =$ Room Temperature;
  $\triangle t = \frac{Heatingtime}{N_{Steps}}$;

  $//Comment:\ Refinement\ loop$
  repeat
  {
    find Paths;
    fill BEM-Operators;
    apply $H^2$-Compression;
    fill FEM-Operators;
    $//Comment:\ Rotation\ loop$
    for (Position$=1$ to Position$=N_{Rotation}$) solve with relaxation:
      { Strongly Coupled FEM/BEM;}
    if (Error-Estimation $< \epsilon_{Refine}$) break;
     else Refine Meshes;
  }

  $//Comment:\ Main\ loop$
  for (Step$=1$ to Step$=N_{Steps}$)
  {
    update Material Parameters($T$);
    $//Comment:\ Rotation\ loop$
    for (Position$=1$ to Position$=N_{Rotation}$) solve with relaxation:
      { Strongly Coupled FEM/BEM;}
    calculate Temperature Distribution $T\big(t = (Step-1)\cdot\triangle t\,,\cdots,t = Step\cdot\triangle t\big)$;
  }
}
```

Figure 1.2: Program of the eddy current approach

```
program IMPEDANCE MODEL
Input: $(I_{Exciting}\,, \omega_{Exciting}\,, \omega_{Rotation}\,, \epsilon_{Refine}\,, N_{Steps}\,, Heatingtime\,, N_{Rotation})$
{
  read Meshes;
  read Material Parameters;
  set $T =$ Room Temperature;
  $\triangle t = \frac{Heatingtime}{N_{Steps}}$;

  $//Comment: \ Refinement\ loop$
  repeat
  {
    find Paths;
    fill BEM-Operators;
    apply $H^2$-Compression;
    fill FEM-Operators;
    $//Comment: \ Rotation\ loop$
    for (Position$= 1$ to Position$= N_{Rotation}$) solve with relaxation:
    {
      solve BEM;
      transfer BEM-result to FEM;
      solve FEM;
    }
    if (Error-Estimation $< \epsilon_{Refine}$) break;
     else Refine Meshes;
  }

  $//Comment: \ Main\ loop$
  for (Step$= 1$ to Step$= N_{Steps}$)
  {
    update Material Parameters($T$);
    $//Comment: \ Rotation\ loop$
    for (Position$= 1$ to Position$= N_{Rotation}$) solve with relaxation:
    {
      solve BEM;
      transfer BEM-result to FEM;
      solve FEM;
    }
    calculate Temperature Distribution $T\big(t = (Step - 1) \cdot \triangle t\,, \cdots, t = Step \cdot \triangle t\big)$;
  }
}
```

Figure 1.3: Program of the impedance model

The *magnetostatic approach* of Section 3.3 is developed in order to get a first rough estimate for the currents, temperatures and hardened zones. It is completely different from the two models above, and its algorithms cannot be reused there. However, it is easy to implement. So it is useful to get a first ’feeling’ for the occuring physical phenomena, for the performance of some numerical features, and for the problems to be expected. The penetration depth is small for good conductors, about $0.1mm$ for steel at room temperature. As a consequence, the bulk of the inductor and the workpiece have little impact on the electromagnetic fields. A perfect conductor can be assumed into which the fields cannot penetrate. The magnetostatic approach uses this assumption, and a boundary integral equation has to be solved which is completely independent of the interior of the conductors and therefore also independent from the material parameters. The result is that the current flows only on the surface. The spatial current in the workpiece is still needed, however, because it is the source of the heat. For this purpose, the surface current is distributed into the interior by applying the skin effect formula of a plane. Here the material coefficients come into play, and although the model is very simple, it yields relatively good results, at least for flat surfaces. It is based on a scalar magnetic potential, and in this model the cutting surfaces themselves are needed. They must be constructed by hand in advance. Here this is sufficient because the magnetostatic approach is only a preliminary study. The algorithm of the model is presented in Figure 1.4.

```
Construct Cutting Surfaces in advance;

program MAGNETOSTATIC MODEL
Input: $(I_{Exciting}, \omega_{Exciting}, \omega_{Rotation}, \epsilon_{Refine}, N_{Steps}, Heatingtime, N_{Rotation})$
{
  read Meshes;
  read Cutting Surfaces;
  read Material Parameters;
  set $T =$ Room Temperature;
  $\triangle t = \frac{Heatingtime}{N_{Steps}}$;

  for (Position$= 1$ to Position$= N_{Rotation}$) solve BEM;

  $//Comment:\ Main\ loop$
  for (Step$= 1$ to Step$= N_{Steps}$)
  {
    update Material Parameters($T$);
    $//Comment:\ Rotation\ loop$
    for (Position$= 1$ to Position$= N_{Rotation}$) calculate Spatial Current;
    calculate Temperature Distribution $T\big(t = (Step-1)\cdot\triangle t, \cdots, t = Step\cdot\triangle t\big)$;
  }
}
```

Figure 1.4: Program of the magnetostatic approach

The outline of this thesis is as follows: First, the physics behind the hardening process and the numerical scheme for solving the thermal problem will be explained in the Chapter *Phase Transitions and Heat Propagation*. Then the hierarchical system of the three models for the electromagnetics is introduced in the Chapter *Electromagnetic Models and Equations*. The description starts from the most precise eddy current approach, continues with the impedance model, and ends at the most simple one, the magnetostatic approach. All the tools which are necessary to solve the developed equations of the eddy current model and the impedance model numerically, including the path algorithm and the compression technique, are presented in the Chapters *Excitation and Discretization* and *Solution Procedures*. The verification of the program with the aid of analytical solutions and the measurements of the surface temperatures is conducted in the Chapter *Validation*. The final comparison of the hardened zone in simulation and reality is shown in the Chapter *Results*. The last Chapter *Conclusions* gives a summary and presents an outlook for future studies.

Chapter 2

Phase Transitions and Heat Propagation

2.1 Solid State Physics

Steel is primarily a mixture of the crystals *ferrite* and *cementite* [BS92]. The ferrite or α-*Fe* is an undeformed body-centered cubic lattice of iron. The cementite consists of Fe_3C with 0.5 to 6 percent of carbon. Except for these states of equilibrium, steel has further meta stable phases at room temperature. They have different properties. One of these meta stable phases is *martensite*. It is hard but also brittle. The hardening process aims at this phase. Martensite can be described as a tetragonal contorted ferric lattice with homogeneously distributed and atomically dissolved carbon. Meta stable means that the time necessary to recover the state of equilibrium is much longer than the lifetime of the part. The hardening process, i.e., the transformation from ferrite to martensite, consists of two steps:

1. Heating (Formation Of Austenite)

If steel is heated above 720^oC, the α-*Fe* transforms into γ-*Fe*, which is a face-centered lattice. The carbon dissolves and diffuses in the ferric lattice, as long as it is homogeneously distributed. After a certain timespan above 720^oC, the material is transformed into *austenite*. This is a homogeneously mixed crystal of γ-*Fe* with imperfections of atomically dissolved carbon. The degree of conversion depends on the speed of heating and on the length of the timespan. The precise description of the regions where the conversion took place can be evaluated with the so-called *time-temperature-austenite-diagram* (ZTA-diagram) [Ben90]. The induction hardening takes approximately three seconds. According to the valid ZTA-diagram, those regions of the workpiece that are heated above 830^oC are considered to be hardened in the simulation.

2. Cooling (Formation Of Martensite)

If the workpiece were cooled down to room temperature the same way as it was heated up, the state of equilibrium would be recovered. So the cooling must be carried out differently. If a fast method similar to a shock is applied, then the carbon atoms stay in their positions in the lattice because diffusion is not possible. They are still homogeneously distributed and atomically dissolved, but γ-*Fe* is converted back into a ferrite. It is now tetragonal contorted due to the carbon atoms [Hor79]. In other words, if a shock-like cooling is applied, the austenite transforms into martensite. The distortion is the reason for the hardness. The material is harder if the imbedded amount of carbon is higher. Of course, this phase transition is also a time-dependent process. Based on the knowledge of the temperature distribution $T(\mathbf{r}, t)$, the hardened zone can be determined with the aid of a *time-temperature-transition-diagram* (ZTU-diagram) [BS92].

If the worpiece is heated inductively, energy will only in a thin layer at the surface be dissipated due to the skin effect. So for sufficient small heating times the workpiece is only in this layer hotter then 720^oC. Hence austenite and martensite can only be built in there, and the workpiece stays flexible in the interior, whereas it is hard and abrasion resistent on the surface.

2.2 Thermal Problem

As discussed in the last section, the thermodynamical processes that lead to a conversion of steel into the desired martensite are complicated. The precise description of the involved phase transitions is not part of this study and they are only briefly taken into account via standard techniques for the calcuation of the temperature distribution with phase changes. The heat conducting equation [LMTS96]

$$\rho \cdot c_p \cdot \frac{\partial T}{\partial t} = \mathrm{div}\,(\kappa \cdot \mathbf{grad}\, T)\ +\ \frac{\sigma \|\mathbf{E}\|^2}{2}\,, \tag{2.1}$$

with the mass density ρ, the heat capacity c_p, the heat conductivity κ, the time t, and the temperature T and has to be solved for this purpose. The source of the heat are the Ohmic losses $\frac{\sigma\|\mathbf{E}\|^2}{2}$ of the eddy current depending on the electric conductivity σ and the electric field $\mathbf{E}$. The material coefficients depend on the temperature according to Figure 5.1. These coefficients are non-smooth at the temperature of 720^oC where the phase transition takes place.

The thermal radiation at the surface has to be taken into account, thus *radiation conditions* are used as boundary conditions. It is *Stefan-Boltzmann's* law that yields the total energy density $S(T)$ of a black-body's radiation at the temperature T

$$S(T) = -\kappa \cdot \mathbf{grad}\, T \cdot \mathbf{n} = \epsilon \cdot \sigma_0 \cdot (T^4 - T_0^4)\,, \tag{2.2}$$

with the Stefan-Boltzmann constant σ_0, the outer normal vector $\mathbf{n}$, and room temperature T_0. The workpiece differs from a black-body, and an empirical factor ϵ between 0.8-0.9 is used to take care of this difference.

The temperature T in the heat conduction equation (2.1) is discretized by means of hat functions ψ_i at the N nodes $i \in \{1 \ldots N\}$ and it yields an equation of the form

$$\mathsf{M} \cdot \dot{\mathbf{T}} = \underbrace{\mathsf{K} \cdot \mathbf{T} + \mathbf{Q}}_{\mathbf{f}(\mathbf{T},t)}\,, \tag{2.3}$$

with the $(N \times N)$-dimensional matrices M, K and the vectors $\mathbf{T},\ \mathbf{Q} \in \mathbb{R}^N$ according to

$$\begin{aligned}
\mathsf{M}_{\mathsf{ij}} &:= \int_\Omega \rho\, c_p \cdot \psi_i \cdot \psi_j \, dV \,, \\
\mathsf{K}_{\mathsf{ij}} &:= -\int_\Omega \kappa \cdot \mathbf{grad}\, \psi_i \cdot \mathbf{grad}\, \psi_j \, dV \,, \\
T_i \in \mathbb{R} \,, & \\
\mathbf{Q}_i &:= \int_\Omega \frac{\sigma \|\mathbf{E}\|^2}{2} \cdot \psi_i \, dV - \int_{\partial\Omega} S \cdot \psi_i \, dS \,,
\end{aligned}$$

with $i,\ j \in \{1 \ldots N\}$. Here $\Omega \in \mathbb{R}^3$ is the conducting domain with the surface $\partial\Omega$. The equation is solved with the aid of an implicit Euler method with a forward difference scheme [LMTS96]. The scheme looks like

$$(\mathbf{M}^n + \theta \triangle t\, \mathbf{K}^n) \cdot \mathbf{T}^{n+1} \;=\; (\mathbf{M}^n - (1-\theta) \triangle t\, \mathbf{K}^n) \cdot \mathbf{T}^n + \triangle t \cdot \mathbf{Q}^n \,, \qquad (2.4)$$

with $0 < \theta < 1$. Here $\mathbf{T}^n$ denotes the vector $\mathbf{T}$ at the nth step, and the same holds for the other items. The inversion of the matrix $\mathbf{M}^n$ that is needed in each step is iteratively done with a preconditioned CG solver.

Chapter 3

Electromagnetic Models and Equations

In this chapter, the three models for the description of the electromagnetic fields are presented. They represent a hierarchical system of approximations of the *eddy current model* in frequency domain, which can be derived from the full *Maxwell equations* [Jac75]

$$
\begin{aligned}
\operatorname{div}\mathbf{D} &= \rho\ , && (3.1)\\
\operatorname{div}\mathbf{B} &= 0\ , && (3.2)\\
\mathbf{curl}\,\mathbf{E} &= -\frac{\partial \mathbf{B}}{\partial t}\ , && (3.3)\\
\mathbf{curl}\,\mathbf{H} &= \mathbf{j} + \frac{\partial \mathbf{D}}{\partial t}\ , && (3.4)
\end{aligned}
$$

with the electric displacement $\mathbf{D}$, the charge density ρ, the magnetic induction $\mathbf{B}$, the electric field $\mathbf{E}$, the time t, the magnetic field $\mathbf{H}$, and the current density $\mathbf{j}$. The eddy current model in frequency domain is a time-harmonic special case of the *quasi-static approximation* of Maxwell's equations. In this approximation the *displacement current* $\frac{\partial \mathbf{D}}{\partial t}$ in *Ampère's law* (3.4) is neglected.

The use of the quasi-static approximation should first be motivated for the case of homogeneous linear conductors $\mathbf{B} = \mu\mathbf{H}$, $\mathbf{D} = \epsilon\mathbf{E}$, $\mathbf{j} = \sigma\mathbf{E}$ with the *magnetic permeability* μ, the *dielectric constant* ϵ, and the *conductivity* σ. The two equations (3.2), (3.3) are automatically fulfilled if electromagnetic potenials $\mathbf{A}$ and ϕ with $\mathbf{B} = \mathbf{curl}\,\mathbf{A}$ and $\mathbf{E} = -(\mathbf{grad}\,\phi + \dot{\mathbf{A}})$ are employed. For the two remaining equations, it then follows

$$
\begin{aligned}
\operatorname{div}(\mathbf{grad}\,\phi + \dot{\mathbf{A}}) &= \frac{-\rho}{\epsilon}\ ,\\
\mathbf{curl}\,\mathbf{curl}\,\mathbf{A} &= -\mu\sigma(\mathbf{grad}\,\phi + \dot{\mathbf{A}}) - \frac{1}{c^2}\frac{\partial}{\partial t}(\mathbf{grad}\,\phi + \dot{\mathbf{A}})\ ,
\end{aligned}
$$

with the speed of light $c = \sqrt{\frac{1}{\epsilon\mu}}$ in the material. For time harmonic processes (where $\frac{\partial}{\partial t}$ can be replaced by $i\omega$) this means that the displacement current can be neglected if $\mu\sigma \gg \frac{\omega}{c^2}$. So for steel and copper at angular frequencies ω of some kHz the quasi-static model is a good approximation. This argumentation cannot be applied for linear non-conductors with $\sigma = 0$. In this case one has to solve the equation

$$
(\triangle - \frac{1}{c^2}\frac{\partial^2}{\partial t^2})\mathbf{A}(\mathbf{x},t) = -\mu\mathbf{j}(\mathbf{x},t) \qquad (3.5)
$$

in *Lorentz-gauge*, with the position vector $\mathbf{x}$. With the aid of retarded potentials this can be solved with [Nol90]

$$\begin{aligned}\mathbf{A}(\mathbf{x},t) &= \mathbf{A}(\mathbf{x})e^{i\omega t},\\ \mathbf{A}(\mathbf{x}) &= \frac{\mu}{4\pi}\int_{\mathbb{R}^3}\frac{e^{\frac{iw}{c}\cdot\|\mathbf{x}-\mathbf{x}'\|}}{\|\mathbf{x}-\mathbf{x}'\|}\mathbf{j}(\mathbf{x}')\,d\mathbf{x}'.\end{aligned}$$

So for the exterior vacuum, the solution of the quasi-static model $\mathbf{A}_{QS}(\mathbf{x}) = \frac{\mu}{4\pi}\int_{\mathbb{R}^3}\frac{\mathbf{j}(\mathbf{x}')}{\|\mathbf{x}-\mathbf{x}'\|}\,d\mathbf{x}'$ is a good approximation if one is only interested in a neighborhood $\|\mathbf{x}-\mathbf{x}'\| < L$ of the exciting currents [Dir96], with $wL/c \ll 1$, $L \in \mathbb{R}_{>0}$. Additionally, to neglect the displacement current always means to neglect space charges. This can be seen at the continuity equation $\operatorname{div}\mathbf{j} = -\dot{\rho}$ and (3.4). So the quasi-static model should only be applied if no big capacities are involved. The material parameters, fequencies, and lengths that are used in the inductive hardening process are in such a range, that the above constraints are fulfilled, and the quasi-static approximation would be applicable if the material was linear and homogeneous.

Steel is a non-homogeneous and ferromagnetic material, thus also non-linear, and it meets the following material relations

$$\mathbf{B} = \mu_0\,\mu_r(\|\mathbf{H}\|,T)\cdot\mathbf{H} = \mu(\|\mathbf{H}\|,T)\cdot\mathbf{H}\,, \tag{3.6}$$

$$\mathbf{D} = \epsilon_0\,\epsilon_r\,\mathbf{E} = \epsilon\,\mathbf{E}\,, \tag{3.7}$$

$$\mathbf{j} = \sigma(T)\mathbf{E}\,, \tag{3.8}$$

with the relative magnetic permeability μ_r depending on the the strength of the magnetic field and the temperature T, the constant $\epsilon_r = 1$ independent of temperature and field, and the temperature-dependent conductivity. In [ABN00] it is shown that the quasi-static approximation is also applicable for such kinds of materials in the limit of small frequencies. This is no proof that the quasi-static approximation can also be applied in the inductive hardening process, but together with the above argumentation for linear-homogeneous materials, it is a good justification.

Splitting off the time-dependency via the approach $\mathbf{B}(\mathbf{x},t) = \mathbf{B}(\mathbf{x})e^{i\omega t}$ for each field and plugging the material relationships into the quasi-static Maxwell's equations yields

$$\operatorname{div}(\epsilon\mathbf{E}) = \rho\,, \tag{3.9}$$

$$\operatorname{div}(\mu\mathbf{H}) = 0\,, \tag{3.10}$$

$$\mathbf{curl}\,\mathbf{E} = -i\omega\mu\mathbf{H}\,, \tag{3.11}$$

$$\mathbf{curl}\,\mathbf{H} = \sigma\mathbf{E}\,. \tag{3.12}$$

At the interface between two media the *jump conditions* [Jac75]

$$\sigma = [\mathbf{n}\cdot\mathbf{D}] \tag{3.13}$$

$$0 = [\mathbf{n}\cdot\mathbf{B}] \tag{3.14}$$

$$0 = [\mathbf{n}\times\mathbf{E}] \tag{3.15}$$

$$\mathbf{k} = [\mathbf{n}\times\mathbf{H}] \tag{3.16}$$

can be derived from Maxwell's equations. Here $\mathbf{n}$ is the normal on the common surface, $\mathbf{k}$ is a surface current and σ is a surface charge density. The surface items are mathematical idealizations that do not exist in physical reality. They are only useful in some special arrangements. Excess charges of a conductor, for example, are located very close to the surface within a distance of some Ångstrøms [Jac75], and the surface density σ is meaningful in a macroscopic sense. In the situation of very good conductors and high frequencies the skin effect restricts the currents to a thin layer at the surface, which from a macroscopic point of view can be seen as a surface current $\mathbf{k}$. This fact will later be used in the magnetostatic approach in Section 3.3.

At infinity the fields have to vanish in order to keep the energy of the electromagnetic fields finite, so *radiation conditions* have to be added to the eddy current model that now can be written as

$$\begin{aligned}
\operatorname{div}(\epsilon\mathbf{E}) &= \rho\,, \quad \rho \text{ has compact support}\,, && (3.17)\\
\operatorname{div}(\mu\mathbf{H}) &= 0\,, && (3.18)\\
\mathbf{curl}\,\mathbf{E} &= -i\omega\mu\mathbf{H}\,, && (3.19)\\
\mathbf{curl}\,\mathbf{H} &= \sigma\mathbf{E}\,, && (3.20)\\
[\mathbf{n}\times\mathbf{E}] &= [\mathbf{n}\times\mathbf{H}] = 0\,, && (3.21)\\
\mathbf{E}(\mathbf{x}) &= O(|\mathbf{x}|^{-2}) \quad , \quad \mathbf{H}(\mathbf{x}) = O(|\mathbf{x}|^{-2}) \quad \text{for } |\mathbf{x}| \to \infty\,. && (3.22)
\end{aligned}$$

The solutions for the electric field $\mathbf{E}$ and the magnetic field $\mathbf{H}$ have to be part of the Hilbert space $\mathbf{X}(\mathbb{R}^3) := \mathbf{H}(\mathbf{curl}, \mathbb{R}^3) \cap \mathbf{H}(\operatorname{div}, \mathbb{R}^3)$, where for an open subset Ω of $\mathbb{R}^3$

$$\begin{aligned}
\mathbf{H}(\mathbf{curl},\Omega) &:= \left\{\mathbf{v}\in\mathbf{L}^2(\Omega);\ \mathbf{curl}\,\mathbf{v}\in\mathbf{L}^2(\Omega)\right\}\,, && (3.23)\\
\mathbf{H}(\operatorname{div},\Omega) &:= \left\{\mathbf{v}\in\mathbf{L}^2(\Omega);\ \operatorname{div}\mathbf{v}\in L^2(\Omega)\right\}\,, && (3.24)\\
L^2(\Omega) &:= \left\{v\,:\,\Omega\to\mathbb{R}\,, \|v\|_{L^2(\Omega)} := \left[\int_\Omega |v(\mathbf{x})|^2\,d\mathbf{x}\right]^{\frac{1}{2}} < \infty\right\}\,, && (3.25)\\
\mathbf{L}^2(\Omega) &:= L^2(\Omega)^3\,, && (3.26)
\end{aligned}$$

equipped with the norms

$$\begin{aligned}
\|\mathbf{v}\|^2_{\mathbf{L}^2(\Omega)} &:= \int_\Omega |v_1(\mathbf{x})|^2 + |v_2(\mathbf{x})|^2 + |v_3(\mathbf{x})|^2\,d\mathbf{x} && (3.27)\\
\|\mathbf{v}\|^2_{\mathbf{H}(\mathbf{curl},\Omega)} &:= \|\mathbf{v}\|^2_{\mathbf{L}^2(\Omega)} + \|\,\mathbf{curl}\,\mathbf{v}\|^2_{\mathbf{L}^2(\Omega)}\,, && (3.28)\\
\|\mathbf{v}\|^2_{\mathbf{H}(\operatorname{div},\Omega)} &:= \|\mathbf{v}\|^2_{\mathbf{L}^2(\Omega)} + \|\operatorname{div}\mathbf{v}\|^2_{L^2(\Omega)}\,, && (3.29)\\
\|\mathbf{v}\|^2_{\mathbf{X}(\Omega)} &:= \|\mathbf{v}\|^2_{\mathbf{L}^2(\Omega)} + \|\,\mathbf{curl}\,\mathbf{v}\|^2_{\mathbf{L}^2(\Omega)} + \|\operatorname{div}\mathbf{v}\|^2_{L^2(\Omega)}\,. && (3.30)
\end{aligned}$$

Note that the norm $\|\mathbf{E}\|^2_{\mathbf{X}(\mathbb{R}^3)}$ is strongly related to the energy of the electromagnetic fields, at least in the charge free case. Divergence and curl have to be understood in the sense of distributions [Wlo82], since the fields may have discontinuities, for example at the interface of two media.

In this work an $\mathbf{E}$-based formulation is used and the magnetic field is eliminated. Then it holds

$$\begin{aligned} \operatorname{div}(\epsilon \mathbf{E}) &= \rho\,, \quad \text{in}\,\Omega^+\,, && (3.31)\\ \mathbf{curl}\,\frac{1}{\mu}\,\mathbf{curl}\,\mathbf{E} &= -i\omega\sigma\mathbf{E}\,, \quad \text{in}\,\mathbb{R}^3\,, && (3.32)\\ [\mathbf{n}\times\mathbf{E}] &= [\mathbf{n}\times\frac{1}{\mu}\,\mathbf{curl}\,\mathbf{E}] = 0\,, \quad \text{at}\,\partial\Omega^-, && (3.33)\\ \mathbf{E}(\mathbf{x}) = O(|\mathbf{x}|^{-2})\,, \quad \mathbf{curl}\,\mathbf{E}(\mathbf{x}) &= O(|\mathbf{x}|^{-2})\,, \quad \text{for}\,|\mathbf{x}|\to\infty\,, && (3.34) \end{aligned}$$

with the conducting domain Ω^- and the exterior vacuum $\Omega^+ = \mathbb{R}^3 \setminus \Omega^-$. The central equation (3.32) is valid everywhere, whereas Coulomb's law (3.31) can only be applied in Ω^+. The reason is that the eddy current model is only an approximation of Maxwell's equations, and if one applies the div-operator on (3.32) there might be inconsistencies in the conducting region Ω^- with $\sigma \neq 0$. So Coulomb's law is a kind of gauging in this model. The jump conditions (3.33) which are chosen at the interface of conducting and non-conducting region are the transmission conditions of normal and tangential component of the electric field.

To find a viable numerical scheme for solving the eddy current model is not an easy task, mainly because of three physical reasons: First, the permeability μ depends on the strength of the magnetic field $\mathbf{H}$, which leads to a non-linear problem in the interior of the conductors. Second, the dominant *skin effect* is a purely local effect, and only adaptively refined grids can be used if the effect is to be resolved and if the amount of storage has to remain sufficiently small at the same time. Third, one has to tackle the unbounded exterior domain.

As far as the interior of the conductors is concerned, a finite element scheme (FEM) based on edge elements offers the most attractive option [Bos98], [Mon92]. Their use is mandatory in order to capture the singularities of the fields at material interfaces [BBHL99], [Bos99], [CDN99], as for example at the interface plates/workpiece. Nodal formulations cannot be used because of their difficulties with the singularities of the fields at reentrant corners [PBT00]. Additionally, a *relaxation method* is used for the non-linear part of the calculation arising from the field dependency of the permeability. To approach the exterior, one often extends the mesh from the interior to the exterior region, and homogeneous boundary conditions are introduced in a sufficiently large distance from the conductors. This technique is not applicable here because the workpiece is rotating. A boundary element method (BEM) is used to deal with the unbounded exterior. So it is possible to use only one Lagrangian mesh that is rotating.

The FEM/BEM parts can be linked properly [Hip02] and the resulting numerical scheme is called eddy current approach. A quasi-optimal error etimator exists for this approach that guarantees the convergence of a conforming Garlerkin discretization. This means that the difference between the approximative numerical solution and the real solution of (3.17)-(3.22) vanishes for decreasing meshwidth $h \to 0$. In the eddy current approach the coupling is strong and symmetric, i.e., FEM and BEM variables are tackled simultaneously in the same symmetric system of equations. The convergence of an iterative solver can be guaranteed. The implementation of the model is complicated because of different reasons. In the interior one has to deal not only with the linear equations of a uniform mesh, but also with adaptive mesh refinement and non-linear methods for the permeability. The temperature distribution has to be calculated there, too. On the boundary, elaborate BEM operators have to be implemented. They need a special treatment if the items have a non-trivial topology. A compression technique also has to be applied for the BEM operators because of the huge amount of storage that they need. So what is desireable is a possibilty to develop the FEM/BEM parts independently, i.e., one searches elctromagnetic models where only a weak coupling of FEM and BEM variables is required.

Such kinds of models can be found by studying the most dominant physical effect, the skin effect. This should first be done for an idealized situation: At the surface of a flat semi-definite, conducting, permeable, and linear medium, a spatially constant magnetic field, $H_x(t) = H_0 \cos \omega t$, is applied parallel to the surface, as shown in Figure 3.1. Then the solutions of (3.17)-(3.22) for the magnetic field and the electric field are given [Jac75] by the real parts of

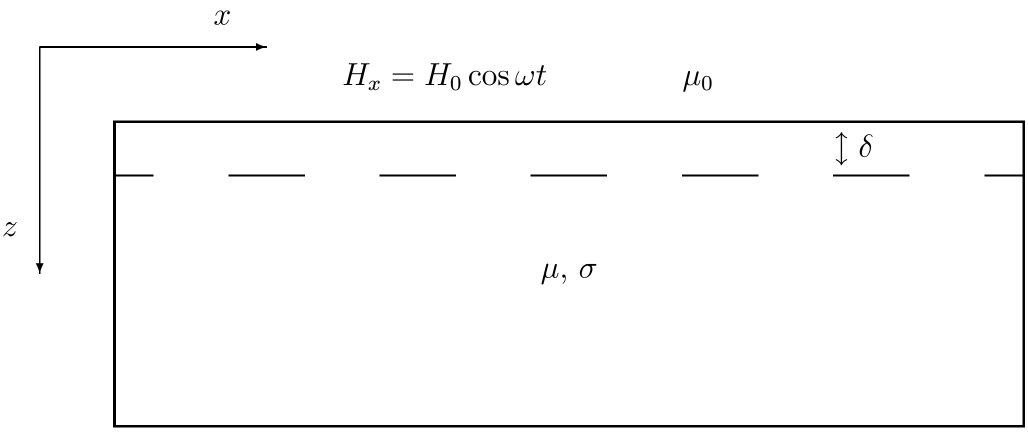

Figure 3.1: Skin effect

$$H_x = H_0 e^{-z/\delta} e^{-i(z/\delta - \omega t)}, \tag{3.35}$$

$$E_y = -(1+i)\sqrt{\frac{\mu\omega}{2\sigma}} H_0 e^{-z/\delta} e^{-i(z/\delta - \omega t)}, \tag{3.36}$$

with the *penetration depth*

$$\delta := \sqrt{\frac{2}{\mu\sigma\omega}}. \tag{3.37}$$

So fields and currents are decreasing in the interior of the conductors and for steel with the given material parameters, frequencies and temperatures one finds a penetration depth in the range of $[0.05mm - 6.0mm]$. A first possibility for an approximation is to neglect the fields in the interior. This leads to the magnetostatic approach of Chapter 3.3, which is only a rough approximation because the penetration depth of some millimeters at high temperatures and strong fields is not small enough to get a good approximation. Another observation is that for flat surfaces the so-called *impedance boundary condition* [SS01]

$$\mathbf{n} \times \mathbf{E} = \eta_1 \cdot \mathbf{n} \times (\mathbf{n} \times \mathbf{H}), \tag{3.38}$$

$$\text{with } \eta_1 := (1+i)\sqrt{\frac{\mu\omega}{2\sigma}}, \tag{3.39}$$

is valid on the surface with outer normal $\mathbf{n}$. This condition can also be used for the decoupling of FEM and BEM part and it follows the impedance model of Chapter 3.2. The implementation of this model is as complex as the implementation of the full eddy current approach because all fundamental components are required, such as the BEM operators, the FEM operators, compression, non-linearity, and adaptivity. But due to the weak coupling it can be programmed by different persons using different software packages, which is a big advantage.

The three schemes are introduced in the following sections. For sake of clear derivations of the central model equations, the necessary mathematical tools are provided in advance in a short introduction at the beginning of the sections.

3.1 Eddy Current Approach

3.1.1 Mathematical Prerequisites

The eddy current approach is a numerical scheme for solving the equations (3.17)-(3.22). The variational formulation is discretized with a Garlerkin method, and unique solvability can be shown with the aid of the *Lax-Milgram theorem*. First of all, this fundamental theorem will be introduced [DL90]. Then a representation formula is presented which is needed to derive the BEM equations of the exterior domain by taking the Dirichlet and Neumann traces. A summary of the properties of the resulting BEM operators is given at the end of this section.

Definition 1 (Sesquilinear Form) *Let V be a vector space on $\mathbb{C}$. A sesquilinear form $(u,v) \to a(u,v)$ on $V \times V$, is a mapping $V \times V \to \mathbb{C}$, with the properties*

$$\begin{aligned} a(u_1+u_2,v) &= a(u_1,v)+a(u_2,v), \\ a(u,v_1+v_2) &= a(u,v_1)+a(u,v_2), \\ a(\lambda u,v) &= \lambda a(u,v), \\ a(u,\lambda v) &= \bar{\lambda} a(u,v). \end{aligned}$$

Definition 2 (Continuous Sesquilinear Form) *Let V be a complex Hilbert space equipped with the norm $\|\cdot\|_V$. The sesquilinear form $(u,v) \to a(u,v)$ on $V \times V$ is called continuous if there exists a constant $c > 0$ with*

$$|a(u,v)| \leq c \cdot \|u\|_V \, \|v\|_V \quad \forall u,v \in V \, .$$

Definition 3 (Antilinear Form, Antidual) *Let V be a topological space over the field $\mathbb{R}$ or $\mathbb{C}$. An antilinear form L on V is an antilinear mapping of V into $\mathbb{C}$:*

$$\begin{aligned} L(v_1+v_2) &= L(v_1)+L(v_2) \\ L(\lambda v) &= \bar{\lambda} L(v) \quad \forall v_1,v_2 \in V \, , \quad \lambda \in \mathbb{C} \end{aligned}$$

The space of the continous antilinear forms [DL90] is called the antidual and is here denoted by V'.

Theorem 1 (Lax-Milgram Theorem) *Let V be a complex Hilbert space equipped with the norm $\| \cdot \|_V$, $a(u,v)$ a continous sesquilinear form on $V \times V$, and $L \in V'$ a continuous antilinear form on V. Then the problem:*

$$\text{Find } u \in V \text{ such that} \quad a(u,v) = L(v), \quad \forall v \in V,$$

is called a variational problem. It has a unique solution if the sesquilinear form $a(u,v)$ is V-elliptic, i.e., if there exists a constant $c > 0$ with

$$|a(v,v)| \quad \geq \quad c \cdot \|v\|_V^2 \quad \forall v \in V$$

Theorem 2 (Representation Formula [Hip02]) *Let $\Omega \subset \mathbb{R}^3$ be a Lipschitz domain with exterior unit normal $\mathbf{n}$ and G the singular function for the Laplacian in three dimensions*

$$G(\mathbf{x},\mathbf{y}) := \frac{1}{4\pi} \frac{1}{|\mathbf{x}-\mathbf{y}|}, \quad \mathbf{x},\, \mathbf{y} \,\in \mathbb{R}^3,\ \mathbf{x} \neq \mathbf{y}. \tag{3.40}$$

If $\mathbf{E} \in C^2(\bar{\Omega})^3$ is a vector field with $\operatorname{div} \mathbf{E}$ and $\mathbf{curl}\,\mathbf{curl}\,\mathbf{E}$ compactly supported and decaying uniformly for $|\mathbf{x}| \to \infty$ like $\mathbf{E}(\mathbf{x}) = O(|\mathbf{x}|^{-1})$ and $\mathbf{curl}\,\mathbf{E}(\mathbf{x}) = O(|\mathbf{x}|^{-1})$, then it holds with $\Gamma := \partial\Omega$

$$\begin{aligned}\mathbf{E}(\mathbf{x}) = &- \mathbf{curl}_\mathbf{x} \int\limits_\Gamma (\mathbf{n} \times \mathbf{E})(\mathbf{y}) G(\mathbf{x},\mathbf{y})\, dS(\mathbf{y}) + \int\limits_\Gamma (\mathbf{n} \times \mathbf{curl}\,\mathbf{E})(\mathbf{y}) G(\mathbf{x},\mathbf{y})\, dS(\mathbf{y}) + \\ &+ \mathbf{grad}_\mathbf{x} \int\limits_\Gamma (\mathbf{n} \cdot \mathbf{E})(\mathbf{y}) G(\mathbf{x},\mathbf{y})\, dS(\mathbf{y}) + \int\limits_\Omega \mathbf{curl}\,\mathbf{curl}\,\mathbf{E}(\mathbf{y}) G(\mathbf{x},\mathbf{y})\, d\mathbf{y} - \\ &- \int\limits_\Omega \operatorname{div} \mathbf{E}(\mathbf{y})\, \mathbf{grad}_\mathbf{x}\, G(\mathbf{x},\mathbf{y})\, d\mathbf{y} \quad , \ \mathbf{x} \in \Omega\,. \end{aligned} \tag{3.41}$$

This is an analogy to the Stratton-Chu formulas for the full Maxwell equations. Subsequently domains, normals, and fields are defined in correspondence with Figure 3.2.

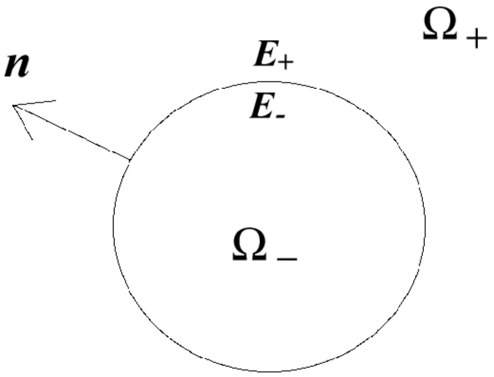

Figure 3.2: Definitions of the domains

The following limits, traces, and boundary operators are needed

$$\mathbf{E}_{\pm} := \lim_{t\to\pm 0} \mathbf{E}(\mathbf{x}+t\mathbf{n})\,, \tag{3.42}$$

$$\gamma_T^{\pm}\mathbf{E}(\mathbf{x}) := \lim_{t\to\pm 0} \mathbf{E}(\mathbf{x}+t\mathbf{n})\times\mathbf{n}\,, \tag{3.43}$$

$$\gamma_D^{\pm}\mathbf{E}(\mathbf{x}) := \mathbf{n}\times\big(\lim_{t\to\pm 0} \mathbf{E}(\mathbf{x}+t\mathbf{n})\times\mathbf{n}\big)\,, \tag{3.44}$$

$$\text{If } \gamma_D^{+}\mathbf{E}(\mathbf{x}) = \gamma_D^{-}\mathbf{E}(\mathbf{x}) \text{ set } \gamma_D\mathbf{E}(\mathbf{x}) := \gamma_D^{+}\mathbf{E}(\mathbf{x})\,, \tag{3.45}$$

$$\gamma_N^{\pm}\mathbf{E}(\mathbf{x}) := \lim_{t\to\pm 0} \big(\mathbf{curl}\,\mathbf{E}(\mathbf{x}+t\mathbf{n})\big)\times\mathbf{n}\,, \tag{3.46}$$

$$\text{If } \gamma_N^{+}\mathbf{E}(\mathbf{x}) = \gamma_N^{-}\mathbf{E}(\mathbf{x}) \text{ set } \gamma_N\mathbf{E}(\mathbf{x}) := \gamma_N^{+}\mathbf{E}(\mathbf{x})\ , \tag{3.47}$$

$$\boldsymbol{\lambda}_{\pm} := \frac{1}{\mu_{\pm}}(\mathbf{curl}\,\mathbf{E}_{\pm}\times\mathbf{n})\,, \tag{3.48}$$

$$\mathbf{CE} := \gamma_D^{+}\ \mathbf{curl}_{\mathbf{x}} \int_{\Gamma} (\mathbf{n}\times\mathbf{E})(\mathbf{y})G(\mathbf{x},\mathbf{y})\,dS(\mathbf{y})\,, \tag{3.49}$$

$$\mathbf{A}\boldsymbol{\lambda} := \gamma_D \int_{\Gamma} \boldsymbol{\lambda}(\mathbf{y})G(\mathbf{x},\mathbf{y})\,dS(\mathbf{y}) \tag{3.50}$$

$$\mathbf{SE} := \gamma_D^{+}\ \mathbf{grad}_{\mathbf{x}} \int_{\Gamma} (\mathbf{n}\cdot\mathbf{E})(\mathbf{y})G(\mathbf{x},\mathbf{y})\,dS(\mathbf{y})\,, \tag{3.51}$$

$$\mathbf{NE} := \gamma_N\ \mathbf{curl}_{\mathbf{x}} \int_{\Gamma} (\mathbf{n}\times\mathbf{E})(\mathbf{y})G(\mathbf{x},\mathbf{y})\,dS(\mathbf{y})\,, \tag{3.52}$$

$$\mathbf{B}\boldsymbol{\lambda} := \gamma_N^{+} \int_{\Gamma} \boldsymbol{\lambda}(\mathbf{y})G(\mathbf{x},\mathbf{y})\,dS(\mathbf{y})\,. \tag{3.53}$$

The BEM operators $\mathbf{C},\mathbf{A},\mathbf{S},\mathbf{N},\mathbf{B}$ exist because the following potentials are continuous mappings

$$\int_{\Gamma} E(\mathbf{y})G(\mathbf{x},\mathbf{y})\,dS(\mathbf{y}) \quad : \quad H^{-\frac{1}{2}}(\Gamma)\to H^1_{loc}(\mathbb{R}^3)\,, \tag{3.54}$$

$$\mathbf{p}_V := \int_{\Gamma} \mathbf{E}(\mathbf{y})G(\mathbf{x},\mathbf{y})\,dS(\mathbf{y}) \quad : \quad \mathbf{H}^{-\frac{1}{2}}(\Gamma)\to \mathbf{H}^1_{loc}(\mathbb{R}^3)\,, \tag{3.55}$$

$$\mathbf{p}_M := \mathbf{curl}_{\mathbf{x}} \int_{\Gamma} (\mathbf{n}\times\mathbf{E})(\mathbf{y})G(\mathbf{x},\mathbf{y})\,dS(\mathbf{y}) \quad : \quad \mathbf{H}_{\perp}^{-\frac{1}{2}}(\Gamma)\to \mathbf{H}(\mathrm{div};\mathbb{R}^3)\,. \tag{3.56}$$

For the definitions of the spaces see the next page and [DL90]. It holds $[\gamma_D\mathbf{p}_V] = [\gamma_N\mathbf{p}_M] = 0$ on the boundary, and the traces γ_D^{+}, γ_N^{+} in $\mathbf{A}$ and $\mathbf{N}$ can be replaced by γ_D and γ_N, see [Hip02] for proofs. The exterior Dirichlet and Neumann traces $\gamma_D^{+},\ \gamma_N^{+}$ can be applied on the representation formula and it follows for constant μ_+ and fields with $\mathbf{curl}\,\mathbf{curl}\,\mathbf{E} = 0$ and $\mathrm{div}\,\mathbf{E} = 0$ that

$$\gamma_D^{+}\mathbf{E}_{+} = \mathbf{CE}_{+} + \mu_{+}\mathbf{A}\boldsymbol{\lambda}_{+} - \mathbf{SE}_{+}\,, \tag{3.57}$$

$$\gamma_N^{+}\mathbf{E}_{+} = \mathbf{NE}_{+} + \mu_{+}\mathbf{B}\boldsymbol{\lambda}_{+}\,. \tag{3.58}$$

This can be transformed into

$$\begin{aligned} \gamma_D^+ \mathbf{E}_+ &= \mathbf{C}(\gamma_D^+ \mathbf{E}_+) + \mu_+ \mathbf{A} \boldsymbol{\lambda}_+ - \mathbf{S}\mathbf{E}_+ \qquad (3.59)\\ \mu_+ \boldsymbol{\lambda}_+ &= \mathbf{N}(\gamma_D^+ \mathbf{E}_+) + \mu_+ \mathbf{B} \boldsymbol{\lambda}_+ . \qquad (3.60) \end{aligned}$$

because of $\gamma_N^+ \mathbf{E}_+ = \mu_+ \boldsymbol{\lambda}_+$, $\mathbf{CE} = \mathbf{C}(\gamma_D^+ \mathbf{E})$, and $\mathbf{NE} = \mathbf{N}(\gamma_D^+ \mathbf{E})$. The spaces where the BEM operators act must be defined precisely for further mathematical analyses. They should not be derived in detail here, but motivated [AH01] by looking at the *Sobolev space*

$$H^1(\Omega) \ := \ \left\{ v \in L^2(\Omega);\ D^\alpha v \in L^2(\Omega) \quad \forall\, |\alpha| \le 1 \right\} . \qquad (3.61)$$

This is the space of all square-integrable functions $v \in L^2(\Omega)$ with each first weak derivative $D^\alpha v \in L^2(\Omega)$ square-integrable. It is an interesting space because each component of $\mathbf{X}(\mathbb{R}^3)$ can also be differentiated once. The *trace theorem* ensures that for *Lipschitz* domains Ω the range of the Dirichlet trace $\gamma_D(H^1(\Omega))$ is another Sobolev space $H^{\frac{1}{2}}(\partial\Omega)$ over the boundary $\partial\Omega$ and equipped with its own norm $\|\cdot\|_{H^{\frac{1}{2}}(\Omega)}$. Its dual is here denoted by $H^{-\frac{1}{2}}(\partial\Omega)$ and $\mathbf{H}^{\frac{1}{2}}(\Gamma)$, $\mathbf{H}^{-\frac{1}{2}}(\Gamma)$ are the three dimensional counterparts. The traces γ_D and γ_T are mappings on $\mathbf{H}_{||}^{\frac{1}{2}}(\Gamma)$, $\mathbf{H}_{\perp}^{\frac{1}{2}}(\Gamma)$, which are generalizations of $\mathbf{H}^{\frac{1}{2}}(\Gamma)$ for non smooth Γ. Roughly speaking, $\mathbf{H}_{||}^{\frac{1}{2}}(\Gamma)$ contains the tangential surface vector fields which are in $\mathbf{H}^{\frac{1}{2}}(\Gamma_i)$ for each smooth component Γ_i of Γ and feature a suitable 'weak tangential continuity' across the edges of the Γ_i. A corresponding 'weak normal continuity' is satisfied by surface vector fields in $\mathbf{H}_{\perp}^{\frac{1}{2}}(\Gamma)$. The associated dual spaces will be denoted by $\mathbf{H}_{||}^{-\frac{1}{2}}(\Gamma), \mathbf{H}_{\perp}^{-\frac{1}{2}}(\Gamma)$. For details and notations see [BC01]. There it is also shown that both traces γ_D and γ_N are continuous mappings

$$\begin{aligned} \gamma_D \ &: \ \boldsymbol{H}(\mathbf{curl};\Omega) \mapsto \mathbf{H}_{\perp}^{-\frac{1}{2}}(\mathrm{curl}_\Gamma, \Gamma)\,, \qquad (3.62)\\ \gamma_N \ &: \ \{\mathbf{v} \in \boldsymbol{H}(\mathbf{curl};\Omega),\ \mathbf{curl}\,\mathbf{curl}\,\mathbf{v} = 0\} \mapsto \mathbf{H}_{||}^{-\frac{1}{2}}(\mathrm{div}_\Gamma, \Gamma)\,, \qquad (3.63) \end{aligned}$$

with

$$\begin{aligned} \mathbf{H}_{\perp}^{-\frac{1}{2}}(\mathrm{curl}_\Gamma, \Gamma) \ &:= \ \{\mathbf{v} \in \mathbf{H}_{\perp}^{-\frac{1}{2}}(\Gamma),\ \mathrm{curl}_\Gamma\, \mathbf{v} \in H^{-\frac{1}{2}}(\Gamma)\}\,, \qquad (3.64)\\ \mathbf{H}_{||}^{-\frac{1}{2}}(\mathrm{div}_\Gamma, \Gamma) \ &:= \ \{\mathbf{v} \in \mathbf{H}_{||}^{-\frac{1}{2}}(\Gamma),\ \mathrm{div}_\Gamma \mathbf{v} \in H^{-\frac{1}{2}}(\Gamma)\}\,, \qquad (3.65)\\ curl_\Gamma \mathbf{v} \ &:= \ \mathbf{n} \cdot (\mathbf{curl}\,\mathbf{V})\,, \qquad (3.66)\\ \mathbf{grad}_\Gamma\, \phi \ &:= \ \mathbf{n} \times (\mathbf{grad}\, \Phi \times \mathbf{n})\,, \qquad (3.67)\\ \mathrm{div}_\Gamma \ &:= \ -\mathbf{grad}_\Gamma^* \ . \qquad (3.68) \end{aligned}$$

Here ϕ is a function on the boundary and $\mathbf{v}$ is a tangential vectorfield on the boundary. Φ and $\mathbf{V}$ are their extensions in the normal direction. The occuring BEM operators are examined in [Hip02]. A first property is represented by the fact that they define continuous linear mappings

$$\begin{aligned} \mathbf{A} \ &: \ \mathbf{H}_{||}^{-\frac{1}{2}}(\Gamma) \mapsto \mathbf{H}_{||}^{\frac{1}{2}}(\Gamma)\,, \qquad (3.69)\\ \mathbf{B} \ &: \ \mathbf{H}_{||}^{-\frac{1}{2}}(\mathrm{div}_\Gamma, \Gamma) \mapsto \mathbf{H}_{||}^{-\frac{1}{2}}(\mathrm{div}_\Gamma, \Gamma)\,, \qquad (3.70)\\ \mathbf{C} \ &: \ \mathbf{H}_{\perp}^{-\frac{1}{2}}(\mathrm{curl}_\Gamma, \Gamma) \mapsto \mathbf{H}_{\perp}^{-\frac{1}{2}}(\mathrm{curl}_\Gamma, \Gamma)\,, \qquad (3.71)\\ \mathbf{N} \ &: \ \mathbf{H}_{\perp}^{-\frac{1}{2}}(\mathrm{curl}_\Gamma, \Gamma) \mapsto \mathbf{H}_{||}^{-\frac{1}{2}}(\mathrm{div}_\Gamma, \Gamma)\,. \qquad (3.72) \end{aligned}$$

Later, the vector fields $\mathbf{E}$ in the BEM operators (3.42)-(3.53) will be identified with the electric field. As a first physical statement, it should be pointed out that a current cannot flow through the surface of a conductor. As a consequence, it follows $\boldsymbol{\lambda} \in \mathbf{H}_{||}^{-\frac{1}{2}}(\mathrm{div}_\Gamma 0, \Gamma)$ with

$$\mathbf{H}_{||}^{-\frac{1}{2}}(\mathrm{div}_\Gamma 0, \Gamma) \;:=\; \{\boldsymbol{\lambda} \in \mathbf{H}_{||}^{-\frac{1}{2}}(\mathrm{div}_\Gamma, \Gamma),\, \mathrm{div}_\Gamma \boldsymbol{\lambda} = 0\}. \tag{3.73}$$

This can be seen by applying the relation $\mathrm{div}_\Gamma(\mathbf{u} \times \mathbf{n}) = \mathbf{curl}\,\mathbf{u} \cdot \mathbf{n}$ to the definition of $\boldsymbol{\lambda}$ in (3.48)

$$\mathrm{div}_\Gamma\, \boldsymbol{\lambda} = \mathrm{div}_\Gamma(\frac{1}{\mu}\,\mathbf{curl}\,\mathbf{E} \times \mathbf{n}) = \mathbf{curl}\,\frac{1}{\mu}\,\mathbf{curl}\,\mathbf{E} \cdot \mathbf{n} = -i\omega\sigma \mathbf{E} \cdot \mathbf{n} = -i\omega \mathbf{j} \cdot \mathbf{n}\,. \quad \square$$

The inner product $\langle :, : \rangle_{\boldsymbol{\tau}}$ is defined as

$$\langle \mathbf{a}, \mathbf{b} \rangle_{\boldsymbol{\tau}} := \int_\Gamma \mathbf{a}(\mathbf{x}) \cdot \overline{\mathbf{b}(\mathbf{x})}\, dS(\mathbf{x}) \tag{3.74}$$

on the boundary, and it holds

$$\begin{aligned}
\langle \boldsymbol{\zeta}, \mathbf{S}\,\mathbf{E} \rangle_{\boldsymbol{\tau}} &= \int_\Gamma \boldsymbol{\zeta}(\mathbf{x}) \cdot \overline{\gamma_D^+\ \mathbf{grad}_\mathbf{x} \int_\Gamma (\mathbf{n} \cdot \mathbf{E})(\mathbf{y}) G(\mathbf{x}, \mathbf{y})\, dS(\mathbf{y})}\, dS(\mathbf{x}) \\
&= \int_\Gamma \boldsymbol{\zeta}(\mathbf{x}) \cdot \overline{\mathbf{grad}_\Gamma \int_\Gamma (\mathbf{n} \cdot \mathbf{E})(\mathbf{y}) G(\mathbf{x}, \mathbf{y})\, dS(\mathbf{y})}\, dS(\mathbf{x}) \\
&= -\int_\Gamma \mathrm{div}_\Gamma\, \boldsymbol{\zeta}(\mathbf{x}) \cdot \overline{\int_\Gamma (\mathbf{n} \cdot \mathbf{E})(\mathbf{y}) G(\mathbf{x}, \mathbf{y})\, dS(\mathbf{y})}\, dS(\mathbf{x}) \\
&= 0 \qquad \forall \boldsymbol{\zeta} \in \mathbf{H}_{||}^{-\frac{1}{2}}(\mathrm{div}_\Gamma\, 0, \Gamma)\,.
\end{aligned} \tag{3.75}$$

The following properties of the BEM operators are derived in [Hip02].

$$\langle \mathbf{B}\boldsymbol{\zeta}, \mathbf{q} \rangle_{\boldsymbol{\tau}} = \langle \boldsymbol{\zeta}, (\mathbf{C} - Id)\mathbf{q} \rangle_{\boldsymbol{\tau}} \quad \forall \mathbf{q} \in \mathbf{H}_{\perp}^{-\frac{1}{2}}(\mathrm{curl}_\Gamma, \Gamma), \boldsymbol{\zeta} \in \mathbf{H}_{||}^{-\frac{1}{2}}(\mathrm{div}_\Gamma 0, \Gamma)\,. \tag{3.76}$$

Theorem 3 *The bilinear form on* $\mathbf{H}_{||}^{-\frac{1}{2}}(\mathrm{div}_\Gamma 0, \Gamma)$ *induced by the operator* $\mathbf{A}$ *is symmetric*

$$\langle \mathbf{A}\boldsymbol{\zeta}, \boldsymbol{\eta} \rangle_{\boldsymbol{\tau}} = \langle \boldsymbol{\zeta}, \mathbf{A}\boldsymbol{\eta} \rangle_{\boldsymbol{\tau}} \quad \forall \boldsymbol{\zeta}, \boldsymbol{\eta} \in \mathbf{H}_{||}^{-\frac{1}{2}}(\mathrm{div}_\Gamma 0, \Gamma)\,, \tag{3.77}$$

and there is a constant $c > 0$ *depending on* Γ *such that*

$$\langle \mathbf{A}\boldsymbol{\lambda}, \boldsymbol{\lambda} \rangle_{\boldsymbol{\tau}} \geq c\, \|\boldsymbol{\lambda}\|^2_{\mathbf{H}_{||}^{-\frac{1}{2}}(\mathrm{div}_\Gamma, \Gamma)} \qquad \forall \boldsymbol{\lambda} \in \mathbf{H}_{||}^{-\frac{1}{2}}(\mathrm{div}_\Gamma 0, \Gamma)\,. \tag{3.78}$$

Theorem 4 *The bilinear form induced by the boundary integral operator* $\mathbf{N}$ *on* $\mathbf{H}_{\perp}^{-\frac{1}{2}}(\mathrm{curl}_\Gamma, \Gamma)$ *is symmetric*

$$\langle \mathbf{p}, \mathbf{N}\mathbf{q} \rangle_{\boldsymbol{\tau}} = \langle \mathbf{N}\mathbf{p}, \mathbf{q} \rangle_{\boldsymbol{\tau}} \quad \forall \mathbf{p}, \mathbf{q} \in \mathbf{H}_{\perp}^{-\frac{1}{2}}(\mathrm{curl}_\Gamma, \Gamma)\,, \tag{3.79}$$

and negative semidefinite. In particular,

$$-\langle \mathbf{N}\mathbf{u}, \mathbf{u} \rangle_{\boldsymbol{\tau}} \geq c\, \|\mathrm{curl}_\Gamma\, \mathbf{u}\|^2_{H^{-\frac{1}{2}}(\Gamma)} \qquad \forall \mathbf{u} \in \mathbf{H}_{\perp}^{-\frac{1}{2}}(\mathrm{curl}_\Gamma, \Gamma)\,, \tag{3.80}$$

holds for some constant $c > 0$.

3.1.2 Symmetric FEM/BEM-Coupling

After this formal preparation, the system of equations used in the eddy current approach can now be derived. In the two different regions Ω_- of the conductors and their exterior Ω_+ (see Figure 3.2), the fundamental equations (3.31)-(3.34) can be written as

$$\mathbf{curl}\,\frac{1}{\mu_-}\,(\mathbf{curl}\,\mathbf{E}_-) \;=\; -i\omega(\sigma\mathbf{E}_- + \mathbf{j}_0) \qquad \forall \mathbf{x} \in \Omega_- \tag{3.81}$$

and

$$\operatorname{div}\mathbf{E}_+ \;=\; 0\,, \tag{3.82}$$

$$\mathbf{curl}\,\mathbf{curl}\,\mathbf{E}_+ \;=\; 0\,, \qquad \forall \mathbf{x} \in \Omega_+\,. \tag{3.83}$$

In the first equation the exciting current $\mathbf{j}_0$ is added and it holds for the real current $\mathbf{j} = \sigma\mathbf{E}_- + \mathbf{j}_0$. The excitation will be specified more precisely in Chapter 4. The jump conditions on the boundary $\partial\Omega_-$ are

$$0 \;=\; \mathbf{n} \times (\mathbf{E}_+ - \mathbf{E}_-)\,, \tag{3.84}$$

$$0 \;=\; \frac{1}{\mu_-}(\mathbf{curl}\,\mathbf{E}_- \times \mathbf{n}) - \frac{1}{\mu_+}(\mathbf{curl}\,\mathbf{E}_+ \times \mathbf{n}) \;=\; \boldsymbol{\lambda}_- - \boldsymbol{\lambda}_+\,. \tag{3.85}$$

Conclusions:

$$\gamma_D\mathbf{E} \;:=\; \gamma_D^-\mathbf{E} = \gamma_D^+\mathbf{E} \tag{3.86}$$

$$\boldsymbol{\lambda} \;:=\; \boldsymbol{\lambda}_- = \boldsymbol{\lambda}_+\,, \tag{3.87}$$

so there is no need to distinguish between the variables of the exterior and the variables of the interior. The equation of the interior domain follows from equation (3.81) by testing and by applying Stoke's theorem

$$-i\omega\int\limits_{\Omega_-}(\sigma\mathbf{E} + \mathbf{j}_0)\cdot\overline{\mathbf{v}}\,d\mathbf{y} = \int\limits_{\Omega_-}\mathbf{curl}\,[\frac{1}{\mu}\,\mathbf{curl}\,\mathbf{E}]\cdot\overline{\mathbf{v}}\,d\mathbf{y}\,, \tag{3.88}$$

$$\Longleftrightarrow$$

$$-i\omega\int\limits_{\Omega_-}(\sigma\mathbf{E} + \mathbf{j}_0)\cdot\overline{\mathbf{v}}\,d\mathbf{y} = \int\limits_{\Omega_-}\frac{1}{\mu}\,\mathbf{curl}\,\mathbf{E}\cdot\mathbf{curl}\,\overline{\mathbf{v}}\,d\mathbf{y} - \int\limits_{\Gamma}(\frac{1}{\mu}\,\mathbf{curl}\,\mathbf{E}\times\mathbf{n})\cdot\overline{\mathbf{v}}\,dS(\mathbf{y})\,. \tag{3.89}$$

With the definition of the continuous sesquilinear form $q(\mathbf{E},\,\mathbf{v})$ and the product $\langle\mathbf{j}_0,\,\mathbf{v}\rangle_{\Omega_-}$

$$q(\mathbf{E},\,\mathbf{v}) \;:=\; i\omega\int\limits_{\Omega_-}\sigma\mathbf{E}\cdot\overline{\mathbf{v}}\,d\mathbf{y} + \int\limits_{\Omega_-}\frac{1}{\mu}\,\mathbf{curl}\,\mathbf{E}\cdot\mathbf{curl}\,\overline{\mathbf{v}}\,d\mathbf{y}\,, \tag{3.90}$$

$$\langle\mathbf{j}_0,\,\mathbf{v}\rangle_{\Omega_-} \;:=\; \int\limits_{\Omega_-}\mathbf{j}_0\cdot\overline{\mathbf{v}}\,d\mathbf{y} \tag{3.91}$$

this formula can be rewritten as

$$q(\mathbf{E},\,\mathbf{v}) \;-\; \langle\boldsymbol{\lambda},\mathbf{v}\rangle_{\boldsymbol{\tau}} \;=\; q(\mathbf{E},\,\mathbf{v}) \;-\; \langle\boldsymbol{\lambda},\gamma_D\mathbf{v}\rangle_{\boldsymbol{\tau}} \;=\; -i\omega\langle\mathbf{j}_0,\,\mathbf{v}\rangle_{\Omega_-}\,. \tag{3.92}$$

For the exterior vacuum, the equations (3.59) and (3.60) are valid because of (3.82) and (3.83), so one finds

$$\begin{aligned} \mu_+ \boldsymbol{\lambda} &= \mathbf{N}(\gamma_D \mathbf{E}) + \mu_+ \mathbf{B}\boldsymbol{\lambda}\,, && (3.93)\\ \gamma_D \mathbf{E} &= \mathbf{C}(\gamma_D \mathbf{E}) + \mu_+ \mathbf{A}\boldsymbol{\lambda} - \mathbf{S}\mathbf{E}\,. && (3.94) \end{aligned}$$

Testing the equations with $\boldsymbol{\zeta} \in \mathbf{H}_{||}^{-\frac{1}{2}}(\mathrm{div}_\Gamma 0, \Gamma)$ and $\mathbf{v} \in \boldsymbol{H}(\mathbf{curl}; \Omega_-)$ yields

$$\begin{aligned} \langle (\mathbf{I} - \mathbf{B})\boldsymbol{\lambda}, \gamma_D \mathbf{v} \rangle_{\boldsymbol{\tau}} \quad - \frac{1}{\mu_+} \langle \mathbf{N}(\gamma_D \mathbf{E}), \gamma_D \mathbf{v} \rangle_{\boldsymbol{\tau}} &= 0\,, && (3.95)\\ \langle \boldsymbol{\zeta}, (\mathbf{I} - \mathbf{C})(\gamma_D \mathbf{E}) \rangle_{\boldsymbol{\tau}} \quad - \quad \mu_+ \langle \boldsymbol{\zeta}, \mathbf{A}\boldsymbol{\lambda} \rangle_{\boldsymbol{\tau}} &= 0\,, && (3.96)\\ q(\mathbf{E}, \mathbf{v}) \quad - \quad \langle \boldsymbol{\lambda}, \gamma_D \mathbf{v} \rangle_{\boldsymbol{\tau}} &= -i\omega \langle \mathbf{j}_0, \mathbf{v} \rangle_{\Omega_-}\,, && (3.97) \end{aligned}$$

where the term $\langle \boldsymbol{\zeta}, \mathbf{S}\,\mathbf{E} \rangle_{\boldsymbol{\tau}}$ dissapears because of equation (3.75). By inserting (3.97) into (3.95), one eventually arrives at the variational problem:

Seek $\boldsymbol{\lambda} \in \mathbf{H}_{||}^{-\frac{1}{2}}(\mathrm{div}_\Gamma 0, \Gamma)$ and $\mathbf{E} \in \boldsymbol{H}(\mathbf{curl}; \Omega_-)$ such that

$$\begin{aligned} q(\mathbf{E}, \mathbf{v}) - \frac{1}{\mu_+} \langle \mathbf{N}(\gamma_D \mathbf{E}), \gamma_D \mathbf{v} \rangle_{\boldsymbol{\tau}} - \langle \mathbf{B}\boldsymbol{\lambda}, \gamma_D \mathbf{v} \rangle_{\boldsymbol{\tau}} &= -i\omega \langle \mathbf{j}_0, \mathbf{v} \rangle_{\Omega_-}\,, && (3.98)\\ \langle \boldsymbol{\zeta}, (\mathbf{C} - \mathbf{I})(\gamma_D \mathbf{E}) \rangle_{\boldsymbol{\tau}} \quad + \quad \mu_+ \langle \boldsymbol{\zeta}, \mathbf{A}\boldsymbol{\lambda} \rangle_{\boldsymbol{\tau}} &= 0\,, && (3.99) \end{aligned}$$

for all $\boldsymbol{\zeta} \in \mathbf{H}_{||}^{-\frac{1}{2}}(\mathrm{div}_\Gamma 0, \Gamma)$ and $\mathbf{v} \in \boldsymbol{H}(\mathbf{curl}; \Omega_-)$.

Theorem 5 (Unique Solvability) *The sesquilinear form $\mathcal{Q}$ induced by the equations* (3.98) *and* (3.99) *is elliptic and continuous, and the variational problem is uniquely solvable.*

Proof: Continuity is a consequence of the continuity of the BEM operators, and ellipticity follows from the theorems 3 and 4 by using the relation (3.76) and $|x + iy| \geq max\{|x|, |y|\} \geq \frac{1}{2}(|x| + |y|)$:

$$\begin{aligned} &\left| \, q(\mathbf{E}, \mathbf{E}) - \frac{1}{\mu_+} \langle \mathbf{N}(\gamma_D \mathbf{E}), \gamma_D \mathbf{E} \rangle_{\boldsymbol{\tau}} - \langle \mathbf{B}\boldsymbol{\lambda}, \gamma_D \mathbf{E} \rangle_{\boldsymbol{\tau}} + \langle \boldsymbol{\lambda}, (\mathbf{C} - \mathbf{I})(\gamma_D \mathbf{E}) \rangle_{\boldsymbol{\tau}} + \mu_+ \langle \boldsymbol{\lambda}, \mathbf{A}\boldsymbol{\lambda} \rangle_{\boldsymbol{\tau}} \right| \\ = \;& \left| \, q(\mathbf{E}, \mathbf{E}) - \frac{1}{\mu_+} \langle \mathbf{N}(\gamma_D \mathbf{E}), \gamma_D \mathbf{E} \rangle_{\boldsymbol{\tau}} + \mu_+ \langle \boldsymbol{\lambda}, \mathbf{A}\boldsymbol{\lambda} \rangle_{\boldsymbol{\tau}} \right| \\ \geq \;& \frac{1}{2} \left(\omega \int\limits_{\Omega_-} \sigma \mathbf{E} \cdot \overline{\mathbf{E}}\, d\mathbf{y} + \int\limits_{\Omega_-} \frac{1}{\mu_-} \mathbf{curl}\,\mathbf{E} \cdot \overline{\mathbf{curl}\,\mathbf{E}}\, d\mathbf{y} - \langle \mathbf{N}(\gamma_D \mathbf{E}), \gamma_D \mathbf{E} \rangle_{\boldsymbol{\tau}} + \langle \mathbf{A}\boldsymbol{\lambda}, \boldsymbol{\lambda} \rangle_{\boldsymbol{\tau}} \right) \\ \geq \;& c \left(\|\mathbf{E}\|^2_{\boldsymbol{H}(\mathbf{curl};\Omega_-)} + \|\mathrm{curl}_\Gamma\, \gamma_D \mathbf{E}\|^2_{H^{-\frac{1}{2}}(\Gamma)} + \|\boldsymbol{\lambda}\|^2_{\mathbf{H}_{||}^{-\frac{1}{2}}(\mathrm{div}_\Gamma, \Gamma)} \right) \\ \geq \;& c \left(\|\mathbf{E}\|^2_{\boldsymbol{H}(\mathbf{curl};\Omega_-)} + \|\boldsymbol{\lambda}\|^2_{\mathbf{H}_{||}^{-\frac{1}{2}}(\mathrm{div}_\Gamma, \Gamma)} \right)\,. \end{aligned}$$

The unknows $\gamma_D \mathbf{E}$ do not need to be considered explicitly since they are included in the unknowns $\mathbf{E}$ of the interior field. Uniqueness now follows from Lax-Milgram's theorem 1. □

The sequilinearform $\mathcal{Q}$ is not symmetric $\mathcal{Q}\{(\mathbf{E},\boldsymbol{\lambda});(\mathbf{v},\boldsymbol{\zeta})\} \neq \overline{\mathcal{Q}\{(\mathbf{v},\boldsymbol{\zeta});(\mathbf{E},\boldsymbol{\lambda})\}}$: Complex conjugation and multiplication with (-1) of equation (3.99) and adding equation (3.98) yields

$$\begin{aligned}
&\mathcal{Q}\{(\mathbf{E},\boldsymbol{\lambda});(\mathbf{v},\boldsymbol{\zeta})\}\\
=\ &\left(q(\mathbf{E},\,\mathbf{v}) - \frac{1}{\mu_+}\left\langle \mathbf{N}(\gamma_D\mathbf{E}),\gamma_D\mathbf{v}\right\rangle_{\boldsymbol{\tau}} - \left\langle \mathbf{B}\boldsymbol{\lambda},\gamma_D\mathbf{v}\right\rangle_{\boldsymbol{\tau}} - \overline{\left\langle \boldsymbol{\zeta},(\mathbf{C}-\mathbf{I})(\gamma_D\mathbf{E})\right\rangle_{\boldsymbol{\tau}}} - \mu_+\left\langle \boldsymbol{\zeta},\mathbf{A}\boldsymbol{\lambda}\right\rangle_{\boldsymbol{\tau}}\right)\\
=\ &\left(q(\mathbf{E},\,\mathbf{v}) - \frac{1}{\mu_+}\left\langle \gamma_D\mathbf{E},\mathbf{N}(\gamma_D\mathbf{v})\right\rangle_{\boldsymbol{\tau}} - \left\langle \boldsymbol{\lambda},(\mathbf{C}-\mathbf{I})(\gamma_D\mathbf{v})\right\rangle_{\boldsymbol{\tau}} - \overline{\left\langle \mathbf{B}\boldsymbol{\zeta},\gamma_D\mathbf{E}\right\rangle_{\boldsymbol{\tau}}} - \mu_+\left\langle \mathbf{A}\boldsymbol{\zeta},\boldsymbol{\lambda}\right\rangle_{\boldsymbol{\tau}}\right)\\
=\ &\overline{\left(\overline{q(\mathbf{E},\,\mathbf{v})} - \frac{1}{\mu_+}\left\langle \mathbf{N}(\gamma_D\mathbf{v}),\gamma_D\mathbf{E}\right\rangle_{\boldsymbol{\tau}} - \overline{\left\langle \boldsymbol{\lambda},(\mathbf{C}-\mathbf{I})\gamma_D\mathbf{v}\right\rangle_{\boldsymbol{\tau}}} - \overline{\left\langle \gamma_D\mathbf{E},\mathbf{B}\boldsymbol{\zeta}\right\rangle_{\boldsymbol{\tau}}} - \mu_+\left\langle \boldsymbol{\lambda},\mathbf{A}\boldsymbol{\zeta}\right\rangle_{\boldsymbol{\tau}}\right)}\\
=\ &\overline{\left(\overline{q(\mathbf{E},\,\mathbf{v})} - \frac{1}{\mu_+}\left\langle \mathbf{N}(\gamma_D\mathbf{v}),\gamma_D\mathbf{E}\right\rangle_{\boldsymbol{\tau}} - \left\langle \mathbf{B}\boldsymbol{\zeta},\gamma_D\mathbf{E}\right\rangle_{\boldsymbol{\tau}} - \overline{\left\langle \boldsymbol{\lambda},(\mathbf{C}-\mathbf{I})\gamma_D\mathbf{v}\right\rangle_{\boldsymbol{\tau}}} - \mu_+\left\langle \boldsymbol{\lambda},\mathbf{A}\boldsymbol{\zeta}\right\rangle_{\boldsymbol{\tau}}\right)}\,,
\end{aligned}$$

by using the theorems 3 and 4 again, and equation (3.76). Unfortunately it holds $\overline{q(\mathbf{E},\,\mathbf{v})} \neq q(\mathbf{v},\,\mathbf{E})$

$$\begin{aligned}
q(\mathbf{E},\,\mathbf{v}) &= i\omega\int_{\Omega_C}\sigma\mathbf{E}\cdot\overline{\mathbf{v}}\,d\mathbf{y} + \int_{\Omega_C}\frac{1}{\mu_-}\,\mathbf{curl}\,\mathbf{E}\cdot\overline{\mathbf{curl}\,\mathbf{v}}\,d\mathbf{y}\\
&= i\omega\overline{\left(\int_{\Omega_C}\sigma\mathbf{v}\cdot\overline{\mathbf{E}}\,d\mathbf{y}\right)} + \overline{\left(\int_{\Omega_C}\frac{1}{\mu_-}\,\mathbf{curl}\,\mathbf{v}\cdot\overline{\mathbf{curl}\,\mathbf{E}}\,d\mathbf{y}\right)}\\
&\neq \overline{\left(i\omega\int_{\Omega_C}\sigma\mathbf{v}\cdot\overline{\mathbf{E}}\,d\mathbf{y}\right)} + \overline{\left(\int_{\Omega_C}\frac{1}{\mu_-}\,\mathbf{curl}\,\mathbf{v}\cdot\overline{\mathbf{curl}\,\mathbf{E}}\,d\mathbf{y}\right)} \;=\; \overline{q(\mathbf{v},\,\mathbf{E})}\,,
\end{aligned}$$

so the symmetry is slightly disturbed by $q(\mathbf{E},\,\mathbf{v})$. This can be cured by splitting into real and imaginary part (see Chapter 4).

3.2 Impedance Model

In the previous section, a formulation of the eddy current model was derived which strongly couples the interior of the conductors with their boundary. So the numerical solving procedure also has to cope with the variables of both regions in one big system of equations arising from the equations (3.98) and (3.99). In terms of implementation, this proves to be much more complicated than if both regions are only weakly or unidirectionally coupled. As a way to reach this simplification, the impedance model will now be introduced. Therefore, the impedance boundary condition of equation (3.38)

$$\begin{aligned}
\gamma_D\mathbf{E} &= \eta\boldsymbol{\lambda} && (3.100)\\
\text{with } \eta &:= (1-i)\sqrt{\frac{\mu_-}{2\sigma\omega}}, && (3.101)
\end{aligned}$$

is plugged into the equation (3.95) and one gets a formulation that can be solved in two steps:

STEP 1: Seek $\boldsymbol{\lambda} \in \mathbf{H}_{||}^{-\frac{1}{2}}(\mathrm{div}_\Gamma 0, \Gamma)$ and $\gamma_D \mathbf{E} \in \mathbf{H}_{\perp}^{-\frac{1}{2}}(\mathrm{curl}_\Gamma, \Gamma) \cap \boldsymbol{L}^2(\Gamma)$ such that

$$\begin{aligned} \left\langle \frac{1}{\eta}\gamma_D \mathbf{E}, \gamma_D \mathbf{v} \right\rangle_{\boldsymbol{\tau}} - \frac{1}{\mu_+} \langle \mathbf{N}(\gamma_D \mathbf{E}), \gamma_D \mathbf{v} \rangle_{\boldsymbol{\tau}} - \langle \mathbf{B}\boldsymbol{\lambda}, \gamma_D \mathbf{v} \rangle_{\boldsymbol{\tau}} &= 0\,, && (3.102)\\ \langle \boldsymbol{\zeta}, (\mathbf{C} - \mathbf{I})(\gamma_D \mathbf{E}) \rangle_{\boldsymbol{\tau}} \quad + \quad \mu_+ \langle \boldsymbol{\zeta}, \mathbf{A}\boldsymbol{\lambda} \rangle_{\boldsymbol{\tau}} &= 0\,, && (3.103) \end{aligned}$$

for all $\boldsymbol{\zeta} \in \mathbf{H}_{||}^{-\frac{1}{2}}(\mathrm{div}_\Gamma 0, \Gamma)$ and $\gamma_D \mathbf{v} \in \mathbf{H}_{\perp}^{-\frac{1}{2}}(\mathrm{curl}_\Gamma, \Gamma) \cap \boldsymbol{L}^2(\Gamma)$.

STEP 2: Seek $\mathbf{E} \in \boldsymbol{H}(\mathbf{curl}; \Omega_-)$ such that

$$q(\mathbf{E},\, \mathbf{v}) \;=\; -i\omega \langle \mathbf{j}_0,\, \mathbf{v} \rangle_{\Omega_-} + \langle \boldsymbol{\lambda}, \gamma_D \mathbf{v} \rangle_{\boldsymbol{\tau}} \qquad (3.104)$$

for all $\mathbf{v} \in \boldsymbol{H}(\mathbf{curl}; \Omega_-)$.

Thus boundary integrals and volume integrals are separated. However, there is no complete unidirectional coupling from step 1 to step 2 because the material coefficients depend on the temperature. These vary slowly, so it is only necessary to update them after a certain time and then repeat the two steps with the new coefficients. This means that the boundary of the conductors is weakly coupled with the interior through the material coefficients. Symmetry is again sligthly disturbed because

$$\left\langle \frac{1}{\eta}\gamma_D \mathbf{E}, \gamma_D \mathbf{v} \right\rangle_{\boldsymbol{\tau}} \neq \overline{\left\langle \frac{1}{\eta}\gamma_D \mathbf{E}, \gamma_D \mathbf{v} \right\rangle_{\boldsymbol{\tau}}}\,.$$

The solution of STEP 1 seems to be zero because of the missing right hand side. The way how to deal with this problem is described in Section 4.1. The impedance model uses the same BEM and FEM operators as the eddy current approach and can be seen as a first step of its implementation. The impedance boundary condition is only valid for a plane surface as described in Chapter 3, so the model is a viable approximation only for relatively 'flat' geometries. One expects problems at edges and corners of the conductors.

3.3 Magnetostatic Approach

3.3.1 Mathematical Prerequisites

The magnetostatic approach is based on a formulation that uses a scalar magnetic potential φ. The Laplace equation is valid for this potential in the simply connected domain $\Omega_E := \mathbb{R}^3 \setminus (\Omega_L \cup \bar{S}_0 \cup \bar{S}_1 \cup \ldots \cup \bar{S}_p)$. Here, $\Omega_L := \Omega_C \cup \Omega_I \cup \Omega_M$ consists of the workpiece Ω_C, the inductor Ω_I, and maybe of some field-concentrating, highly permeable, non-conducting, and homogeneous plates Ω_M. As shown in Figure 3.3, cutting surfaces S are sometimes necessary in order to get a simply connected domain.

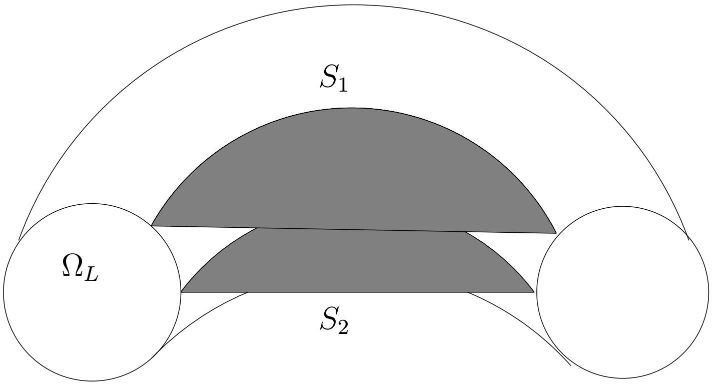

Figure 3.3: Cutting surfaces

Theorem 6 (Green's Theorem [Kos94]) *The solution of the Laplace problem*

$$\triangle\varphi = 0 \quad \forall \mathbf{x} \in \Omega_E \,, \tag{3.105}$$

can be written as

$$\alpha(\mathbf{x})\varphi(\mathbf{x}) = V(\frac{\partial\varphi}{\partial\mathbf{n}})(\mathbf{x}) - K(\varphi)(\mathbf{x}) \,, \quad \mathbf{x} \in \partial\Omega_E \,, \tag{3.106}$$

on the boundary $\partial\Omega_E$, with the single layer potential

$$V(\frac{\partial\varphi}{\partial\mathbf{n}})(\mathbf{x}) := \int\limits_{\partial\Omega_E} G(\mathbf{x},\mathbf{y})\frac{\partial\varphi}{\partial\mathbf{n}}(\mathbf{y})\,dS(\mathbf{y}), \qquad \mathbf{x} \in \partial\Omega_E,\ \frac{\partial\varphi}{\partial\mathbf{n}} \in H^{-\frac{1}{2}}(\partial\Omega_E)$$

and the double layer potential

$$K(\varphi)(\mathbf{x}) := \int\limits_{\partial\Omega_E} \frac{\partial G(\mathbf{x},\mathbf{y})}{\partial\mathbf{n}(\mathbf{y})}\varphi(\mathbf{y})\,dS(\mathbf{y}), \qquad \mathbf{x} \in \partial\Omega_E,\ \varphi \in L^2(\partial\Omega_E)\,.$$

The function $\alpha(\mathbf{x})$ is the solid angle which is equal to $\frac{1}{2}$ where $\partial\Omega_E$ is smooth and can have different values at edges and corners.

The potentials have to be evaluated on the cutting surfaces S for both sides. Let S denote a generic, piecewise smooth cutting surface endowed with a crossing direction given by a unit normal vector field $\mathbf{n}(\mathbf{y})$, $\mathbf{y} \in S$. The normal vector points from side S^- to S^+ (see Figure 3.4).

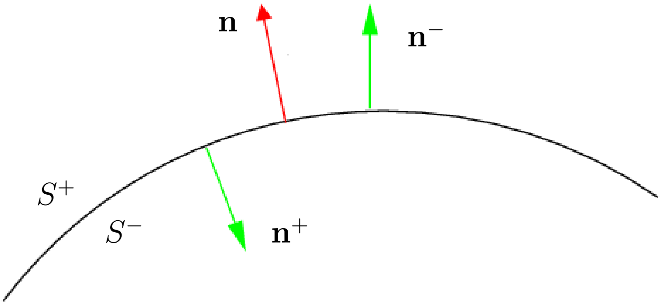

Figure 3.4: Notations for cutting surfaces

For the single layer potential restricted to S follows

$$\begin{aligned} V_{|S}(\frac{\partial\varphi}{\partial\mathbf{n}})(\mathbf{x}) &= \int\limits_{S^+} G(\mathbf{x},\mathbf{y})\frac{\partial\varphi}{\partial\mathbf{n}^+}(\mathbf{y})\,dS(\mathbf{y}) + \int\limits_{S^-} G(\mathbf{x},\mathbf{y})\frac{\partial\varphi}{\partial\mathbf{n}^-}(\mathbf{y})\,dS(\mathbf{y}) \\ &= -\int\limits_{S} G(\mathbf{x},\mathbf{y})\left[\frac{\partial\varphi}{\partial\mathbf{n}}\right]_S dS(\mathbf{y})\,, \quad \forall\mathbf{x}\in\mathbb{R}^3\,. \end{aligned} \tag{3.107}$$

Similarily one finds for the double layer potential

$$K_{|S}(\varphi)(\mathbf{x}) = -\int\limits_S \frac{\partial G(\mathbf{x},\mathbf{y})}{\partial\mathbf{n}(\mathbf{y})}\,[\varphi]_S\; dS(\mathbf{y})\,, \quad \forall\mathbf{x}\in\partial\Omega_E\,.$$

Using this, it can be concluded from (3.106) that there is a representation

$$\begin{aligned} \alpha(\mathbf{x})\varphi(\mathbf{x}) \;&=\; \int\limits_{\partial\Omega_L} G(\mathbf{x},\mathbf{y})\frac{\partial\varphi}{\partial\mathbf{n}}(\mathbf{y}) - \frac{\partial G(\mathbf{x},\mathbf{y})}{\partial\mathbf{n}(\mathbf{y})}\varphi(\mathbf{y})\,dS(\mathbf{y}) \\ &\quad+\sum_S\int\limits_S \frac{\partial G(\mathbf{x},\mathbf{y})}{\partial\mathbf{n}(\mathbf{y})}\,[\varphi]_{S_I}\; dS(\mathbf{y})\,, \quad \forall\mathbf{x}\in\partial\Omega_E\,. \end{aligned} \tag{3.108}$$

3.3.2 A Model for Perfect Conductors

For C45 steel at $\theta = 20°\text{C}$, frequencies of $10kHz$ and $B < 1T$ the penetration depth is negligible $\delta \approx 0,1\text{mm}$. In this situation the interior of the conductors can be ignored. Yet, the situation changes with increasing temperature or field strength. Then conductivity and permeability are decreasing: For C45 steel at $\theta = 1000°\text{C}$, frequencies of 10kHz and $B > 2T$ one gets $\delta \approx 5\text{mm}$. Nevertheless, in the magnetostatic approach the interior of Ω_C and Ω_I will be ignored for the BEM part. This is only a rough estimate, and the numerical results have to be checked carefully.

If the fields inside of the conductors are ignored, there is only a surface current $\mathbf{k}$ flowing. The relevant equations of the quasi-static model (3.9)-(3.16) can then be reduced to

$$\mathbf{curl}\,\mathbf{H} = 0, \quad \text{div}(\mu\mathbf{H}) = 0, \quad \oint_{\partial A} \mathbf{H}\cdot\vec{ds} = I, \quad [\mathbf{n}\times\mathbf{H}] = \mathbf{k}, \quad [\mathbf{n}\cdot\mathbf{B}] = 0\,. \tag{3.109}$$

The line integral along a path around the inductor or the workpiece is the total current flowing in the part. According to Figure 3.5 this can be seen with Ampere's law

$$I = \int_A \mathbf{j}\,d\mathbf{S} = \int_A \mathbf{curl}\,\mathbf{H}\,d\mathbf{S} = \oint_{\partial A} \mathbf{H}\cdot\vec{ds}\,. \tag{3.110}$$

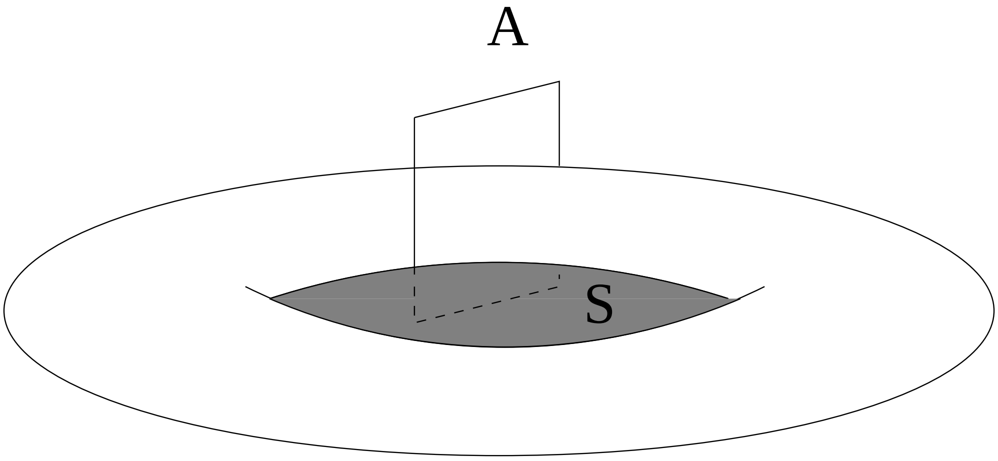

Figure 3.5: Path and cutting surface

Assuming vanishing fields inside the conductors one ends up with

$$\mathbf{n} \times \mathbf{H} = \mathbf{k} \quad , \quad \mathbf{H} \cdot \mathbf{n} = 0 \, , \quad \forall \mathbf{x} \in \Omega_C \cup \Omega_I$$

for the jump conditions in (3.109).

In every domain it holds $\mathbf{curl}\,\mathbf{H} = 0$ and a magnetic scalar potential $\mathbf{H} = -\,\mathbf{grad}\,\varphi$ can be used [AR90, Bos91]. Yet, its existence is guaranteed on simply connected domains only. To reach this, one has to introduce *cutting surfaces* $S_I := S_0, S_1, \dots, S_p$, $p \in \mathbb{N}$. These have to meet the following requirements:

1. Each of the S_κ has to be an open subset of a piecewise smooth two-dimensional manifold.
2. $\partial S_I \subset \partial \Omega_I$ and $\partial S_\kappa \subset \partial \Omega_C$, $\kappa = 1, \dots, p$.
3. $\Omega_E := \mathbb{R}^3 \setminus (\Omega_L \cup \bar{S}_0 \cup \bar{S}_1 \cup \dots \cup \bar{S}_p)$ is simply connected.

Here, the existence of such a set of cutting surfaces is taken for granted. Sloppily speaking, the number p corresponds to the number of holes in Ω_C. In the current setting Ω_I has exactly one hole, so that the cutting surface S_I is always needed. The specification of the cutting surfaces must be done manually because it is no algorithm available for their automatical construction. For a more profound discussion of cutting surfaces see [Bos98] and the references cited therein. For the sake of simplicity, $p = 1$ is set in the sequel, i.e., there is exactly one hole in the workpiece to which the cutting surface S_C is to belong. Besides, S_I and S_C must not cut through the deflection plates. Denoting by $[\varphi]_S$ the jump of φ across some externally oriented surface, equation (3.110) can be transformed into

$$[\varphi]_{S_I} = I \quad , \quad [\varphi]_{S_C} = I_C \; , \tag{3.111}$$

where $I \in \mathbb{R}$ is the fixed current in the inductor and $I_C \in \mathbb{R}$ corresponds to the (unknown) total eddy current around the hole of Ω_C. Note that one can dispense with an exciting spatial current $\mathbf{j}^I$ in this case, as the total current flowing in the inductor is known in advance. With the aid of the scalar potential, the system of equations of the magnetostatic approach reads as

$$\boxed{\begin{array}{rcll} \triangle\varphi &=& 0 & \text{in } \Omega_E \,, \\ \dfrac{\partial\varphi}{\partial\mathbf{n}} &=& 0 & \text{on } \partial\Omega_C \cup \Omega_I \,, \\ [\varphi]_S = \left[\mu\frac{\partial\varphi}{\partial\mathbf{n}}\right]_S &=& 0 & \text{on } \partial\Omega_M \,, \\ \multicolumn{4}{c}{[\varphi]_S = I \ , \ [\varphi]_{S_C} = \text{const} = I_C \,,} \\ \multicolumn{4}{c}{\left[\frac{\partial\varphi}{\partial\mathbf{n}}\right]_S = 0, \ S \in \{S_I, S_C\} \,.} \end{array} \qquad (3.112)}$$

Be aware that this system of equations (3.112) does not have a unique solution, because one can impose arbitrary constant jumps $[\varphi]_{S_C}$ with (3.112) still remaining solvable. This is a very important observation since all formulations based on (3.112) need extra conditions to achieve uniqueness. It can be shown [HOQ00] that the solution for $\mathbf{H}$ is not affected by the choice of the cutting surfaces.

The representation formula (3.108) can now be used to determine φ. It follows with the jump conditions in equation (3.112)

$$\begin{aligned} \alpha(\mathbf{x})\varphi(\mathbf{x}) = \ & - \int\limits_{\partial\Omega_C\cup\Omega_I} \frac{\partial G(\mathbf{x},\mathbf{y})}{\partial\mathbf{n}(\mathbf{y})}\varphi(\mathbf{y})\,dS(\mathbf{y}) \\ & + \int\limits_{\partial\Omega_M} G(\mathbf{x},\mathbf{y})\frac{\partial\varphi}{\partial n}(\mathbf{y}) - \frac{\partial G(\mathbf{x},\mathbf{y})}{\partial\mathbf{n}(\mathbf{y})}\varphi(\mathbf{y})\,dS(\mathbf{y}) \\ & + \ I_C \cdot \int\limits_{S_C} \frac{\partial G(\mathbf{x},\mathbf{y})}{\partial\mathbf{n}(\mathbf{y})}\,dS(\mathbf{y}) + I \cdot \int\limits_{S_I} \frac{\partial G(\mathbf{x},\mathbf{y})}{\partial\mathbf{n}(\mathbf{y})}\,dS(\mathbf{y}) \,. \end{aligned} \tag{3.113}$$

Boundary integral equations on $\partial\Omega_M$ also come into play ($\beta = 1 - \alpha$):

$$\beta(\mathbf{x})\varphi_M(\mathbf{x}) = \int\limits_{\partial\Omega_M} G(\mathbf{x},\mathbf{y})\frac{\partial\varphi_M}{\partial\mathbf{n}_M}(\mathbf{y}) - \frac{\partial N(\mathbf{x},\mathbf{y})}{\partial\mathbf{n}_M(\mathbf{y})}\varphi_M(\mathbf{y})\,dS(\mathbf{y}) \,. \tag{3.114}$$

The transmission conditions on $\partial\Omega_M$

$$\varphi - \varphi_M = 0 \quad , \quad \frac{\partial\varphi}{\partial\mathbf{n}} - \mu_r\frac{\partial\varphi_M}{\partial\mathbf{n}} = 0$$

provide the necessary link between (3.114) and (3.113). First, they enable the conversion of (3.114) into

$$\beta(\mathbf{x})\varphi(\mathbf{x}) = \int\limits_{\partial\Omega_M} -G(\mathbf{x},\mathbf{y})\frac{1}{\mu_r}\frac{\partial\varphi}{\partial\mathbf{n}}(\mathbf{y}) + \frac{\partial G(\mathbf{x},\mathbf{y})}{\partial\mathbf{n}(\mathbf{y})}\varphi(\mathbf{y})\,dS(\mathbf{y}) \,, \tag{3.115}$$

where μ_r is the constant relative permeability inside Ω_M. Using this in (3.113), one finally gets

$$
\left(\alpha(\mathbf{x})+\mu_r\beta(\mathbf{x})\right)\varphi(\mathbf{x})+\int\limits_{\Omega_C\cup\Omega_I}\frac{\partial G(\mathbf{x},\mathbf{y})}{\partial\mathbf{n}(\mathbf{y})}\varphi(\mathbf{y})\,dS(\mathbf{y})-(\mu_r-1)\int\limits_{\partial\Omega_M}\frac{\partial G(\mathbf{x},\mathbf{y})}{\partial\mathbf{n}(\mathbf{y})}\varphi(\mathbf{y})\,dS(\mathbf{y})
$$

$$
-I_C\cdot\int\limits_{S_C}\frac{\partial G(\mathbf{x},\mathbf{y})}{\partial\mathbf{n}(\mathbf{y})}\,dS(\mathbf{y})=I\cdot\int\limits_{S_I}\frac{\partial G(\mathbf{x},\mathbf{y})}{\partial\mathbf{n}(\mathbf{y})}\,dS(\mathbf{y})\;, \tag{3.116}
$$

with

$$
\alpha(\mathbf{x})=\begin{cases}\frac{1}{2} & \text{, if } \mathbf{x}\in\partial\Omega_C\cup\Omega_I\;,\\ \frac{1}{2} & \text{, if } \mathbf{x}\in\partial\Omega_M\;,\\ 1 & \text{, if } \mathbf{x}\in\overset{o}{\Omega}_E\end{cases}\qquad\text{and}\qquad\beta(\mathbf{x})=\begin{cases}0 & \text{, if } \mathbf{x}\in\partial\Omega_C\cup\Omega_I\;,\\ \frac{1}{2} & \text{, if } \mathbf{x}\in\partial\Omega_M\;,\\ 0 & \text{, if } \mathbf{x}\in\overset{o}{\Omega}_E\end{cases}
$$

for smooth boundaries. If Ω_C is simply connected, i.e., $S_C=\emptyset$, (3.116) is a valid boundary integral equation of the second kind for the unknown function $\varphi\in H^{\frac{1}{2}}(\partial\Omega_L)$. It has a unique solution [DL90, Vol. 4,Ch. XI,§2,Thm. 5]. Yet, as already noted in Sect. 2, if there is a hole in Ω_C, (3.116) is underdetermined because it does not allow to fix the jump $I_C=[\varphi]_{S_C}$. Therefore, one has to incorporate additional information. It was not possible to include Faraday's law. Another idea is to minimize the field energy. In the current setting, the electric field energy can be neglected, what remains is the energy of the magnetic field. In order to translate the minimization of magnetic energy into an equation for $[\varphi]_{S_C}=I_C$, one first notes that

$$
\begin{aligned}
E_{\text{mag}} &=\frac{1}{2}\int\limits_{\mathbb{R}^3}\mathbf{H}(\mathbf{x})\cdot\mathbf{B}(\mathbf{x})d\mathbf{x}\\
&=\frac{1}{2}\int\limits_{\Omega_A}\langle\mu\,\mathbf{grad}\,\varphi,\mathbf{grad}\,\varphi\rangle\;d\mathbf{x}+\frac{1}{2}\int\limits_{\Omega_M}\langle\mu\,\mathbf{grad}\,\varphi_M,\mathbf{grad}\,\varphi_M\rangle\;d\mathbf{x}
\end{aligned}
$$

where $\Omega_A:=\Omega_E\setminus\Omega_M$. Due to $\triangle\varphi=\triangle\varphi_M=0$ one finds with

$$
\int\limits_{\Omega}\langle\mathbf{grad}\,f,\mathbf{grad}\,f\rangle\;d\mathbf{x}=\int\limits_{\Omega}\left[\operatorname{div}(f\cdot\mathbf{grad}\,f)-\triangle f\right]\;d\mathbf{x}
$$

that

$$
E_{\text{mag}}=\frac{1}{2}\int\limits_{\partial\Omega_A}\mu\frac{\partial\varphi}{\partial\mathbf{n}}\cdot\varphi\,dS+\frac{1}{2}\int\limits_{\partial\Omega_M}\mu\frac{\partial\varphi_M}{\partial\mathbf{n}_M}\cdot\varphi_M\,dS\;.
$$

As a consequence of the boundary and transmission conditions for φ, one ends up with the expression

$$
E_{\text{mag}}=\frac{I\cdot\mu_0}{2}\int\limits_{S_I}\frac{\partial\varphi}{\partial\mathbf{n}}\,dS\;+\;\frac{I_C\cdot\mu_0}{2}\int\limits_{S_C}\frac{\partial\varphi}{\partial\mathbf{n}}\,dS\;. \tag{3.117}
$$

Next, recall lemma 2 from [DL90, Vol. 4,Ch. XI,Part B,§2], which states that for a double layer potential on a piecewise smooth surface Γ

$$u(\mathbf{x}) = \int_{\Gamma} g(\mathbf{y}) \frac{\partial G(\mathbf{x},\mathbf{y})}{\partial \mathbf{n}(\mathbf{y})}\, dS(\mathbf{y}) \tag{3.118}$$

the gradient away from Γ is given by

$$\mathbf{grad}\, u(\mathbf{x}) = \int_{\Gamma} (\mathbf{n}(y) \times \mathbf{grad}\, g(\mathbf{y})) \times \mathbf{grad}_{\mathbf{y}}\, G(\mathbf{x},\mathbf{y})\, dS(\mathbf{y}) \qquad \forall \mathbf{x} \notin \Gamma\ . \tag{3.119}$$

Now slightly different cutting surfaces S'_I and S'_C are assumed for the computation of φ. Then the expression (3.117) for the magnetic energy remains the same. Moreover, (3.116) provides the following double layer representation for all $\mathbf{x} \in \overset{o}{\Omega} := \mathbb{R}^3 \setminus (\Omega_L \cup \Omega_M \cup S'_I \cup S'_C)$:

$$\begin{aligned}
\varphi(\mathbf{x}) = \ & - \int_{\Omega_C \cup \Omega_I} \frac{\partial G(\mathbf{x},\mathbf{y})}{\partial \mathbf{n}(\mathbf{y})} \varphi(\mathbf{y})\, dS(\mathbf{y}) + (\mu_r - 1) \cdot \int_{\partial \Omega_M} \frac{\partial G(\mathbf{x},\mathbf{y})}{\partial \mathbf{n}(\mathbf{y})} \varphi(\mathbf{y})\, dS(\mathbf{y}) \\
& + \int_{S'^{+}_I} \frac{\partial G(\mathbf{x},\mathbf{y})}{\partial \mathbf{n}(\mathbf{y})}\, \varphi^{+}(\mathbf{y})\, dS(\mathbf{y}) + \int_{S'^{+}_C} \frac{\partial G(\mathbf{x},\mathbf{y})}{\partial \mathbf{n}(\mathbf{y})}\, \varphi^{+}(\mathbf{y})\, dS(\mathbf{y}) - \\
& - \int_{S'^{-}_I} \frac{\partial G(\mathbf{x},\mathbf{y})}{\partial \mathbf{n}(\mathbf{y})}\, \varphi^{-}(\mathbf{y})\, dS(\mathbf{y}) + \int_{S'^{-}_C} \frac{\partial G(\mathbf{x},\mathbf{y})}{\partial \mathbf{n}(\mathbf{y})}\, \varphi^{-}(\mathbf{y})\, dS(\mathbf{y})\ .
\end{aligned}$$

Then (3.119) immediately yields for all $\mathbf{x} \in \overset{o}{\Omega}$

$$\begin{aligned}
\mathbf{grad}\, \varphi(\mathbf{x}) = (\mu_r - 1) \cdot & \int_{\partial \Omega_M} (\mathbf{n}(y) \times \mathbf{grad}\, \varphi(\mathbf{y})) \times \mathbf{grad}_{\mathbf{y}}\, G(\mathbf{x},\mathbf{y})\, dS(\mathbf{y}) - \\
& - \int_{\partial \Omega_C \cup \Omega_I} (\mathbf{n}(y) \times \mathbf{grad}\, \varphi(\mathbf{y})) \times \mathbf{grad}_{\mathbf{y}}\, G(\mathbf{x},\mathbf{y})\, dS(\mathbf{y})\ ,
\end{aligned}$$

as the contributions of different sides of cutting surfaces cancel due to the equality of tangential gradients of φ^{+} and φ^{-}. This results from the jump conditions at the cutting surfaces. It should be pointed out that without deflection plates Ω_M, the above formula is the familiar *Biot-Savart law*. The magnetic field energy (3.117) can now be written as

$$\begin{aligned}
E_{\mathrm{mag}} = \frac{1}{2}\mu_0 I \cdot \int\limits_{S_I} \mathbf{n}(\mathbf{x}) \cdot \Bigg[(\mu_r - 1) \int\limits_{\partial\Omega_M} & (\mathbf{n}(y) \times \mathbf{grad}\,\varphi(\mathbf{y})) \times \mathbf{grad}_{\mathbf{y}}\, G(\mathbf{x},\mathbf{y})\, dS(\mathbf{y}) \\
& - \int\limits_{\partial\Omega_C \cup \Omega_I} (\mathbf{n}(y) \times \mathbf{grad}\,\varphi(\mathbf{y})) \times \mathbf{grad}_{\mathbf{y}}\, G(\mathbf{x},\mathbf{y})\, dS(\mathbf{y}) \Bigg]\, dS(\mathbf{x}) + \\
+ \frac{1}{2}\mu_0 I_C \cdot \int\limits_{S_C} \mathbf{n}(\mathbf{x}) \cdot \Bigg[(\mu_r - 1) \int\limits_{\partial\Omega_M} & (\mathbf{n}(y) \times \mathbf{grad}\,\varphi(\mathbf{y})) \times \mathbf{grad}_{\mathbf{y}}\, G(\mathbf{x},\mathbf{y})\, dS(\mathbf{y}) \\
& - \int\limits_{\partial\Omega_C \cup \Omega_I} (\mathbf{n}(y) \times \mathbf{grad}\ \varphi(\mathbf{y})) \times \mathbf{grad}_{\mathbf{y}}\, G(\mathbf{x},\mathbf{y})\, dS(\mathbf{y}) \Bigg]\, dS(\mathbf{x})\ .
\end{aligned} \tag{3.120}$$

One has to find the minimum of E_{mag} with respect to the independent variable I_C. Please note that φ also depends on I_C in a linear affine fashion as can be seen in (3.116). This means that one actually has to minimize a quadratic function in I_C, which can easily be done analytically: First, one uses (3.116) to calculate solutions φ_{10} and φ_{01} for the particular total currents $I = 1$, $I_C = 0$ and $I = 0$, $I_C = 1$, respectively. The general solution of (3.116) is then given by

$$\varphi(\mathbf{x}) \ = \ I \cdot \varphi_{10}(\mathbf{x}) \ + \ I_C \cdot \varphi_{01}(\mathbf{x})\ . \tag{3.121}$$

Insert (3.121) in (3.120), and the induced total eddy current I_C results from the condition

$$0 \ = \ \frac{\partial E_{\mathrm{mag}}(\varphi(I_C))}{\partial I_C}\ .$$

From this one finds

$$\begin{aligned}
I_C \ = \frac{I}{2} \cdot \Bigg\{ - \int\limits_{S_I} \mathbf{n}(\mathbf{x}) \cdot \Bigg[(\mu_r - 1) \int\limits_{\partial\Omega_M} & (\mathbf{n}(y) \times \mathbf{grad}\,\varphi_{01}(\mathbf{y})) \times \mathbf{grad}_{\mathbf{y}}\, G(\mathbf{x},\mathbf{y})\, dS(\mathbf{y}) \\
& + \int\limits_{\partial\Omega_C \cup \Omega_I} (\mathbf{n}(y) \times \mathbf{grad}\,\varphi_{01}(\mathbf{y})) \times \mathbf{grad}_{\mathbf{y}}\, G(\mathbf{x},\mathbf{y})\, dS(\mathbf{y}) \Bigg]\, dS(\mathbf{x}) \\
- \int\limits_{S_C} \mathbf{n}(\mathbf{x}) \cdot \Bigg[(\mu_r - 1) \int\limits_{\partial\Omega_M} & (\mathbf{n}(y) \times \mathbf{grad}\,\varphi_{10}(\mathbf{y})) \times \mathbf{grad}_{\mathbf{y}}\, G(\mathbf{x},\mathbf{y})\, dS(\mathbf{y}) \\
& + \int\limits_{\partial\Omega_C \cup \Omega_I} (\mathbf{n}(y) \times \mathbf{grad}\,\varphi_{10}(\mathbf{y})) \times \mathbf{grad}_{\mathbf{y}}\, G(\mathbf{x},\mathbf{y})\, dS(\mathbf{y}) \Bigg]\, dS(\mathbf{x}) \Bigg\} \\
\Bigg/ \Bigg\{ \int\limits_{S_C} \mathbf{n}(\mathbf{x}) \cdot \Bigg[(\mu_r - 1) \int\limits_{\partial\Omega_M} & (\mathbf{n}(y) \times \mathbf{grad}\,\varphi_{01}(\mathbf{y})) \times \mathbf{grad}_{\mathbf{y}}\, G(\mathbf{x},\mathbf{y})\, dS(\mathbf{y}) \\
& - \int\limits_{\partial\Omega_C \cup \Omega_I} (\mathbf{n}(y) \times \mathbf{grad}\,\varphi_{01}(\mathbf{y})) \times \mathbf{grad}_{\mathbf{y}}\, G(\mathbf{x},\mathbf{y})\, dS(\mathbf{y}) \Bigg]\, dS(\mathbf{x}) \Bigg\}.
\end{aligned}$$

As soon as one knows I_C, (3.121) gives the desired unique solution of the *surface eddy current problem* of equation (3.112).

3.3.3 Boundary Element Method and Spatial Current

The magnetostatic approach differs to a high degree from both the eddy current approach and the impedance model, therefore, it also has to be implemented differently. The implementation of the magnetostatic approach is only coarsly described in this section, whereas the two other models are treated in detail in the following two chapters.

For the magnetostatic approach, the surfaces of Ω_I, Ω_M and Ω_C are equipped with a shape regular surface mesh Γ_h composed of flat rectangles. Discretization of the boundary integral equations (3.116) relies on a piecewise constant approximation φ_h of φ and is based on *midpoint collocation* [Hac89, Sect. 4.4]. The singular collocation integrals over the elements are evaluated exactly by using the stable analytic expression derived by O. Steinbach[1]. Thus one gets linear systems of equations for the unknown coefficients of the piecewise linear approximations of φ_{10} and φ_{01}. They are solved iteratively by means of the BiCGStab Krylov method [vdV92]. Since the discrete integral operator of the second kind is well conditioned, only a moderate number of iterations has to be carried out.

The ultimate goal is to compute the spatial current distribution in the workpiece. So far, the interior of the conductors has been neglected. It can be taken into consideration by employing the skin effect formula: For any $\mathbf{x} \in \Omega_C$ which is fairly close to the surface, denote the nearest point on the surface by $\mathbf{x}_\partial \in \partial\Omega_C$. For almost all $\mathbf{x} \in \Omega_C$ this point is uniquely defined. Then one sets

$$\mathbf{j}(\mathbf{x}) = \mathbf{j}_0 \cdot e^{-\frac{1+i}{\delta}\cdot z} \quad , \quad \delta = \sqrt{\frac{2}{\sigma\mu\omega}} \tag{3.122}$$

where $z := |\mathbf{x} - \mathbf{x}_\partial|$. $\mathbf{j}_0$ is fixed for all $\mathbf{x}$ belonging to $\mathbf{x}_\partial$ by the condition

$$\mathbf{k}(\mathbf{x}_\partial) = \int_0^\infty \mathbf{j}(\mathbf{x}(z))\, dz$$

where $\mathbf{k}(\mathbf{x}_\partial)$ is the surface current density in $\mathbf{x}_\partial$. Now the material parameters are incorporated into the model. Clearly, their temperature dependence can also be taken into accout.

---

[1] Private communication with Dr. Olaf Steinbach, University of Stuttgart

Chapter 4

Excitation and Discretization

In this chapter it is shown how the desired excitation is incorporated into the eddy current approach and the impedance model, how these models are discretized, and how the occuring BEM operators can be implemented. The path algorithm that is necessary in both models is also introduced.

4.1 Excitation

As yet, the right hand sides of the systems of equations for eddy current approach and impedance model are prescribed currents in the interior of the conductors. However, this is not what is needed because the process for a given geometry and material is determined by the exciting total current and its frequency only. The equations must represent this fact. To achieve this, one first takes a look at the unknown $\boldsymbol{\lambda} \in \mathbf{H}_{||}^{-\frac{1}{2}}(\mathrm{div}_\Gamma 0, \Gamma)$. The surface divergence of $\boldsymbol{\lambda}$ automatically vanishes if one employs continuous surface potentials $\boldsymbol{\lambda} = \mathbf{curl}_\Gamma\, \phi := \gamma_D(\mathbf{grad}\, \phi) \times \mathbf{n}$, but this is only possible for simply connected surfaces. For non simply connected domains with holes, such as the inductor of Figure 4.1, one has to add topological vector fields $\boldsymbol{\eta}_k$ to cope with

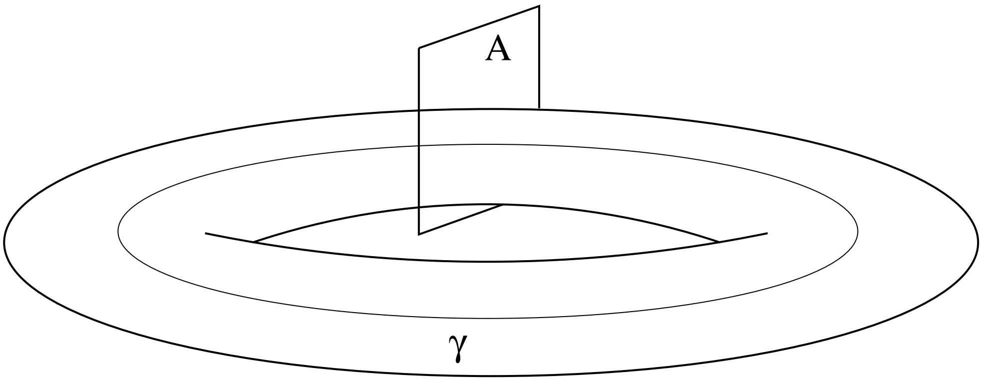

Figure 4.1: Inductor with hole and path γ

possible jumps of the potential at paths γ_k circumventing the holes, and to complete the kernel of div_Γ. Similar to the magnetostatic approach, these paths can be seen as traces of cutting surfaces that patch the L holes of the configuration. If $\boldsymbol{\eta}_k = \mathbf{curl}_\Gamma\, \phi_k$ is a vector field derived from an arbitrary potential ϕ_k with a jump of size one $[\phi_k]_{\gamma_k} = 1$ at an arbitrary path γ_k circumventing hole k, then each $\boldsymbol{\lambda} \in \mathbf{H}_{||}^{-\frac{1}{2}}(\mathrm{div}_\Gamma 0, \Gamma)$ can, with a scaling factor $\frac{1}{\mu_+}$, be written as

$$\boldsymbol{\lambda} = \frac{1}{\mu_+}\left(\mathbf{curl}_\Gamma\, \phi + \sum_{k=1}^{L} \alpha_k \cdot \boldsymbol{\eta}_K\right) \quad \text{with } \alpha_k \in \mathbb{C}\,.$$

After inserting this into the equations (3.98)-(3.99) and (3.102)-(3.103), and by using $\mu_+ = \mu_0$ one ends up with

$$\begin{aligned}
&\mu_0\, F(\mathbf{E},\, \mathbf{v}) + \langle V(\mathrm{curl}_\Gamma\, \gamma_D \mathbf{E}), \mathrm{curl}_\Gamma\, \gamma_D \mathbf{v}\rangle_{\boldsymbol{\tau}} && (4.1)\\
&\qquad - \langle \mathbf{B}(\mathbf{curl}_\Gamma \phi), \gamma_D \mathbf{v}\rangle_{\boldsymbol{\tau}} - \sum_{k=1}^{L} \alpha_k \, \langle \mathbf{B}\boldsymbol{\eta}_k, \gamma_D \mathbf{v}\rangle_{\boldsymbol{\tau}} \;=\; -i\mu_0\omega\langle \mathbf{j}_0,\, \mathbf{v}\rangle_{\Omega_-}\,, &&\\
&\langle \gamma_D \mathbf{E}, \mathbf{B}(\mathbf{curl}_\Gamma \psi)\rangle_{\boldsymbol{\tau}} + \langle \mathbf{A}(\mathbf{curl}_\Gamma \phi), \mathbf{curl}_\Gamma \psi\rangle_{\boldsymbol{\tau}} && (4.2)\\
&\qquad + \sum_{k=1}^{L} \alpha_k \, \langle \mathbf{A}\boldsymbol{\eta}_k, \mathbf{curl}_\Gamma \psi\rangle_{\boldsymbol{\tau}} \;=\; 0\,, &&\\
&\left\langle \gamma_D \mathbf{E}, \mathbf{B}\boldsymbol{\eta}_j\right\rangle_{\boldsymbol{\tau}} + \left\langle \mathbf{A}(\mathbf{curl}_\Gamma \phi), \boldsymbol{\eta}_j\right\rangle_{\boldsymbol{\tau}} + \sum_{k=1}^{L} \alpha_k \left\langle \mathbf{A}\boldsymbol{\eta}_k, \boldsymbol{\eta}_j\right\rangle_{\boldsymbol{\tau}} \;=\; 0\,. && (4.3)
\end{aligned}$$

Here $F(\mathbf{E},\, \mathbf{v})$ is defined as

$$F(\mathbf{E},\, \mathbf{v}) := \begin{cases} q(\mathbf{E},\, \mathbf{v}) & \text{for the } \textit{eddy current approach}\,,\\ \left\langle \frac{1}{\eta}\gamma_D \mathbf{E}, \gamma_D \mathbf{v}\right\rangle_{\boldsymbol{\tau}} & \text{for the } \textit{impedance model}\,, \end{cases} \qquad (4.4)$$

and the relation

$$\langle \mathbf{N}(\gamma_D \mathbf{E}), \gamma_D \mathbf{v}\rangle_{\boldsymbol{\tau}} = -\,\langle \mathrm{curl}_\Gamma\, \gamma_D \mathbf{v}, V(\mathrm{curl}_\Gamma\, \gamma_D \mathbf{E})\rangle_{\boldsymbol{\tau}} \qquad (4.5)$$

was used [Hip02] with the ordinary scalar single layer potential V. The physical meaning of the new unknows α_k should be described for the inductor of Figure 4.1. Each inductor is equivalent to this one because each inductor has exactly one hole. It holds

$$\begin{aligned}
I_{exc} \;&=\; \int_A \mathbf{j}\, d\mathbf{S} = \int_{\partial A} \mathbf{H}\, d\mathbf{s} \;=\; \int_{\partial A} (\mathbf{n} \times (\mathbf{H} \times \mathbf{n})\, d\mathbf{s} \;=\; \int_{\partial A} (\mathbf{n} \times (\frac{-1}{i\mu_0\omega}\, \mathbf{curl}\, \mathbf{E} \times \mathbf{n}))\, d\mathbf{s}\\
&=\; \int_{\partial A} (\mathbf{n} \times \frac{-1}{i\mu_0\omega}[\mathbf{curl}_\Gamma\, \phi + \alpha_{exc} \cdot \boldsymbol{\eta}])\, d\mathbf{s} \;=\; \int_{\partial A} (\mathbf{n} \times (\frac{-\alpha_{exc}}{i\mu_0\omega} \cdot \boldsymbol{\eta})\, d\mathbf{s}\\
&=\; \int_{\partial A} (\mathbf{n} \times (\frac{-\alpha_{exc}}{i\mu_0\omega} \cdot \gamma_D(\mathbf{grad}\, \phi_{exc}) \times \mathbf{n})\, d\mathbf{s} \;=\; \int_{\partial A} \frac{-\alpha_{exc}}{i\mu_0\omega} \cdot \gamma_D(\mathbf{grad}\, \phi_{exc})\, d\mathbf{s}\\
&=\; \frac{-\alpha_{exc}}{i\mu_0\omega} \cdot [\phi_{exc}]_\gamma \;=\; \frac{-\alpha_{exc}}{i\mu_0\omega}\,,
\end{aligned}$$

with the exciting current $I_{exc} \in \mathbb{R}$. So $\alpha_k = -i\, \mu_0\;\omega\, I_k$ is proportional to the total current $I_k \in \mathbb{R}$ which flows around hole k. In the case of the inductor, this is not an unknown and can be put on the right hand side of the system of equations (4.1)-(4.3), where the prescribed current $\mathbf{j}_0$ can now be dropped. It must be pointed out that due to this fixing, equation (4.3) must not be tested for the inductor. Then it is obvious that the new formulation cannot be equivalent to the variational problems (3.98)-(3.99) and (3.102)-(3.103) any more since the excitation is attached to the boundary, which is a set of measure zero. Therefore there is no current density $\mathbf{j}_0$ in Ω_- that can generate this excitation. Uniqueness of the new variational problem can still be shown as in the last chapter, and it can finally be written as:

Seek $\mathbf{E} \in \boldsymbol{H}(\mathbf{curl};\Omega_-)$, a continuous potential ϕ, and $L-1$ unknowns $\alpha_k \in \mathbb{C}$ such that

$$\begin{aligned} &\mu_0\, F(\mathbf{E},\, \mathbf{v}) + \langle V(\mathrm{curl}_\Gamma\, \gamma_D \mathbf{E}), \mathrm{curl}_\Gamma\, \gamma_D \mathbf{v}\rangle_{\boldsymbol{\tau}} \\ &\quad - \langle \mathbf{B}(\mathbf{curl}_\Gamma \phi), \gamma_D \mathbf{v}\rangle_{\boldsymbol{\tau}} - \sum_{k=1}^{L-1} \alpha_k \langle \mathbf{B}\boldsymbol{\eta}_k, \gamma_D \mathbf{v}\rangle_{\boldsymbol{\tau}} = -i\mu_0 \omega I_{exc} \langle \mathbf{B}\boldsymbol{\eta}_k, \gamma_D \mathbf{v}\rangle_{\boldsymbol{\tau}}\ , \end{aligned} \tag{4.6}$$

$$\begin{aligned} &\langle \gamma_D \mathbf{E}, \mathbf{B}(\mathbf{curl}_\Gamma \psi)\rangle_{\boldsymbol{\tau}} + \langle \mathbf{A}(\mathbf{curl}_\Gamma \phi), \mathbf{curl}_\Gamma \psi\rangle_{\boldsymbol{\tau}} \\ &\quad + \sum_{k=1}^{L-1} \alpha_k \langle \mathbf{A}\boldsymbol{\eta}_k, \mathbf{curl}_\Gamma \psi\rangle_{\boldsymbol{\tau}} = i\mu_0 \omega I_{exc} \langle \mathbf{A}\boldsymbol{\eta}_k, \mathbf{curl}_\Gamma \psi\rangle_{\boldsymbol{\tau}}\ , \end{aligned} \tag{4.7}$$

$$\begin{aligned} &\left\langle \gamma_D \mathbf{E}, \mathbf{B}\boldsymbol{\eta}_j\right\rangle_{\boldsymbol{\tau}} + \left\langle \mathbf{A}(\mathbf{curl}_\Gamma \phi), \boldsymbol{\eta}_j\right\rangle_{\boldsymbol{\tau}} \\ &\quad + \sum_{k=1}^{L-1} \alpha_k \left\langle \mathbf{A}\boldsymbol{\eta}_k, \boldsymbol{\eta}_j\right\rangle_{\boldsymbol{\tau}} = i\mu_0 \omega I_{exc} \left\langle \mathbf{A}\boldsymbol{\eta}_k, \boldsymbol{\eta}_j\right\rangle_{\boldsymbol{\tau}}\ , \end{aligned} \tag{4.8}$$

for all test fields $\mathbf{v} \in \boldsymbol{H}(\mathbf{curl};\Omega_-)$, for all continuous potentials ψ, and for all $L-1$ topological vector fields $\boldsymbol{\eta}_k$. Here $L \in \mathbb{R}$ is the total number of holes in the workpiece and the inductor.

4.2 Discretization

The domain Ω_- of the conductors is equipped with a triangulation Ω_h arising from CAD data files consisting of tetrahedra. This triangulation also induces a surface mesh Γ_h consisting of triangles. Linear edge elements are used as conforming finite element space for $\boldsymbol{H}(\mathbf{curl};\Omega_-)$, and the space is designated by $\boldsymbol{\mathcal{ND}}_1(\Omega_h)$. The discretized electric field $\mathbf{E}_h$ and its test field $\mathbf{v}_h$ are part of this space. What remains on the surface is the trace $\boldsymbol{\mathcal{ND}}_1(\Gamma_h)$ of this space, and $\gamma_D \mathbf{E}_h$, $\gamma_D \mathbf{v}_h$ are part of it. The discrete potentials ϕ_h and ψ_h are chosen in the space of the piecewise continuous linear functions $\mathcal{S}_1(\Gamma_h)$. For this kind of conforming Garlerkin finite element discretization, a quasi-optimal a priori-error estimator can be established. This means that the error of the discretized solution of (4.6)-(4.8) vanishes for decreasing meshwidths h. For a more detailed discussion of the above topics see [Hip02].

In the following, the basis functions of the boundary operators are examined. For this purpose, it is always the impedance model $F(\mathbf{E},\, \mathbf{v}) := \left\langle \frac{1}{\eta}\gamma_D \mathbf{E}, \gamma_D \mathbf{v}\right\rangle_{\boldsymbol{\tau}}$ which is chosen in equation (4.4) as it involves only boundary operators. If the eddy current approach is to be applied, it is easy to replace this definition by $F(\mathbf{E},\, \mathbf{v}) := q(\mathbf{E},\, \mathbf{v})$.

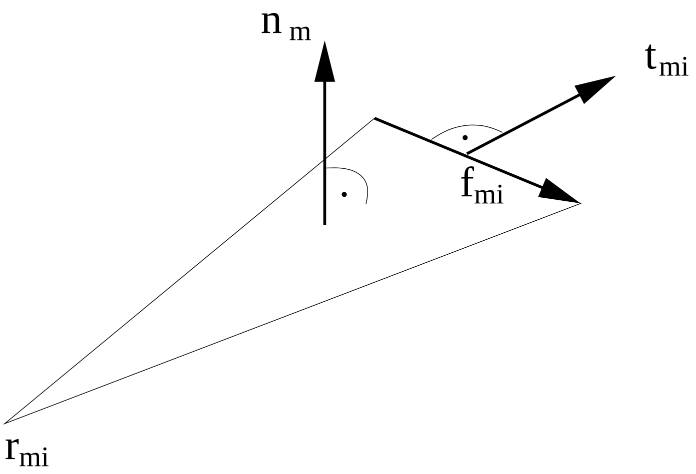

Figure 4.2: Settings for the definition of basis functions of $\mathcal{S}_1(\Gamma_h)$

4.2.1 Basis Functions of $\mathcal{S}_1(\Gamma_h)$, $\boldsymbol{\mathcal{ND}}_1(\Gamma_h)$,

All occuring functions of the boundary part of (4.6)-(4.8) can be written as linear combinations of basis functions of $\boldsymbol{\mathcal{ND}}_1(\Omega_h)$ and $\mathbf{curl}_\Gamma\mathcal{S}_1(\Gamma_h)$. This also holds for each topological vector field $\boldsymbol{\eta}_k$ with jump at the path γ_k, if the surface-curl is restricted to $\Gamma \setminus \gamma_k$. Furthermore, all functions can be derived from the basis functions ψ_{mi} of the space $\mathcal{S}_1(\Gamma_h)$.

In the following $m,\ i,\ j,\ k$ are integer numbers and the vectors $\mathbf{f}_{mi},\ \mathbf{t}_{mi},\ \mathbf{n}_m,\ \mathbf{r}_{mi}$ in $\mathbb{R}^3$ are defined according to Figure 4.2. Their absolute value is denoted by thin characters, $f_{mi} := \|\mathbf{f}_{mi}\|$ is an example. It holds $t_{mi} = n_m = 1$ by definition, and $\mathbf{r} \in \mathbb{R}^3$ is the position vector.

Definition 4 (Basis functions of $\mathcal{S}_1(\Gamma_h)$) *Basis functions ψ_i of $\mathcal{S}_1(\Gamma_h)$ are hat functions on node i, defined by*

$$\psi_i(\mathbf{r}) := \sum_m \varphi_{mi}(\mathbf{r})\,, \tag{4.9}$$

with the index m running over all triangles adjacent to node i and

$$\varphi_{mi}(\mathbf{r}) := -\frac{f_{mi}}{2\cdot T_m}\,(\mathbf{r}\ - \mathbf{r}_{mk})\cdot \mathbf{t}_{mi} \quad k \neq i \tag{4.10}$$

with support of $\varphi_{mi} := triangle\ m$, and $T_m :=$ area of triangle m.

The potential ϕ can now be formulated in terms of these basis functions as

$$\mathbf{curl}_\Gamma\,\phi = \sum_{nodes\ i} \phi_i \cdot \mathbf{curl}_\Gamma\,\psi_i \quad \text{with } \phi_i \in \mathbb{C}. \tag{4.11}$$

Theorem 7 *The linear functions $\varphi_{mi}(\mathbf{r})$ are also basis functions of $\mathcal{S}_1(\Gamma_h)$, and it holds $\varphi_{mi}(\mathbf{r}_{mn}) = \delta_{in}$.*

Proof: Let i, k, and j be the three nodes with associated edges on the opposite side in the triangle, and Ω_{ij} be the angle between the edges i and j. Then there are three cases:
Case 1: $n = k \implies (\mathbf{r}_{mk} - \mathbf{r}_{mk}) = 0 \implies \varphi_{mk}(\mathbf{r}_{mn}) = 0$
Case 2: $n = j \implies (\mathbf{r}_{mj} - \mathbf{r}_{mk}) \perp \mathbf{t}_{mi} \implies \varphi_{mj}(\mathbf{r}_{mn}) = 0$
Case 3: $n = i \implies$

$$\begin{aligned}\varphi_{mi}(\mathbf{r}_{mi}) &:= -\frac{f_{mi}}{2 \cdot T_m}(\mathbf{r}_{mi} - \mathbf{r}_{mk}) \cdot \mathbf{t}_{mi} = -\frac{f_{mi} \cdot (\mathbf{f}_{mj} \cdot \mathbf{t}_{mi})}{2 \cdot 0.5 \cdot ||\mathbf{f}_{mi} \times \mathbf{f}_{mj}||} \\ &= -\frac{f_{mi} \cdot (f_{mj} \cdot cos[\Omega_{ij} + \pi/2])}{||\mathbf{f}_{mi} \times \mathbf{f}_{mj}||} = \frac{f_{mi} \cdot f_{mj} \cdot sin[\Omega_{ij}]}{||\mathbf{f}_{mi} \times \mathbf{f}_{mj}||} = 1\end{aligned}$$

□

It follows for $\mathbf{curl}_\Gamma \mathcal{S}_1(\Gamma_h)$ that

$$\begin{aligned}\mathbf{curl}_\Gamma\, \varphi_{mi} &= \gamma_D(\mathbf{grad}\, \varphi_{mi}) \times \mathbf{n}_m = \gamma_D(-\frac{f_{mi}}{2 \cdot T_m}\mathbf{t}_{mi}) \times \mathbf{n}_m \\ &= -\frac{f_{mi}}{2 \cdot T_m} \cdot (\mathbf{t}_{mi} \times \mathbf{n}_m) = -\frac{\mathbf{f}_{mi}}{2 \cdot T_m}\,.\end{aligned} \tag{4.12}$$

The topological vector fields $\boldsymbol{\eta}_k = \mathbf{curl}_\Gamma\, \phi_k$ arise from a potential ϕ_k with a jump of size one $[\phi_k]_{\gamma_k} = 1$ at a path γ_k circling hole k. The paths can automatically be generated as a series of edges, see Section 4.4. Then the topological vector fields can uniquely be defined as

$$\boldsymbol{\eta}_k := \sum_{nodes\ mi} \boldsymbol{\eta}_{k,mi} \cdot \mathbf{curl}_\Gamma\, \varphi_{mi}(\mathbf{r}) \tag{4.13}$$

with

$$\boldsymbol{\eta}_{k,mi} := \begin{cases} 1 & \text{if node } i \text{ is on path } \gamma_k \text{ and triangle } m \text{ is on the 'right side'}\,, \\ 0 & \text{else}\,. \end{cases} \tag{4.14}$$

Here the ’right side’ is defined according to Figure 4.3, where the resulting $\boldsymbol{\eta}_k$ is depicted as arrows.

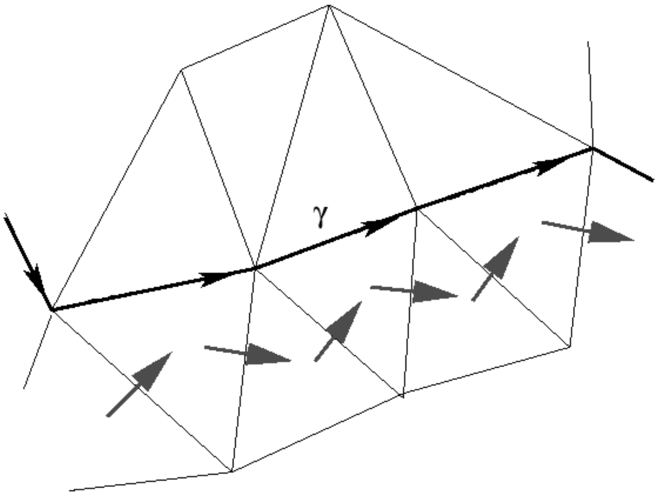

Figure 4.3: Topological vector field along path γ

Definition 5 (Basis functions of $\boldsymbol{\mathcal{ND}}_1(\Gamma_h)$) *The basis functions of $\boldsymbol{\mathcal{ND}}_1(\Gamma_h)$ in a single tetrahedron are*

$$\mathbf{b}_{mk} := \varphi_{mi} \cdot \mathbf{grad}\, \varphi_{mj} \;-\; \varphi_{mj} \cdot \mathbf{grad}\, \varphi_{mi} \,, \tag{4.15}$$

with support of $\mathbf{b}_{mk} := triangle\ m.$

Theorem 8 *It holds*

$$\mathbf{b}_{mk} = \frac{1}{2 \cdot T_m} (\mathbf{r} - \mathbf{r}_{mk}) \times \mathbf{n}_m \,. \tag{4.16}$$

Proof:

$$\begin{aligned}
\mathbf{b}_{mk} &= \frac{f_{mi} \cdot f_{mj}}{4 \cdot T_m^2} \left\{[(\mathbf{r} - \mathbf{r}_{mk}) \cdot \mathbf{t}_{mi}] \cdot \mathbf{t}_{mj} \;-\; (\mathbf{r} - \mathbf{r}_{mk}) \cdot \mathbf{t}_{mj}] \cdot \mathbf{t}_{mi}]\right\} \\
&= \frac{f_{mi} \cdot f_{mj}}{4 \cdot T_m^2} (\mathbf{r} - \mathbf{r}_{mk}) \times (\mathbf{t}_{mj} \times \mathbf{t}_{mi}) \\
&= \frac{f_{mi} \cdot f_{mj}}{4 \cdot T_m^2} (\mathbf{r} - \mathbf{r}_{mk}) \times (\mathbf{n}_m \cdot sin(\Omega_{ij})) \\
&= \frac{1}{2 \cdot T_m} (\mathbf{r} - \mathbf{r}_{mk}) \times \mathbf{n}_m
\end{aligned}$$

□

Theorem 9 *The basis functions of $\boldsymbol{\mathcal{ND}}_1(\Gamma_h)$ are tangentially continuous, except for the sign: $(\hat{\mathbf{f}}_{mk} \cdot \mathbf{b}_{mk})\hat{\mathbf{f}}_{mk} = \pm(\hat{\mathbf{f}}_{ni} \cdot \mathbf{b}_{ni})\hat{\mathbf{f}}_{ni}$ if edge(mk)=edge(ni), with unit vectors $\hat{\mathbf{f}}_{mk} := \frac{\mathbf{f}_{mk}}{f_{mk}}$ and $\hat{\mathbf{f}}_{ni} := \frac{\mathbf{f}_{ni}}{f_{ni}}$.*

Proof: The vector $\hat{\mathbf{f}}_{mk}$ lies in the plane orthogonal to $\mathbf{t}_{mk}$. This plane has the basis functions $\hat{\mathbf{f}}_{mk}$ and $\mathbf{n}_m$. As $\mathbf{b}_{mk}$ has only components orthogonal to $\mathbf{n}_m$, it follows

$$\begin{aligned}
(\hat{\mathbf{f}}_{mk} \cdot \mathbf{b}_{mk})\hat{\mathbf{f}}_{mk} &= [\mathbf{t}_{mk} \times \mathbf{b}_{mk}] \times \mathbf{t}_{mk} = \left(\frac{-\mathbf{n}_m}{2 \cdot T_m} \cdot [(\mathbf{r} - \mathbf{r}_{mk}) \cdot \mathbf{t}_{mk}]\right) \times \mathbf{t}_{mk} \\
&= \left(\frac{-\mathbf{n}_m}{2 \cdot T_m} \cdot \frac{2 \cdot T_m}{f_{mk}}\right) \times \mathbf{t}_{mk} = \frac{-\mathbf{n}_m}{f_{mk}} \times \mathbf{t}_{mk} \\
&= \frac{\mathbf{f}_{mk}}{f_{mk}^2} = \pm \frac{\mathbf{f}_{ni}}{f_{ni}^2} \,.
\end{aligned}$$

□

In the CAD data files, the order of the points in a triangle is fixed and they define the outer normal by a right hand rule. Then it always holds $\hat{\mathbf{f}}_{mk} = -\hat{\mathbf{f}}_{ni}$. The electric field must be tangentially continuous at the interface of two triangles. At the edge j with basis functions $\mathbf{b}_{mk}$ and $\mathbf{b}_{ni}$ on the adjacent triangles m and n, this forces $\mathbf{E} = E_j \cdot \gamma_D \mathbf{v}_j$ with $\gamma_D \mathbf{v}_j := [sign(\mathbf{b}_{mk})\mathbf{b}_{mk} + sign(\mathbf{b}_{ni})\mathbf{b}_{ni}]$, depending on the orientation of the basis functions. For the discretized electric field one finds

$$\gamma_D \mathbf{E} = \sum_{edges\ j} E_j \cdot \gamma_D \mathbf{v}_j \quad \text{with } E_j \in \mathbb{C} \,. \tag{4.17}$$

The surface curl of the basis functions can be written as

$$\begin{aligned} \mathrm{curl}_\Gamma\, \mathbf{b}_{mk} &= \mathbf{n}_m \cdot \mathbf{curl}\, \mathbf{b}_{mk} \;=\; \mathbf{n}_m \cdot (\mathbf{grad} \times \mathbf{b}_{mk}) \\ &= \frac{\mathbf{n}_m}{2 \cdot T_m} \cdot [\mathbf{grad} \times (\mathbf{r} \times \mathbf{n}_m)] \;=\; \frac{\mathbf{n}_m}{2 \cdot T_m} \cdot [-\mathbf{n}_m (\mathbf{grad}\, \mathbf{r})] \;=\; \frac{-3}{2 \cdot T_m} \;. \end{aligned} \tag{4.18}$$

Now all occuring functions can be expressed with the basis functions that can be obtained from fundamental triangle properties.

4.2.2 Matrix Representation

With the knowledge of the basis functions, the system of equations (4.6)-(4.8) can now be represented in terms of a matrix. It consists of some submatrices which are defined as:

$$\mathsf{M}_{\Re_{i,\,k}} := \mu_0 \left\langle \Re[\frac{1}{\eta}] \cdot \gamma_D \mathbf{v}_k, \gamma_D \mathbf{v}_i \right\rangle_{\boldsymbol{\tau}} + \langle V(\mathrm{curl}_\Gamma\, \gamma_D \mathbf{v}_k), \mathrm{curl}_\Gamma\, \gamma_D \mathbf{v}_i \rangle_{\boldsymbol{\tau}} \;, \tag{4.19}$$

$$\mathsf{M}_{\Im_{i,\,k}} := \mu_0 \left\langle \Im[\frac{1}{\eta}] \cdot \gamma_D \mathbf{v}_k, \gamma_D \mathbf{v}_i \right\rangle_{\boldsymbol{\tau}} \;, \tag{4.20}$$

$$\mathsf{Q}_{i,\,k} := \langle \mathbf{A}(\mathbf{curl}_\Gamma \psi_k), \mathbf{curl}_\Gamma \psi_i \rangle_{\boldsymbol{\tau}} \;, \tag{4.21}$$

$$\mathsf{B}_{i,\,k} := \langle \mathbf{B}(\mathbf{curl}_\Gamma \psi_i), \gamma_D \mathbf{v}_k \rangle_{\boldsymbol{\tau}} \;, \tag{4.22}$$

with the aid of the abbreviations '$\Re :=$ real part' and '$\Im :=$ imaginary part', and the indices i for the rows and k for the columns. Let Nn be the number of nodes and Ne be the number of edges, then the matrices $\mathsf{M}_\Re$ and $\mathsf{M}_\Im$ are $(Ne \times Ne)$-dimensional, Q is $(Nn \times Nn)$-dimensional, and B is $(Nn \times Ne)$-dimensional. All matrices are real valued, and it holds $\mathsf{Q} = \mathsf{Q}^T$, $\mathsf{M}_\Re = \mathsf{M}_\Re^T$, and $\mathsf{M}_\Im = \mathsf{M}_\Im^T$. The right hand side is denoted by

$$\mathbf{R}_{\mathbf{E},\,i} := \langle \mathbf{B}\boldsymbol{\eta}, \gamma_D \mathbf{v}_i \rangle_{\boldsymbol{\tau}} \;, \tag{4.23}$$

$$\mathbf{R}_{\phi,\,i} := \langle \mathbf{A}\boldsymbol{\eta}, \mathbf{curl}_\Gamma \psi_i \rangle_{\boldsymbol{\tau}} \;, \tag{4.24}$$

$$\mathbf{R}_{\alpha,\,i} := \langle \mathbf{A}\boldsymbol{\eta}, \boldsymbol{\eta}_i \rangle_{\boldsymbol{\tau}} \;. \tag{4.25}$$

One has to solve the following equation for the impedance model

$$\begin{pmatrix} \mathsf{M}_\Re & -\mathsf{M}_\Im & -\mathsf{B}^T & 0 \\ -\mathsf{M}_\Im & -\mathsf{M}_\Re & 0 & \mathsf{B}^T \\ -\mathsf{B} & 0 & -\mathsf{Q} & 0 \\ 0 & \mathsf{B} & 0 & \mathsf{Q} \end{pmatrix} \begin{pmatrix} \mathbf{E}_\Re \\ \mathbf{E}_\Im \\ \boldsymbol{\phi}_\Re \\ \boldsymbol{\phi}_\Im \end{pmatrix} = \mu_0 \omega I_{exc.} \cdot \begin{pmatrix} 0 \\ \mathbf{R}_\mathbf{E} \\ 0 \\ \mathbf{R}_\phi \end{pmatrix} \;, \tag{4.26}$$

in the case that the workpiece has no hole, i.e. L=1. The occuring matrix is symmetric but not positive definite.

With $(L-1)$ holes in the workpiece, one additionally needs the $(Ne \times (L-1))$-dimensional matrix F_{up}, the $(Nn \times (L-1))$-dimensional matrix F_{do}, and the $((L-1) \times (L-1))$-dimensional matrix H

$$\mathsf{F}_{\mathsf{up}i,k} := \langle \mathbf{B}\boldsymbol{\eta}_k, \gamma_D \mathbf{v}_i \rangle_{\boldsymbol{\tau}} \;, \tag{4.27}$$

$$\mathsf{F}_{\mathsf{do}i,k} := \langle \mathbf{A}\boldsymbol{\eta}_k, \mathbf{curl}_\Gamma \psi_i \rangle_{\boldsymbol{\tau}} \;, \tag{4.28}$$

$$\mathsf{H}_{i,k} := \langle \mathbf{A}\boldsymbol{\eta}_k, \boldsymbol{\eta}_i \rangle_{\boldsymbol{\tau}} \;, \tag{4.29}$$

and in this most general case one has to solve the problem

$$\boxed{\begin{pmatrix} \mathsf{M}_{\Re} & -\mathsf{M}_{\Im} & -\mathsf{B}^T & 0 & -\mathsf{F}_{\mathsf{up}} & 0 \\ -\mathsf{M}_{\Im} & -\mathsf{M}_{\Re} & 0 & \mathsf{B}^T & 0 & \mathsf{F}_{\mathsf{up}} \\ -\mathsf{B} & 0 & -\mathsf{Q} & 0 & -\mathsf{F}_{\mathsf{do}} & 0 \\ 0 & \mathsf{B} & 0 & \mathsf{Q} & 0 & \mathsf{F}_{\mathsf{do}} \\ -{\mathsf{F}_{\mathsf{up}}}^T & 0 & -{\mathsf{F}_{\mathsf{do}}}^T & 0 & -\mathsf{H} & 0 \\ 0 & {\mathsf{F}_{\mathsf{up}}}^T & 0 & {\mathsf{F}_{\mathsf{do}}}^T & 0 & \mathsf{H} \end{pmatrix} \begin{pmatrix} \mathbf{E}_{\Re} \\ \mathbf{E}_{\Im} \\ \boldsymbol{\phi}_{\Re} \\ \boldsymbol{\phi}_{\Im} \\ \boldsymbol{\alpha}_{\Re} \\ \boldsymbol{\alpha}_{\Im} \end{pmatrix} = \mu_0 \omega I_{exc.} \cdot \begin{pmatrix} 0 \\ \mathbf{R}_{\mathbf{E}} \\ 0 \\ \mathbf{R}_{\phi} \\ 0 \\ \mathbf{R}_{\alpha} \end{pmatrix} . \qquad (4.30)}$$

4.3 Semi-Analytical Integration of the Kernels

In order to get a exact solution, it is necessary to calculate the occuring matrix entries of (4.19)-(4.22) , (4.27)-(4.29) as accurately as possible. The entries consist of boundary integrals over the triangles $\triangle_m$ and $\triangle_n$ which have the form

$$\int\limits_{\triangle_n}\int\limits_{\triangle_m} f(\mathbf{x},\, \mathbf{y})\, dS(\mathbf{x})\, dS(\mathbf{y})\,,$$

with a singular function f at $\mathbf{x} = \mathbf{y}$. It is due to the singularities that a numerical Gaussian quadrature scheme is not applicable for both integrals. A semi-analytical approach[1] is utilized, where the interior integral is calculated analytically and the exterior integral is evaluated by a Gaussian quadrature scheme.

Plugging the basis functions and relations of Section 4.2.1 into the operators $\mathsf{M}_{\Re}$ of equation (4.19), $\mathsf{M}_{\Im}$ of equation (4.20), and for Q of equation (4.21), one gets

$$\begin{aligned} \mu_0 \left\langle \Re[\frac{1}{\eta}] \cdot \mathbf{b}_{nk}, \mathbf{b}_{mi} \right\rangle_{\boldsymbol{\tau}} \;+\; \langle V(\mathrm{curl}_\Gamma\, \mathbf{b}_{nk}), \mathrm{curl}_\Gamma\, \mathbf{b}_{mi} \rangle_{\boldsymbol{\tau}} \;=& \qquad (4.31) \\ \int\limits_{\triangle_n}\int\limits_{\triangle_m} \left((\mathbf{b}_{nk} \cdot \mathbf{b}_{mn}) \cdot \mu_0 \cdot \Re[\frac{1}{\eta}] \cdot \delta_{nm} \;+\; \frac{9}{4T_nT_m} G(\mathbf{x},\mathbf{y}) \right) dS(\mathbf{x})\, dS(\mathbf{y})\,,& \end{aligned}$$

$$\mu_0 \left\langle \Im[\frac{1}{\eta}] \cdot \mathbf{b}_{nk}, \mathbf{b}_{mi} \right\rangle_{\boldsymbol{\tau}} \;=\; \int\limits_{\triangle_n}\int\limits_{\triangle_m} (\mathbf{b}_{nk} \cdot \mathbf{b}_{mn}) \left(\mu_0 \cdot \Im[\frac{1}{\eta}] \cdot \delta_{nm} \right) dS(\mathbf{x})\, dS(\mathbf{y})\,, \qquad (4.32)$$

$$\begin{aligned} \langle \mathbf{curl}_\Gamma \varphi_{nk}, \mathbf{A}(\mathbf{curl}_\Gamma \varphi_{mi}) \rangle_{\boldsymbol{\tau}} \;&=\; \left\langle \frac{\mathbf{f}_{nk}}{2 \cdot T_n}, \mathbf{A}(\frac{\mathbf{f}_{mi}}{2 \cdot T_m}) \right\rangle_{\boldsymbol{\tau}} \qquad (4.33) \\ &=\; \int\limits_{\triangle_n}\int\limits_{\triangle_m} \frac{1}{4\, T_n\, T_m} (\mathbf{f}_{nk} \cdot \mathbf{f}_{mi}) \cdot G(\mathbf{x},\mathbf{y})\, dS(\mathbf{x})\, dS(\mathbf{y})\,. \end{aligned}$$

---

[1] I am indebted to Dr. Olaf Steinbach, University of Stuttgart, for the analytical interior integration of single layer and double layer potential (private communication).

So all three operators consist of a single layer potential, either vector or scalar valued. The analytical integrations are done by Dr. O. Steinbach and are therefore not be repeated here. For the operator B it follows

$$
\begin{aligned}
&\langle \mathbf{B}(\boldsymbol{\lambda}), \gamma_D \mathbf{v} \rangle_{\boldsymbol{\tau}} \\
&\quad = \int_\Gamma \mathbf{B}(\boldsymbol{\lambda})(\mathbf{x}) \cdot \gamma_D \mathbf{v}(\mathbf{x})\, dS(\mathbf{x}) \;=\; \int_\Gamma \gamma_N^+ \int_\Gamma \boldsymbol{\lambda}(\mathbf{y}) G(\mathbf{x},\mathbf{y})\, dS(\mathbf{y}) \cdot \gamma_D \mathbf{v}(\mathbf{x})\, dS(\mathbf{x}) \\
&\quad = \int_\Gamma \left[\mathbf{curl}_{\mathbf{x}}^+ \Big[\int_\Gamma \boldsymbol{\lambda}(\mathbf{y}) G(\mathbf{x},\mathbf{y})\, dS(\mathbf{y}) \Big] \times \mathbf{n}_{\mathbf{x}} \right] \cdot \gamma_D \mathbf{v}(\mathbf{x})\, dS(\mathbf{x}) \\
&\quad = \int_\Gamma \left[\Big(\int_\Gamma \mathbf{grad}_{\mathbf{x}}\, G(\mathbf{x},\mathbf{y}) \times \boldsymbol{\lambda}(\mathbf{y})\, dS(\mathbf{y}) - \frac{1}{2} \mathbf{n}_{\mathbf{x}} \times \boldsymbol{\lambda}(\mathbf{x}) \Big) \times \mathbf{n}_{\mathbf{x}} \right] \gamma_D \mathbf{v}(\mathbf{x})\, dS(\mathbf{x}) \\
&\quad = \int_\Gamma \int_\Gamma \left[\boldsymbol{\lambda}(\mathbf{y}) [\mathbf{n}_{\mathbf{x}} \cdot \mathbf{grad}_{\mathbf{x}}\, G(\mathbf{x},\mathbf{y})] - \mathbf{grad}_{\mathbf{x}}\, G(\mathbf{x},\mathbf{y}) [\boldsymbol{\lambda}(\mathbf{y}) \cdot \mathbf{n}_{\mathbf{x}}] \right] \gamma_D \mathbf{v}(\mathbf{x})\, dS(\mathbf{y})\, dS(\mathbf{x}) \\
&\qquad\qquad - \frac{1}{2} \int_\Gamma \boldsymbol{\lambda}(\mathbf{x}) \cdot \gamma_D \mathbf{v}(\mathbf{x})\, dS(\mathbf{x})\,,
\end{aligned}
$$

by using the jump condition [Rei93]

$$
\mathbf{curl}_{\mathbf{x}}^+ \int_\Gamma \boldsymbol{\lambda}(\mathbf{y}) G(\mathbf{x},\mathbf{y})\, dS(\mathbf{y}) \;=\; \int_\Gamma \mathbf{curl}_{\mathbf{x}} \left[\boldsymbol{\lambda}(\mathbf{y}) G(\mathbf{x},\mathbf{y}) \right] dS(\mathbf{y}) - \frac{1}{2} \mathbf{n}(\mathbf{x}) \times \boldsymbol{\lambda}(\mathbf{x})\,.
$$

This can be expressed by the basis functions. Then one has to integrate

$$
\begin{aligned}
&\langle \mathbf{B}(\mathbf{curl}_\Gamma\, \varphi_{ni}), \mathbf{b}_{mk} \rangle_{\boldsymbol{\tau}} \;= \\
&\int_{\triangle_n} \int_{\triangle_m} \left[-\frac{\mathbf{f}_{ni}}{2 \cdot T_n} [\mathbf{n}_{\mathbf{x}} \cdot \mathbf{grad}_{\mathbf{x}}\, G(\mathbf{x},\mathbf{y})] + \mathbf{grad}_{\mathbf{x}}\, G(\mathbf{x},\mathbf{y}) [\frac{\mathbf{f}_{ni}}{2 \cdot T_n} \cdot \mathbf{n}_{\mathbf{x}}] \right] \mathbf{b}_{mk}(\mathbf{x})\, dS(\mathbf{x})\, dS(\mathbf{y}) \\
&\qquad + \delta_{mn} \cdot \frac{1}{2} \int_{\triangle_m} \frac{\mathbf{f}_{ni}}{2 \cdot T_n} \mathbf{b}_{mk}(\mathbf{x})\, dS(\mathbf{x}) \\
&= \int_{\triangle_n} \int_{\triangle_m} [\frac{\mathbf{f}_{ni}}{2 \cdot T_n} \mathbf{b}_{mk}(\mathbf{x})] \cdot [\frac{\delta_{mn}}{2\, T_m} - \mathbf{n}_{\mathbf{x}} \cdot \mathbf{grad}_{\mathbf{x}}\, G(\mathbf{x},\mathbf{y})]\, dS(\mathbf{x})\, dS(\mathbf{y}) \\
&\qquad + \int_{\triangle_n} \int_{\triangle_m} [\frac{\mathbf{f}_{ni}}{2 \cdot T_n} \cdot \mathbf{n}_m] \cdot [\mathbf{b}_{mk}(\mathbf{x}) \cdot \mathbf{grad}_{\mathbf{x}}\, G(\mathbf{x},\mathbf{y})]\, dS(\mathbf{x})\, dS(\mathbf{y})\,.
\end{aligned}
\tag{4.34}
$$

The first integral consists of an easily integrable diagonal part and a double layer potential. The second integral is a modified double layer potential. Note that the kernel is vector-valued.

As an example for the analytical integration of the inner integral, the modified double layer potential is chosen and integrated below.

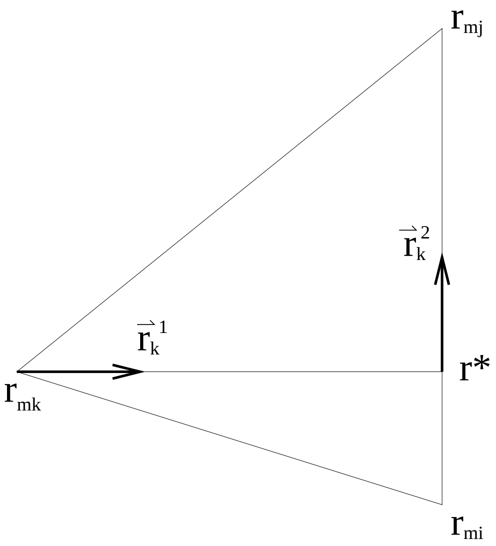

Figure 4.4: Settings for the analytical integration

Therefore the notation of Figure 4.4 is used and every position vector $\mathbf{r}$ can be expressed as $\mathbf{r} \;=\; \mathbf{r}_{mk} + s\,\mathbf{r}_k^1 + t\,\mathbf{r}_k^2 + \tau\,\mathbf{n}_m$ with $t,\ s,\ \tau \in \mathbb{R}$, and it holds

$$\mathbf{b}_{mk} \;=\; \frac{1}{2\cdot T_m}\,(s\,\mathbf{r}_k^1 + t\,\mathbf{r}_k^2)\times\mathbf{n}_m \;=\; \frac{1}{2\cdot T_m}\,(t\,\mathbf{r}_k^1 - s\,\mathbf{r}_k^2)\,.$$

With the definitions

$$\begin{aligned} s_k \;&:=\; \|\mathbf{r}^* - \mathbf{r}_{mk}\|\,, \quad t_k \;:=\; \|\mathbf{r}_{mi} - \mathbf{r}_{mj}\|\,, \quad t^* \;:=\; \|\mathbf{r}^* - \mathbf{r}_{mi}\|\,, \\ \alpha_1 \;&:=\; -\frac{t^*}{s_k}\,, \quad \alpha_2 \;:=\; -\frac{t_k - t^*}{s_k}\,, \quad \mathbf{y} \;=\; \mathbf{r}_{mk} + s_y\,\mathbf{r}_k^1 + t_y\,\mathbf{r}_k^2 + \tau_y\,\mathbf{n}_m \end{aligned}$$

one obtains

$$\begin{aligned} &\int\limits_{\triangle_m} \mathbf{b}_{mk}(\mathbf{x})\cdot\mathbf{grad}_{\mathbf{x}}\,G(\mathbf{x},\mathbf{y})\,dS(\mathbf{x}) \\ &\quad=\; \frac{1}{4\,\pi}\int\limits_{\triangle_m}\mathbf{b}_{mk}(\mathbf{x})\cdot\frac{\mathbf{x}\,-\,\mathbf{y}}{||\mathbf{x}\,-\,\mathbf{y}||^3}\,dS(\mathbf{x}) \\ &\quad=\; \frac{1}{8\,\pi T_m}\int\!\!\int(t\,\mathbf{r}_k^1 - s\,\mathbf{r}_k^2)\cdot\frac{(s-s_y)\cdot\mathbf{r}_k^1\;+\;(t-t_y)\cdot\mathbf{r}_k^2\;+\tau_y\cdot\mathbf{n}_m}{[(s-s_y)^2\;+\;(t-t_y)^2\;+\;\tau_y^2]^{3/2}}\,dt\,ds \\ &\quad=\; \frac{1}{8\,\pi T_m}\int\!\!\int\frac{(s-s_y)\cdot t\;-\;(t-t_y)\cdot s}{[(s-s_y)^2\;+\;(t-t_y)^2\;+\;\tau_y^2]^{3/2}}\,dt\,ds \\ &\quad=\; \frac{1}{8\,\pi T_m}\Big[\int t\int\frac{s-s_y}{[(s-s_y)^2\;+\;(t-t_y)^2\;+\;\tau_y^2]^{3/2}}\,ds\,dt \\ &\qquad\qquad -\int s\int\frac{t-t_y}{[(s-s_y)^2\;+\;(t-t_y)^2\;+\;\tau_y^2]^{3/2}}\,dt\,ds\Big] \end{aligned}$$

$$
\begin{aligned}
&= \frac{1}{8\,\pi T_m}\Big[\int_{-t^*}^{0} t \int_{t/\alpha_1}^{s_k} \frac{s-s_y}{[(s-s_y)^2\,+\,(t-t_y)^2\,+\,\tau_y^2]^{3/2}}\,ds\,dt \\
&\qquad\qquad + \int_{0}^{t_k-t^*} t \int_{t/\alpha_2}^{s_k} \frac{s-s_y}{[(s-s_y)^2\,+\,(t-t_y)^2\,+\,\tau_y^2]^{3/2}}\,ds\,dt \\
&\qquad\quad - \int_{0}^{s_k} s \int_{\alpha_1 s}^{\alpha_2 s} \frac{t-t_y}{[(s-s_y)^2\,+\,(t-t_y)^2\,+\,\tau_y^2]^{3/2}}\,dt\,ds\Big] \\
&= \frac{1}{8\,\pi T_m}\Big[\int_{-t^*}^{0} t \int_{t/\alpha_1-s_y}^{s_k-s_y} \frac{x}{[x^2\,+\,(t-t_y)^2\,+\,\tau_y^2]^{3/2}}\,dx\,dt \\
&\qquad\qquad + \int_{0}^{t_k-t^*} t \int_{t/\alpha_2-s_y}^{s_k-s_y} \frac{x}{[x^2\,+\,(t-t_y)^2\,+\,\tau_y^2]^{3/2}}\,dx\,dt \\
&\qquad\quad - \int_{0}^{s_k} s \int_{\alpha_1 s-t_y}^{\alpha_2 s-t_y} \frac{x}{[x^2\,+\,(s-s_y)^2\,+\,\tau_y^2]^{3/2}}\,dx\,ds\Big]\,.
\end{aligned}
$$

The inner integral can be found in integral tables $\int x\cdot[x^2\,+\,a^2]^{-3/2}\,dx = -[x^2\,+\,a^2]^{-1/2}$, then what remains for the outer integral is

$$
\begin{aligned}
& 8\,\pi T_m \cdot \int_{\triangle_m} \mathbf{b}_{mk}(\mathbf{x})\cdot \mathbf{grad}_{\mathbf{x}}\, G(\mathbf{x},\mathbf{y})\,dS(\mathbf{x}) \\
&= \int_{-t^*}^{0} \left|\frac{-t}{[x^2\,+\,(t-t_y)^2\,+\,\tau_y^2]^{1/2}}\right|_{x=t/\alpha_1-s_y}^{s_k-s_y} dt + \int_{0}^{t_k-t^*} \left|\frac{-t}{[x^2\,+\,(t-t_y)^2\,+\,\tau_y^2]^{1/2}}\right|_{x=t/\alpha_2-s_y}^{s_k-s_y} dt \\
&\quad + \int_{0}^{s_k} \left|\frac{s}{[x^2\,+\,(s-s_y)^2\,+\,\tau_y^2]^{1/2}}\right|_{x=\alpha_1 s-t_y}^{\alpha_2 s-t_y} ds \\
&= \int_{-t^*}^{t_k-t^*} \frac{-t}{[(s_k-s_y)^2\,+\,(t-t_y)^2\,+\,\tau_y^2]^{1/2}}\,dt \\
&\quad + \int_{-t^*}^{0} \frac{t}{[(t/\alpha_1-s_y)^2\,+\,(t-t_y)^2\,+\,\tau_y^2]^{1/2}}\,dt + \int_{0}^{t_k-t^*} \frac{t}{[(t/\alpha_2-s_y)^2\,+\,(t-t_y)^2\,+\,\tau_y^2]^{1/2}}\,dt \\
&\quad + \int_{0}^{s_k} \frac{s}{[(\alpha_2 s-t_y)^2\,+\,(s-s_y)^2\,+\,\tau_y^2]^{1/2}}\,ds - \int_{0}^{s_k} \frac{s}{[(\alpha_1 s-t_y)^2\,+\,(s-s_y)^2\,+\,\tau_y^2]^{1/2}}\,ds
\end{aligned}
$$

$$
\begin{aligned}
= \quad & \int\limits_{-t^*}^{t_k - t^*} \frac{-t}{[t^2 - 2t_y \cdot t + (s_k - s_y)^2 + t_y^2 + \tau_y^2]^{1/2}}\, dt \\
+ & \int\limits_{-t^*}^{0} \frac{t}{[(1/\alpha_1^2 + 1) \cdot t^2 - 2(s_y/\alpha_1 + t_y) \cdot t + s_y^2 + t_y^2 + \tau_y^2]^{1/2}}\, dt \\
+ & \int\limits_{0}^{t_k - t^*} \frac{t}{[(1/\alpha_2^2 + 1) \cdot t^2 - 2(s_y/\alpha_2 + t_y) \cdot t + s_y^2 + t_y^2 + \tau_y^2]^{1/2}}\, dt \\
+ & \int\limits_{0}^{s_k} \frac{s}{[(\alpha_2^2 + 1) \cdot s^2 - 2(\alpha_2 t_y + s_y) \cdot s + t_y^2 + s_y^2 + \tau_y^2]^{1/2}}\, ds \\
- & \int\limits_{0}^{s_k} \frac{s}{[(\alpha_1^2 + 1) \cdot s^2 - 2(\alpha_1 t_y + s_y) \cdot s + t_y^2 + s_y^2 + \tau_y^2]^{1/2}}\, ds\,.
\end{aligned}
$$

All these integrals are of the same form which can also be looked up in integral tables

$$
\int \frac{x}{\sqrt{ax^2 + bx + c}} dx \; = \begin{cases} \frac{\sqrt{ax^2+bx+c}}{a} - \frac{b}{2a}\big(\frac{1}{\sqrt{a}} \cdot arsinh[\frac{2ax+b}{\sqrt{4ac-b^2}}]\big) & \text{if } 4ac - b^2 > 0,\; a > 0 \\ \frac{\sqrt{ax^2+bx+c}}{a} - \frac{b}{2a}\big(\frac{1}{\sqrt{a}} \cdot \ln|\, 2ax - b\,|\big) & \text{if } 4ac - b^2 = 0,\; a > 0. \end{cases}
$$

Now all matrix entries of (4.19)-(4.22) are described in terms of the fundamental basis functions and are integrated semi-analytically. The entries (4.27)-(4.29) can easily be derived from these expressions.

4.4 Paths

As already stated in Section 4.1, the excitation is to be integrated into the impedance model and into the eddy current approach by imposing jumps of the scalar magnetic potential on closed paths, i.e., cycles that circle the hole in the inductor. Jumps also have to be imposed on paths around holes in the workpiece in order to determine the total currents that flow around these holes. The cycles have to be constructed automatically by the program and not by the user for different reasons: First, it is annoying to construct paths by hand for a complicated geometry or for a triangulation with many faces. Second, for some geometries it is very difficult to find the desired cycles, i.e., a path that circumvents the hole. More precisely, such a cycle is a *non-contractable* cycle [Jän01] that is *bounding* with respect to the *exterior* (short ncbe). Bounding with respect to the exterior in simple words means that the cycle is the boundary of a cutting surface that lies exclusively in the exterior of the conductor. An example is the cycle γ_1 in Figure 4.5. Cycle γ_2 in Figure 4.5 is non-contractable and bounding with respect to the interior (short ncbi). It is prohibited to impose a current on such a cycle because the current would flow through the vacuum.

This section presents the algorithm for the automatical construction of the relevant cycles. The algorithm is based on the triangulation Γ_h of the surface and the path consists of an ordered series

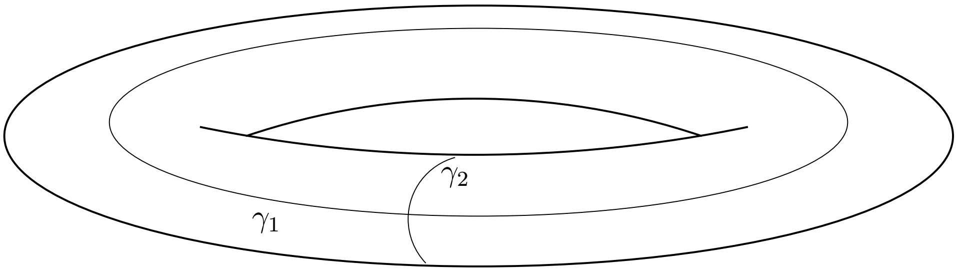

Figure 4.5: Representatives of the basis of $H_1(\Gamma_h, \mathbb{Z})$

of surface vertices connected by surface edges. The intention is to explain the functionality of the algorithm, not to prove every detail. Rigorous proofs can be looked up in [HO01]. The following definitions, theorems, and proofs are, like the above definition of 'bounding', to be understood in the sense of an explanation. Some aspects are illustrated by using the torus as an example, but the algorithm, of course, can be applied to arbitrary parts. Note that the inductor is always equivalent to a torus since it has exactly one hole.

It is clear that there is not only γ_1 which is ncbe. Closed paths γ_1' which are equivalent to γ_1 are called *homotopic* cycles, written as $\gamma_1 \simeq \gamma_1'$. This means that they can be transformed continuously into γ_1 on the surface [Knö96]. It is obvious that γ_2 cannot be transformed into γ_1 on the surface, so $\gamma_1 \not\simeq \gamma_2$.

Definition 6 (Basis of $H_1(\Gamma_h, \mathbb{Z})$, Betti number) *The cycles $(\gamma_1, \cdots, \gamma_{2N})$ are called a representative of the basis of the homology group $H_1(\Gamma_h, \mathbb{Z})$ if each closed path on the surface Γ_h is homotopic to a linear combination (of integer numbers $\in \mathbb{Z}$) of $(\gamma_1, \cdots, \gamma_{2N})$. The rank of this basis is called Betti number and it is two times the number of holes N in the surface.*

The cycles γ_1 and γ_2 of Figure 4.5 are representatives of a basis for the torus. The path algorithm consists of the following two steps:

1. Find a representative of the basis, see Section 4.4.1
2. Construct N linear independent cycles that are ncbe, see Section 4.4.2

Step one of this algorithm is purely combinatorial and relies on interpreting the triangulation Γ_h of the surface $\Gamma := \partial\Omega$ of the item as a graph. Therefore some assumptions on the geometry of Ω have to be made. A demand is that Ω has a Lipschitz-continuous boundary, that is, Γ has to have a local representation as the graph of a Lipschitz-continuous function [Gri85, Sect 1.2.1]. Topologically speaking, this forces $\bar{\Omega}$ to be homeomorphic to a compact domain with smooth boundary. Firstly, this implies $\partial\Gamma = \emptyset$ and that each face is part of a tetrahedron. A second consequence is that Γ is orientable. Thus, we can fix an orientation of $\partial\Omega$ and endow all triangles with the induced orientation. Thirdly, the surface is 'locally flat' in the sense that exactly two faces are incident to each edge. Situations like the 'double cone' and 'double ridge' depicted in Figure 4.6 are ruled out.

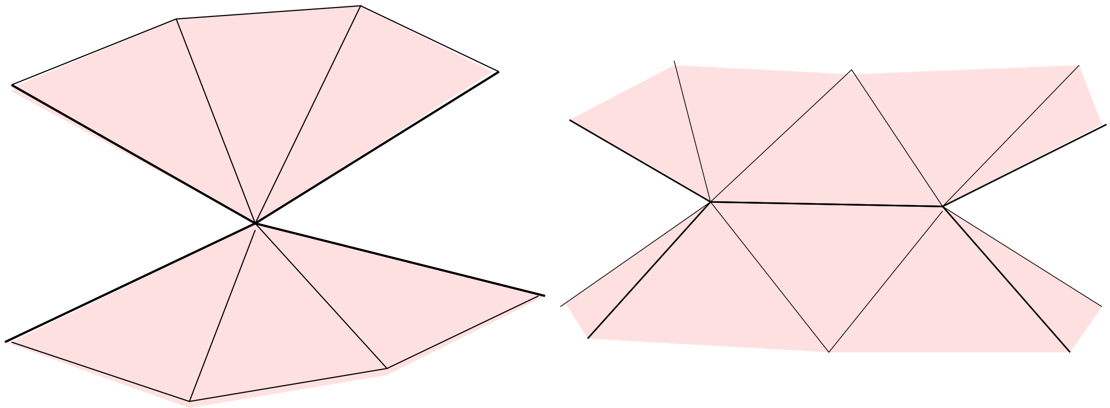

Figure 4.6: Surface configurations not possible in the case of a Lipschitz-polyhedron

At first glance it seems that one can successfully tackle the problem in an entirely discrete setting, relying on the connectivity of Ω_h alone. Yet, consider a plain triangulated torus. Cut it at its small circle, twist by 2π and reconnect as in Fig. 4.7. If the first cycle was ncbe, this operation will render it non-relevant. Possible new representatives of the basis are $(\gamma_3,\ \gamma_1)$ or $(\gamma_3,\ \gamma_2)$. However, the combinatorial description of the mesh remains the same. It is evident that it is impossible to find the desired cycles merely by using combinatorial information about Ω_h. Unless one wants to use an exterior mesh, one also has to rely on information about the geometry of Ω. This is done in step two, where the cycles are classified and the ones relevant are constructed.

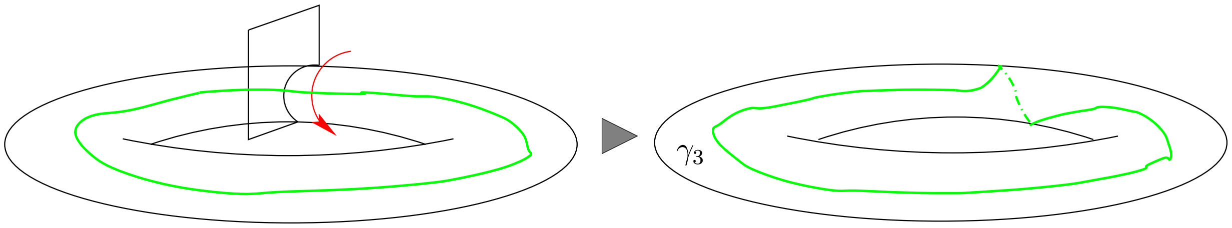

Figure 4.7: Destroying ncbe-cycle

4.4.1 Find a Basis

The example of a hollow torus shows that not every item has a surface that consists of only one component. But it is possible to restrict the explanation to this case because the algorithm *find a basis* can be applied to each component separately. In order to introduce the algorithm, some definitions must be made: Denote by $\mathcal{S}_0 := \mathcal{V}_h, \mathcal{S}_1 := \mathcal{E}_h$, and $\mathcal{S}_2 := \mathcal{F}_h$ the sets of vertices, edges, and faces of the surface mesh Γ_h covering Γ. An l-simplex $\mathbf{x} \in \mathcal{S}_l$ is contained in another k-simplex $\mathbf{y} \in \mathcal{S}_k$, $\mathbf{x} \prec \mathbf{y}$, if all vertices of $\mathbf{x}$ are vertices of $\mathbf{y}$ as well. The k-simplicial neighborhood of $\mathbf{x} \in \mathcal{S}_l$ is defined as

$$\mathcal{S}_k(\mathbf{x}) := \{\mathbf{y} \in \mathcal{S}_k,\ \mathbf{x} \prec \mathbf{y} \textbf{ or } \mathbf{y} \prec \mathbf{x}\}\ .$$

With these notations, the three internal steps of the algorithm *find a basis* can be written as

1.1 build face-tree according to Figure 4.8,

1.2 build node-tree according to Figure 4.10,

1.3 build cycles according to Figure 4.12.

```
$\mathcal{D}_h := \mathcal{F}_h$; $\mathcal{E}_h^D := \emptyset$;
while ($\mathcal{D}_h \neq \emptyset$) {
   Pick $\mathbf{t} \in \mathcal{D}_h$; Q := $\emptyset$; Q.push_back($\mathbf{t}$); $\mathcal{D}_h := \mathcal{D}_h \setminus \{\mathbf{t}\}$;
   while ($Q \neq \emptyset$) {
      t := Q.pop_front();
      for each ($\mathrm{e}' \in \mathcal{S}_1(\mathbf{t})$) {
         $\{\mathbf{t}'\} := \mathcal{S}_2(\mathrm{e}') \setminus \{\mathbf{t}\}$;
         if ($\mathbf{t}' \in \mathcal{D}_h$)   { $\mathcal{D}_h := \mathcal{D}_h \setminus \{\mathbf{t}'\}$; Q.push_back($\mathbf{t}'$); $\mathcal{E}_h^D := \mathcal{E}_h^D \cup \{\mathrm{e}'\}$; }
   }}}
```

Figure 4.8: Algorithm build face-tree

After the face-tree is built in step 1.1, one finds a situation as shown in Figure 4.9 for the example of the torus of Figure 4.5. In Figure 4.9, the torus is cut along the cycles γ_1 and γ_2, and opposite sides must be identified.

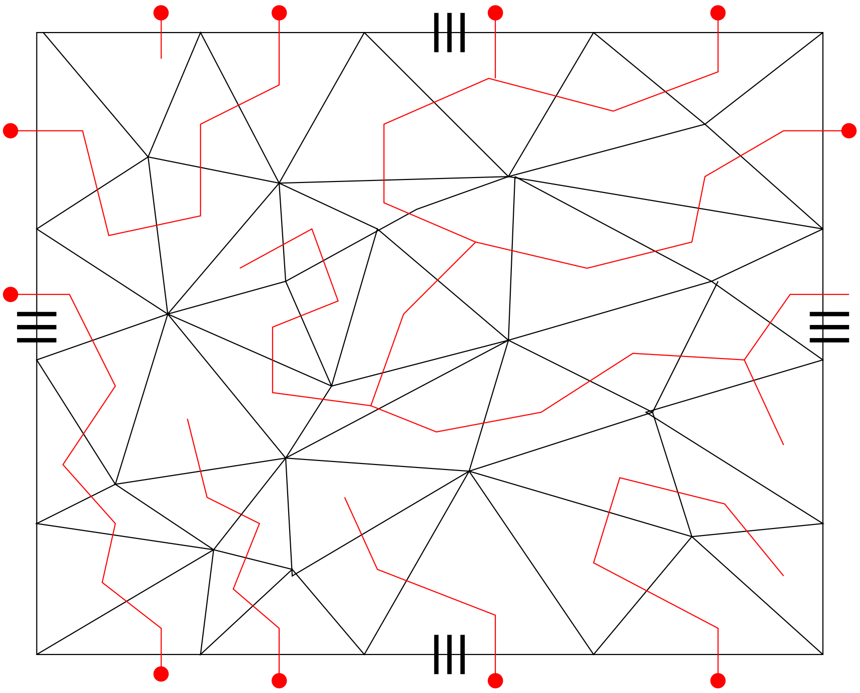

Figure 4.9: Face-tree in the case of a triangulated torus, which is represented by identifying opposite sides of a rectangle. Output of the algorithm from Figure 4.8.

The edges which are ’part of the tree’, i.e., those edges which are touched by the connecting lines of the faces, are collected in the set $\mathcal{E}_h^D$. Its complement, i.e., the set of the remaining edges, is denoted by $\mathcal{E}_\flat^i$.

Theorem 10 *No cycle in $\mathcal{E}_\flat^i$ is contractable.*

Proof: If a contractable cycle existed the surface would consist of the ’interior’ of this cycle and the ’exterior’. The faces of these regions would not have a connection, and this is a contradiction to the fact that the faces are connected by the face-tree. □

Theorem 11 *Each cycle γ on the surface is homotopic to a cycle in $\mathcal{E}_\flat^i$.*

Proof: To prove this, one takes a cycle γ that can have edges in $\mathcal{E}_h^D$, and wipes it off into $\mathcal{E}_\flat^i$. This continuous transformation can always be done according to the following algorithm. First, fix an arbitrary $\mathbf{t}_r \in \mathcal{F}_h$ as ’root’ of the face-tree. This makes it possible to assign to each triangle $\mathbf{t}$ in the tree a unique number $d(\mathbf{t}) \in \mathbb{N}$, its distance to the root, i.e., the length of the unique path in the tree connecting $\mathbf{t}$ and $\mathbf{t}_r$. Then it is also possible to establish a distance function for the edges ’in the tree’

$$d(\mathbf{e}) := \min\{d(\mathbf{t}), \mathbf{e} \prec \mathbf{t}\}, \quad \mathbf{e} \in \mathcal{E}_h^D \ .$$

One sorts the edges of the cycle γ with respect to this ’distance function’. Let $\mathbf{e}_j$ be the edge with the smallest distance in the cycle γ. Select the face $\mathbf{t}_j$ adjacent to the edge $\mathbf{e}_j$ that has the bigger distance from the root and replace the edge $\mathbf{e}_j$ in the cycle γ by the two other edges in $\mathbf{t}_j$. These new edges might either lie in $\mathcal{E}_\flat^i$ or again in $\mathcal{E}_h^D$. The crucial point is that if they are in $\mathcal{E}_h^D$, then their distance to the root is bigger than the distance of $\mathbf{e}_j$! So, repeating this construction, one arrives at a cycle $\tilde{\gamma}$ in $\mathcal{E}_\flat^i$ with $\tilde{\gamma} \simeq \gamma$. □

The last theorem ensures that a representative of a basis of $H_1(\Gamma_h, \mathbb{Z})$ is included in $\mathcal{E}_\flat^i$. The remaining task is to explicitely construct the cycles, i.e., the series of points. Therefore, one first builds a node-tree in $\mathcal{E}_\flat^i$ according to the algorithm presented in Figure 4.10 (the edges in $\mathcal{E}_\flat^i$ are connected [HO01]). Due to theorem 10 one finds exactly $2N$ edges, which would close the node-tree and collects them in the set $\mathcal{E}_*^i$. Starting from the nodes of these edges, one constructs the cycles by climbing up the node-tree tree to its root, according to the algorithm of Figure 4.12. The cycles in this algorithm are stored as $2N$ lists of edges, but this structure can easily be converted into the desired series of nodes.

```
$\mathcal{L}_h := \mathcal{V}_h;\ \mathcal{E}^i_* := \emptyset;$
while $(\mathcal{L}_h \neq \emptyset)$ {
  Pick $\mathbf{v} \in \mathcal{L}_h$; $\mathbf{v}$.depth := 0; $\mathcal{L}_h := \mathcal{L}_h \setminus \{\mathbf{v}\}$; Q := $\emptyset$; Q.push_back$(\mathbf{v})$;
  while $(Q \neq \emptyset)$ {
    $\mathbf{v}$ := Q.pop_front();
    for each $(\mathrm{e}' \in \mathcal{S}_1(\mathbf{v}) \setminus \mathcal{E}_h^D)$ {
      $\{\mathbf{v}'\} := \mathcal{S}_0(\mathrm{e}') \setminus \{\mathbf{v}\}$;
      if $(\mathbf{v}' \in \mathcal{L}_h)$  { $\mathcal{L}_h := \mathcal{L}_h \setminus \{\mathbf{v}'\}$; Q.push_back$(\mathbf{v}')$; $\mathbf{v}'$.depth = $\mathbf{v}$.depth$+1$; }
      else  { $\mathcal{E}^i_* := \mathcal{E}^i_* \cup \{\mathrm{e}'\}$; }
    }}}
```

Figure 4.10: Algorithm build node-tree

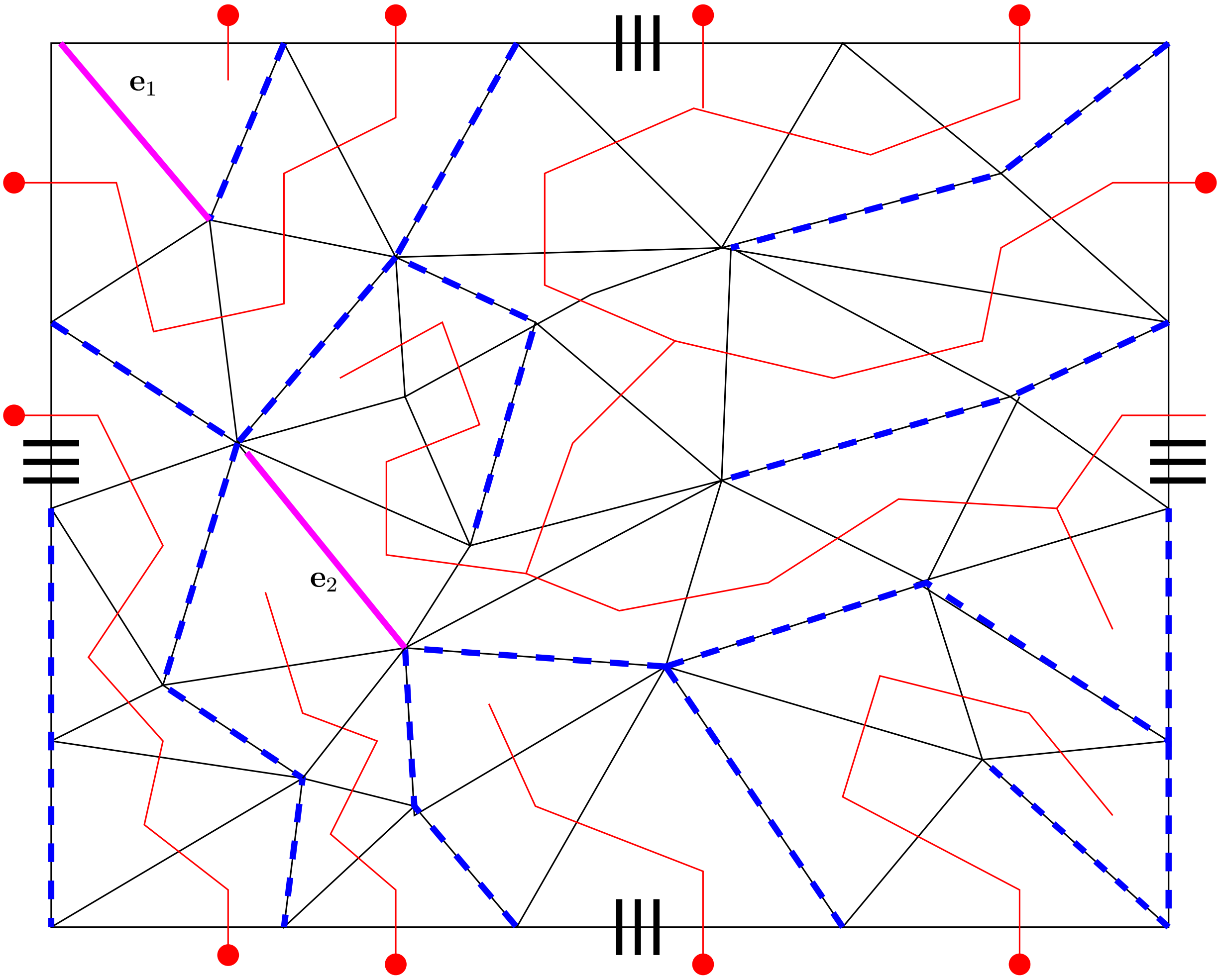

Figure 4.11: Construction of the node-tree (dashed lines) on the torus according to the algorithm of Figure 4.10, yielding $\mathcal{E}^i_* := \{\mathrm{e}_1, \mathrm{e}_2\}$.

```
for each ($e \in \mathcal{E}^i_*$) {
   list<Edge> $s_e$; $s_e := \emptyset$; $\{x, y\} := \mathcal{S}_0(e)$; $s_e$.push_back($e$);
   do {
      while ($x$.depth > $y$.depth) {
         for each ($e' \in \mathcal{S}_1(x) \setminus \mathcal{E}^D_h$) {
            $\{z\} := \mathcal{S}_0(e') \setminus \{x\}$;
            if ($z$.depth < $x$.depth)   { $s_e$.push_back($e'$); $x \leftarrow z$; break; }}}
      while ($x$.depth $\leq$ $y$.depth and $x \neq y$) {
         for each ($e' \in \mathcal{S}_1(y) \setminus \mathcal{E}^D_h$) {
            $\{z\} := \mathcal{S}_0(e') \setminus \{y\}$;
            if ($z$.depth $\leq$ $y$.depth)   { $s_e$.push_front($e'$); $y \leftarrow z$; break; }}}
   }
   while ($x \neq y$); }
```

Figure 4.12: Algorithm build cycles

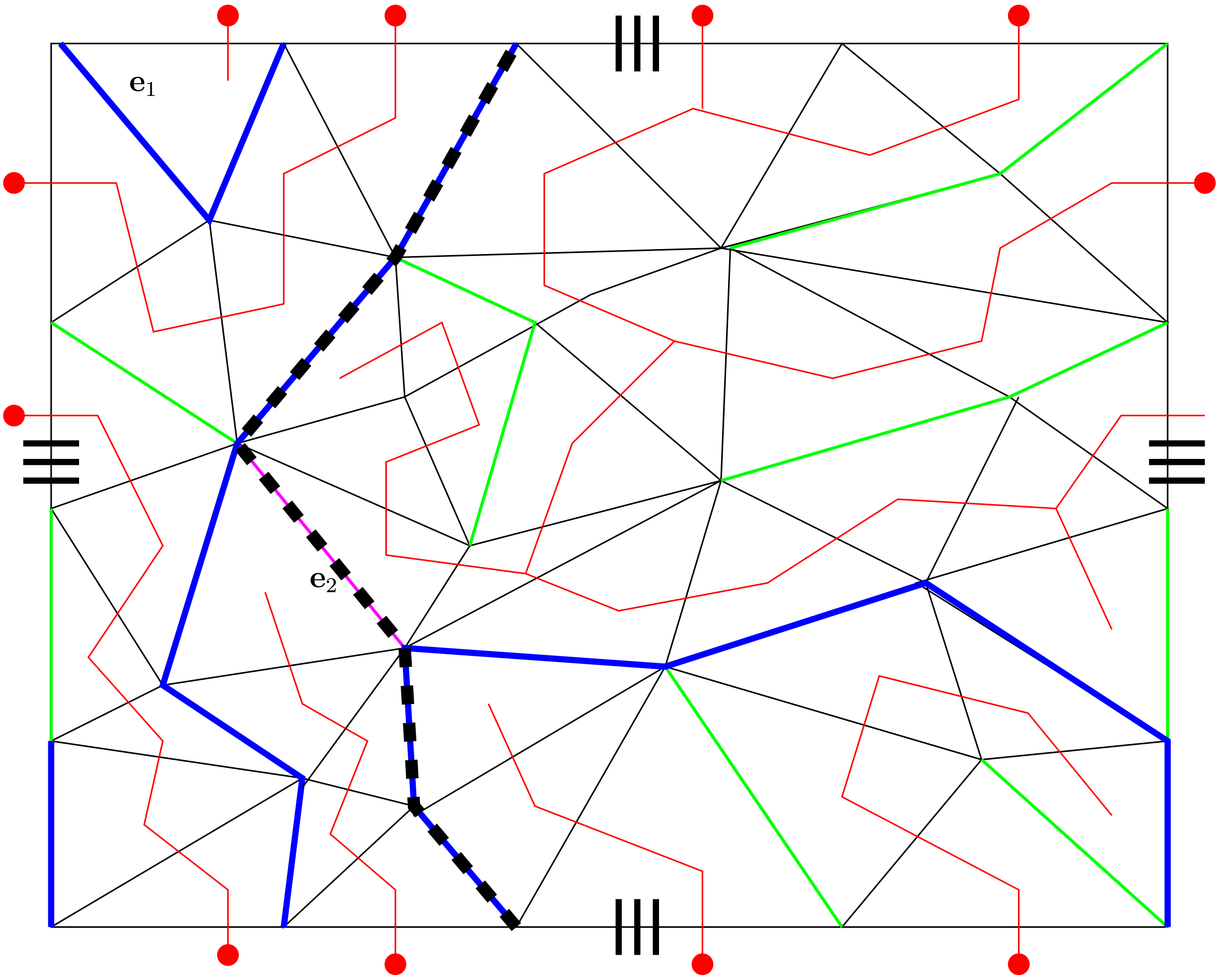

Figure 4.13: Two circuits s_{e_1} (solid) and s_{e_2} (dashed) on the triangulated torus as produced by the algorithm of Figure 4.12.

4.4.2 Construct Linear Independent ncbe-Cycles

As pointed out in Section 4.4, finding ncbe-generators of $H_1(\Gamma_h, \mathbb{Z})$ involves geometric considerations, because one has to distinguish between ncbe-cycles, ncbi-cycles, and mixed cycles. All these types of cycles can occur in the basis. A look at Figure 4.5 in combination with the knowledge of Biot-Savart's law gives an idea of how to cope with that problem. If cycle γ_1 is submerged into the interior of the torus $\gamma_1 \to \gamma_1\!\downarrow$ and a loop-current of strength one is imposed on this cycle, then a current of 1 Ampère flows through cycle γ_2.

$$\begin{aligned} 1 &= \int\limits_{\gamma_2} \mathbf{H}\, d\vec{s}(\mathbf{y}) \\ &= -\int\limits_{\gamma_2} \left[\int\limits_{\gamma_1\downarrow} \mathbf{grad}_{\mathbf{y}}\, G(\mathbf{x},\mathbf{y}) \times d\vec{s}(\mathbf{x}) \right] d\vec{s}(\mathbf{y}) \\ &= -\int\limits_{\gamma_2} \int\limits_{\gamma_1\downarrow} \mathbf{grad}_{\mathbf{y}}\, G(\mathbf{x},\mathbf{y}) \cdot (d\vec{s}(\mathbf{x}) \times d\vec{s}(\mathbf{y})) \end{aligned} \tag{4.35}$$

Here G is again the singular function of the Laplacian. The situation is illustrated in the left picture of Figure 4.14. If both cycles change their roles, like in the right picture, and γ_2 is submerged into the torus, no current will flow through γ_1. So this process of submerging one cycle and testing it with an other one seems to be the key to the desired geometrical information. In order to extend the idea to a more general setting, the *relative linking number* $L(\gamma, \gamma')$ of two cycles γ and γ' is defined as

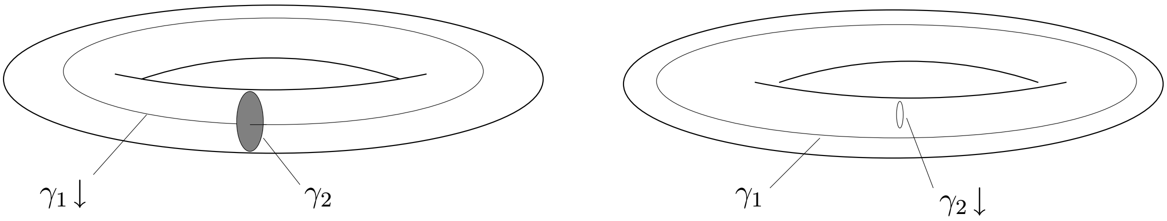

Figure 4.14: Left submerge γ_1, right submerge γ_2

$$L(\gamma, \gamma') := -\int\limits_{\gamma} \int\limits_{\gamma'} \mathbf{grad}_{\mathbf{y}}\, G(\mathbf{x},\mathbf{y}) \cdot (d\vec{s}(\mathbf{x}) \times d\vec{s}(\mathbf{y}))\,. \tag{4.36}$$

The mapping from two cycles into $\mathbb{Z}$ by submerging and testing can now be written as

$$\langle \gamma', \gamma \rangle := L(\gamma\!\downarrow, \gamma') \tag{4.37}$$

in compact format. For the torus it holds $\langle \gamma_2, \gamma_1 \rangle = 1$ and $\langle \gamma_1, \gamma_2 \rangle = \langle \gamma_1, \gamma_1 \rangle = \langle \gamma_2, \gamma_2 \rangle = 0$. This can be ordered as a matrix

$$A := (\langle \gamma_j, \gamma_i \rangle)_{i,j=1}^{2N} \in \mathbb{Z}^{2N,2N}\ . \tag{4.38}$$

Each cycle on the surface of the torus is homotopic to a cycle $\delta = \sum_{j=1}^{2N} \kappa_j \gamma_j$, and one finds the relevant ncbe-cycle [2] as the kernel of the matrix $\vec{\kappa} \in \mathrm{Ker}(A^T)$. This fact can also be proved for other representatives that consist not only of purely ncbe- and ncbi-cycles. Furthermore, it can be generalized for the case of N holes [HO01]. Thus the following approach to the construction of the relevant surface cycles can be used:

2.1 Compute the matrix A by evaluation of the pairing $\langle \cdot, \cdot \rangle$.

2.2 Use Gaussian elimination with full pivoting in $\mathbb{Z}$ to obtain an integral basis for $\mathrm{Ker}(A^T)$. Every basis vector will define a combination of $\gamma_1, \dots, \gamma_{2N}$ that provides a relevant cycle.

The first step of this scheme needs to be discussed in more detail because one has to provide an algorithm for computing representatives of the submerged cycles $\gamma_i \downarrow$, $i = 1, \dots, 2N$. It turns out to be most efficient to split the task into

2.1.1 the computation of shifted surface cycles $\hat{\gamma}_i$, $i = 1, \dots, 2N$, which clear all vertices of Γ_h, and satisfy $\hat{\gamma}_i \simeq \gamma_i$,

2.1.2 replace every cycle γ_i by its submerged cycle $\gamma_i \downarrow$ such that $\hat{\gamma}_i \cap \gamma_i \downarrow = \emptyset$,

2.1.3 compute linking numbers $\langle \gamma_i, \gamma_k \rangle$.

The new cycles are given by sequences of points. The restriction in 2.1.1 to cycles that clear all vertices of Γ_h is necessary to avoid complications in the numerical integration of the linking numbers at singularities of G. The algorithm for the construction of the shifted paths as midpoints of edges is presented in Figure 4.15, whereas Figure 4.16 illustrates the result.

```
Given: A cycle as a sequence of points $(\mathbf{v}_1, \dots, \mathbf{v}_N)$
list<Point> $P := \emptyset$;
Pick $\{\mathbf{t}\} \in \{\mathcal{S}_2(\mathbf{v}_1) \cap \mathcal{S}_2(\mathbf{v}_2)\}$;
for $(i = 1, i \le N, i++)$ {
  $\{\mathbf{e}_{current}\} = \mathcal{S}_1(\mathbf{v}_i) \cap \mathcal{S}_1(\mathbf{v}_{i+1})$;
  $\{\mathbf{e}_{next}\} = \mathcal{S}_1(\mathbf{v}_{i+1}) \cap \mathcal{S}_1(\mathbf{v}_{i+2})$;
  $\{\mathbf{p}\} = \mathcal{S}_0(\mathbf{t}) \setminus \mathcal{S}_0(\mathbf{e}_{current})$;
  $\{\mathbf{e}_{connect}\} = \mathcal{S}_1(\mathbf{v}_{i+1}) \cap \mathcal{S}_1(\mathbf{p})$;
  while $(\mathbf{e}_{current} \neq \mathbf{e}_{next})$ {
    $P$.push_back(midpoint of $\mathbf{e}_{connect}$);
    $\{\mathbf{t}\} = \mathcal{S}_2(\mathbf{e}_{connect}) \setminus \{\mathbf{t}\}$;
    $\{\mathbf{p}\} = \mathcal{S}_0(\mathbf{t}) \setminus \mathcal{S}_0(\mathbf{e}_{connect})$;
    $\{\mathbf{e}_{connect}\} = \mathcal{S}_1(\mathbf{v}_{i+1}) \cap \mathcal{S}_1(\mathbf{p})$; }}
```

Figure 4.15: Construction of a shifted cycle $(\mathbf{p}_1, \mathbf{p}_2, \cdots)$. Note that $\mathbf{v}_{N+1} := \mathbf{v}_1$.

---

[2] in the case of the torus it is γ_1

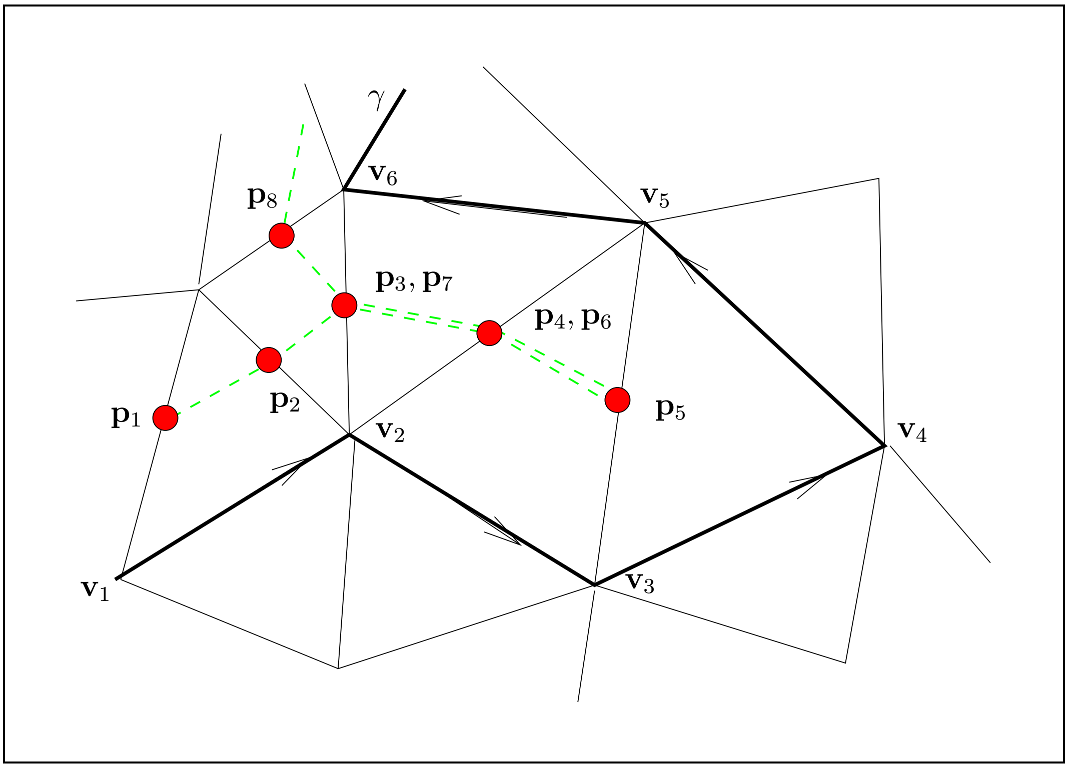

Figure 4.16: Shift a cycle

One gets the submerged paths by inserting the center of gravity of a tetrahedron adjacent to two consecutive vertices $\mathbf{v}_i$, $\mathbf{v}_{i+1}$. The simple algorithm is shown in Figure 4.17. Only at this stage the volume mesh Ω_h is used!

```
Given: A cycle as a sequence of points $(\mathbf{v}_1, \dots, \mathbf{v}_N)$
list<Point> $U$:= $\emptyset$;
for $(i = 1; i \leq N; i++)$ {
   $U$.push_back($\mathbf{v}_i$);
   $T$ := tetrahedron adjacent to $\mathbf{v}_i$ and $\mathbf{v}_{i+1}$ ;
   $U$.push_back(center of gravity of $T$);}
```

Figure 4.17: Submerging of a cycle. Output is polygon $(\mathbf{u}_1\,, \mathbf{u}_2\,, \cdots)$.

Next, one has to compute the relative linking number of a submerged cycle $\gamma\!\downarrow$ and a shifted cycle $\hat{\gamma}$. Analytic expressions are available for the inner integrals. For the outer integrals one has to resort to numerical quadrature. Here, it is important to take into account the singular behavior of the kernel $G(\mathbf{x}, \mathbf{y})$ for $\mathbf{x} \rightarrow \mathbf{y}$. It entails an *adaptive* approach to quadrature: A Gauß-Legendre quadrature formula of order $2n$ (i.e., with n nodes), $n \in \mathbb{N}$, on each interval of an equidistant subdivision of $[0; 1]$ into k_{ij}, $k_{ij} \in \mathbb{N}$, parts. Adaptivity will be achieved by adjusting k_{ij} depending on the relative position of the line segments $[\mathbf{u}_i, \mathbf{u}_{i+1}]$ and $[\mathbf{p}_i, \mathbf{p}_{i+1}]$. Due to the construction of $(\mathbf{u}_1\,, \mathbf{u}_2\,, \cdots)$, and $(\mathbf{p}_1\,, \mathbf{p}_2\,, \cdots)$ they have no common points!

4.4.3 Summary

The complete algorithm for the construction of the relevant paths now looks as follows:

1. Find a representative of the basis
    - 1.1 Build face-tree
    - 1.2 Build node-tree
    - 1.3 Build cycles
2. Construct N linear independent ncbe-cycles
    - 2.1 Compute matrix A by evaluation of the pairing $\langle\cdot,\cdot\rangle$
        - 2.1.1 Shift surface cycles
        - 2.1.2 Submerge cycles
        - 2.1.3 Compute $\langle\gamma_i,\gamma_k\rangle$.
    - 2.2 Gaussian elimination to obtain $\mathrm{Ker}(A^T)$

For shape-regular, quasiuniform families of meshes, the asymptotic complexity of the algorithm is shown [HO01] to be $O(M^2)$, where M is the number of edges of Γ_h. A typical example for a workpiece to be hardened is the cylinder of Figure 4.18 with two intersecting holes drilled through it. For a workpiece this is nothing special, but from a topological point of view, nontrivial cycles have to be constructed.

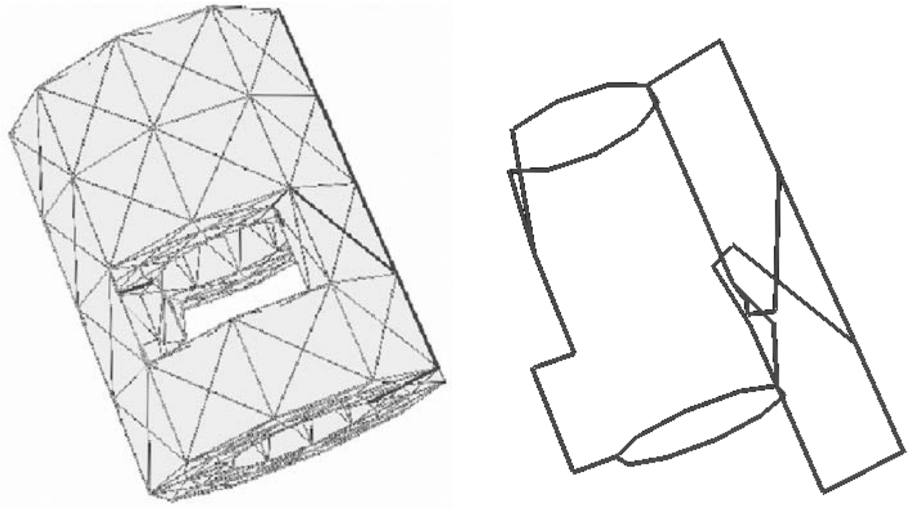

Figure 4.18: Surface mesh (left) and cycles $\gamma_1,\ldots,\gamma_6$ (right)

Another example is the so-called trefoil knot. Topologically, this knot has the most elaborate complexity, where cutting surfaces are hard to construct. The path algorithm is also able to cope with this kind of problem. Figure 4.19 qualitatively shows the x-, y-, and z-components of the surface current, which is fully automatically calculated by the impedance model. Note that the current flows around the knot.

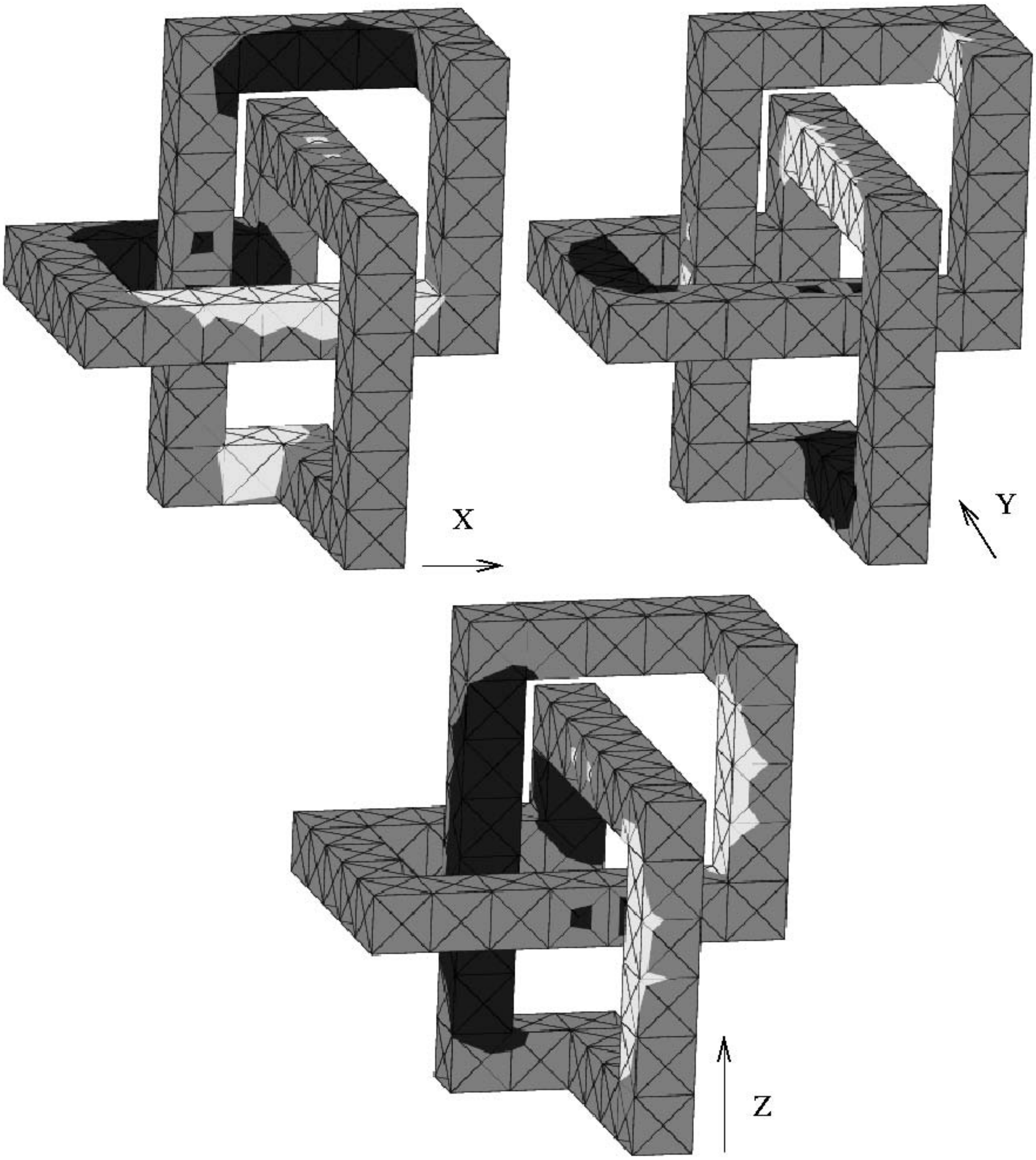

Figure 4.19: Surface current components of the trefoil knot. Black positive, white negative.

Chapter 5

Solution Procedures

This chapter presents some practically important facts about the implementation of a solver for eddy current approach and impedance model. First it is shown how to handle the FEM part, especially the non-linear ferromagnetic permeability. Then the iterative solver is determined by some experiments with a small test problem that can also be solved exactly with a direct solver. The compression technique for the BEM operators is introduced in the last section of this chapter.

5.1 Solution in the Interior

The sesquilinear form $q(\mathbf{E}, \mathbf{v})$ of the FEM part in equation (3.90) that has to be evaluated is discretized with linear edge elements. The resulting matrix is here called A_{FEM}.

In the *impedance model* an equation of the form $A_{FEM}\,\mathbf{x} = \mathbf{b}$ must be solved for a given right hand side $\mathbf{b}$ (from the BEM part). This is done by applying a preconditioned iterative solver of Krylov type. Several complex and real solvers have been tested.

If a *fixpoint iteration* (Picard method) [Kol02] is used to master the non-linear μ_r, then a *complex solver* can be used for the FEM part. Nearly every method is convergent with different preconditioners. The fixpoint iteration with complex solver is used for the impedance model.

Splitting the equations into real and imaginary parts is mandatory if the fast *Newton-Raphson method* [Kol02] operates at the non-linearity of μ_r because some occuring complex derivatives are no more meaningful. Unfortunately only a BiCGstab method or a CGS method, preconditionned with an incomplete ILU decomposition, are convergent in this real case [vR01]. The ILU decomposition needs so much storage that this method is not applicable for realistic problems.

In the *eddy current approach* the FEM and BEM parts are strongly coupled in one big system and must be solved simultaneously. An option is to split the system of equations into real and imaginary parts in order to keep the matrix symmetric. But in this case the same problem with the ILU decomposition as described above occurs in the rows of the FEM part unknowns. Nevertheless the splitting is used here for the eddy current approach because it is only tested with small test examples. The preconditioner of the BEM part is the same as in the impedance model, and it will be presented in Section 5.2.

The skin effect is the most important difficulty in the interior and a *local residual based error estimator* [BHHW00] is used to resolve the strong decrease of the fields at the most important points, i.e., at positions where a strong current is flowing. Thus the mesh is chiefly refined at the surface of the conductors. The error estimator uses a Helmhotz type decomposition of the error in energy norm $\mathbf{e} := \|\mathbf{E} - \tilde{\mathbf{E}}_h\|$ between the correct solution $\mathbf{E}$ and the approximative solution $\tilde{\mathbf{E}}_h$. It splits the error into its **curl**-free part and into its weakly solenoidal part on the mesh Ω_h. Each error can be estimated locally, thus their addition is used for adaptive grid refinement.

5.1.1 Material Parameters

In general, it is very difficult to find good experimental data concerning the behavior of the material. All measurements for the verification of the program are made with workpieces of C45 steel. Fortunately, the material parameters of this type of steel can be found in [Stu62]. Figure 5.1 shows the temperature dependency of *heat capacity*, *heat conductivity*, and *electric resistence*.

The material is typically ferromagnetic, and the relative magnetic permeability μ_r depends on the absolute value of the strength of the field, according to Figure 5.2. So one has to deal with a non-linearity in the governing equations. Due to the variation of the field strength during a period, one has to use an average value [LNA86], the so-called *effective relative permeability*

$$\mu_r^{eff} := \frac{\omega}{2\pi} \int\limits_0^{2\pi/\omega} \mu_r\big(\|B_0\|\big)\, dt\,, \tag{5.1}$$

with the real part $\mathbf{B}_0$ of the solution $\mathbf{B} = \frac{-1}{i\omega}\,\mathbf{curl}\,\mathbf{E} = (\mathbf{B}_{real}(\mathbf{x}) + i\mathbf{B}_{imag}(\mathbf{x}))\cdot e^{i\omega t}$. It can be written as

$$\mathbf{B}_0(\mathbf{x},\, t) = \mathbf{B}_{real}(\mathbf{x})\cos(\omega t) - \mathbf{B}_{imag}(\mathbf{x})\sin(\omega t)\,. \tag{5.2}$$

In this form, μ_r^{eff} has to be calculated at each timestep and each point in the mesh. This is discontenting, and what is needed is a possibility to calculate μ_r^{eff} only once in advance. The following remarks show how to transform $\mathbf{B}_0$ in a more pleasant format. Adding a phase α does not have any impact if an average value has to be built, and one gets

$$\mathbf{B}_0(\mathbf{x},\, t) \;=\; \mathbf{B}_{real}(\mathbf{x})\cos(\omega t + \alpha) - \mathbf{B}_{imag}(\mathbf{x})\sin(\omega t + \alpha)\,. \tag{5.3}$$

This equation describes an ellipse

$$\mathbf{B}_0(\mathbf{x},\, t) \;=\; \mathbf{B}_1\cos(\omega t) + \mathbf{B}_2\sin(\omega t)\,, \tag{5.4}$$

$$\text{with } \mathbf{B}_1\cdot\mathbf{B}_2 \;=\; 0\,. \tag{5.5}$$

The principal axes $\mathbf{B}_1$ and $\mathbf{B}_2$ lie in the same plane as $\mathbf{B}_{real}$ and $\mathbf{B}_{imag}$. Equation (5.3) can be transformed into

$$\begin{aligned}\mathbf{B}_0 &= \mathbf{B}_{real}\big[\cos(\omega t)\cos\alpha - \sin(\omega t)\sin\alpha\big] - \mathbf{B}_{imag}\big[\sin(\omega t)\cos\alpha + \cos(\omega t)\sin\alpha\big]\\ &= \big[\mathbf{B}_{real}\cos\alpha - \mathbf{B}_{imag}\sin\alpha\big]\cos(\omega t) - \big[\mathbf{B}_{real}\sin\alpha + \mathbf{B}_{imag}\cos\alpha\big]\sin(\omega t)\,,\end{aligned}$$

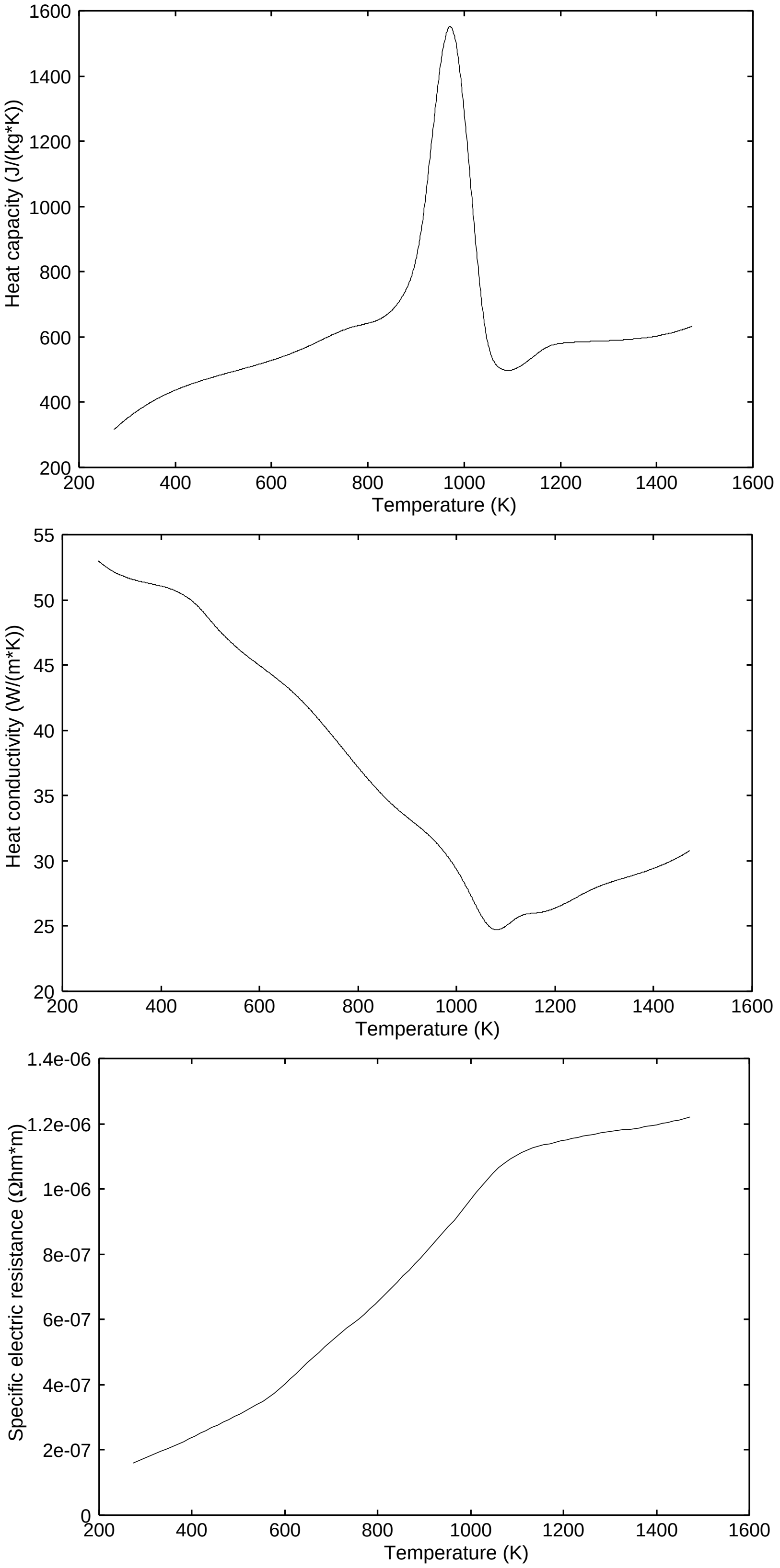

Figure 5.1: Heat capacity, heat conductivity, and electric resistence

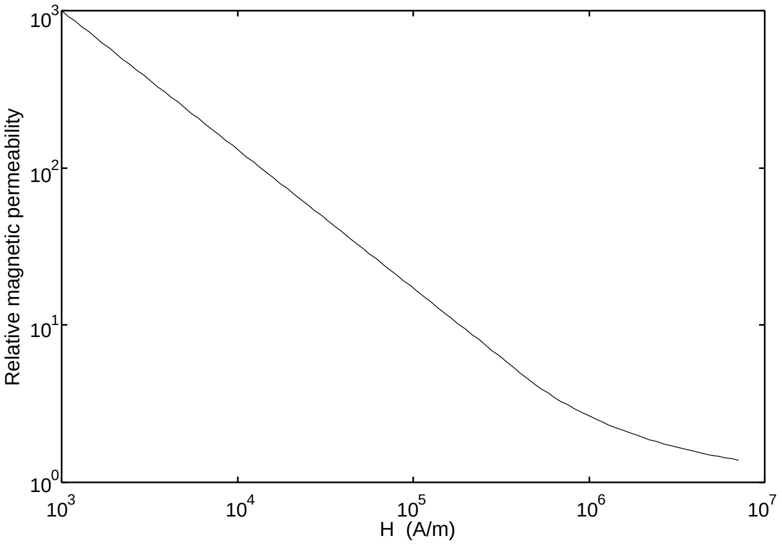

Figure 5.2: Relative magnetic permeability

with the aid of the addition theorems for sine and cosine. One finds

$$\begin{aligned}\mathbf{B}_1 &= \mathbf{B}_{real}\cos\alpha - \mathbf{B}_{imag}\sin\alpha\,, &(5.6)\\ \mathbf{B}_2 &= -\mathbf{B}_{real}\sin\alpha - \mathbf{B}_{imag}\cos\alpha\,. &(5.7)\end{aligned}$$

Condition (5.5) is used to determine alpha

$$\begin{aligned}0 &= -\mathbf{B}_{real}^2\cos\alpha\sin\alpha - \mathbf{B}_{real}\mathbf{B}_{imag}\cos^2\alpha + \mathbf{B}_{real}\mathbf{B}_{imag}\sin^2\alpha + \mathbf{B}_{imag}^2\sin\alpha\cos\alpha\\ &= (\mathbf{B}_{imag}^2 - \mathbf{B}_{real}^2)\cdot\cos\alpha\sin\alpha + (2\sin^2\alpha - 1)\cdot\mathbf{B}_{real}\mathbf{B}_{imag}\\ &= (\mathbf{B}_{imag}^2 - \mathbf{B}_{real}^2)\cdot\frac{\sin(2\alpha)}{2} - cos(2\alpha)\cdot\mathbf{B}_{real}\mathbf{B}_{imag}\,,\end{aligned}$$

$$\Longrightarrow \qquad \alpha = \begin{cases}\frac{1}{2}\arctan\left(\frac{2\cdot\mathbf{B}_{real}\cdot\mathbf{B}_{imag}}{(\mathbf{B}_{imag}^2-\mathbf{B}_{real}^2)}\right) & \text{if } \mathbf{B}_{imag}^2 \neq \mathbf{B}_{real}^2\,,\\ \frac{\pi}{4} & \text{else}\ .\end{cases}$$

The effective permeability now looks like

$$\mu_r^{eff} = \frac{\omega}{2\pi}\int_0^{2\pi/\omega} \mu_r\Big(\sqrt{\mathbf{B}_1^2\cos^2(\omega t) + \mathbf{B}_2^2\sin^2(\omega t)}\Big)\,dt\,, \qquad (5.8)$$

depending only on the absolute values of $\mathbf{B}_1$ and $\mathbf{B}_2$. A table of this function can be calculated in advance with the aid of the values of Figure 5.2, which have to be transformed from $\mu_r(H)$ to $\mu_r(B)$ first.

The *magnetic permeability* also depends on the temperature. Therefore, an analytical correction

$f(T)$ is used, which finally leads to

$$\begin{aligned}
\mu(T) &= \mu_r^{new} \cdot \mu_0\,, && (5.9)\\
\text{with } \mu_r^{new} &= \begin{cases} 1.0 + (\mu_r^{eff} - 1.0) \cdot f(T) & \text{if } T < 1042\,K\,,\\ 1.0 & \text{else}\ , \end{cases} && (5.10)\\
\text{and } f(T) &= \left(\frac{1042^2 - T^2}{1042^2 - 293^2}\right)^{\frac{1}{4}}\ . && (5.11)
\end{aligned}$$

Above the Curie-temperature of 1042 Kelvin, the small permanent magnetic moments of the material cannot orient themselves any more, and the relative permeability is constant one. Figure 5.3 shows the correction. The non-linearity arising from the ferromagnetic behavior of the material is mastered by applying a *relaxation scheme* at each timestep.

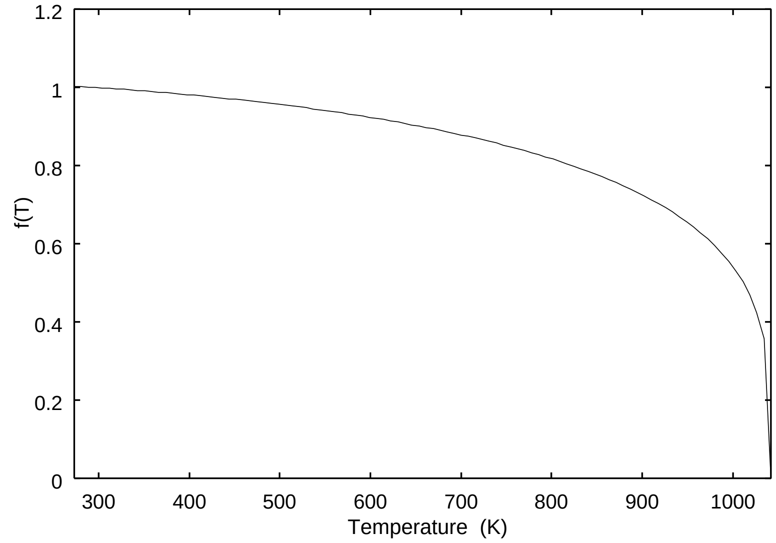

Figure 5.3: Correction $f(T)$

The inductor is made of copper. Its permeability is constant $\mu_r = 1$. The temperature dependency of the electric resistence is chosen to be

$$\rho_{el}(T) = 1.7 \cdot 10^{-8} \cdot T\ , \tag{5.12}$$

according to [Sta88]. The temperature of the inductor is not calculated in the program, however it is assumed that the water cooled inductor homogeneously has a third of the maximum temperature of the workpiece.

5.2 Iterative Solver for the BEM Part

For the BEM part of the *impedance model* one has to solve the equation $A\mathbf{x} = \mathbf{b}$, with

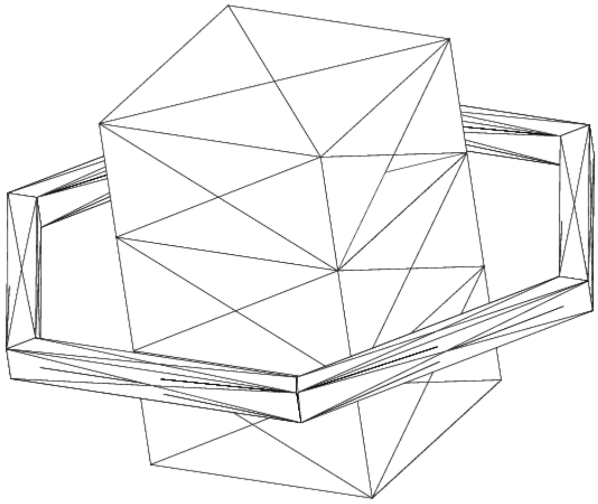

Figure 5.4: Test example

$$\mathsf{A}\mathbf{x} := \begin{pmatrix} \mathsf{M}_{\Re} & -\mathsf{M}_{\Im} & -\mathsf{B}^T & 0 & -\mathsf{F}_{\mathsf{up}} & 0 \\ -\mathsf{M}_{\Im} & -\mathsf{M}_{\Re} & 0 & \mathsf{B}^T & 0 & \mathsf{F}_{\mathsf{up}} \\ -\mathsf{B} & 0 & -\mathsf{Q} & 0 & -\mathsf{F}_{\mathsf{do}} & 0 \\ 0 & \mathsf{B} & 0 & \mathsf{Q} & 0 & \mathsf{F}_{\mathsf{do}} \\ -\mathsf{F}_{\mathsf{up}}{}^T & 0 & -\mathsf{F}_{\mathsf{do}}{}^T & 0 & -\mathsf{H} & 0 \\ 0 & \mathsf{F}_{\mathsf{up}}{}^T & 0 & \mathsf{F}_{\mathsf{do}}{}^T & 0 & \mathsf{H} \end{pmatrix} \begin{pmatrix} \mathbf{E}_{\Re} \\ \mathbf{E}_{\Im} \\ \boldsymbol{\phi}_{\Re} \\ \boldsymbol{\phi}_{\Im} \\ \boldsymbol{\alpha}_{\Re} \\ \boldsymbol{\alpha}_{\Im} \end{pmatrix}, \qquad (5.13)$$

see equation (4.30). If the strongly coupled *eddy current approach* is to be applied, the operators $\mathsf{M}_{\Re}$ and $\mathsf{M}_{\Im}$ have to be replaced by the discretized sesquilinear form $q(\mathbf{E}, \mathbf{v})$. The equation needs to be solved more than a hundred times per simulation run. This is necessary because of the rotation of the workpiece and the numerous updates of the material parameters after temperature changes. Thus the use of a slow direct solver is impossible. Furthermore a direct solver needs too much storage. Instead, a fast iterative solver has to be applied. Numerical experiments were made with the aid of the program packages[1] LAPACK and MATLAB in order to determine the adequate solver. Therefore, the realistic but small and coarse discretized test example of Figure 5.4 was used. The matrix A is symmetric but not positive definite. For problems of this kind, the *Minimal Residual Method* (MINRES) is often recommended [PS75], [Hac91] because it is stable and convergent. However, in this case MINRES turns out to be unstable. The simpler *Conjugate Residual Method* (CR) [Saa95] of Figure 5.5 is the better choice. For the test problem, the condition number was found to be $3.8 \cdot 10^4$. This bad conditioning can be cured by applying the preconditioned version of Figure 5.6, where the alternative equation $\mathsf{P}^{-1}\mathbf{b} = \mathsf{P}^{-1}\mathsf{A}\mathbf{x}$ is solved with an adequate preconditioner P. For the practical implementation, the preconditioned CR can be rewritten in such a way that the matrix vector multiplication and the preconditioner must be applied only once per iteration. This version is shown in Figure 5.7.

---

[1] For LAPACK see http://www.netlib.org, and for MATLAB see http://www.mathworks.com/

```
Given:   $\mathbf{x}_0 :=$ initial guess ,   $tol :=$ tolerance
         $it_{max} :=$ maximum number of iterations

$\mathbf{r} = \mathbf{p} = \mathbf{b} - \mathsf{A}\mathbf{x}_0$
$res_{it} = res_0 = r, \quad it = 0$
while [ $it < it_{max}$ AND $res_{it} > tol \cdot res_0$ ]
    $\alpha = \frac{<\mathbf{r}, \mathsf{A}\mathbf{r}>}{<\mathsf{A}\mathbf{p}, \mathsf{A}\mathbf{p}>}$
    $\mathbf{x} = \mathbf{x} + \alpha \cdot \mathbf{p}$
    $\mathbf{r}_1 = \mathbf{r} - \alpha \cdot \mathsf{A}\mathbf{p}$
    $\beta = \frac{<\mathbf{r}_1, \mathsf{A}\mathbf{r}_1>}{<\mathbf{r}, \mathsf{A}\mathbf{r}>}$
    $\mathbf{p} = \mathbf{r}_1 + \beta \cdot \mathbf{p}$
    $\mathbf{r} = \mathbf{r}_1$
    $res_{it} = r, \quad it = it + 1$
end while
```

Figure 5.5: Conjugate residual method

```
$\mathbf{r} = \mathbf{p} = \mathsf{P}^{-1}(\mathbf{b} - \mathsf{A}\mathbf{x}_0)$
$res_{it} = res_0 = r, \quad it = 0$
while [ $it < it_{max}$ AND $res_{it} > tol \cdot res_0$ ]
    $\alpha = \frac{<\mathbf{r}, \mathsf{A}\mathbf{r}>}{<\mathsf{P}^{-1}\mathsf{A}\mathbf{p}, \mathsf{A}\mathbf{p}>}$
    $\mathbf{x} = \mathbf{x} + \alpha \cdot \mathbf{p}$
    $\mathbf{r}_1 = \mathbf{r} - \alpha \cdot \mathsf{P}^{-1}\mathsf{A}\mathbf{p}$
    $\beta = \frac{<\mathbf{r}_1, \mathsf{A}\mathbf{r}_1>}{<\mathbf{r}, \mathsf{A}\mathbf{r}>}$
    $\mathbf{p} = \mathbf{r}_1 + \beta \cdot \mathbf{p}$
    $\mathbf{r} = \mathbf{r}_1$
    $res_{it} = r, \quad it = it + 1$
end while
```

Figure 5.6: Preconditioned conjugate residual method

```
$\mathbf{r} = \mathbf{p} = \mathsf{P}^{-1}(\mathbf{b} - \mathsf{A}\mathbf{x}_0)$
$\mathbf{y} = \mathbf{w} = \mathsf{A}\mathbf{r}$
$res_{it} = res_0 = r, \quad it = 0$
while [ $it < it_{max}$ AND $res_{it} > tol \cdot res_0$ ]
    $\mathbf{q} = \mathsf{P}^{-1}\mathbf{w}$
    $\alpha = \frac{< \mathbf{r}, \mathbf{y} >}{< \mathbf{q}, \mathbf{w} >}$
    $\mathbf{x} = \mathbf{x} + \alpha \cdot \mathbf{p}$
    $\mathbf{r}_1 = \mathbf{r} - \alpha \cdot \mathbf{q}$
    $\mathbf{y}_1 = \mathsf{A}\mathbf{r}_1$
    $\beta = \frac{< \mathbf{r}_1, \mathbf{y}_1 >}{< \mathbf{r}, \mathbf{y} >}$
    $\mathbf{p} = \mathbf{r}_1 + \beta \cdot \mathbf{p}$
    $\mathbf{w} = \mathbf{y}_1 + \beta \cdot \mathbf{w}$
    $\mathbf{r} = \mathbf{r}_1, \quad \mathbf{y} = \mathbf{y}_1$
    $res_{it} = r, \quad it = it + 1$
end while
```

Figure 5.7: Implemented conjugate residual method

5.2.1 Preconditioning

As already noted, the condition number of the small test example was found to be $3.8 \cdot 10^4$. So preconditioning is mandatory if the number of iterations is to be small. A good preconditioner P of A has to meet the following requirements: First, the preconditioning must be independent of the discretization of the problem, i.e. the spectrum of $\mathsf{P}^{-1}\mathsf{A}$ must be bounded independently of the meshwidth h, and second, the condition number of $\mathsf{P}^{-1}\mathsf{A}$ must be small compared with the condition number of A.

First of all, the properties of the sesquilinear form $\mathcal{Q}$ induced by the equations (3.98) and (3.99) are examined. It holds

$$
\begin{aligned}
|\mathcal{Q}(\mathbf{E}, \boldsymbol{\lambda})| &= \left| q(\mathbf{E},\, \mathbf{E}) - \frac{1}{\mu_+} \left\langle \mathbf{N}(\gamma_D \mathbf{E}), \gamma_D \mathbf{E} \right\rangle_{\boldsymbol{\tau}} + \mu_+ \left\langle \boldsymbol{\lambda}, \mathbf{A}\boldsymbol{\lambda} \right\rangle_{\boldsymbol{\tau}} \right| \\
&= \left\langle \frac{1}{\eta} \gamma_D \mathbf{E}, \gamma_D \mathbf{E} \right\rangle_{\boldsymbol{\tau}} - \left\langle \mathbf{N}(\gamma_D \mathbf{E}), \gamma_D \mathbf{E} \right\rangle_{\boldsymbol{\tau}} + \left\langle \mathbf{A}\boldsymbol{\lambda}, \boldsymbol{\lambda} \right\rangle_{\boldsymbol{\tau}} \\
&= i\omega \int\limits_{\Omega_-} \sigma \mathbf{E} \cdot \overline{\mathbf{E}}\, d\mathbf{y} + \int\limits_{\Omega_-} \frac{1}{\mu_-} \,\mathbf{curl}\,\mathbf{E} \cdot \overline{\mathbf{curl}\,\mathbf{E}}\, d\mathbf{y} - \left\langle \mathbf{N}(\gamma_D \mathbf{E}), \gamma_D \mathbf{E} \right\rangle_{\boldsymbol{\tau}} + \left\langle \mathbf{A}\boldsymbol{\lambda}, \boldsymbol{\lambda} \right\rangle_{\boldsymbol{\tau}}
\end{aligned}
$$

The following inequality is valid for every complex number $z = a + ib$

$$\frac{1}{\sqrt{2}} \cdot |a+b| \;\leq\; |z| \;\leq\; |a| + |b| \,. \tag{5.14}$$

It follows with $\langle \mathbf{N}(\gamma_D \mathbf{E}), \gamma_D \mathbf{E} \rangle_{\boldsymbol{\tau}} \leq 0$ that

$$\begin{aligned} \frac{1}{\sqrt{2}} \left(\omega \int\limits_{\Omega_-} \sigma \mathbf{E} \cdot \overline{\mathbf{E}} \, d\mathbf{y} + \int\limits_{\Omega_-} \frac{1}{\mu_-} \mathbf{curl}\, \mathbf{E} \cdot \overline{\mathbf{curl}\, \mathbf{E}} \, d\mathbf{y} + \langle \mathbf{A} \boldsymbol{\lambda}, \boldsymbol{\lambda} \rangle_{\boldsymbol{\tau}} \right) \quad &\leq \quad |\mathcal{Q}(\mathbf{E}, \boldsymbol{\lambda})| \quad \leq \\ \omega \int\limits_{\Omega_-} \sigma \mathbf{E} \cdot \overline{\mathbf{E}} \, d\mathbf{y} + \int\limits_{\Omega_-} \frac{1}{\mu_-} \mathbf{curl}\, \mathbf{E} \cdot \overline{\mathbf{curl}\, \mathbf{E}} \, d\mathbf{y} - \langle \mathbf{N}(\gamma_D \mathbf{E}), \gamma_D \mathbf{E} \rangle_{\boldsymbol{\tau}} + \langle \mathbf{A} \boldsymbol{\lambda}, \boldsymbol{\lambda} \rangle_{\boldsymbol{\tau}} \,. \end{aligned}$$

Using the Cauchy-Schwartz inequality together with the continuity of $\mathbf{N}$, and the continuity of the trace operator leads to

$$\begin{aligned} - \langle \mathbf{N}(\gamma_D \mathbf{E}), \gamma_D \mathbf{E} \rangle_{\boldsymbol{\tau}} \;\; &\leq \;\; \| \mathbf{N}(\gamma_D \mathbf{E}) \|_{\mathbf{H}_{||}^{-\frac{1}{2}}(\mathrm{div}_\Gamma, \Gamma)} \cdot \| \gamma_D \mathbf{E} \|_{\mathbf{H}_{\perp}^{-\frac{1}{2}}(\mathrm{curl}_\Gamma, \Gamma)} \\ &\leq \;\; c \cdot \| \gamma_D \mathbf{E} \|^2_{\mathbf{H}_{\perp}^{-\frac{1}{2}}(\mathrm{curl}_\Gamma, \Gamma)} \leq c_1 \cdot \| \mathbf{E} \|^2_{\boldsymbol{H}(\mathbf{curl}; \Omega)} \,. \end{aligned}$$

One finds with $\bar{D}\big[(\mathbf{E}, \boldsymbol{\lambda}), (\mathbf{v}, \boldsymbol{\zeta})\big] := \omega \int\limits_{\Omega_-} \sigma \mathbf{E} \cdot \overline{\mathbf{v}} \, d\mathbf{y} + \int\limits_{\Omega_-} \frac{1}{\mu_-} \mathbf{curl}\, \mathbf{E} \cdot \overline{\mathbf{curl}\, \mathbf{v}} \, d\mathbf{y} + \langle \mathbf{A} \boldsymbol{\lambda}, \boldsymbol{\zeta} \rangle_{\boldsymbol{\tau}}$ that

$$\frac{1}{\sqrt{2}} \cdot \bar{D}\big[(\mathbf{E}, \boldsymbol{\lambda}), (\mathbf{E}, \boldsymbol{\lambda})\big] \;\leq\; |\mathcal{Q}(\mathbf{E}, \boldsymbol{\lambda})| \;\leq\; \bar{c} \cdot \bar{D}\big[(\mathbf{E}, \boldsymbol{\lambda}), (\mathbf{E}, \boldsymbol{\lambda})\big] \,.$$

So the spectrum of the discrete operator assoziated with the sesquilinear form $\mathcal{Q}$ depends only on the norm bounds of the operators, thus it is bounded independent of the meshwidht h. Let $\bar{\mathsf{P}}$ be the discrete operator assoziated with the sesquilinear form $\bar{D}$, and $\bar{\mathsf{A}}$ be the discrete operator assoziated with the sesquilinear form $\mathcal{Q}$, then the spectrum of the operator $\bar{\mathsf{P}}^{-1}\bar{\mathsf{A}}$ is also bounded independent of the meshwidht h.

For the impedance model $q(\mathbf{E},\, \mathbf{E})$ has to be replaced by $\left\langle \frac{1}{\eta} \gamma_D \mathbf{E}, \gamma_D \mathbf{E} \right\rangle_{\boldsymbol{\tau}}$ and

$$\mathsf{P} := \begin{pmatrix} \mathsf{M}_{\Re} + \mathsf{M}_{\Im} & 0 & 0 & 0 & 0 & 0 \\ 0 & \mathsf{M}_{\Re} + \mathsf{M}_{\Im} & 0 & 0 & 0 & 0 \\ 0 & 0 & \mathsf{Q} & 0 & 0 & 0 \\ 0 & 0 & 0 & \mathsf{Q} & 0 & 0 \\ 0 & 0 & 0 & 0 & \mathsf{H} & 0 \\ 0 & 0 & 0 & 0 & 0 & \mathsf{H} \end{pmatrix} \tag{5.15}$$

is used as a preconditioner for A. This was tested with the small example of Figure 5.4, and the condition number decreased from $3.8 \cdot 10^4$ for A to 4.0 for the preconditioned system $\mathsf{P}^{-1}\mathsf{A}$.

5.2.2 Numerical Experiments

The amount of time and storage for solving the test example of Figure 5.4 is small enough to allow quick numerical experiments in order to find the adequate solver for the preconditioner. Five solvers were tested.

- A direct solver (ideal preconditioning).
- A conjugate gradient (CG) method [DH91]. with a fixed number of steps (15).
- A CG method with a fixed decrease of 0.01 of the relative residual.
- A Gauss Seidel method [Oev96] with a fixed number of steps (40, 60).
- No preconditioning.

These solvers for the preconditioner were used in the CR-solver applied to the problem $\mathsf{P}^{-1}\mathsf{A}\mathbf{x} = \mathsf{P}^{-1}\mathbf{b}$ with different right-hand sides $\mathbf{b}$:

- A right-hand side $\mathbf{b}_0$ with a known constant solution of $\mathbf{x}_0 = 1, 1, 1...$,
- and a realistic right-hand side $\mathbf{b}_1$ of the test example.

Different quantities of the approximation $\mathbf{x}[i]$ were analyzed at each step i of the iteration:

- The most significant quantity is the difference $\|\mathbf{x}[i] - \mathbf{x}_0\|$ between the approximation and the exact solution. (This can only be evaluated in the case where the solution $\mathbf{x}_0$ is known.)
- The euklidian residual $\|\mathsf{A}\mathbf{x}[i] - \mathbf{b}\|$.
- The iterative residual res_{it} (see Figure 5.7).

The following graphs show the results for the known constant solution $\mathbf{x}_0$ when an ordinary non-restarted CR is used:

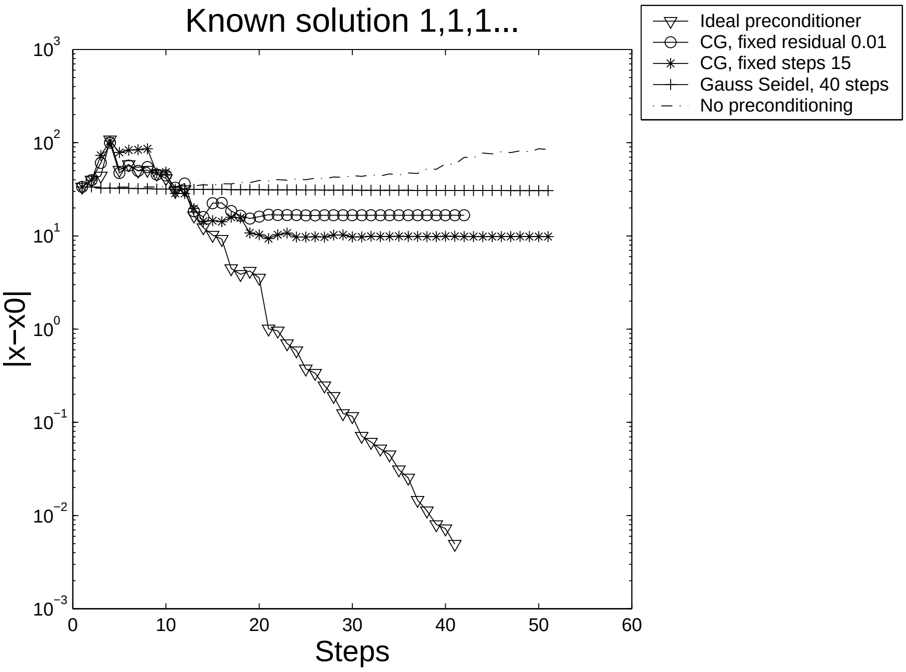

Figure 5.8: $\|\mathbf{x}[i] - \mathbf{x}_0\|$ for CR-method, solution is known

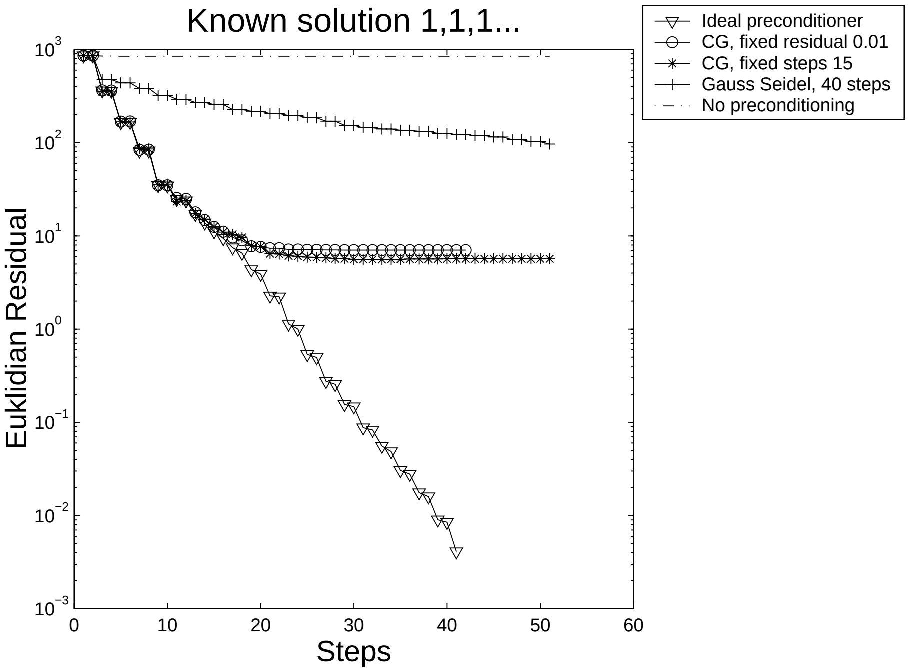

Figure 5.9: Euklidian residual for CR-method, solution is known

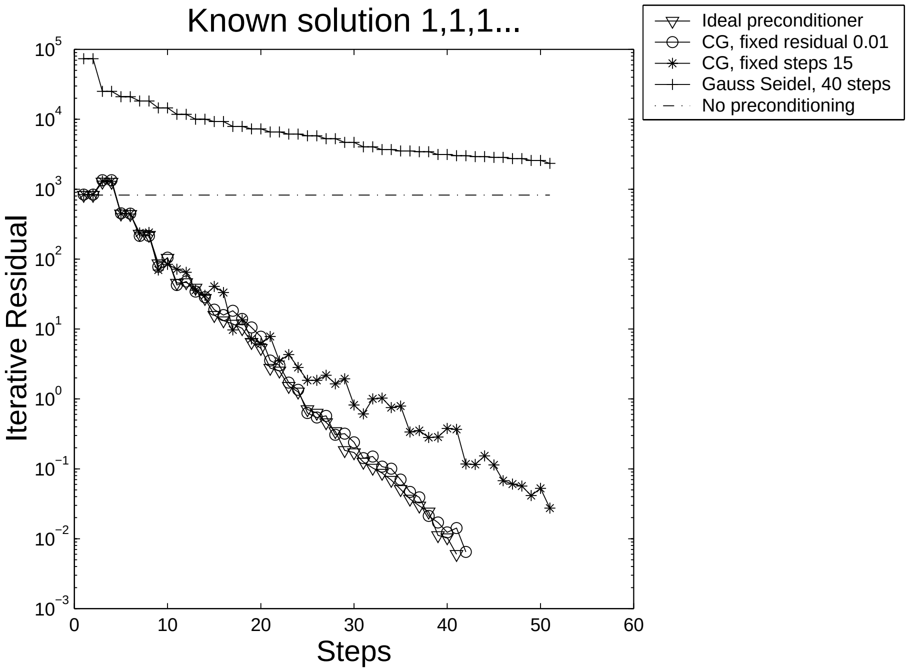

Figure 5.10: Iterative residual for CR-method, solution is known

The decrease of the error $\|\mathbf{x}[i] - \mathbf{x}_0\|$ and the decrease of the euklidian residual stalls after approximately 20 steps. The residual vectors were supposed to be non-orthogonal and the same quantities were measured again for a restarted CR. The restart was made every fifteenth step, and the Figures 5.11, 5.12, and 5.13 show the results.

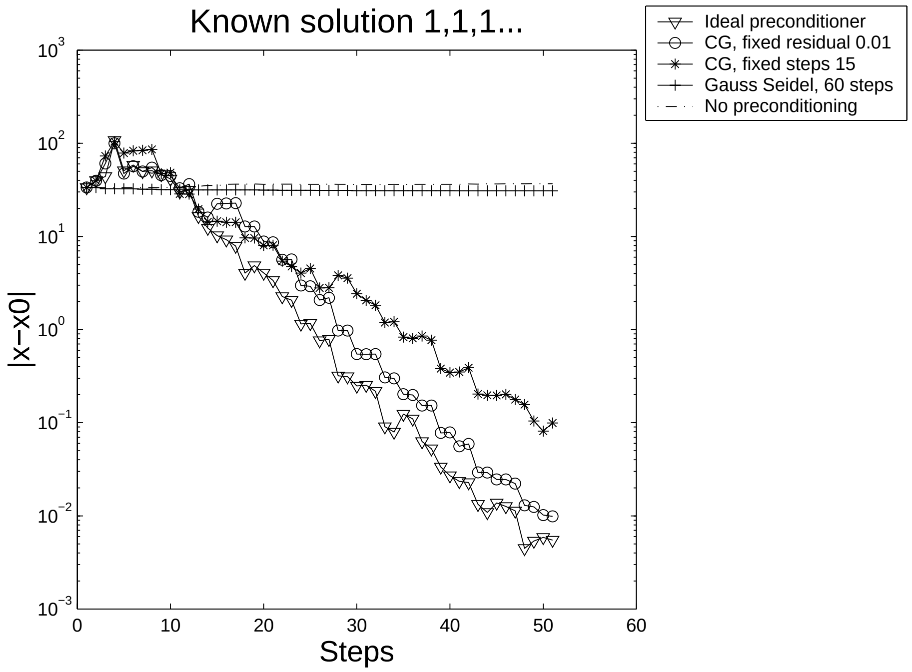

Figure 5.11: $\|\mathbf{x}[i] - \mathbf{x}_0\|$ for restarted CR-method, solution is known

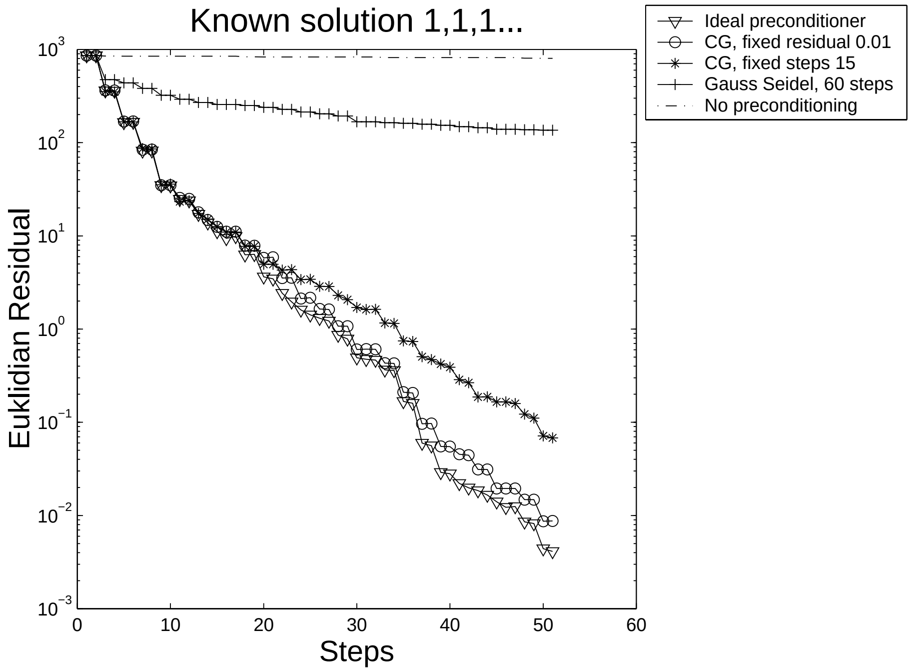

Figure 5.12: Euklidian residual for restarted CR-method, solution is known

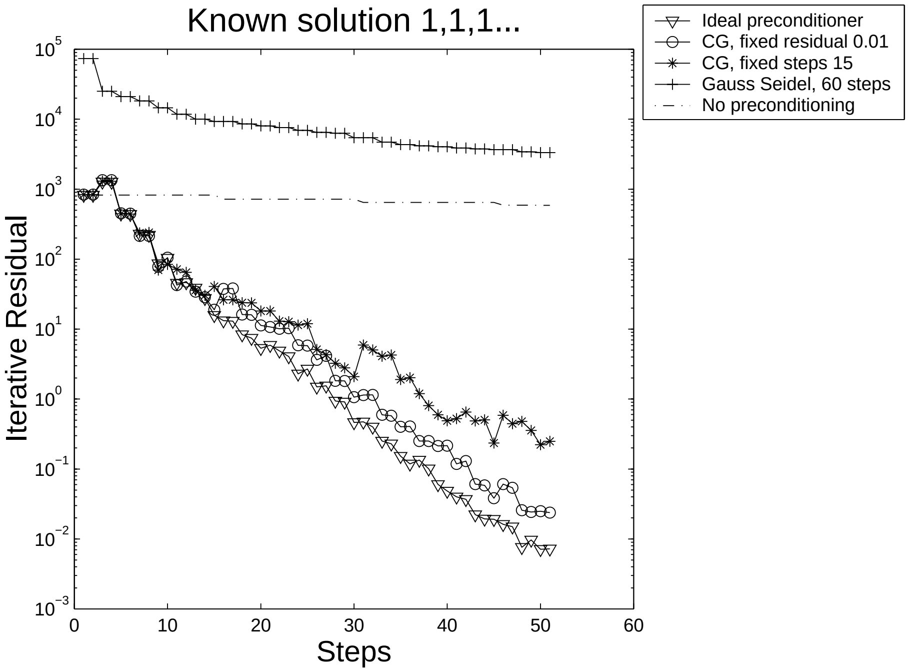

Figure 5.13: Iterative residual for restarted CR-method, solution is known

So restarting seems to cure the problems, and the methods were also tested for the realistic right hand side of an exciting current in the inductor of Figure 5.4. The results are presented in the next two Figures 5.14 and 5.15. The difference of the approximation and the exact solution cannot be calculated as the exact solution is unknown.

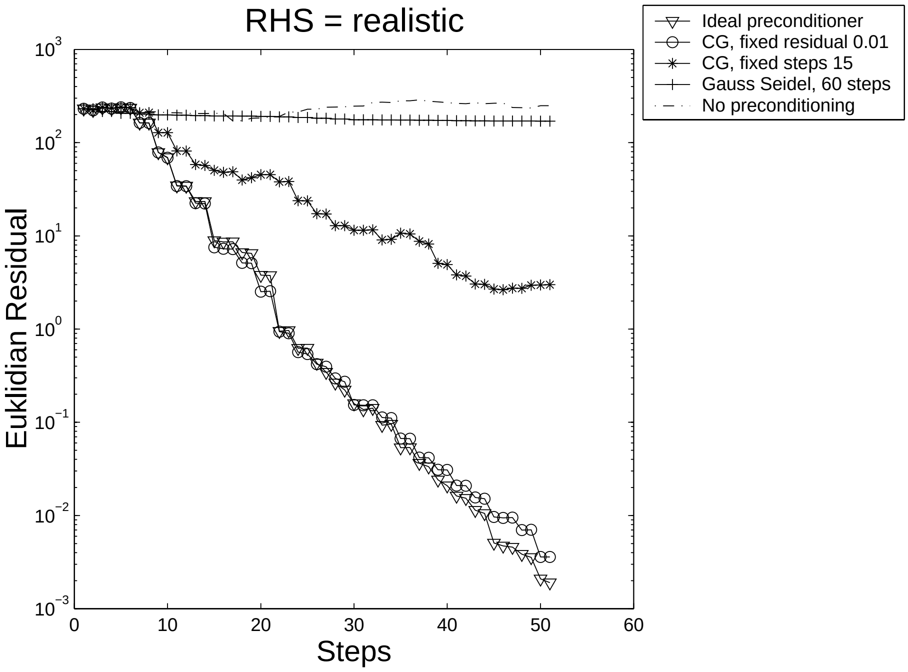

Figure 5.14: Euklidian residual for restarted CR-method, realistic right-hand side

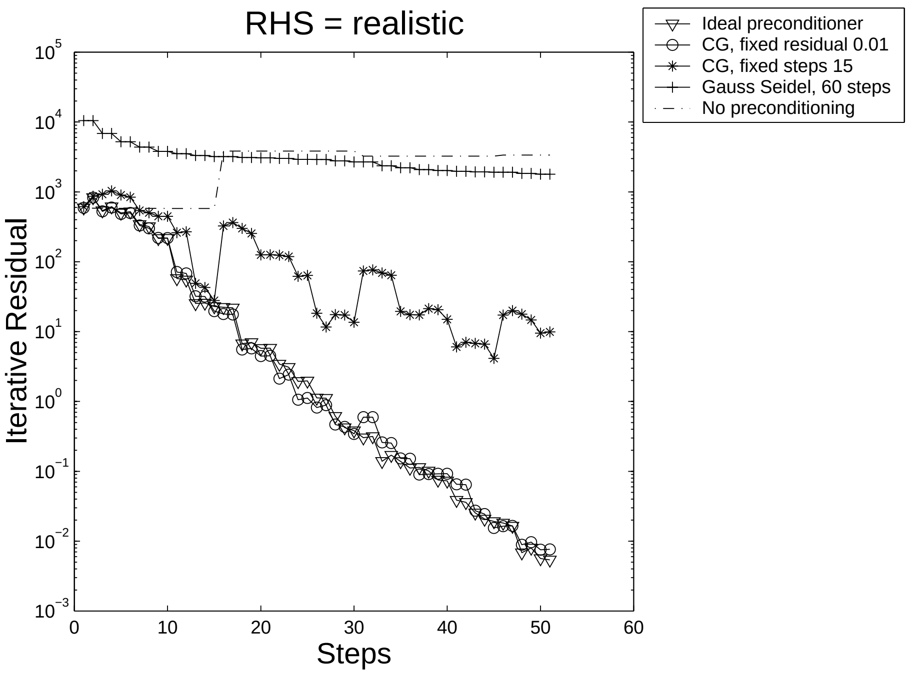

Figure 5.15: Iterative residual for restarted CR-method, realistic right-hand side

The ideal preconditioned method is the quickest one to converge, but as the direct solver needs too much storage, it cannot be applied. The *restarted CR method with CG preconditioner* is the second best. In the same number of steps, it yields the most accurate results if a fixed decrease of the relative residual is used as the stopping criterion for the preconditioner. In this case, the CG preconditioner needs approximately 25 steps for a decrease of 0.01 of its relative residual whereas the CR needs a similar number of steps for a decrease of 0.001. As these are convenient small numbers, this method is applied in the simulation.

5.2.3 Kernel Elimination

The matrices $\mathsf{M}_{\Re}$ and $\mathsf{M}_{\Im}$ in equation (5.13) are symmetric and positive definite. Due to possible gauging of the scalar potential, Q is symmetric but only positive semidefinite: On each of the connected components a constant vector can be added to the solution. So these gauging vectors constitute the kernel of Q. Its dimension D is the number of connected components of the configuration. B has the same kernel. In order to analyze its influence on the CR method, the kernel was removed and the numerical experiments of the last Section 5.2.2 were repeated. There are different possibilities to dispose of the kernel, but the aim is to do it in such a way, that the condition of A remains unchanged.

Definition 7
$\rho(\mathsf{Q}) := \{$*Eigenvalues* λ *of* $\mathsf{Q}\}$
$\rho_>(\mathsf{Q}) := \{$*Eigenvalues* λ *of* $\mathsf{Q} \quad | \quad \lambda > 0\}$
$\lambda_{min}(\mathsf{Q}) := \{\lambda_{min} \in \rho_>(\mathsf{Q}) \quad | \quad \lambda_{min} \leq \lambda \; \forall \; \lambda \in \rho_>(\mathsf{Q})\}$
$\lambda_{max}(\mathsf{Q}) := \{\lambda_{max} \in \rho_>(\mathsf{Q}) \quad | \quad \lambda_{max} \geq \lambda \; \forall \; \lambda \in \rho_>(\mathsf{Q})\}$

Define for every i^{th}-component with n_i nodes a constant vector $\mathbf{K}_i^T$ by $\mathbf{K}_i := (k_{i1},\, k_{i2},\, k_{i3}.....)$ with $k_{im} = 0$ if node m is not on the i^{th}-component and $k_{im} = 1$ if node m is on the i^{th}-component. The length of $\mathbf{K}_i$ is $dim(\mathsf{Q})$:= dimension of $\mathsf{Q} = \sum_{i=1}^{D} n_i$. Then $\{\mathbf{K}_1^T,\, \mathbf{K}_2^T ...\}$ is the kernel of Q.

Theorem 12 *The replacement* $\mathsf{Q} \;\rightarrow\; \mathsf{Q}_1 := \mathsf{Q} + \sum_{i=1}^{D} c_i\, \mathbf{K}_i^T \mathbf{K}_i$, *with*

$$c_i = \frac{trace(\mathsf{Q})}{n_i \cdot (dim(\mathsf{Q}) - D)}$$

enforces

$$\rho(\mathsf{Q}_1) = \{\rho_>(\mathsf{Q}) \cup \frac{trace(\mathsf{Q})}{dim(\mathsf{Q}) - D}\}$$

$$\lambda_{min}(\mathsf{Q}_1) \leq \frac{trace(\mathsf{Q})}{dim(\mathsf{Q}) - D} \leq \lambda_{max}(\mathsf{Q}_1),$$

so the kernel is eliminated and the condition number $\lambda_{max}(\mathsf{Q})/\lambda_{min}(\mathsf{Q})$ *remains unchanged.*

Proof: For every matrix it holds

$$trace(\mathsf{Q}) \;=\; \sum_i k_i \lambda_i \,,$$

with the order k_i of λ_i. For the symmetric and positive semidefinite matrix Q it follows

$$\lambda_{min}(\mathsf{Q}) \;\leq\; \frac{trace(\mathsf{Q})}{dim(\mathsf{Q}) - D} \;\leq \lambda_{max}(\mathsf{Q}) \;.$$

For every $\mathbf{K}_i^T$ one finds:

$$\mathsf{Q}_1 \cdot \mathbf{K}_i^T \;=\; c_i \cdot \mathbf{K}_i^T \cdot (\mathbf{K}_i \mathbf{K}_i^T) \;=\; c_i \cdot n_i \cdot \mathbf{K}_i^T \;=\; \frac{trace(\mathsf{Q})}{dim(\mathsf{Q}) - D} \cdot \mathbf{K}_i^T$$

Let $\mathbf{x}_k$ be an eigenvector of Q with eigenvalue $\lambda_k > 0$. Then $\mathbf{K}_i^T \mathbf{K}_i \mathbf{x}_k \;=\; 0$ because $\mathbf{K}_i^T \mathbf{K}_i$ has rank 1 with eigenvector $\mathbf{K}_i^T \in$ kernel(Q). It follows

$$\mathsf{Q}_1 \cdot \mathbf{x}_k = \lambda_k \cdot \mathbf{x}_k \;.$$

So all eigenvectors of Q_1 are found. □

The kernel of A was eliminated with the aid of this method ($\mathsf{A} \rightarrow \mathsf{A}_1$). Then the CR method was applied to the new matrix A_1 but no significant differences to the results of Section 5.2.2 were found. Thus the elimination of the kernel seems to be not necessary and it is not eliminated in the program.

5.3 H^2-Matrix Approximation

The triangulation of the boundary Γ of the workpiece, the inductor and the plates must be fine enough to meet two different demands. First, the geometry of the items must be described in a satisfactory way, and second, the desired precision of the solution must be achieved. This means that a number $N \geq 10000$ of surface triangles must be used for typical workpieces. The occuring BEM operators in A of equation (5.13) are dense. A matrix-vector multiplication for n unknowns needs $O(n^2)$ operations, and the amount of storage is of the same order. Parts with $N = 10000$ surface triangles have approximately 15000 edges and 5000 nodes. For the storage requirements of the matrices in A this means:

$\mathsf{M}_{\Re}$ needs $15000^2 \cdot$ size of(double) = $1.67 GByte,$

$\mathsf{M}_{\Im}$ needs $15000^2 \cdot$ size of(double) = $1.67 GByte,$

B needs $15000 \cdot 5000 \cdot$ size of(double) = $0.56 GByte,$

Q needs $5000^2 \cdot$ size of(double) = $0.18 GByte.$

So more than 4 GBytes are needed, a volume that cannot be mastered by standard computers of the present generation. A compression technique must be applied to the four different operators. Parts of their kernels are vector-valued, and each component consists of either a single layer potential, a double layer potential or a modified double layer potential. Each of these potentials has an *asymptotically smooth* kernel $k_j(\mathbf{x}, \mathbf{y})$ in each component j, i.e., there are constants $C_{as}(n, m) \in \mathbb{R}_{>0}$ satisfying

$$|\partial_x^\alpha \partial_y^\beta k_j(\mathbf{x}, \mathbf{y})| \leq C_{as}(|\alpha|, |\beta|) \, \|\mathbf{x} - \mathbf{y}\|^{-|\alpha| - |\beta|} \, |k_j(\mathbf{x}, \mathbf{y})| \tag{5.16}$$

for all multi-indices $\alpha, \beta \in \mathbb{N}_0^3$ and all $\mathbf{x}, \mathbf{y} \in \mathbb{R}^3$. In the terms of physics, this means that the potentials describe rapidly decreasing interactions between the boundary regions at $\mathbf{x}$ and $\mathbf{y}$. Still these are long distance interactions because the variables are coupled in the kernels, depending on $(\mathbf{x} - \mathbf{y})$. As all regions are linked to each other, the resulting matrix is dense. A common strategy for compression is to approximate the kernels in the so-called *farfield*, i.e., in regions that are far away from each other, whereas one sticks to exact kernels in the *nearfield*. *Panel clustering methods* are widely used [HN89][Sau99]. They are based on Taylor expansions of the kernel function in the farfield, and if they are used, derivatives in all directions of all three kernels are required up to a certain degree. This is avoided by applying the *H^2-matrix approximation by interpolation* [HB01]. In this method, the kernel function is approximated by a polynomial Tschebyscheff interpolation [Oev96], so only pointwise evaluations of the three kernels have to be performed. The entire domain $\Gamma \times \Gamma$, where the kernel $k(\mathbf{x}, \mathbf{y})$ is to be integrated, is subdivided into pairs $\Gamma_\tau \times \Gamma_\sigma$ of clusters τ, σ, i.e., unions of contiguous triangles. The polynomial interpolation is made on admissible pairs. These are pairs with clusters of sufficient distance. The coefficients of the interpolation are stored in matrices which are nested in a special way. Those so-called H^2-matrices were first introduced in [HKS00]. The nesting can be utilized for saving storage and allows to perform a quick multiplication. The amount of storage and the number of operations necessary for a matrix-vector multiplication are of order $O(np^3)$. Here $p \in \mathbb{N}$ is the polynomial order and n is the number of unknowns. The following sections sketch several aspects of the implementation of the *H^2-matrix approximation method*. Numerical experiments with several test problems were made and the H^2-method is compared with the uncompressed standard method. Similar experiments are presented in [Gie00].

5.3.1 Interpolation and Multiplication

In order to achieve a compact representation, the kernel functions and the finite element functions are split into their components. Then the remaining discrete BEM operators can be written as

$$\mathsf{K}_{il} = \int\limits_{\Gamma_{\mathbb{T}_i}} \int\limits_{\Gamma_{\mathbb{T}_l}} k_{il}(\mathbf{x},\mathbf{y})\Psi_i(\mathbf{x})\Phi_l(\mathbf{y})d\mathbf{x}d\mathbf{y}\,, \quad i,\, l \in \mathbb{N}_0\,, \tag{5.17}$$

for not necessarily identical finite element basis functions $\Psi_i,\, \Phi_l$ with local support on the surface-triangles $\mathbb{T}_i,\, \mathbb{T}_l$. The matrix K is to be compressed and the matrix-vector multiplication $\mathbf{v} = \mathsf{K}\mathbf{u}$ with $\mathbf{u}(\mathbf{x}) := \sum\limits_i u_i\Psi_i(\mathbf{x})$, $u_i \in \mathbb{R}$ has to be performed.

In the H^2-matrix approximation method one has to distinguish two different steps: The *preparation* of the matrix-vector multiplication which needs to be performed only once even for several multiplications, and the *matrix-vector multiplication* itself. For preparation, the mentioned clusters τ of contiguous triangles are built on the surface Γ. They are not necessarily disjoint, thus can overlap. The resulting *clustering* of the surface $\Gamma = \bigcup\limits_\tau \Gamma_\tau$ is organized in a hierarchical structure, a binary tree. The root-cluster of the tree is the whole surface. Each cluster τ that is not a leaf-cluster is subdivided into two son-clusters, forming the set $S(\tau)$. This is done in a geometrical way. The leaf-clusters consist of less then a fixed number $l_{min} \in \mathbb{N}$ of triangles. A recursive algorithm for the automatic construction of such a geometrical binary tree can be found in [Gie00]: First the center of gravity $\mathbf{z}^i$ of each surface-triangle $\mathbb{T}_i$ has to be built. Then the algorithm *geometric_bisection*($\mathcal{Z}$) of Figure 5.16 is called, with the index set $\mathcal{Z} = 1..N$ of the surface-triangles. The output of the procedure is a binary tree of the centers of gravity of the triangles.

In a second step, axiparallel quadratic bounding boxes B_τ have to be built around each cluster τ. The interpolation with the aid of tensor products of Lagrange polynomials [Oev96] is made on *admissible pairs* of such boxes, i.e., on boxes with small radii compared with their distance

$$\max\{diam(B_\tau),\, diam(B_\sigma)\} \;\leq\; 2\eta \cdot dist(B_\tau,\, B_\sigma). \tag{5.18}$$

Here $\eta\, \in]0,1[$ is a parameter controlling the precision of the interpolation, and it needs to be fixed in this intervall to ensure the desired asymptotic behavior of the error. On an admissible pair of clusters $\Gamma_\sigma \times \Gamma_\tau$, one approximates the kernel function $k(\mathbf{x},\mathbf{y})$ by its interpolant

$$\tilde{k}_{\tau\times\sigma}(\mathbf{x},\mathbf{y}) \quad = \quad \sum_{\iota\in I}\sum_{\kappa\in I} k(\mathbf{x}^\sigma_\iota,\mathbf{y}^\tau_\kappa)\cdot p^\sigma_\iota(\mathbf{x})\cdot p^\tau_\kappa(\mathbf{y})\,, \tag{5.19}$$

$$\text{with } \; p^\sigma_\iota(\mathbf{x}) := L^{\sigma,1}_t(x_1)L^{\sigma,2}_l(x_2)L^{\sigma,3}_m(x_3) \;\text{ and }\; \mathbf{x}^\sigma_\iota := (x^{\sigma,1}_t, x^{\sigma,2}_l, x^{\sigma,3}_m). \tag{5.20}$$

```
input: $\mathcal{Z} = \{\mathbf{z}^i,\ 1 \le i \le k\}$
output: binary tree $\mathcal{T}$
procedur $\mathcal{T}$ = geometric_bisection($\mathcal{Z}$)
{
  if $|\mathcal{Z}| \ge l_{min}$
  {
        let $\delta_j := \max_{i=1\cdots k} z^i_j - \min_{i=1\cdots k} z^i_j$,   component $j = 1,2,3$ ;
        let $l \in \{1,2,3\}$ such that $\delta_l = \max \delta_j$ ;
        split $\mathcal{Z} = \mathcal{Z}_1 \cup \mathcal{Z}_2$ such that
            $||\mathcal{Z}_1| - |\mathcal{Z}_2|| \le 1$ and $\forall x \in \mathcal{Z}_1,\ y \in \mathcal{Z}_2 : x_l \le y_l$ ;
        $\mathcal{T} \to son_1$ = geometric_bisection($\mathcal{Z}_1$) ;
        $\mathcal{T} \to son_2$ = geometric_bisection($\mathcal{Z}_2$) ;

  }
  else { $\mathcal{T} := \mathcal{Z}$ ; }
}
```

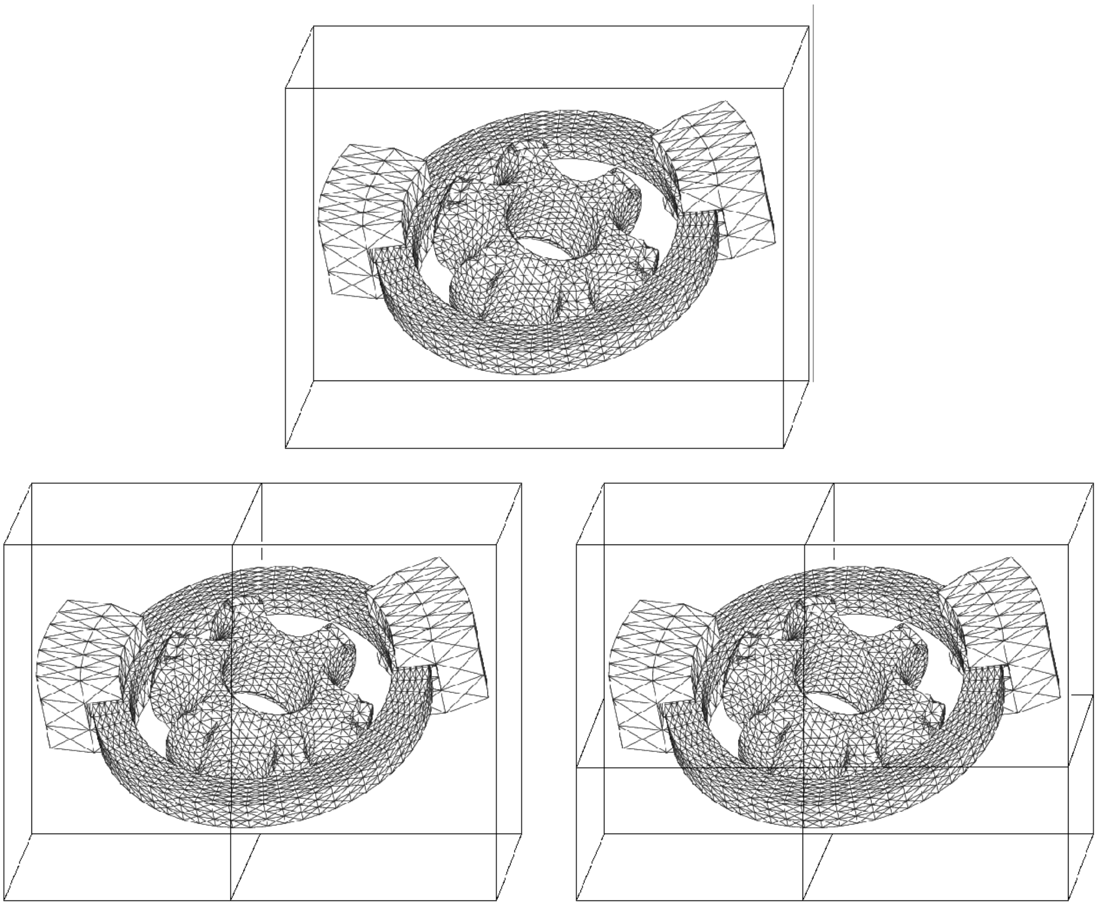

Figure 5.16: Algorithm geometric bisection

Here $p_\iota^\sigma(\mathbf{x})$ is defined as a tensor product of Lagrange polynomials $L_t^{\sigma,1}(x_1)L_l^{\sigma,2}(x_2)L_m^{\sigma,3}(x_3)$ in the three directions on the cluster σ. The set of indices I is defined as $I := \{(t,l,m) \in \mathbb{N}^3 : t,l,m \leq p\}$ for the polynomial order p and it holds $\iota := (t,l,m) \in I$. The respective intervals of the Lagrange interpolation in the three directions are given by the axiparallel quadratic bounding box B_σ around the cluster. The sample points $\mathbf{x}_\iota^\sigma \in \mathbb{R}^3$ are tensor products of roots of Tschebyscheff polynomials [Oev96] in this box. With this notation, the interpolating operator $\tilde{\mathsf{K}}_{il}$ of equation (5.17) can be written as

$$\begin{aligned}
\tilde{\mathsf{K}}_{il} &= \sum_{\iota\in I}\sum_{\kappa\in I}\int\limits_{\Gamma_\sigma}\int\limits_{\Gamma_\tau} k(\mathbf{x}_\iota^\sigma,\mathbf{y}_\kappa^\tau)p_\iota^\sigma(\mathbf{x})p_\kappa^\tau(\mathbf{y})\Psi_i(\mathbf{x})\Phi_l(\mathbf{y})d\mathbf{x}d\mathbf{y} \qquad (5.21)\\
&= \sum_{\iota\in I}\sum_{\kappa\in I} k(\mathbf{x}_\iota^\sigma,\mathbf{y}_\kappa^\tau)\int\limits_{\Gamma_\sigma} p_\iota^\sigma(\mathbf{x})\Psi_i(\mathbf{x})d\mathbf{x}\int\limits_{\Gamma_\tau} p_\kappa^\tau(\mathbf{y})\Phi_l(\mathbf{y})d\mathbf{y}\,, \quad i,\, l\in\mathbb{N}_0\,, \quad \iota,\,\kappa\in I\,,
\end{aligned}$$

on the admissible clusters σ and τ with $supp(\Psi_i) \subseteq \sigma$ and $supp(\Phi_l) \subseteq \tau$. So the variables $\mathbf{x}$ and $\mathbf{y}$ are no longer coupled! This leads to the required compression. Equation (5.21) can be transformed into the compact format $\tilde{\mathsf{K}}_{il} = \mathbf{V}^\sigma \mathsf{S}^{\sigma\times\tau}\mathbf{W}^{\tau T}$ with the matrices $\mathbf{V}^\sigma$ and $\mathbf{W}^\tau$

$$\mathsf{V}_{i\iota}^\sigma := \int\limits_{\Gamma_\sigma} p_\iota^\sigma(\mathbf{x})\Psi_i(\mathbf{x})d\mathbf{x}, \qquad (5.22)$$

$$\mathsf{W}_{l\kappa}^\tau := \int\limits_{\Gamma_\tau} p_\kappa^\tau(\mathbf{y})\Phi_l(\mathbf{y})d\mathbf{y}\,, \qquad (5.23)$$

and the $(p+1)^6$-dimensional matrix

$$\mathsf{S}_{\iota\kappa}^{\sigma\times\tau} := k(\mathbf{x}_\iota^\sigma,\mathbf{y}_\kappa^\tau). \qquad (5.24)$$

The polynomials corresponding to father clusters σ can be expressed exactly in terms of polynomials corresponding to son clusters σ' by

$$p_\iota^\sigma(\mathbf{x}) = \sum_{\lambda\in I} p_\iota^\sigma(\mathbf{x}_\lambda^{\sigma'})p_\lambda^{\sigma'}(\mathbf{x})\,. \qquad (5.25)$$

With the definition of the transfer matrices $\mathsf{B}_{\lambda\iota}^{\sigma',\sigma} := p_\iota^\sigma(\mathbf{x}_\lambda^{\sigma'})$ between father and son, it can easily be seen that the matrices $\mathbf{V}^\sigma$ and $\mathbf{W}^\tau$ are nested, i.e., $\mathbf{V}^\sigma = \mathbf{V}^{\sigma'}\mathsf{B}^{\sigma',\sigma}$ and $\mathbf{W}^\tau = \mathbf{W}^{\tau'}\mathsf{B}^{\tau',\tau}$.

The multiplication has to be performed on the domain associated with $\Gamma\times\Gamma$. There are many possibilities to cover this domain with pairs of clusters, but one searches a covering that is in some sense ideal. It should only consist of admissible pairs of clusters or pairs of leaf-clusters, and the total number of pairs should be minimal. This covering is called *minimal partitioning* $\mathcal{P}$. It can be constructed by calling the algorithm *divide(*$\Gamma\times\Gamma$, $\emptyset$*)* of Figure 5.17 presented in [Sau99].

The approximate matrix-vector multiplication $\tilde{\mathbf{v}} = \tilde{\mathsf{K}}\mathbf{u}$ is realized on $\mathcal{P}$. The kernel function remains unchanged in the nearfield consisting of non-admissible leaf-clusters and is replaced by its interpolant on admissible farfield pairs

$$\tilde{\mathsf{K}} = \mathsf{K}_{\text{Nearfield}} + \sum_{adm.\ \sigma\times\tau}\left(\mathbf{V}^\sigma\mathsf{S}^{\sigma\times\tau}\mathbf{W}^{\tau T}\right)\,. \qquad (5.26)$$

```
procedure divide($\Gamma_\sigma \times \Gamma_\tau, \mathcal{P}$)
{
    if ($S(\sigma) = S(\tau) = \emptyset$) then {$\mathcal{P} = \mathcal{P} \cup (\Gamma_\sigma \times \Gamma_\tau)$ ;}
    else
    {
        if (($B_\sigma, B_\tau$) are admissible) then { $\mathcal{P} = \mathcal{P} \cup (\Gamma_\sigma \times \Gamma_\tau)$ ;}
        else
        {
            if ($S(\sigma) = \emptyset$) then {for all $\tau' \in S(\tau)$ call divide($\Gamma_\sigma \times \Gamma_{\tau'}, \mathcal{P}$) ;}
            else
            {
                if ($S(\tau) = \emptyset$) then {for all $\sigma' \in S(\sigma)$ call divide($\Gamma_{\sigma'} \times \Gamma_\tau, \mathcal{P}$) ;}
                else {for all pairs of sons $\sigma' \subset S(\sigma)$, $\tau' \subset S(\tau)$ call divide($\Gamma_{\sigma'} \times \Gamma_{\tau'}, \mathcal{P}$) ;}
            }
        }
    }
}
```

Figure 5.17: Algorithm divide

The multiplication of Figure 5.18 consists of three steps, see also Figure 5.19:

- the *Forward Transformation* , where the values of the vector $\mathbf{u}$ are transported from the leaves to the clusters,
- the *Multiplication* $\tilde{\mathbf{v}} = \tilde{\mathsf{K}}\mathbf{u}$ on the clusters,
- and the *Backward Transformation* , where the result $\tilde{\mathbf{v}}$ is transported from the clusters to the leaves.

```
procedure $H^2$ Multiplication
{
    $\mathbf{v} = 0$ ;
    Forward_Transformation($\Gamma$) ;
    for all $\Gamma_\sigma \times \Gamma_\tau \subset \mathcal{P}$ call Multiply($\sigma \times \tau$) ;
    Backward_Transformation($\Gamma$) ;
}
```

Figure 5.18: The multiplication $\tilde{\mathbf{v}} = \tilde{\mathsf{K}}\mathbf{u}$

```
procedure Forward_Transformation($\sigma$)
{
    if ($S(\sigma) \neq \emptyset$) then { $\forall \sigma' \in S(\sigma)$ call Forward_Transformation($\sigma'$)};
    $\mathbf{x}_\sigma = 0$ ;    $\mathbf{y}_\sigma = 0$ ;
    if ($S(\sigma) = \emptyset$) then { $\mathbf{x}_\sigma = \mathsf{W}^{\sigma T}\mathbf{u}_\sigma$};
    else {$\forall \sigma' \in S(\sigma)$ $\mathbf{x}_\sigma = \mathbf{x}_\sigma + \mathsf{B}^{\sigma',\sigma T}\mathbf{x}_{\sigma'}$};
}


procedure Multiply($\sigma \times \tau$)
{
    if ($S(\sigma) = S(\tau) = \emptyset$) then { for all $\mathbb{T}_i \in \sigma$ set $\mathbf{v}_i = \mathbf{v}_i + \sum_{\mathbb{T}_j \in \tau} \mathsf{K}_{ij}\mathbf{u}_j$ ;}
    else { $\mathbf{y}_\sigma = \mathbf{y}_\sigma + \mathsf{S}^{\sigma\times\tau}\mathbf{x}_\tau$};
}


procedure Backward_Transformation($\sigma$)
{
    if ($S(\sigma) = \emptyset$) then { $\mathbf{v}_\sigma = \mathbf{v}_\sigma + \mathsf{V}^\sigma\mathbf{y}_\sigma$};
    else
    {
        for all sons $\sigma' \in S(\sigma)$
        {
            $\mathbf{y}_{\sigma'} = \mathbf{y}_{\sigma'} + \mathsf{B}^{\sigma',\sigma}\mathbf{y}_\sigma$ ;
            call Backward_Transformation($\sigma'$);
        }
    }
}
```

Figure 5.19: Algorithms for the multiplication $\mathbf{v} = \mathsf{K}\mathbf{u}$

5.3.2 Numerical Experiments

It is shown in [HB01], that for the scalar examples explained in the previous Section 5.3.1, the amount of storage and the number of operations necessary for a matrix-vector multiplication are of order $O(np^3)$. It it also shown that the error of the approximation can be bounded and satisfies the estimate

$$\|k - \tilde{k}_{\tau\times\sigma}\|_{\infty,\mathcal{B}_\tau\times\mathcal{B}_\sigma} \le C(p)\,\eta^{p+1}\|k\|_{\infty,\mathcal{B}_\tau\times\mathcal{B}_\sigma}\,. \tag{5.27}$$

So for $0 < \eta < 1$ the error decreases with increasing order p of the interpolation.

In a first numerical experiment, this predicted behavior of the H^2*-matrix approximation method* was tested using the typical geometry of the induction heating setting, as shown in Figure 5.20.

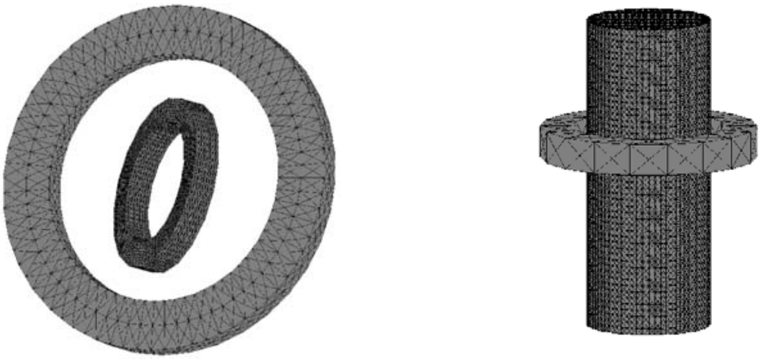

Figure 5.20: Test geometries A and B

A *single layer* with kernel $k(\mathbf{x},\mathbf{y}) = \frac{1}{4\pi}\frac{1}{\|\mathbf{x}-\mathbf{y}\|}$ was compressed. It was discretized with a Garlerkin method and constant finite element basis functions $\Psi_i = \Phi_i$. The resulting matrix K was multiplied by a vector ten times. The storage and cpu-time requirements for the uncompressed standard method and the interpolating $\mathbf{H}^2$-method were compared. The order of interpolation was set to be 2 and the admissibility parameter η was set to be 0.99. This turned out to be sufficient. The measured data is defined as follows:

n := Number of unknowns (=Number of panels)
Size of double = 8 Byte
Standard storage = $n^2 \cdot 8\ Byte$
$\mathbf{H}^2$storage := Storage needed for the $\mathbf{H}^2$ interpolation
Standard time := Time for filling + 10 multiplications standard method
$\mathbf{H}^2$ Time := Time for filling + 10 multiplications $\mathbf{H}^2$ method
$\|\mathsf{K}\|_2$:= $\sup\limits_{\|\mathbf{y}\|=1} \|\mathsf{K}\cdot\mathbf{y}\|$
$\mathsf{K}_{\mathbf{H}^2}$:= Interpolated matrix
Relative error := $\dfrac{\|\mathsf{K}-\mathsf{K}_{\mathbf{H}^2}\|_2}{\|\mathsf{K}\|_2}$

In each case the time for filling amounts to 90% of the total time. The Euklidian operator norm was calculated with the aid of a vector iteration. Table (5.21) shows the results that are computed on a Sun Ultra 450 computer with a 300 MHz Ultrasparc-II CPU.

n	*Standard storage*	$\mathbf{H}^2$ *storage*	*Standard time*	$\mathbf{H}^2$ *time*	*Relative error*
730	4 MB	2.3 MB	54 sec	49 sec	0.00044
2752	57 MB	14 MB	12 min	4 min	0.00067
7488	427 MB	45 MB	1.5 h	10.2 min	0.00065
11520	1012 MB	75 MB	3.7 h	21.7 min	0.0007
17312	2286 MB	91 MB	8.5 h	25 min	-

Figure 5.21: Time, storage and errors for single layer potential

The first four rows were produced by interpolation on the geometry A of Figure 5.20 and the last example on geometry B. The error was not calculated for this example because the vector iteration would have taken days. The compression rate is higher for 'flat' pieces as the admissibility condition can be fulfilled for bigger clusters.

So the H^2-technique seems to work well. Next, the matrix of the impedance model was compressed, and equation (4.30) was solved for the geometries of Figure 5.20. As a first difference to the above example, it should be pointed out that the unknowns are now located on the edges and the nodes of the geometry. This means that the tree also normally has to be constructed over the edges and the nodes to reach an optimal compression rate. Therefore two trees have to be constructed. In practice, however, especially the coupling of both trees in mixed operators is complicated. Only one tree was built in this program over the triangles. As a consequence some edges and nodes on the boundary of the triangle-clusters appear twice. This is acceptable, however, as can be seen from the compression rates in Figure 5.22. The occuring BEM operators arising from the matrices $\mathsf{M}_{\Re}$, $\mathsf{M}_{\Im}$, B, and Q can be found in the equations (4.31) - (4.34), and are repeated here for convenience

$$\mathsf{M} \longrightarrow \int\limits_{\triangle_n}\int\limits_{\triangle_m} \left((\mathbf{b}_{nk} \cdot \mathbf{b}_{mn}) \cdot \mu_0 \cdot \Re[\frac{1}{\eta}] \cdot \delta_{nm} \; + \; \frac{9}{4T_nT_m} G(\mathbf{x},\mathbf{y}) \right) dS(\mathbf{x})\, dS(\mathbf{y}) \, ,$$

$$\mathsf{Q} \longrightarrow \int\limits_{\triangle_n}\int\limits_{\triangle_m} \frac{1}{4\,T_n\,T_m} (\mathbf{f}_{nk} \cdot \mathbf{f}_{mi}) \cdot G(\mathbf{x},\mathbf{y})\, dS(\mathbf{x})\, dS(\mathbf{y}) \, .$$

$$\mathsf{B} \longrightarrow \int\limits_{\triangle_n}\int\limits_{\triangle_m} [\frac{\mathbf{f}_{ni}}{2 \cdot T_n} \mathbf{b}_{mk}(\mathbf{x})] \cdot [\frac{\delta_{mn}}{2\,T_m} - \mathbf{n}_{\mathbf{x}} \cdot \mathbf{grad}_{\mathbf{x}}\, G(\mathbf{x},\mathbf{y})]\, dS(\mathbf{x})\, dS(\mathbf{y})$$

$$+ \int\limits_{\triangle_n}\int\limits_{\triangle_m} [\frac{\mathbf{f}_{ni}}{2 \cdot T_n} \cdot \mathbf{n}_m] \cdot [\mathbf{b}_{mk}(\mathbf{x}) \cdot \mathbf{grad}_{\mathbf{x}}\, G(\mathbf{x},\mathbf{y})]\, dS(\mathbf{x})\, dS(\mathbf{y}) \, .$$

The diagonal part of M consists of scalar products of linear edge functions, and it does not need to be compressed. The non-diagonal part is a scalar single layer potential with constant basis functions.

The constant $\mathbf{f}$-basis functions of the single layer potential of Q are vector-valued. So the matrices $\mathbf{V}$ of equation (5.22), for the operator Q denoted by $\mathbf{V}_{\mathsf{Q}}$, have to be adapted to this fact and extended to three dimensions. There is no need to store the matrices $\mathbf{W}_{\mathsf{Q}}$ of equation (5.23) because the basis functions are the same and it holds $\mathbf{W}_{\mathsf{Q}} = \mathbf{V}_{\mathsf{Q}}$. The transfer matrices of equation (5.25) are identical for all three operators and have to be calculated and stored only once.

The next operator B is the most complicated one. The basis functions are vector-valued and mixed, consisting of $\mathbf{b}$- and $\mathbf{f}$-basis functions, and one needs $\mathbf{W}_{\mathsf{B}}$ and $\mathbf{V}_{\mathsf{B}}$. As $\mathbf{V}_{\mathsf{B}} = \mathbf{V}_{\mathsf{Q}}$, $\mathbf{V}_{\mathsf{B}}$ does not have to be calculated again. A problem occurs for the double layer potential because the normal is defined on the triangles and cannot be generalized for a cluster of triangles.

$$\mathsf{K}_{il} = \int\limits_{\Gamma_{\mathbb{T}_i}} \int\limits_{\Gamma_{\mathbb{T}_l}} \frac{\partial}{\partial n_x} G(\mathbf{x},\mathbf{y})_{il} \Psi_i(\mathbf{x}) \Phi_l(\mathbf{y}) d\mathbf{x} d\mathbf{y} \tag{5.28}$$

This can be cured with the recipe introduced in [HB01], where the derivative of the polynomial kernel interpolant is used

$$\begin{aligned} \tilde{\mathsf{K}}_{il} &= \int\limits_{\Gamma_{\mathbb{T}_i}} \int\limits_{\Gamma_{\mathbb{T}_l}} \frac{\partial}{\partial n_x} \tilde{G}(\mathbf{x},\, \mathbf{y})_{il} \Psi_i(\mathbf{x}) \Phi_l(\mathbf{y}) d\mathbf{x} d\mathbf{y} \\ &= \sum_{\iota \in I} \sum_{\kappa \in I} G(\mathbf{x}_\iota^\sigma, \mathbf{y}_\kappa^\tau) \int\limits_{\Gamma_\sigma} \frac{\partial}{\partial n_x} p_\iota^\sigma(\mathbf{x}) \cdot \Psi_i(\mathbf{x}) d\mathbf{x} \int\limits_{\Gamma_\tau} p_\kappa^\tau(\mathbf{y}) \Phi_l(\mathbf{y}) d\mathbf{y} \,. \end{aligned} \tag{5.29}$$

The problems occuring in the modified double layer potential can be mastered in a similar fashion. Its kernel is vector-valued, but splitting it up into its components does not cause any problems.

All in all, the elaborate operators can be compressed without major difficulties by the H^2-matrix approximation technique. Lots of matrices must be calculated only once and can be reused for different operators. This automatically saves a lot of storage and enhances the efficiency of the algorithm. The solution of equation (4.30) can additionally be accelerated by using the nearfield of the operator Q as a preconditioner of the second row of P, as defined in equation (5.15). This row is solved with a *conjugate gradient method*, which in the standard method is preconditioned with a *Jacobi preconditioner*. This *Jacobi preconditioner* of P can now be replaced by the nearfield matrix $\mathsf{Q}_{Nearfield}$ which can be inverted with a *Gaussian elimination scheme*. The direct solver is implemented in a sparse format and does not need much storage because the nearfield matrix is sparse, too. Table 5.22 shows the performance of the H^2-matrix approximation for the impedance model compared with the uncompressed standard method. The solver was stopped when the residual had decreased to a value below 0.0001 times the residual in the first step. The documented time is again the time needed for filling the matrices and solving the system. The number of unknowns is defined as

$$n := 2 \cdot (\text{ number of edges + number of nodes + number of holes in the workpiece}) \,.$$

The relative error is defined here as the difference between the surface current $\gamma_D \mathbf{j}$ of the H^2-solution and that of the standard solution

$$\text{relative error} := \int_\Gamma \frac{\|\gamma_D \mathbf{j}_{H^2}(\mathbf{x}) - \gamma_D \mathbf{j}_{st.}(\mathbf{x})\|}{\|\gamma_D \mathbf{j}_{st.}(\mathbf{x})\|} \, dS_{\mathbf{x}} \,,$$

n	*Standard storage*	$\mathbf{H}^2$ *storage*	*Standard time*	$\mathbf{H}^2$ *time*	*Relative error*
2948	22.7 MB	15.5 MB	19.75 min	15.0 min	0.00139
6916	125.3 MB	35.0 MB	1.9 h	43.3 min	0.00250
11420	342.0 MB	71.0 MB	6.7 h	1.6 h	0.00146
23840	954.1 MB	93.4 MB	14.6 h	2.4 h	0.00218
46724	5725.0 MB	333.0 MB	-	9.0 h	-

Figure 5.22: Time, storage, and errors for the impedance model

because the current is the most important final result of the calculations of the electromagnetic part. Again, the first four rows were produced by interpolation on the geometry A of Figure 5.20 and the last on geometry B. Storage requirements and calculation times are strongly reduced, and geometries consisting of 20000 surface faces can be calculated.

Another special feature is implemented due to the fact that the workpiece rotates with a frequency of $50Hz$. If the material data is updated 20 times per simulation and the equation is solved for 10 positions per rotation, then the equation is to be solved 200 times. Even with the H^2-technique, it is impossible to store the data of all theses matrices, so they have to be exported to a hard disk. Moreover, they cannot completely be filled so often in an acceptable timespan. By looking at the positions of the material parameters in the equations, the solution to the problem becomes obvious. The material parameters only occur in the diagonal part of the operator M, which is small and can be calculated fast. So updating of the parameters is an easy, quick task. Rotation is a bigger challenge. The BEM operators change only for items that are moving relative to each other. Parts of the operators which describe workpiece/workpiece interactions (w/w) or inductor/inductor interactions (i/i) need to be calculated only once. But how to reach this goal in the H^2 context where everything is linked together in the tree? The option chosen here is to apply the algorithm *geometric bisection* separately for workpiece and inductor. Then each cluster consists exclusively of workpiece triangles or inductor triangles. In this case, the matrices $\mathbf{V}$, $\mathbf{W}$ and $\mathbf{B}$ do not change during the rotation and have to be calculated only once (except for the useless $\mathbf{B}$ of the root)! After merging the two resulting trees under one big root, one finds the situation of Figure 5.23. If the algorithm *divide* is now applied to this new tree, each pair of admissible clusters belongs either to w/w or i/i or to the interaction w/i between workpiece and inductor. The nearfield and the matrices $\mathbf{S}$ have to be refreshed only for the w/i pairs. This is a big advantage because the interesting part with the biggest number of triangles is the workpiece, and w/w does not have to be refreshed.

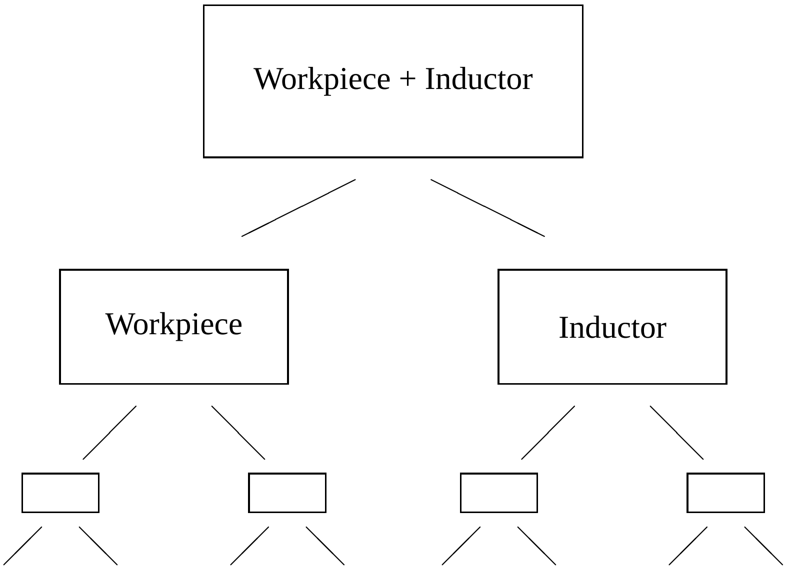

Figure 5.23: Tree

Chapter 6

Validation

Several tests were made in order to check the correctness of the results of the program. First of all separated and uncoupled features of the program are tested, such as the temperature calculation, the BEM part or the FEM part. Analytical solutions of special configurations often exist, and the simulation results can be compared with these. This is the most reliable possibility for verification because no experimental errors are involved. For the electromagnetic part, analytical solutions of the eddy current problem are developed for highly symmetric settings with homogeneous materials. In Section 6.1 this is done for a sphere and a cylinder excited by a circular current loop . No analytical solutions are available for less symmetric geometries or if non-linearities are involved. In this case one has to rely on experiments. Measurements of the surface temperature during the hardening of a cylinder were made with the aid of a thermographical camera. The evolution of the temperature in the experiment and in a simulation are compared in Section 6.5. Most important is the prediction of the location of the hardened zone. These final results are presented in Section 7.

6.1 Analytical Solutions

6.1.1 Conducting Sphere in the Alternating Field of a Current Loop

In this section, an analytical solution of the eddy current model is developed for a homogeneous sphere excited by a circular current loop. For axial symmetry all quantities can be considered independent of ϕ in spherical coordinates. If $\mathbf{B}$ additionally has no ϕ-component, then the vector potential $\mathbf{B} = \mathbf{curl}\,\mathbf{A}$ can be considered as

$$\mathbf{A} = A_\phi(r,\theta) \cdot e^{i\omega t} \cdot \mathbf{e}_\phi\,, \quad \text{with}\;\; A_\phi(r,\theta) \in \mathbb{C}\,. \tag{6.1}$$

The coordinate axes are chosen according to Figure 6.1. It can easily be shown that for homogeneous material parameters and in Coulomb gauge the magnetic vector potential $\mathbf{A}$ is equivalent to the electric field $\mathbf{E}$ in the eddy current model. With the ansatz

$$A_\phi(r,\theta) = \frac{R(r)}{\sqrt{r}} \cdot T(\theta), \quad \text{with}\;\; R(r),\, T(\theta) \in \mathbb{C}\,, \tag{6.2}$$

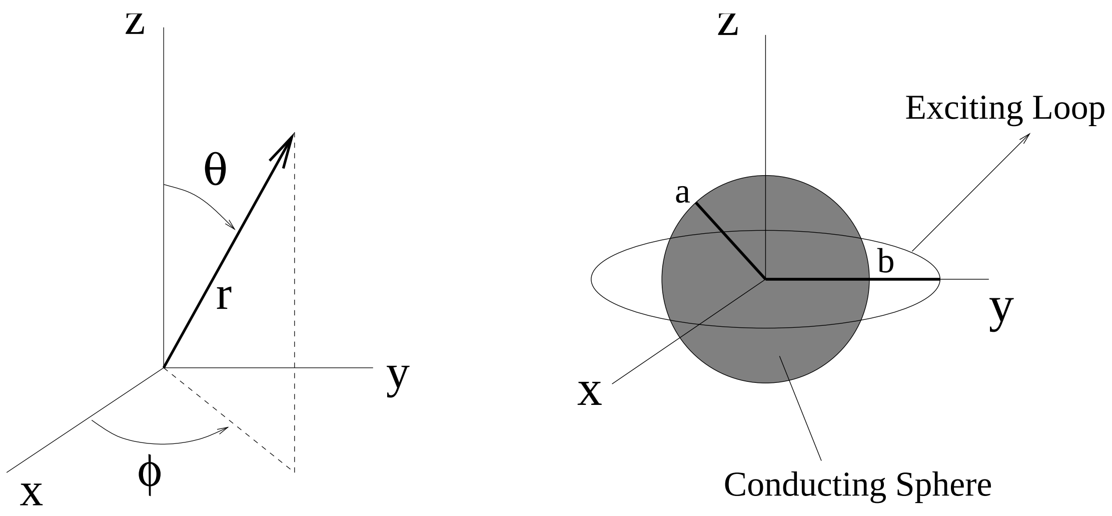

Figure 6.1: Setting sphere

equation (3.32) can be transformed into

$$\frac{r^2}{R}\,\frac{d^2R}{dr^2}+\frac{r}{R}\,\frac{dR}{dr}-\frac{1}{4}-ikr^2+\frac{\sqrt{1-u^2}}{T}\,\frac{d^2}{du^2}[\sqrt{1-u^2}\cdot T]=0\,, \tag{6.3}$$

with $k := \omega\sigma\mu$ and $u := \cos\theta$. When setting the terms involving r equal to $n(n+1)$, with $n \in \mathbb{Z}$, and those involving θ to $-n(n+1)$ it follows [Smy68, p. 375]

$$\text{Legendre diff. eqn.}\quad 0 \;=\; (1-u^2)\,\frac{d^2T_n}{du^2}-2u\,\frac{dT_n}{du}-\frac{T_n}{1-u^2}+n(n+1)T_n\,, \tag{6.4}$$

$$\text{Bessel diff. eqn.}\quad 0 \;=\; \frac{d^2R_n}{dr^2}+\frac{1}{r}\,\frac{dR_n}{dr}+\left(-ik-\frac{(n+\frac{1}{2})^2}{r^2}\right)R_n\,. \tag{6.5}$$

It can be shown [FK98, p. 85] that T_n is only bounded if $n > 0$ is a positiv integer. The solution of the system of equations (6.4), (6.5) is [FK98, p. 91], [Smy68, p. 375]

$$T_n(\theta) \;=\; C_{1n}\,P_n^1(u)\;+\;C_{2n}\,Q_n^1(u)\,, \tag{6.6}$$

$$R_n(r) \;=\; C_{3n}\,J_{n+\frac{1}{2}}(ir\sqrt{ik})\;+\;C_{4n}\,J_{-n-\frac{1}{2}}(ir\sqrt{ik}) \qquad k \neq 0\,, \tag{6.7}$$

$$R_n(r) \;=\; C_{5n}\,r^{n+\frac{1}{2}}\;+\;C_{6n}\,r^{-n-\frac{1}{2}} \qquad k = 0\,, \tag{6.8}$$

with the coefficients $C_{1n}\ldots C_{6n} \in \mathbb{C}$, with the *associated Legendre functions* P_n^1 and Q_n^1 of first and second kind, and with the *Bessel functions* $J_{n+\frac{1}{2}}, J_{-n-\frac{1}{2}}$. It holds $C_{2n} = 0$ because $Q_n^1(u)$ is unbounded [Smy68, p. 155, 158]. The vector potential of a circular current loop with the radius b and the current I is [Jac75, p. 144]

$$A_\phi^C(r,\theta) \;=\; -\frac{Ib\mu_0}{4}\sum_{n=0}^{\infty}\frac{(-1)^n(2n-1)!!}{2^n(n+1)!}\cdot P_{2n+1}^1(u)\cdot\frac{r^{2n+1}}{b^{2n+2}} \quad \text{for } r \leq b\,, \tag{6.9}$$

$$A_\phi^{CE}(r,\theta) \;=\; -\frac{Ib\mu_0}{4}\sum_{n=0}^{\infty}\frac{(-1)^n(2n-1)!!}{2^n(n+1)!}\cdot P_{2n+1}^1(u)\cdot\frac{b^{2n+1}}{r^{2n+2}} \quad \text{for } b < r\,, \tag{6.10}$$

$$\text{with } (2n-1)!! \;:=\; (2n-1)\cdot(2n-3).....\cdot 5\cdot 3\cdot 1\,, \qquad (2\cdot 0-1)!! := 1\,.$$

The complete vector potential is a superposition of the solution of the sphere and the loop. It consists of three parts in the following three regions: The interior of the sphere (A^I_ϕ), the region between the sphere and the loop (A^O_ϕ), and the exterior region (A^E_ϕ). These vector potentials can be written as

$$\begin{aligned}
A^I_\phi(r,\theta) &= \sum_{n=1}^{\infty} r^{-\frac{1}{2}} \cdot [C_{3n} J_{n+\frac{1}{2}}(ir\sqrt{ik}) + C_{4n} J_{-n-\frac{1}{2}}(ir\sqrt{ik})] \cdot C_{1n} P^1_n(u) \qquad r < a\,, && (6.11)\\
A^O_\phi(r,\theta) &= \left(\sum_{n=1}^{\infty} [C_{5n}\, r^n \;+\; C_{6n}\, r^{-n-1}] \cdot C_{1n} P^1_n(u)\right) + A^C_\phi(r,\theta) \qquad a < r < b\,, && (6.12)\\
A^E_\phi(r,\theta) &= \left(\sum_{n=1}^{\infty} [C_{5n}\, r^n \;+\; C_{6n}\, r^{-n-1}] \cdot C_{1n} P^1_n(u)\right) + A^{CE}_\phi(r,\theta) \qquad b < r\,. && (6.13)
\end{aligned}$$

A must vanish for $r \to \infty$, so it follows $C_{5n} = 0$. In the case of $x \to 0$, the rule [AI70, 9.1.7]

$$J_\nu(x) = \left(\frac{x}{2}\right)^\nu \cdot \frac{1}{\Gamma(\nu+1)} + O(|x|^{\nu+1}) \qquad \nu \in \mathbb{C},\ \nu \neq -1,\ -2,\ -3, \ldots.. \tag{6.14}$$

with the gamma function Γ shows that $C_{4n} = 0$ if $A^I_\phi(r,\theta)$ is finite at $r = 0$. It remains

$$\begin{aligned}
A^I_\phi(r,\theta) &= \sum_{n=1}^{\infty} B^I_n \cdot r^{-\frac{1}{2}} \cdot J_{n+\frac{1}{2}}(ir\sqrt{ik}) \cdot P^1_n(u) \qquad r < a\,, && (6.15)\\
A^O_\phi(r,\theta) &= \left(\sum_{n=1}^{\infty} B^O_n \cdot r^{-n-1} \cdot P^1_n(u)\right) + A^C_\phi(r,\theta) \qquad a < r < b\,, && (6.16)\\
A^E_\phi(r,\theta) &= \left(\sum_{n=1}^{\infty} B^O_n \cdot r^{-n-1} \cdot P^1_n(u)\right) + A^{CE}_\phi(r,\theta) \qquad b < r\,. && (6.17)
\end{aligned}$$

The unknown coefficients B^I_n, $B^O_n \in \mathbb{C}$ can be fixed by taking into account the jump conditions in coulomb gauge $[\mathbf{n} \cdot \mathbf{B}] = [\mathbf{n} \times \mathbf{H}] = 0$ on the surface of the sphere $(r = a)$. If $\mathbf{B}$ is integrated over a Stokesian loop C, one finds

$$0 = \int_S \mathbf{B} \cdot \mathbf{n}\, dS = \int_C \mathbf{A}\, d\mathbf{s} \quad \Longrightarrow \quad 0 = [\mathbf{n} \times \mathbf{A}]\,, \tag{6.18}$$

with the first jump condition. Integration of the Coulomb gauge condition over a Gaussian pillbox V yields

$$0 = \int_V \operatorname{div} \mathbf{A}\, dV = \int_S \mathbf{A} \cdot \mathbf{n}\, dS \quad \Longrightarrow \quad 0 = [\mathbf{n} \cdot \mathbf{A}]\,, \tag{6.19}$$

so one finds $[\mathbf{A}] = 0$. Together with $[\mathbf{n} \times \mathbf{H}] = 0$, this can be written as

$$\begin{aligned}
A^I_\phi(a,\theta) &= A^O_\phi(a,\theta)\,, && (6.20)\\
\frac{1}{\mu_r}\frac{\partial}{\partial r}(r\, A^I_\phi(r,\theta))\bigg|_{r=a} &= \frac{\partial}{\partial r}(r\, A^O_\phi(r,\theta))\bigg|_{r=a}\,, &&\\
\Leftrightarrow \quad \frac{1}{\mu_r}\left(A^I_\phi(a,\theta) + a\frac{\partial A^I_\phi(r,\theta)}{\partial r}\bigg|_{r=a}\right) &= \left(A^O_\phi(a,\theta) + a\frac{\partial A^O_\phi(r,\theta)}{\partial r}\bigg|_{r=a}\right), && (6.21)
\end{aligned}$$

which has to be valid for all θ. The exciting vector potential consists only of odd associated Legendre functions. This, their linear independence and (6.21) suggest $B_n^I = B_n^O = 0$ for even n. It remains for the two interesting regions

$$\begin{aligned} A_\phi^I(r,\theta) &= \sum_{n=0}^{\infty} A_n^I \cdot r^{-\frac{1}{2}} \cdot J_{2n+\frac{3}{2}}(ir\sqrt{ik}) \cdot P_{2n+1}^1(u)\,, && (6.22)\\ A_\phi^O(r,\theta) &= \sum_{n=0}^{\infty} A_n^O \cdot r^{-2n-2} \cdot P_{2n+1}^1(u) - \frac{Ib\mu_0}{4}\frac{(-1)^n(2n-1)!!}{2^n(n+1)!}\frac{r^{2n+1}}{b^{2n+2}}P_{2n+1}^1(u)\,. && (6.23)\end{aligned}$$

The jump conditions (6.20), (6.21) together with $J_y'(x) = J_{y-1}(x) - \frac{y}{x}J_y(x)$ are fulfilled if

$$\begin{aligned} A_n^I \cdot a^{-\frac{1}{2}} \cdot J_{2n+\frac{3}{2}} &= A_n^O \cdot a^{-2n-2} - A_{\phi n}^C \cdot a^{2n+1}\,, && (6.24)\\ \frac{A_n^I}{\mu_r}\Big(a^{-\frac{1}{2}}J_{2n+\frac{3}{2}} &+ a \cdot \Big\{ -\frac{1}{2}a^{-\frac{3}{2}}J_{2n+\frac{3}{2}} + a^{-\frac{1}{2}}(i\sqrt{ik})[J_{2n+\frac{1}{2}} - \frac{2n+\frac{3}{2}}{ia\sqrt{ik}}J_{2n+\frac{3}{2}}]\Big\}\Big) && (6.25)\\ &= A_n^O a^{-2n-2} - A_{\phi n}^C a^{2n+1} + A_n^O(-2n-2)a^{-2n-2} - A_{\phi n}^C(2n+1)a^{2n+1}\,, \end{aligned}$$

with

$$J_y = J_y(ia\sqrt{ik}) \quad \text{and} \quad A_{\phi n}^C = \frac{Ib\mu_0}{4}\frac{(-1)^n(2n-1)!!}{2^n(n+1)!\,b^{2n+2}}\,.$$

This is equivalent to

$$\begin{aligned} A_n^I &= \frac{A_n^O \cdot a^{-2n-\frac{3}{2}} - A_{\phi n}^C \cdot a^{2n+\frac{3}{2}}}{J_{2n+\frac{3}{2}}}\,, && (6.26)\\ \frac{A_n^I}{\mu_r}\Big(J_{2n+\frac{3}{2}} &- \frac{1}{2}J_{2n+\frac{3}{2}} + a(i\sqrt{ik})J_{2n+\frac{1}{2}} - (2n+\frac{3}{2})J_{2n+\frac{3}{2}}\Big) && (6.27)\\ &= A_n^O a^{-2n-\frac{3}{2}} - A_{\phi n}^C a^{2n+\frac{3}{2}} + A_n^O(-2n-2)a^{-2n-\frac{3}{2}} - A_{\phi n}^C(2n+1)a^{2n+\frac{3}{2}}\,, \end{aligned}$$

which leads to

$$\frac{A_n^O \cdot a^{-2n-\frac{3}{2}} - A_{\phi n}^C \cdot a^{2n+\frac{3}{2}}}{\mu_r}\Big(1 - \frac{1}{2} + a(i\sqrt{ik})\frac{J_{2n+\frac{1}{2}}}{J_{2n+\frac{3}{2}}} - (2n+\frac{3}{2})\quad\Big)$$
$$= A_n^O(-2n-1)a^{-2n-\frac{3}{2}} - A_{\phi n}^C(2n+2)a^{2n+\frac{3}{2}}\,,$$

$$\Longleftrightarrow$$

$$\frac{A_n^O - A_{\phi n}^C a^{4n+3}}{\mu_r}\Big(ai\sqrt{ik}\frac{J_{2n+\frac{1}{2}}}{J_{2n+\frac{3}{2}}} - 2n - 1\Big) = A_n^O(-2n-1) - A_{\phi n}^C(2n+2)a^{4n+3}\,,$$

$$\Longleftrightarrow$$

$$A_n^O\Big(ai\sqrt{ik}\frac{J_{2n+\frac{1}{2}}}{J_{2n+\frac{3}{2}}} - 2n - 1 + \mu_r(2n+1)\Big) = A_{\phi n}^C a^{4n+3}\Big(ai\sqrt{ik}\frac{J_{2n+\frac{1}{2}}}{J_{2n+\frac{3}{2}}} - 2n - 1 - \mu_r(2n+2)\Big)\,.$$

With these relations it finally follows

$$A_\phi^I(r,\theta) = \sum_{n=0}^{\infty} A_n^I \cdot r^{-\frac{1}{2}} \cdot J_{2n+\frac{3}{2}}(ir\sqrt{ik}) \cdot P_{2n+1}^1(u)\,, \tag{6.28}$$

$$A_\phi^O(r,\theta) = \sum_{n=0}^{\infty} A_n^O \cdot r^{-2n-2} \cdot P_{2n+1}^1(u) - A_{\phi n}^C \cdot r^{2n+1} \cdot P_{2n+1}^1(u)\,, \tag{6.29}$$

with,

$$A_n^O = A_{\phi n}^C a^{4n+3} \frac{\left(ai\sqrt{ik}\frac{J_{2n+\frac{1}{2}}(ia\sqrt{ik})}{J_{2n+\frac{3}{2}}(ia\sqrt{ik})} - 2n - 1 - \mu_r(2n+2)\right)}{\left(ai\sqrt{ik}\frac{J_{2n+\frac{1}{2}}(ia\sqrt{ik})}{J_{2n+\frac{3}{2}}(ia\sqrt{ik})} - 2n - 1 + \mu_r(2n+1)\right)}\,, \tag{6.30}$$

$$A_n^I = \frac{A_n^O \cdot a^{-2n-\frac{3}{2}} - A_{\phi n}^C \cdot a^{2n+\frac{3}{2}}}{J_{2n+\frac{3}{2}}(ia\sqrt{ik})}\,, \tag{6.31}$$

$$A_{\phi n}^C = \frac{Ib\mu_0}{4} \frac{(-1)^n (2n-1)!!}{2^n (n+1)!\, b^{2n+2}}\,, \tag{6.32}$$

$$k = \omega\sigma\mu = \omega\sigma\mu_r\mu_0\,, \tag{6.33}$$

$$u = \cos\theta\,. \tag{6.34}$$

The potential was calculated numerically with the aid of the program package MATLAB[1]. Therefore, a mesh of the sphere was built in the two dimensions r and ϕ, consisting of equidistant grid points (r_m, ϕ_n). The potential $A_\phi^I(r,\theta)$ was calculated adaptively at each of these points. This was done by adding $k \in \mathbb{N}$ terms of the series

$$A_\phi^{I,k}(r_m,\theta_n) = \sum_{n=0}^{k} A_n^I \cdot r_m^{-\frac{1}{2}} \cdot J_{2n+\frac{3}{2}}(ir_m\sqrt{ik}) \cdot P_{2n+1}^1(u_n)\,.$$

k is increased until the sum remains unchanged at each grid point, i.e. until the difference of the sum in consecutive steps $|A_\phi^{I,k_{i+1}} - A_\phi^{I,k_i}|$ was smaller than a certain criterion.

Figure 6.2 illustrates the result for a sphere with radius $a = 5\,cm$, the conductivity $\sigma = 2 \cdot 10^6\,(\Omega m)^{-1}$, and a relative magnetic permeability of $\mu_r = 10$. It is excited by a loop current of $I = 1\,kA$, $\omega = 2\pi \cdot 10kHz$, with a radius of $b = 6.5\,cm$. These are typical material parameters, excitations, and dimensions in the hardening context. The first graph shows the spatial current density in the plane $z = 0$, the second graph shows the current density on the surface along a longitude.

---

[1] http://www.mathworks.com/

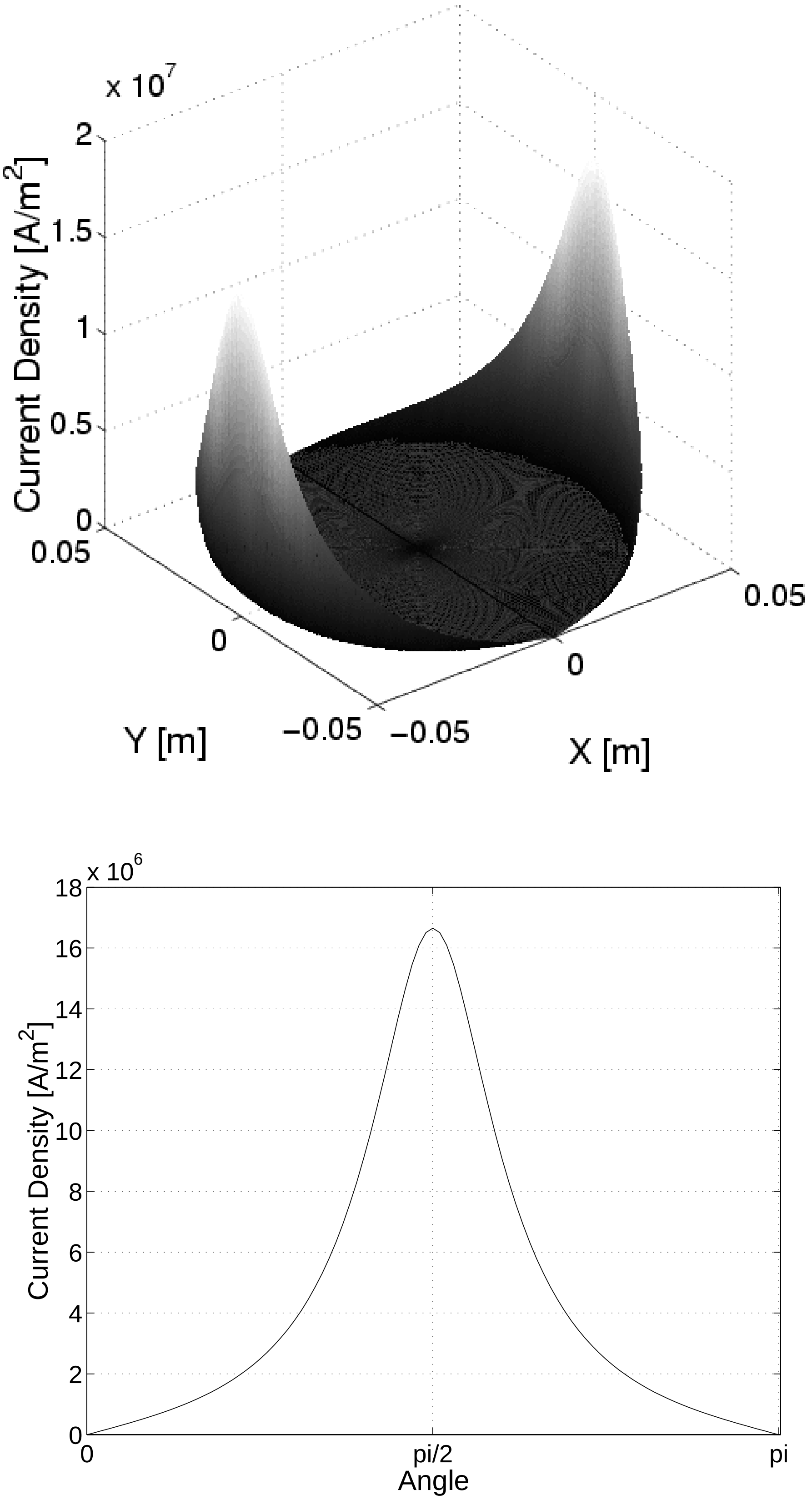

Figure 6.2: Eddy current in a sphere

Verification: Asymptotic for the Vacuum $\sigma \to 0,\ \mu_r = 1$.

In order to check the result, the vacuum-limit $\sigma \to 0,\ \mu_r = 1$ can be calculated. It follows from (6.14) that

$$\begin{aligned} x \cdot \frac{J_{2n+\frac{1}{2}}(x)}{J_{2n+\frac{3}{2}}(x)} \quad &\to \quad x \cdot \frac{\left(\frac{x}{2}\right)^{2n+\frac{1}{2}} \cdot \frac{1}{\Gamma(2n+\frac{1}{2}+1)}}{\left(\frac{x}{2}\right)^{2n+\frac{3}{2}} \cdot \frac{1}{\Gamma(2n+\frac{3}{2}+1)}} \quad = \quad 2 \cdot \frac{\Gamma(2n+\frac{3}{2}+1)}{\Gamma(2n+\frac{1}{2}+1)} \\ &= \quad 2 \cdot \frac{(2n+\frac{1}{2}+1) \cdot \Gamma(2n+\frac{1}{2}+1)}{\Gamma(2n+\frac{1}{2}+1)} \quad = \quad 4n+3\,, \end{aligned}$$

so $A_n^O = 0$. If this is inserted into equation (6.28), it remains

$$\begin{aligned} A_\phi^I(r,\theta) \quad &= \quad \sum_{n=0}^{\infty} \frac{-A_{\phi n}^C \cdot a^{2n+\frac{3}{2}}}{J_{2n+\frac{3}{2}}(ia\sqrt{ik})} \cdot r^{-\frac{1}{2}} \cdot J_{2n+\frac{3}{2}}(ir\sqrt{ik}) \cdot P_{2n+1}^1(u)\,, \\ \frac{J_{2n+\frac{3}{2}}(ir\sqrt{ik})}{J_{2n+\frac{3}{2}}(ia\sqrt{ik})} \quad &\to \quad \frac{\left(\frac{ir\sqrt{ik}}{2}\right)^{2n+\frac{3}{2}} \cdot \frac{1}{\Gamma(2n+\frac{3}{2}+1)}}{\left(\frac{ia\sqrt{ik}}{2}\right)^{2n+\frac{3}{2}} \cdot \frac{1}{\Gamma(2n+\frac{3}{2}+1)}} \quad = \quad \frac{r^{2n+\frac{3}{2}}}{a^{2n+\frac{3}{2}}}\,, \\ \Rightarrow \quad A_\phi^I(r,\theta) \quad &= \quad \sum_{n=0}^{\infty} -A_{\phi n}^C \cdot r^{2n+1} \cdot P_{2n+1}^1(u)\,. \end{aligned}$$

This means that the vector potential derived from the limit $\sigma \to 0$ and $\mu_r = 1$ is the same as the vacuum solution (6.9)!

Special Case: $\sigma = \infty$.

The calculation is started at equation (6.15). Using the rule [AI70, 9.2.1] for $|z| \to \infty$

$$J_\nu(z) = \sqrt{\frac{2}{\pi z}} \left(\cos\left(z - \frac{1}{2}\nu\pi - \frac{1}{4}\pi\right) + e^{|\Im z|} O(|z|^{-1}) \right) \qquad |\text{arg } z| < \pi$$

with the imaginary part $\Im z$ of z, and arg $z =$ arg $x + iy = \arctan \frac{y}{x}$, leads to

$$A_\phi^I(r,\theta) \quad = \quad \sum_{n=1}^{\infty} B_n^I \cdot r^{-\frac{1}{2}} \cdot \sqrt{\frac{2}{\pi i r\sqrt{ik}}} \cos\left(ir\sqrt{ik} - \frac{1}{2}(n+\frac{1}{2})\pi - \frac{1}{4}\pi\right) \cdot P_n^1(u)\,.$$

This means that $B_n^I = 0$ if the vector potential should remain finite for $k \to \infty$. The jump condition (6.21) is no longer valid because there is a surface current flowing. So (6.20) alone fixes the coefficients A_n^O. Condition (6.24) implies

$$\begin{aligned} A_n^O \quad &= \quad A_{\phi n}^C \cdot a^{4n+\frac{7}{2}}\,, \\ \Longrightarrow \quad A_\phi^O(r,\theta) \quad &= \quad \sum_{n=0}^{\infty} A_n^O \cdot r^{-2n-\frac{5}{2}} \cdot P_{2n+1}^1(u) - A_{\phi n}^C \cdot r^{2n+1} \cdot P_{2n+1}^1(u) \\ &= \quad \sum_{n=0}^{\infty} A_{\phi n}^C \cdot P_{2n+1}^1(u) \left(a^{4n+\frac{7}{2}} \cdot r^{-2n-\frac{5}{2}} - r^{2n+1} \right)\,. \end{aligned}$$

The surface current follows from the right side of (6.25) with the aid of $[\mathbf{n} \times \mathbf{H}] = \mathbf{k}$

$$\begin{aligned}
\mathbf{k}(\theta) &= \\
&= \frac{1}{\mu_0 a}\sum_{n=0}^{\infty}\left(A_n^O a^{-2n-2} - A_{\phi n}^C a^{2n+1} + A_n^O(-2n-2)a^{-2n-2} - A_{\phi n}^C(2n+1)a^{2n+1}\right) P_{2n+1}^1(u)\,\mathbf{e}_\phi \\
&= \frac{1}{\mu_0 \cdot a}\sum_{n=0}^{\infty}\left(A_n^O \cdot (-2n-1)a^{-2n-2} - A_{\phi n}^C(2n+2)a^{2n+1}\right) P_{2n+1}^1(u) \cdot \mathbf{e}_\phi \\
&= \frac{1}{\mu_0 \cdot a}\sum_{n=0}^{\infty}\left(A_{\phi n}^C \cdot (-2n-1)a^{2n+1} - A_{\phi n}^C(2n+2)a^{2n+1}\right) P_{2n+1}^1(u) \cdot \mathbf{e}_\phi \\
&= \frac{-1}{\mu_0 \cdot a}\sum_{n=0}^{\infty}\left(A_{\phi n}^C \cdot (4n+3) \cdot a^{2n+1}\right) P_{2n+1}^1(u) \cdot \mathbf{e}_\phi\,. \qquad (6.35)
\end{aligned}$$

The surface current was calculated in the same way as before in the case of a finite conductivity, by adding the terms of the sum until a certain precision was reached. Figure 6.3 shows the surface current $\|\mathbf{k}\|$ of the perfect conducting sphere along a longitude. Dimensions and excitation remained unchanged from the last example of a non-perfect conducting sphere: Radius $a = 5\,cm$, exciting current $I = 1\,kA$, loop radius $b = 6.5\,cm$, and $\omega = 2\pi \cdot 10kHz$. Now, material parameters and frequency have no influence on the solution.

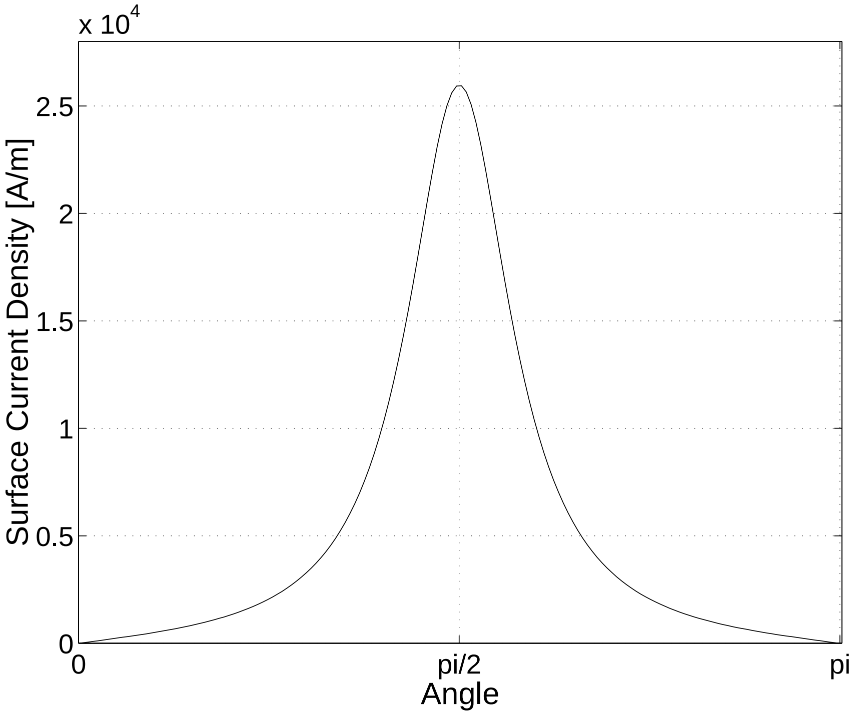

Figure 6.3: Perfect conducting sphere

6.1.2 Conducting Cylinder in the Alternating Field of a Current Loop

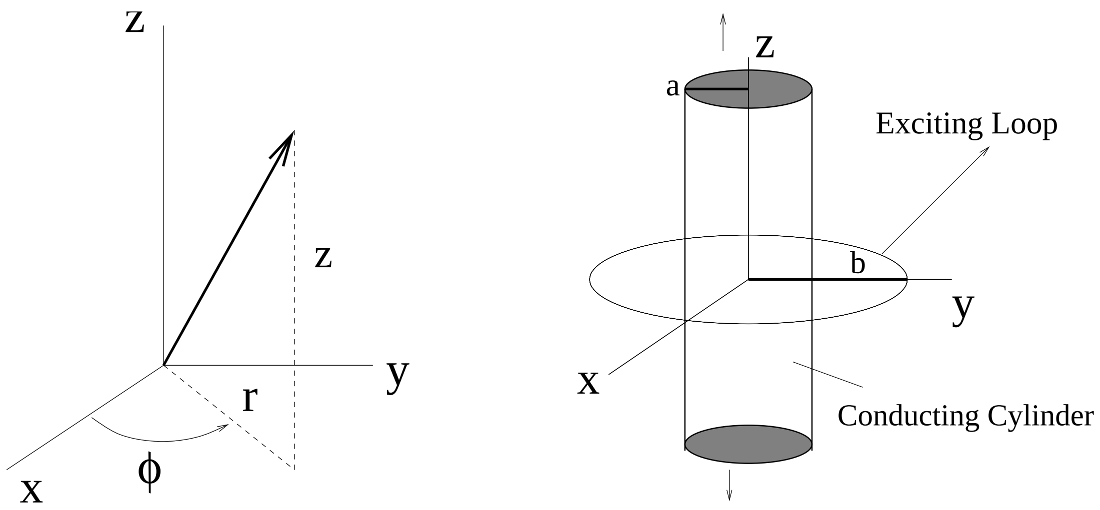

Figure 6.4: Setting cylinder

In this section, an analytical solution of the eddy current model is developed for a homogeneous, infinite long cylinder excited by a circular current loop. For axial symmetry all quantities can be considered independent of ϕ in cylindrical coordinates. If additionally $\mathbf{B}$ has no ϕ-component, then the vector potential $\mathbf{B} = \mathbf{curl}\,\mathbf{A}$ can be considered as

$$\mathbf{A} = A_\phi(r,z) \cdot e^{i\omega t} \cdot \mathbf{e}_\phi \,, \quad \text{with } A_\phi(r,z) \in \mathbb{C}\,. \tag{6.36}$$

In Coulomb gauge equation (3.32) can be transformed into ($k = \omega\sigma\mu$)

$$0 \;=\; \left[\frac{d^2 A_\phi}{dr^2} + \frac{1}{r}\frac{dA_\phi}{dr} - \frac{A_\phi}{r^2} + \frac{d^2 A_\phi}{dz^2} + ikA_\phi\right].$$

With the ansatz

$$A_\phi(r,z) = R(r) \cdot T(z), \quad \text{with } R(r),\, T(z) \in \mathbb{C}\,, \tag{6.37}$$

it follows

$$0 = \frac{1}{R}\frac{d^2R}{dr^2} + \frac{1}{R \cdot r}\frac{dR}{dr} + \frac{1}{T}\frac{d^2T}{dz^2} + ik - \frac{1}{r^2}\,. \tag{6.38}$$

By setting the terms involving r equal to p^2, $p \in \mathbb{R}$, and those involving z to $-p^2$, one finds

$$0 \;=\; \frac{d^2T(p,z)}{dz^2} + p^2 T(p,z)\,, \tag{6.39}$$

$$\text{Bessel diff. eqn.} \quad 0 \;=\; \frac{d^2R(p,r)}{dr^2} + \frac{1}{r}\frac{dR(p,r)}{dr} + \left(ik - p^2 - \frac{1}{r^2}\right) R(p,r)\,. \tag{6.40}$$

The solution of the system of equations (6.39), (6.40) is [FK98, p.90, 91], [AI70, 9.1.1]

$$T(p,z) \;=\; C_{1n}\, e^{ipz} \;+\; C_{2n}\, e^{-ipz}\,, \tag{6.41}$$

$$R(p,r) \;=\; C_{3n}\, J_1(r\sqrt{ik-p^2}) \;+\; C_{4n}\, J_{-1}(r\sqrt{ik-p^2}) \qquad k \neq 0 \tag{6.42}$$

$$R(p,r) \;=\; C_{5n}\, H_1^{(1)}(irp) \;+\; C_{6n}\, H_1^{(2)}(irp) \qquad k = 0, \tag{6.43}$$

with the coefficients $C_{1n} \dots C_{6n} \in \mathbb{C}$, with $p > 0$, and with the *Hankel functions* $H_1^{(1)}$ and $H_1^{(2)}$.

The infinite long and homogeneous cylinder lies in the coordinate system according to Figure 6.4. The loop in $z = 0$ causes $C_{1n} = C_{2n}$. As in Section 6.1.1, C_{4n} must vanish. Because of the behavior of the Hankel functions for $|z| \to \infty$ [AI70, 9.2]

$$\begin{aligned} H_\nu^{(1)}(z) &\sim \sqrt{\frac{2}{\pi z}}\, e^{i(z-\frac{1}{2}\nu\pi-\frac{1}{4}\pi)} \qquad (-\pi < \arg z < 2\pi) && (6.44)\\ H_\nu^{(2)}(z) &\sim \sqrt{\frac{2}{\pi z}}\, e^{-i(z-\frac{1}{2}\nu\pi-\frac{1}{4}\pi)} \qquad (-2\pi < \arg z < \pi)\,, && (6.45) \end{aligned}$$

it also holds $C_{6n} = 0$. For the vector potential, it remains

$$\begin{aligned} A_\phi^I(r,z) &= \int_0^\infty C^I(p)\cdot J_1(r\sqrt{ik-p^2})\cdot \cos(pz)\,dp \qquad r < a\,,\ C^I(p) \in \mathbb{C}\,, && (6.46)\\ A_\phi^O(r,z) &= \int_0^\infty C^O(p)\cdot H_1^{(1)}(irp)\cdot\cos(pz)\,dp + A_\phi^C(r,z) \quad r > a\,,\ C^O(p)\in\mathbb{C}\,. && (6.47) \end{aligned}$$

Here a is the radius of the cylinder. The vector potential of a circular current loop with the radius b and the exciting current I in spherical coordinates is [Jac75, p. 142]

$$A_\phi^C(r_s,\theta) = \frac{Ib\mu_0}{4\pi}\int_0^{2\pi} \frac{\cos\phi'\,d\phi'}{(b^2+r_s^2-2br_s\sin\theta\cos\phi')^{\frac{1}{2}}}\,.$$

Transformation in cylindrical coordinates with $r_s^2 = r^2 + z^2$ and $r = r_s\sin\theta$ yields

$$A_\phi^C(r,z) = \frac{Ib\mu_0}{4\pi}\int_0^{2\pi} \frac{\cos\phi'\,d\phi'}{(b^2+r^2+z^2-2br\cos\phi')^{\frac{1}{2}}}\,. \qquad (6.48)$$

With the aid of [BS89, p. 622, p.619] one finds

$$\begin{aligned} A_\phi^C(r,z) &= \frac{Ib\mu_0}{4\pi}\int_0^{2\pi}\left(\sqrt{\frac{2}{\pi}}\int_0^\infty \sqrt{\frac{2}{\pi}}K_0(p\sqrt{b^2+r^2-2br\cos\phi'})\cos(pz)dp\right)\cos\phi'\,d\phi'\\ &= \int_0^\infty\left(\frac{Ib\mu_0}{2\pi^2}\int_0^{2\pi}K_0(p\sqrt{b^2+r^2-2br\cos\phi'})\cos\phi'\,d\phi'\right)\cos(pz)dp\,, && (6.49) \end{aligned}$$

with the *modified Bessel function* K_0. The unknown coefficients C^I and C^O can be fixed by taking into account the jump conditions (6.20) and (6.21) on the surface of the cylinder $(r = a)$

$$\begin{aligned} A_\phi^I(a,z) &= A_\phi^O(a,z)\,, && (6.50)\\ \frac{1}{\mu_r}\frac{\partial}{\partial r}(r\,A_\phi^I(r,z))\bigg|_{r=a} &= \frac{\partial}{\partial r}(r\,A_\phi^O(r,z))\bigg|_{r=a}\,,\\ \Leftrightarrow\quad \frac{1}{\mu_r}\left(A_\phi^I(a,z) + a\frac{\partial A_\phi^I(r,z)}{\partial r}\bigg|_{r=a}\right) &= \left(A_\phi^O(a,z) + a\frac{\partial A_\phi^O(r,z)}{\partial r}\bigg|_{r=a}\right)\,. && (6.51) \end{aligned}$$

The z-dependent part can now be separated. Using the relations [AI70, 9.6.27] and [AI70, 9.1.27]

$$\begin{aligned}
\frac{dK_0(x)}{dx} &= -K_1(x)\,, \\
\frac{dH_1^{(1)}(x)}{dx} &= H_0^{(1)}(x) - \frac{1}{x}H_1^{(1)}(x)\,, \\
\frac{dJ_1(x)}{dx} &= J_0(x) - \frac{1}{x}J_1(x)\,,
\end{aligned}$$

in the jump conditions results in

$$C^I(p)\tilde{J}_1(p) = C^O(p)\tilde{H}_1(p) + \frac{Ib\mu_0}{2\pi^2}\int_0^{2\pi} \tilde{K}_0(p,\phi')\cos\phi'\,d\phi'\,, \tag{6.52}$$

$$\begin{aligned}
&\frac{C^I(p)}{\mu_r}\left(\tilde{J}_1(p) + a\left[\tilde{J}_0(p) - \frac{1}{a\sqrt{ik-p^2}}\tilde{J}_1(p)\right]\sqrt{ik-p^2}\right) = \\
&\qquad C^O(p)\left(\tilde{H}_1(p) + a\left[\tilde{H}_0(p) - \frac{1}{iap}\tilde{H}_1(p)\right]ip\right) + \frac{Ib\mu_0}{2\pi^2}\int_0^{2\pi}\left[\tilde{K}_0(p,\phi')\cos\phi'\right. \\
&\qquad\qquad \left. -a\tilde{K}_1(p,\phi')\cos\phi'\frac{p\cdot(a-b\cos\phi')}{\sqrt{b^2+a^2-2ba\cos\phi'}}\,d\phi'\right]\,,
\end{aligned} \tag{6.53}$$

with

$$\begin{aligned}
\tilde{K}_0(p,\phi') &= K_0(p\sqrt{b^2+a^2-2ba\cos\phi'})\,, \qquad \tilde{K}_1(p,\phi') = K_1(p\sqrt{b^2+a^2-2ba\cos\phi'})\,, \\
\tilde{J}_0(p) &= J_0(a\sqrt{ik-p^2})\,, \qquad \tilde{J}_1(p) = J_1(a\sqrt{ik-p^2})\,, \\
\tilde{H}_0(p) &= H_0(iap)\,, \qquad \tilde{H}_1(p) = H_1(iap)\,.
\end{aligned}$$

The two equations (6.52) and (6.53) can be transformed into

$$C^I(p)\tilde{J}_1(p) = C^O(p)\tilde{H}_1(p) + R_0(p)\,, \tag{6.54}$$

$$\frac{a\sqrt{ik-p^2}\,C^I(p)}{\mu_r}\tilde{J}_0(p) = iap\,C^O(p)\,\tilde{H}_0(p) + R_0(p) - a\,R_1(p)\,, \tag{6.55}$$

with

$$\begin{aligned}
R_0(p) &= \frac{Ib\mu_0}{2\pi^2}\int_0^{2\pi}\tilde{K}_0(p,\phi')\cos\phi'\,d\phi'\,, \\
R_1(p) &= \frac{Ib\mu_0}{2\pi^2}\int_0^{2\pi}\tilde{K}_1(p,\phi')\cos\phi'\frac{p(a-b\cos\phi')}{\sqrt{b^2+a^2-2ba\cos\phi'}}\,d\phi'\,.
\end{aligned}$$

It follows

$$C^I(p) = \frac{1}{\tilde{J}_1(p)}\left(C^O(p)\tilde{H}_1(p) + R_0(p)\right)\,, \tag{6.56}$$

$$a\sqrt{ik-p^2}\,C^I(p)\,\tilde{J}_0(p) = \mu_r(iap\,C^O(p)\,\tilde{H}_0(p) + R_0(p) - a\,R_1(p))\,. \tag{6.57}$$

Equation (6.57) is equivalent to

$$a\sqrt{ik-p^2}\,\frac{\tilde{J}_0(p)}{\tilde{J}_1(p)}\,(C^O(p)\tilde{H}_1(p)+R_0(p)) \quad = \quad \mu_r(iap\,C^O(p)\,\tilde{H}_0(p)+R_0(p)-a\,R_1(p))$$

$$\Longleftrightarrow$$

$$(a\sqrt{ik-p^2}\,\frac{\tilde{J}_0(p)}{\tilde{J}_1(p)}\,\tilde{H}_1(p)-\mu_r iap\,\tilde{H}_0(p))\,C^O(p) \quad = \quad \mu_r R_0(p)-\mu_r\,a\,R_1(p)-a\sqrt{ik-p^2}\,\frac{\tilde{J}_0(p)}{\tilde{J}_1(p)}\,R_0(p)$$

$$\Longleftrightarrow$$

$$C^O(p) \quad = \quad \frac{\tilde{J}_1(p)\mu_r(R_0(p)-aR_1(p))-a\sqrt{ik-p^2}\,\tilde{J}_0(p)\,R_0(p)}{a\sqrt{ik-p^2}\,\tilde{J}_0(p)\,\tilde{H}_1(p)-\tilde{J}_1(p)\mu_r iap\,\tilde{H}_0(p)}\,.$$

Finally it remains

$$A^I_\phi(r,z) = \int_0^\infty C^I(p)\cdot J_1(r\sqrt{ik-p^2})\cdot\cos(pz)\,dp \qquad r<a\,, \tag{6.58}$$

$$A^O_\phi(r,z) = \int_0^\infty C^O(p)\cdot H_1^{(1)}(irp)\cdot\cos(pz)\,dp\,+\,A^C_\phi(r,z) \qquad r>a\,, \tag{6.59}$$

$$C^O(p) = \frac{J_1(a\sqrt{ik-p^2})\mu_r(R_0(p)-aR_1(p))-a\sqrt{ik-p^2}\,J_0(a\sqrt{ik-p^2})\,R_0(p)}{a\sqrt{ik-p^2}\,J_0(a\sqrt{ik-p^2})\,H_1^{(1)}(iap)-J_1(a\sqrt{ik-p^2})\,\mu_r iap\,H_0^{(1)}(iap)}, \tag{6.60}$$

$$C^I(p) = \frac{1}{J_1(a\sqrt{ik-p^2})}\,(C^O(p)H_1^{(1)}(iap)+R_0(p))\,, \tag{6.61}$$

$$R_0(p) = \frac{Ib\mu_0}{2\pi^2}\int_0^{2\pi}K_0(p\sqrt{b^2+a^2-2ba\cos\phi'})\cos\phi'\,d\phi'\,, \tag{6.62}$$

$$R_1(p) = \frac{Ib\mu_0}{2\pi^2}\int_0^{2\pi}K_1(p\sqrt{b^2+a^2-2ba\cos\phi'})\cos\phi'\frac{p(a-b\cos\phi')}{\sqrt{b^2+a^2-2ba\cos\phi'}}\,d\phi'\,, \tag{6.63}$$

$$A^C_\phi(r,z) = \frac{Ib\mu_0}{4\pi}\int_0^{2\pi}\frac{\cos\phi'\,d\phi'}{(b^2+r^2+z^2-2br\cos\phi')^{\frac{1}{2}}}\,, \tag{6.64}$$

$$k = \omega\sigma\mu \quad = \quad \omega\sigma\mu_r\mu_0\,. \tag{6.65}$$

The potential was again calculated numerically with the aid of the program package MATLAB[2]. Therefore, a mesh of the cylinder was built in the two dimensions r and z, consisting of equidistant grid points (r_m, z_n) (the infinite long cylinder was cut). Similar to the sphere, the potential

---

[2] http://www.mathworks.com/

$A_\phi^I(r,z)$ was calculated adaptively at each of these points: One defines

$$A_\phi^{I,x}(r_m, z_n) := \int_0^x C^I(p) \cdot J_1(r_m\sqrt{ik - p^2}) \cdot \cos(pz_n)\, dp$$

and increases x as long as a certain precision is reached. Figure 6.5 shows the result for a cylinder with the radius $a = 2\,cm$, the conductivity $\sigma = 2 \cdot 10^6\,(\Omega m)^{-1}$, and a relative magnetic permeability of $\mu_r = 10$. It is excited by a loop current of $I = 1\,kA$, $\omega = 2\pi \cdot 10kHz$, with a radius of $2.5\,cm$. The first graph shows the spatial current density in the plane $x = 0$, and the second graph shows the current density on the surface along the $z-$axis.

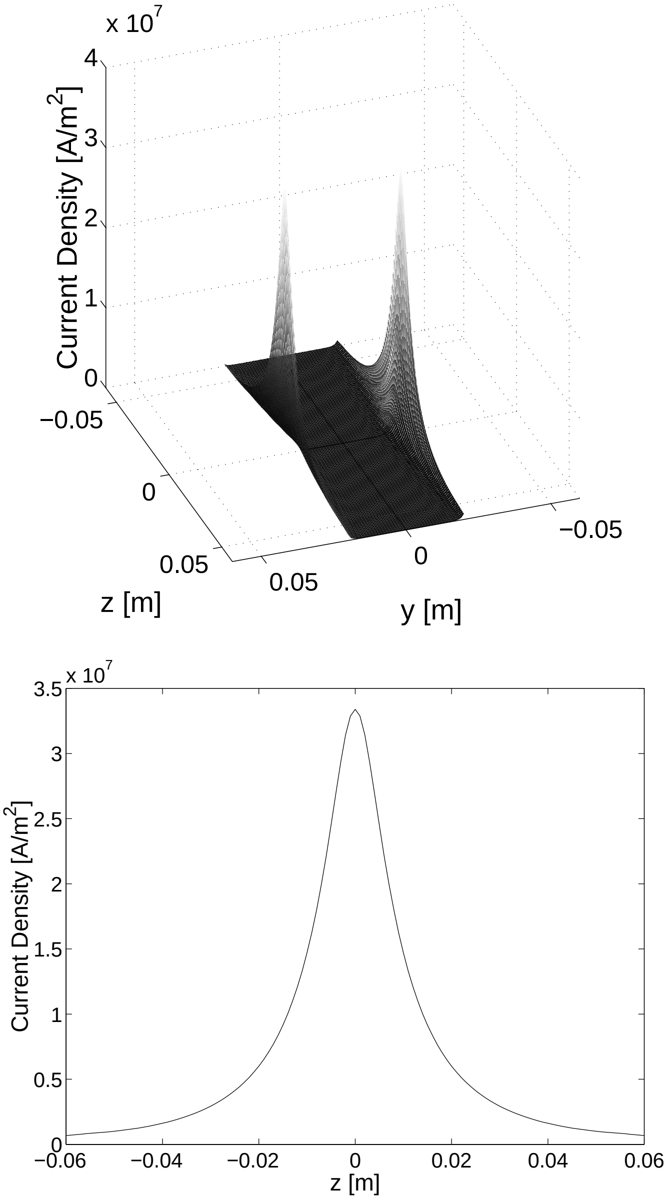

Figure 6.5: Eddy current in cylinder

6.2 Validation of the Magnetostatic Approach

The magnetostatic approach (3.116) is applied to the sphere of Figure 6.6. The mesh has 2880 surface faces. According to Section 3.3.3 this means that the system of equations has 2880 real valued unknowns due to the discretization by collocation with constant basis functions. The parameters of the setting are: The sphere radius $a = 5\,cm$, the exciting current $I = 1\,kA$, the loop radius $b = 6.5\,cm$, and $\omega = 2\pi \cdot 10kHz$.

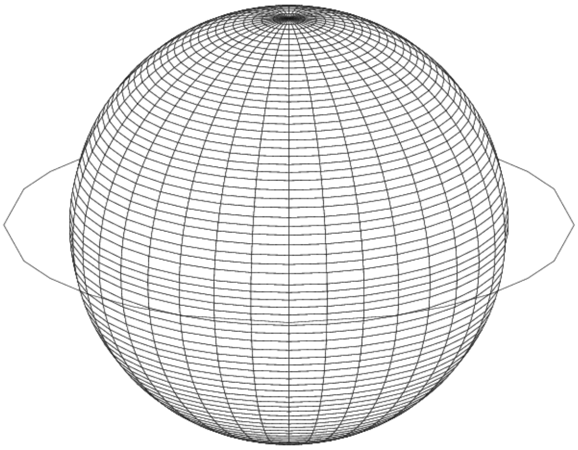

Figure 6.6: Mesh sphere

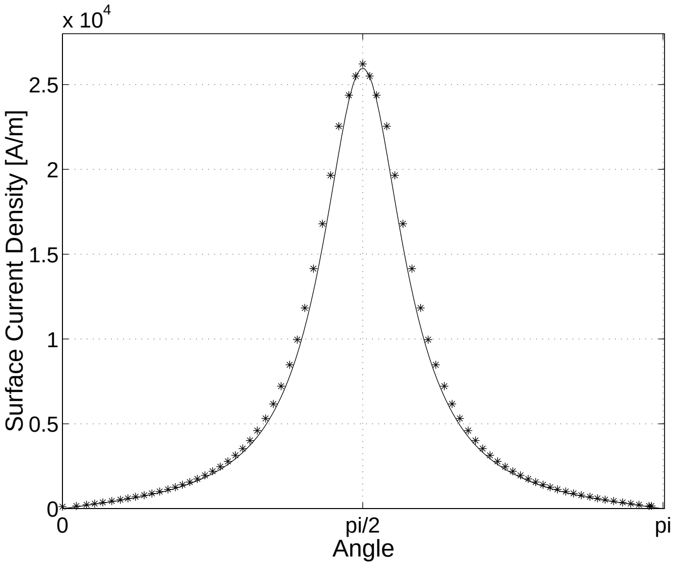

Figure 6.7: Comparison analytical solution / magnetostatic approach

Figure 6.7 shows the surface current density on a perfect conducting sphere along a longitude. The analytical solution of equation (6.35) is drawn as a solid line (-). The dotted curve (*) is the numerical solution of the magnetostatic approach (3.116). The calculated surface current in the numerical computations is very close to the analytical solution of the perfect conducting sphere. The curve remains the same for all μ_r, σ, and ω, because the material parameters are not involved in the calculations of the surface current. Of course, steel is not a perfect conductor, but what is interesting in the simulation of inductive heating is the spatial current. This is done in the postprocessing step of equation (3.122), and here the material parameters come into play. Nevertheless, the magnetostatic approach is only a crude method. However, it also has advantages compared with the two other approaches: The number of unknowns is much smaller and it is much easier to implement.

6.3 Validation of the Impedance Model

6.3.1 The Current Density at the Surface in the Impedance Model

The calculation of the current density of the surface can be carried out in two different ways in the BEM part of the impedance model. If $\mathbf{E}_S, \boldsymbol{\lambda}_S$ are the solutions of (3.102)-(3.103) then the current density can be computed by $\mathbf{j}_\mathbf{E} := \sigma \mathbf{E}_S$. The second possibility is to use the impedance condition $\gamma_D \mathbf{E} = \eta \boldsymbol{\lambda}$ of equation (3.100) and calculate the current density by $\mathbf{j}_{\boldsymbol{\lambda}} := \sigma \eta \boldsymbol{\lambda}_S$. The two current densities are different. This can be seen in Figure 6.8, where these items are presented for the same cylinder that was also used in the numerical experiment of Section 6.3.3. The Figure shows the current densities at the surface along the z-axis,with $\|\mathbf{j}_{\boldsymbol{\lambda}}\|$ depicted by (+), $\|\mathbf{j}_\mathbf{E}\|$ depicted by (- -), their average value $0.5 \cdot \|\mathbf{j}_\mathbf{E} + \mathbf{j}_{\boldsymbol{\lambda}}\|$ depicted by (*), and the analytical solution depicted by (-). For definition of the axes see Figure 6.4.

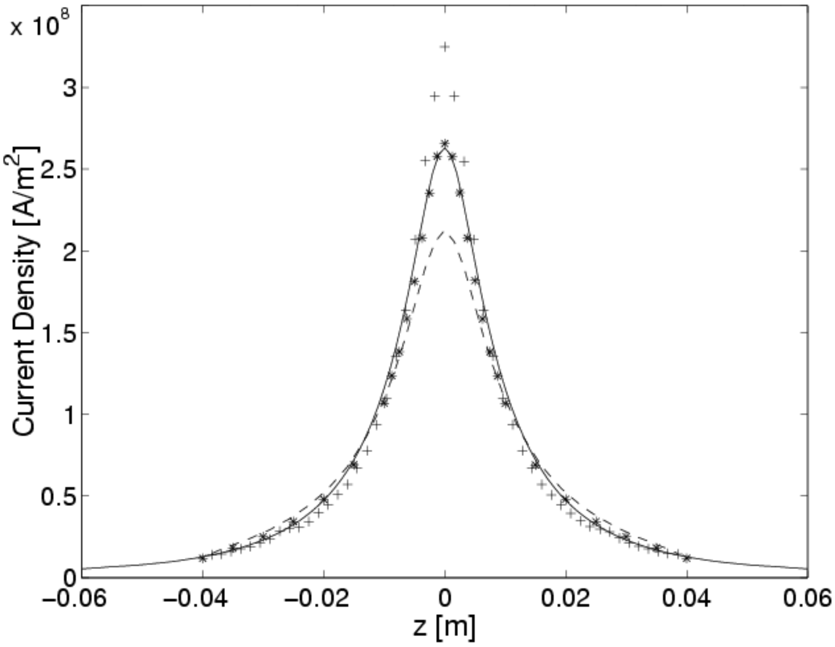

Figure 6.8: Different current densities at the surface of the cylinder of Section 6.3.3

So the average value seems to be the best way for the calculation of the current density, and in the following this method is used for the computation of the current density at the surface in the BEM part of the impedance model. The two different currents $\mathbf{j}_{\mathbf{E}}, \mathbf{j}_{\boldsymbol{\lambda}}$ were examined for decreasing meshwidths and their difference remained approximately the same. In theory there is no proof available that the difference vanishes for decreasing meshwidths.

As the right hand side of the FEM part of equation (3.104) one needs

$$\left[\frac{1}{\mu}\,\mathbf{curl}\,\mathbf{E}\times\mathbf{n}\right]_{BEM}$$

from the BEM part. This is also computed by using an average value according to

$$\left[\frac{1}{\mu}\,\mathbf{curl}\,\mathbf{E}\times\mathbf{n}\right]_{BEM} := 0.5\cdot\left(\boldsymbol{\lambda}_S + \frac{1}{\eta}\mathbf{E}_S\right)\,,$$

where $\mathbf{E}_S$ is used at the center of gravity of each face.

6.3.2 Sphere

The evaluated numerical results of the impedance model of (3.102)-(3.104) and the analytical solution of (6.28)-(6.34) are compared in Figure 6.10. As before the same sphere is used, with: The sphere radius $a = 5\,cm$, the exciting current $I = 1\,kA$, the loop radius $b = 6.5\,cm$, and $\omega = 2\pi\cdot 10kHz$. The mesh that is used is shown in Figure 6.9. It has 2214 faces, 3321 edges, and 1109 nodes at the surface, thus a system of equations with 4430 complex unknowns has to be solved for the BEM part.

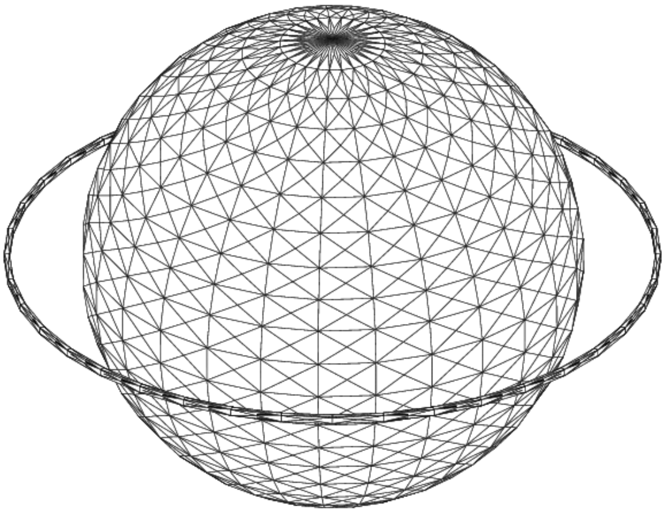

Figure 6.9: Mesh sphere

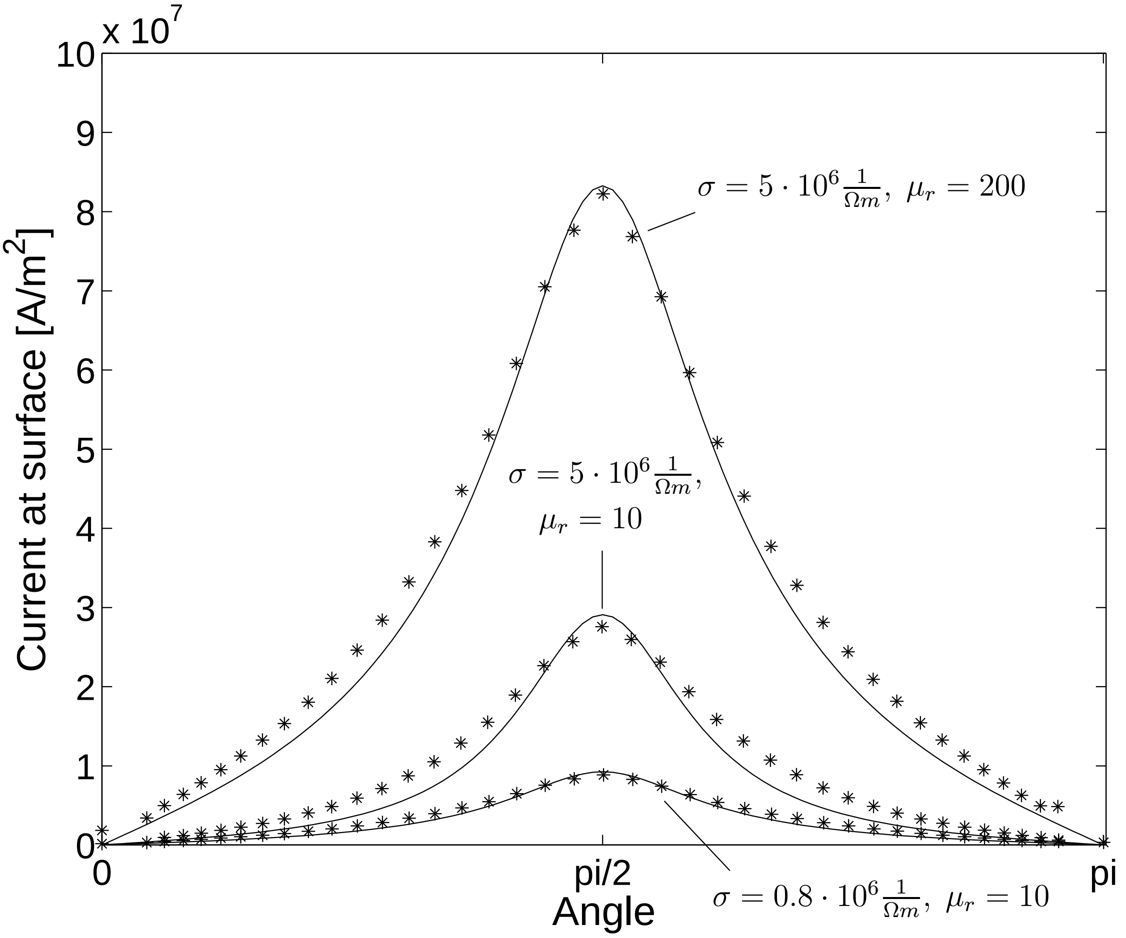

Figure 6.10: Comparison analytical solution / impedance model

The (average) current density at the surface calculated by the BEM part (3.102)-(3.103) of the impedance model (depicted by *) is in good agreement with the analytical solution (depicted by -) of the quasi-static approximation for a wide range of material parameters. A big advantage of the approach is that it has no problems coping with very small penetration depths. The penetration depth is $\delta = 0.16\,mm$ for the combination $\sigma = 5.0 \cdot 10^6 \frac{1}{\Omega m}$, $\mu_r = 200$, and a frequency of $10\,kHz$. This is a typical value at the beginning of the hardening process, when the temperature is low and the conductivity is high. Note that the triangles of the mesh are much bigger than $0.16\,mm$, and that it is not necessary to compute with smaller triangles to get a good current at the surface.

6.3.3 Cylinder

A refined mesh is used in the case of the cylinder with a radius of $2\,cm$ and an exciting loop current with a radius of $2.5\,cm$. Figure 6.11 shows the setting and the refined mesh with 8272 faces, 12408 edges, and 4138 nodes at the surface, i.e. 16546 complex unknowns for the BEM part.

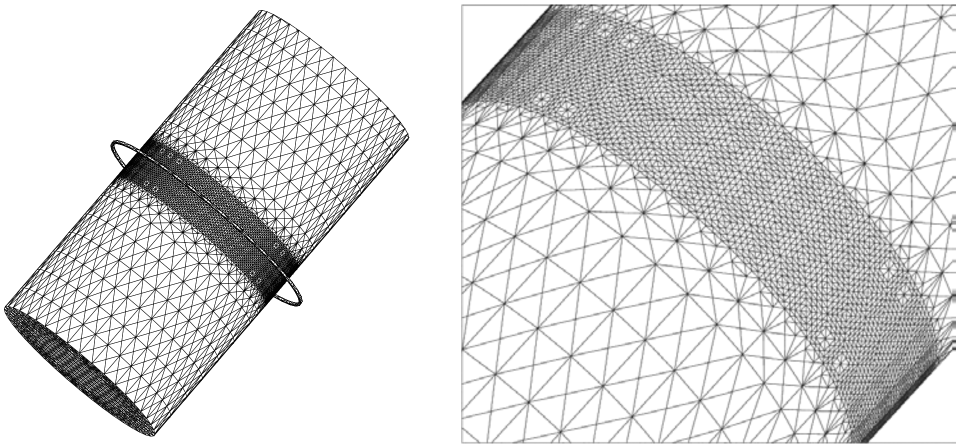

Figure 6.11: Refined mesh cylinder

The next Figure 6.12 shows the same mesh in the interior of the cylinder in the plane $z = 0$. For definition of the axes see Figure 6.4. The mesh has a total of 245538 edges, and the FEM part has the same number of complex unknowns.

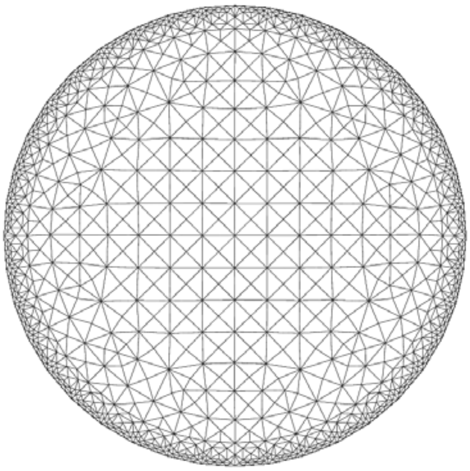

Figure 6.12: Interior mesh cylinder

The solution of the impedance approach of (3.102)-(3.104) and the analytical solution of (6.58)-(6.65) are compared in Figure 6.13. The exciting current is $I = 7875\,A$ and $\omega = 2\pi \cdot 10kHz$. The homogeneous material parameters are $\sigma = 2 \cdot 10^6\,(\Omega m)^{-1}$ and $\mu_r = 10$.

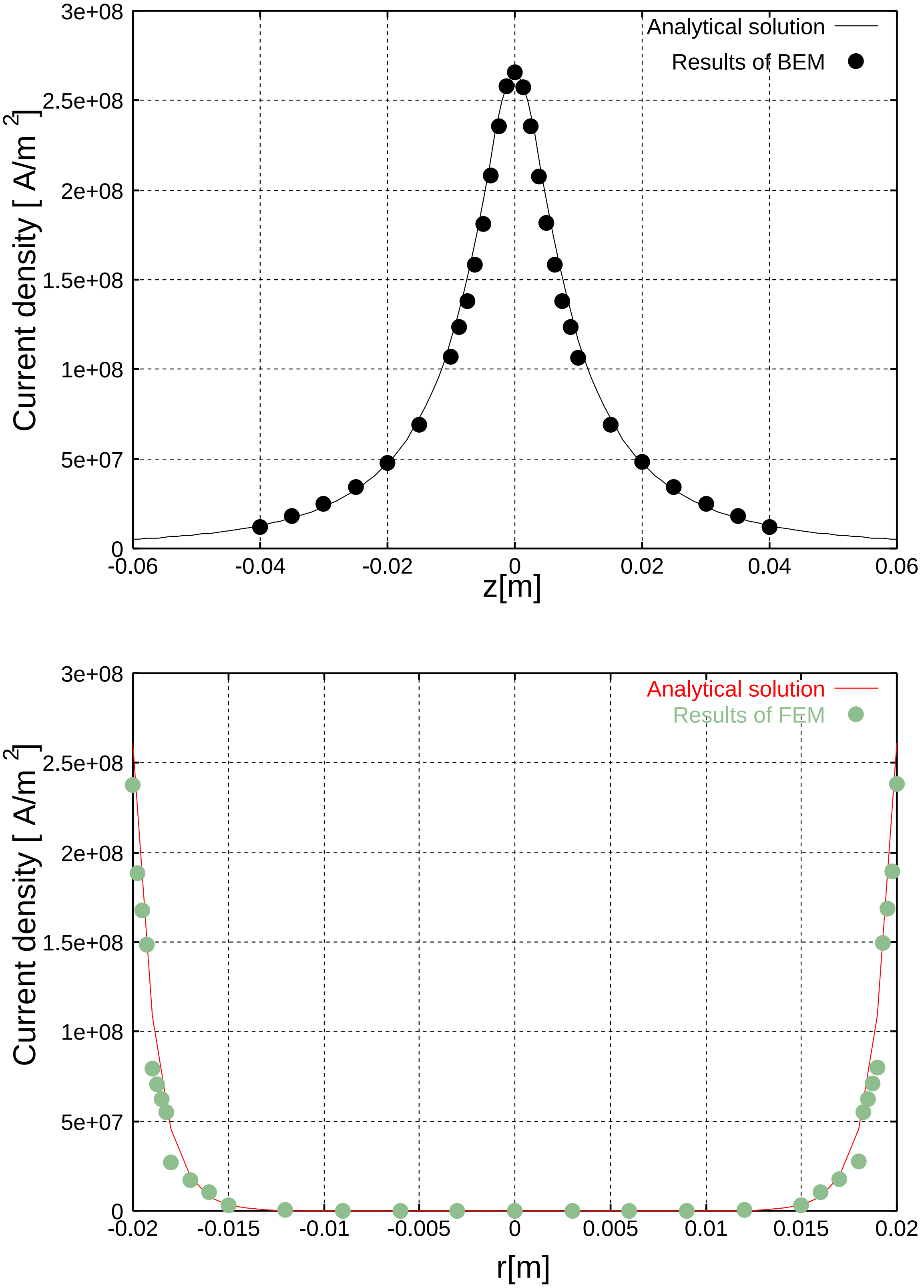

Figure 6.13: Comparison analytical solution / impedance approach

The first graph of Figure 6.13 presents the (average) current density on the surface along the $z-$axis, as computed by the BEM part of the equations (3.102)-(3.103). As already observed at the sphere, the solution of the impedance approach and the analytical solution agree very well.

The second graph in Figure 6.13 shows the current density in the interior of the cylinder along the line $x = z = 0$, as computed by the FEM part of equation (3.104). The numerical result has jumps because the edge elements are discontinuous in the normal direction at the interface of two tetrahedra. The penetration depth is $\delta = 1.1\,mm$ in this example. The mesh is graded in the interior, and the meshwidth decreases toward the surface in order to resolve the skin effect. The meshwidth is approximately $h = 0.5\,mm$ at the surface.

6.4 Validation of the Eddy Current Approach

The eddy current approach (3.98)-(3.99) is verified by comparison with the analytical solution (6.28)-(6.34) of the sphere. The sphere of Figure 6.9 is refined twice, and the result is the mesh of Figure 6.14 with a total of 144569 edges and 5348 surface nodes. So a system of equations with 149917 complex unknowns has to be solved for the eddy current approach. The right picture in Figure 6.14 shows the interior mesh in a plane at the equator. The mesh is constructed by rotation. This is the only reason why there are small elements in the center of the sphere.

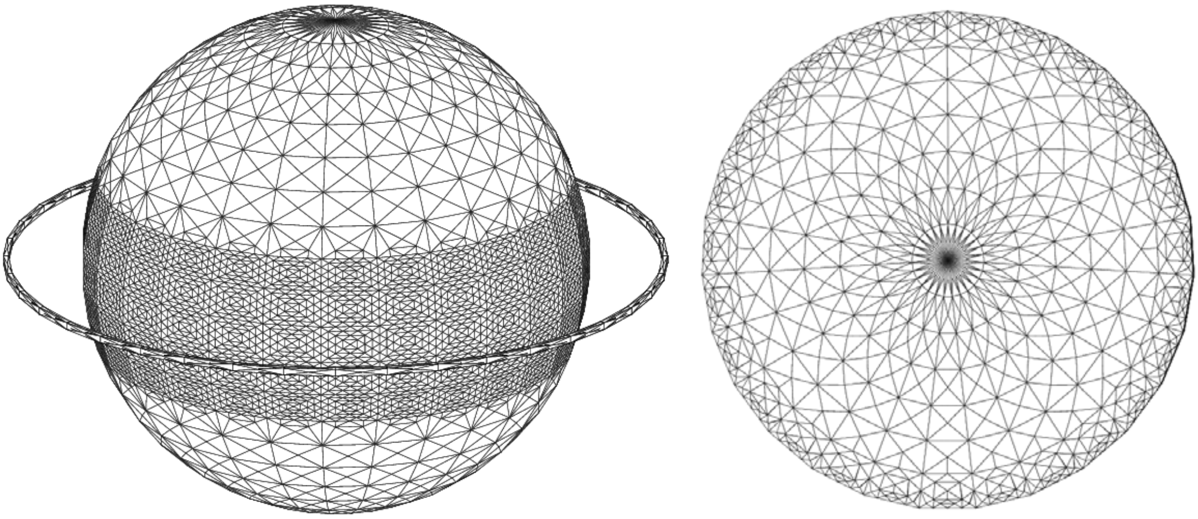

Figure 6.14: Refined mesh sphere

The solutions of the eddy current approach (depicted by *) and the analytical solutions (depicted by -) are compared in Figure 6.15 for different conductivities but a constant magnetic permeability of $\mu_r = 1.0$. The exciting current is $I = 1000\,A$ and $\omega = 2\pi \cdot 10kHz$. The figure shows the current at the surface, and numerical and analytical results agree well for these examples. The penetration depth varies between $\delta = 2.3\,mm$ and $\delta = 5.6\,mm$.

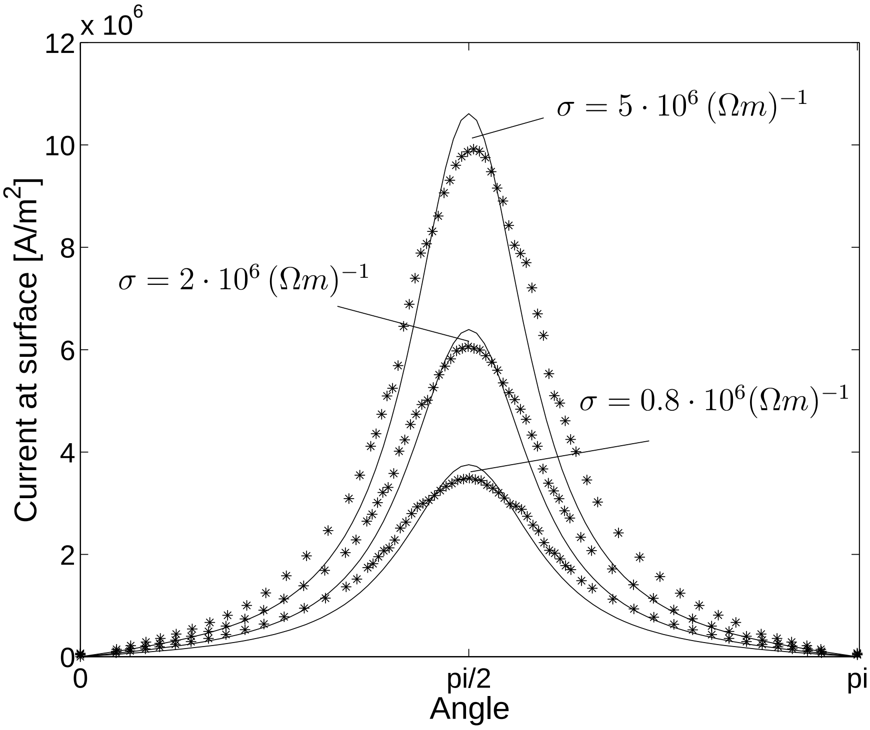

Figure 6.15: Comparison analytical solution / eddy current approach

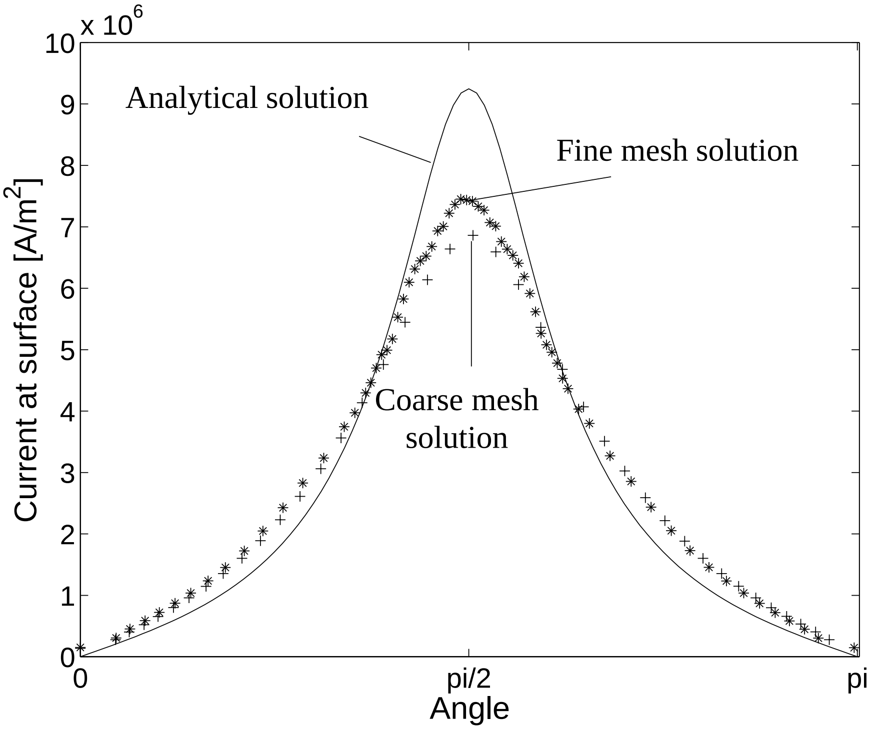

Figure 6.16: Solution for $\sigma = 0.8 \cdot 10^6\,(\Omega m)^{-1}$ and $\mu_r = 10.0$

Results are worse for smaller penetration depths. The penetration depth is $\delta = 1.7\,mm$ for a conductivity of $\sigma = 0.8 \cdot 10^6\,(\Omega m)^{-1}$ and $\mu_r = 10.0$. Figure 6.16 shows the result of the eddy current approach in this case. The numerical result and the analytical solution are not in good accordance for this example. It seems as if the mesh is too coarse. If this hypothesis was true for the fine mesh of Figure 6.14 then the results would be worse for the coarser mesh in Figure 6.9. To verify this, the eddy current approach was calculated on the coarser mesh of Figure 6.9 and the results did indeed get worse. As a conlusion it should be pointed out that the eddy current approach with the most convenient properties seems to have difficulties if the meshwidth is too big. This is not a surprise, but the consequence is that the impedance approach is prefered for the simulation of inductive hardening, because a wide range of material parameters with small penetration depths occur there.

6.5 Measurements of the Surface Temperature

Besides the theoretical possibilities for the validation of the program, there were also experiments made in order to check the correctness of the predicted temperatures. This was done by using a cylinder and an inductor with the shape of a torus. The mesh is shown in Figure 6.17. The cylinder was made of steel C45, it had a radius of $2cm$, and it was $10cm$ long. The torus was made of copper, it had an interior radius of $2.5cm$, an exterior radius of $3.5cm$, and its height was $1cm$. Three currents were used for the excitation: $10500A$, $7875A$, and $5250A$. The frequency was $10kHz$. In the first 0.2 seconds of the heating phase, only 50% of the exciting current is used, due to the power regulation of the heating machine. The maximum heating time was six seconds.

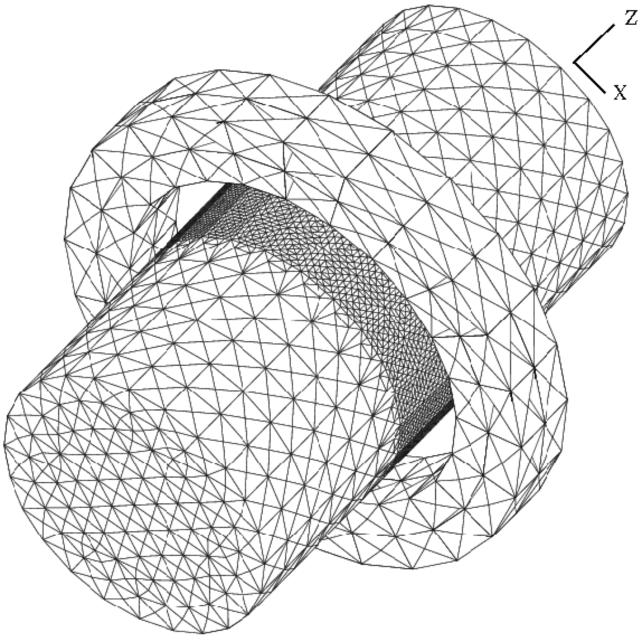

Figure 6.17: Setting experiment

The maximum surface temperature of the cylinder during the heating phase was measured with the aid of a thermographical camera. Of course, the maximum surface temperature is located at the center of the cylinder, close to the inductor. The next Figure 6.18 shows the measured maximum surface temperature in the experiment (depicted by a solid line) in comparison with the maximum surface temperature calculated by the magnetostatic approach (depicted by a dashed line and ’o’).

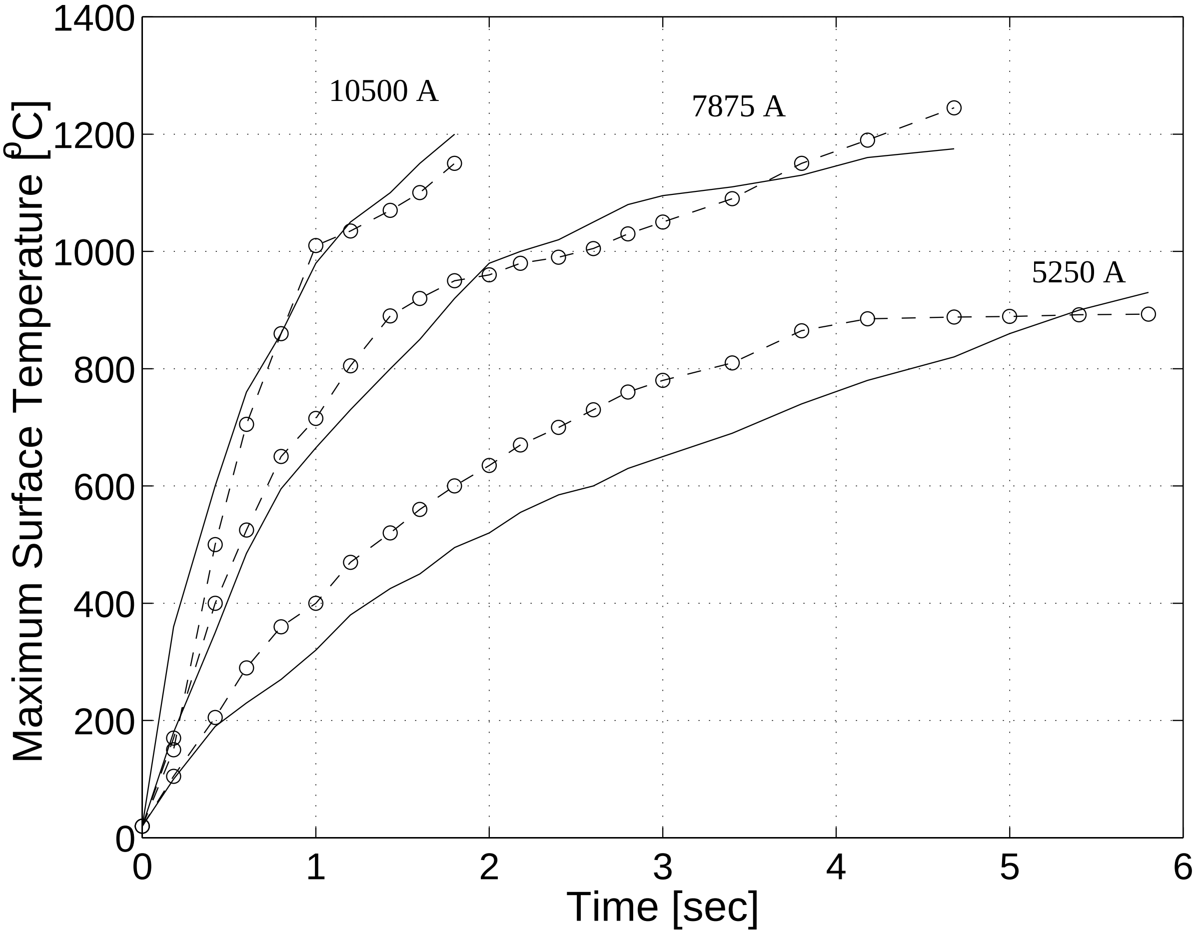

Figure 6.18: Surface temperature in the simulation with the magnetostatic approach and in the experiment

Although the magnetostatic approach gives only a crude approximation of the currents, the measured temperature can be reproduced very well. However, the cylinder is a ’flat’ geometry, and the problems expected for the magnetostatic approach occur at edges and corners. There, the impedance model gives a better approximation.

Unfortunately the results of the impedance model are worse, as can be seen in Figure 6.19. There, the surface temperature as predicted by the simulation (depicted by a dashed line and ’o’) are compared with the experimental data (depicted by a solid line) for the two exciting currents $10500A$ and $5250A$.

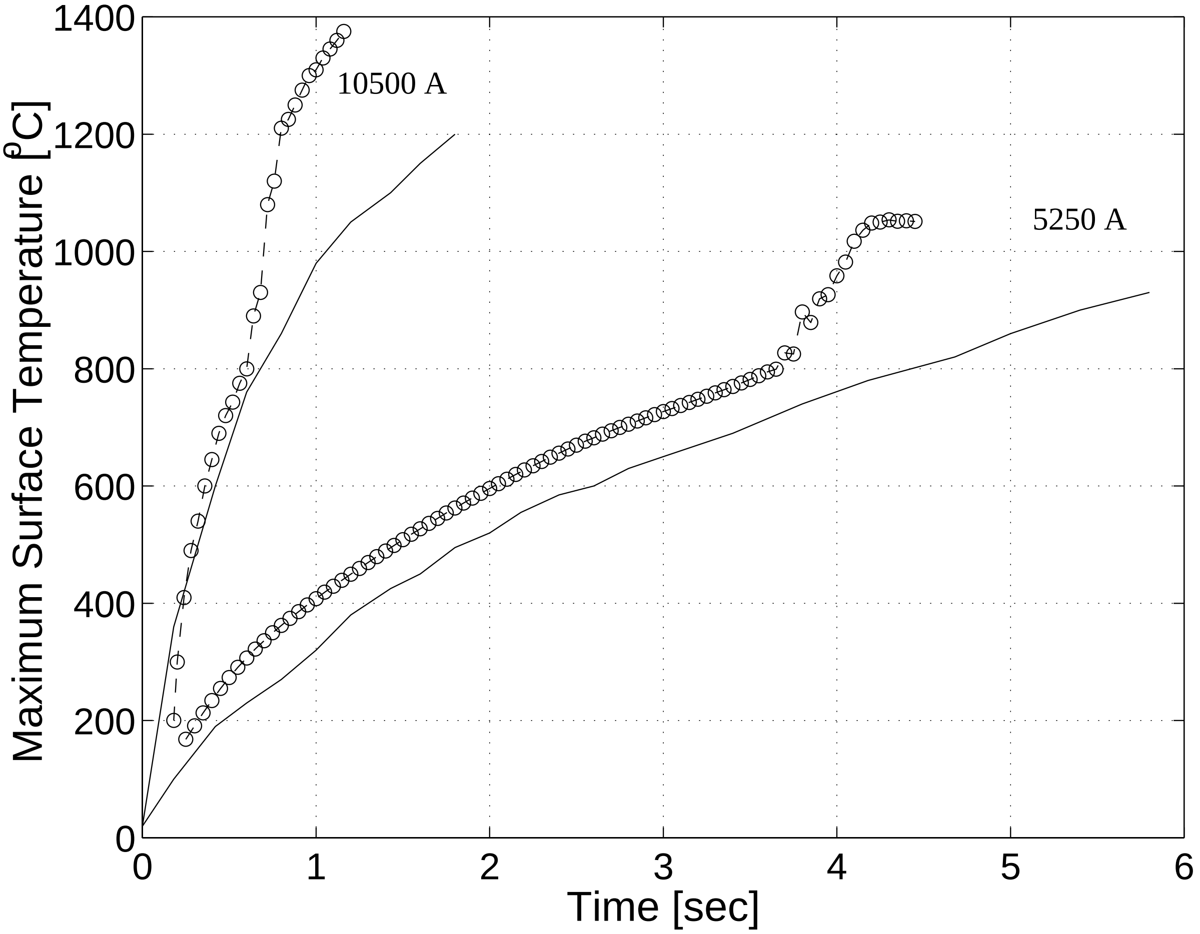

Figure 6.19: Surface temperature in the simulation with the impedance model and in the experiment

The behavior is the same for both exciting currents: The results are close to the measured data until the critical temperature of 800^oC is reached. Then the temperature at the surface increases rapidly in the simulation and big differences can be observed to the measured data. Approximately at 800^oC the phase transition takes place and all the material coefficients change their values dramatically. We do not know the exact reason for the instability of the simulation, but we made the same calculation for constant electric material parameters ($\mu_r = 10,\ \sigma = 2.0 \cdot 10^6\,(\Omega m)^{-1}$). Then the unstable behavior vanished. Thus it seems to be a problem of the electromagnetic calculations. This is a surprise because the electromagnetic calculations were checked carefully, as can be seen in the last sections.

In order to verify the BEM part at high temperatures, I made an additional test for typical material parameters at 1000^0C: The conductivity was supposed to be $\sigma = 0.8 \cdot 10^6\,(\Omega m)^{-1}$, and the permeability is one above the Curie-temperature. With these material parameters, the analytical solution (6.58)-(6.65) of the homogeneous cylinder excited by a loop current was again compared with the result of the impedance model (3.102)-(3.104) for an exciting current of $5250A$ and a frequency of $10kHz$. Figure 6.20 shows the curves. The same was done for typical material parameters at 500^oC in order to compare the current density at different temperatures. At 500^oC the following parameters are considered: $\mu_r = 10,\ \sigma = 2.0{\cdot}10^6\,(\Omega m)^{-1}$. The analytical solutions are depicted by solid lines and the results of the impedance model are depicted by *.

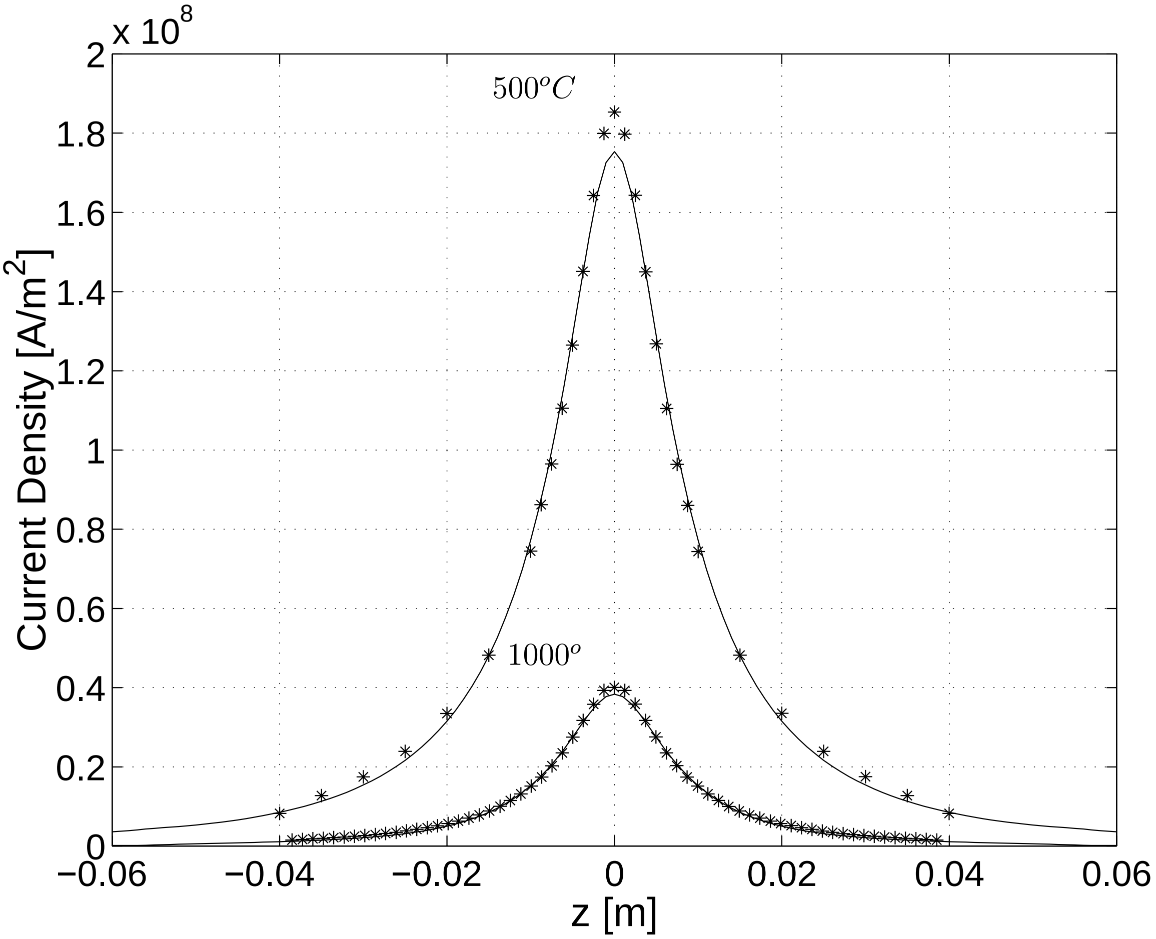

Figure 6.20: Comparison analytical solution / impedance approach for typical material parameters at 1000^oC and 500^oC

So the BEM part seems to work well at high temperatures and the current density is much smaller than for low temperatures. We believe the problem to be hidden in the FEM part. It may be caused by the heavily changing material parameters, especially the temperature and field dependent magnetic permeability. Due to the decrease of the magnetic field and due to the strong gradient of the temperature at the surface, the relative magnetic permeability increases from 1 to 1000 within a few milimeters, and it seems as if it is impossible to take this effect into account with our kind of meshes. However we do not exactly know if this is really the reason and unfortunately we were running out of time in the project, so we did not have the possibility to fix the problem.

Chapter 7

Results

The final goal of the simulation is the correct prediction of the hardened zone in the workpiece, i.e. the region with a temperature above 830^oC, see Section 2.1. Therefore, the cylinder of the experiment of the last Section 6.5 is used. The heating phase was interrupted after a certain time $\triangle t$, and the workpiece was quenched under a shower. It was cut in the plane $x = 0$ and then it was polished. The hardened zone, i.e. the martensite has other optical properties than the non-hardened zone, i.e. the ferrite-cementite mixture. Thus the hardened zone can be distinguished optically from the non-hardened zone after the polish.

Figure 7.1 compares the predicted hardened zone as computed by the magnetostatic approach (gray) with the real hardened zone of the workpiece, depicted by the black line in the pictures for the exciting current $7875A$, and a frequency of $10kHz$ after $\triangle t = 4s,\ 5s\ ,6s$. Figure 7.2 compares the same entities for an exciting current of $10500A$ and for $\triangle t = 1s,\ 1.5s\ ,2s$. The results agree very well in the beginning of the heating phase for both exciting currents, whereas there are some differences for longer heating times.

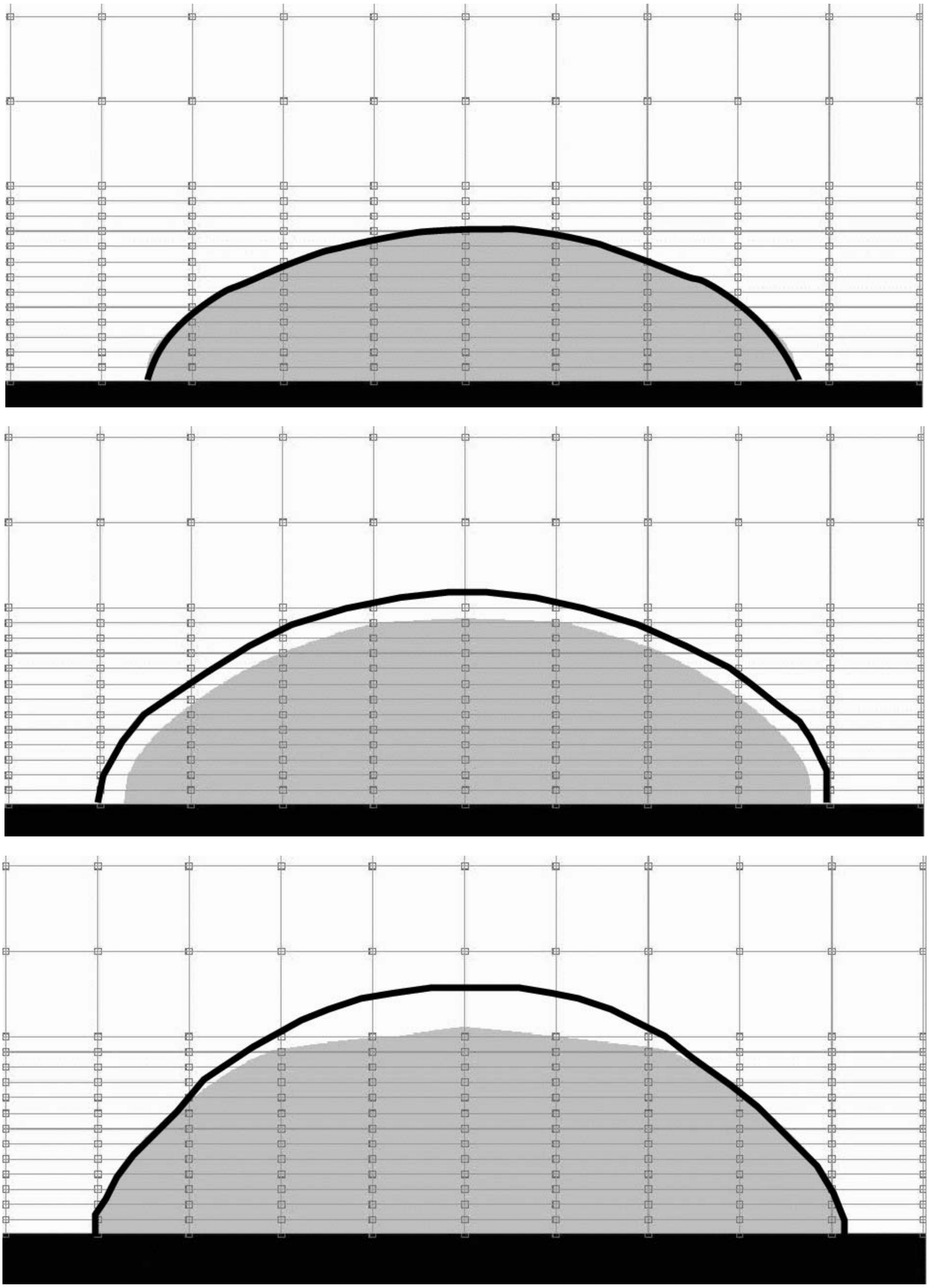

Figure 7.1: Hardened zone in the magnetostatic approach and in the experiment after $\triangle t = 4s,\ 5s\ ,6s$ for an exciting current of $7875A$. In reality the pictures are $11mm$ in height and their width is $25mm$.

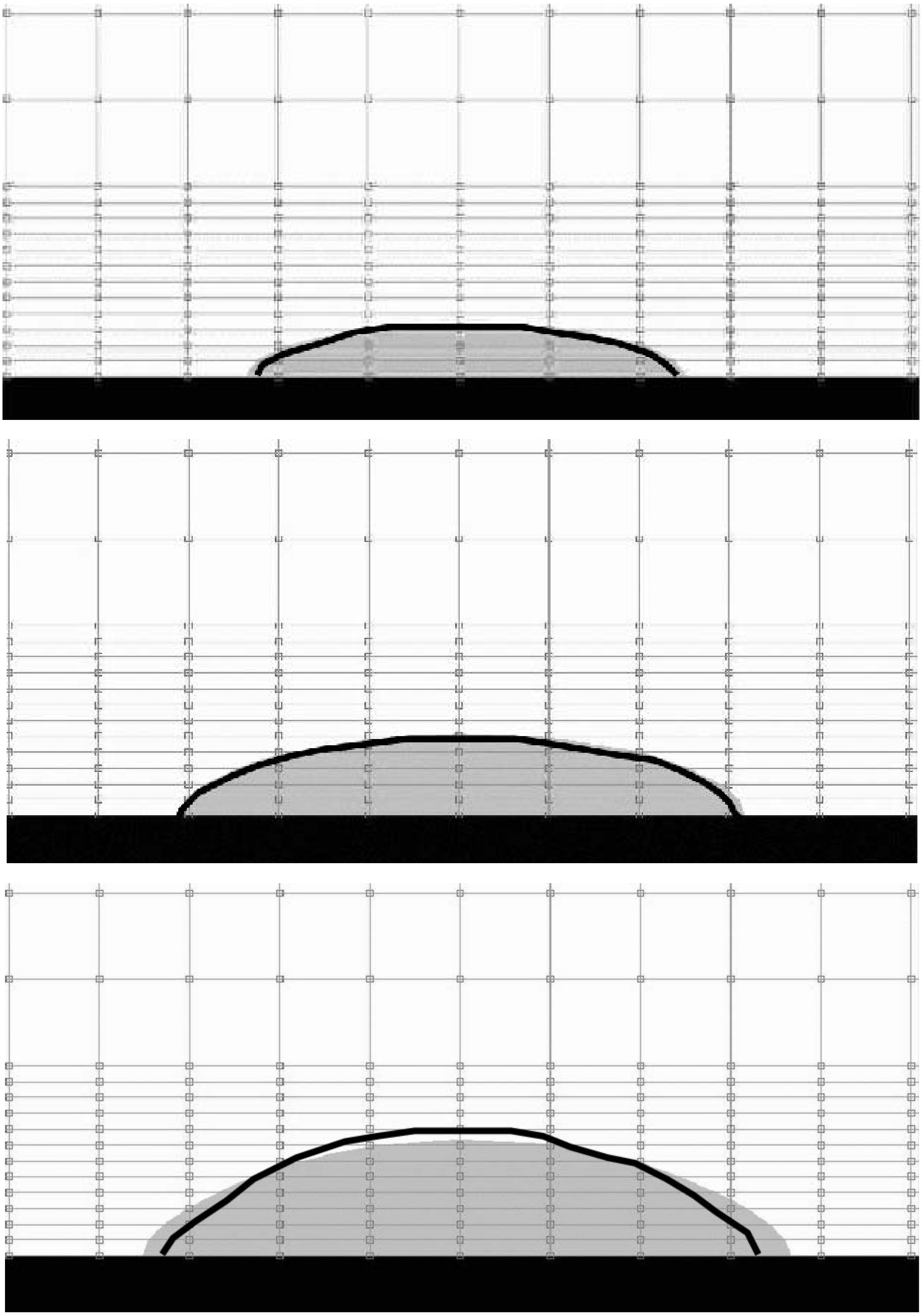

Figure 7.2: Hardened zone in the magnetostatic approach and in the experiment after $\triangle t = 1s,\ 1.5s\ ,2s$ for an exciting current of $10500A$. In reality the pictures are $11mm$ in height and their width is $25mm$.

As an example for a real life item, the benchmark problem that is used in our project is simulated. The setting is the same as in Figure 1.1. In practice, this workpiece is used as a joint of a driveshaft of a car. Figure 7.3 shows the current density at the surface of the workpiece and the inductor. The results are produced with the magnetostatic approach. Dark colours indicate a strong current. One can see the impact of the plates on the workpiece and on the inductor. No experimental data is available for this workpiece, thus the results of the simulation cannot be compared with the real hardened item.

Figure 7.3: Current in workpiece and inductor

Chapter 8

Conclusions

The focus of this dissertation lay on the boundary element methods that are used in the electromagnetic part of the simulation of the inductive hardening process. Therefore, three approaches based on the quasistatic model of Maxwell's equations were developed and implemented. The three approaches differ in the effort that is necessary for the implementation and in the degree of approximation.

The crudest model, which is the easiest one to implement, is the *magnetostatic approach*. Our program is already in practical use in the industry. For the experiment with the cylinder, the predicted hardened zones are close to the real hardened zones, although the approach does not have the ability to deal with a wide range of material parameters precisely. People from the industry who are using the program told me, that problems occur at edges and corners, as expected.

In theory it is shown that the *eddy current approach* avoids these errors at edges and corners if the meshwidth is small enough. For small penetration depths I found that the meshwidth must be made so small, that the number of elements of the mesh is much too big for standard computers of the present generation. Thus this approach cannot be used for the simulation of the inductive hardening process. However, for conductors with a penetration depth $\delta > 3mm$ the model seems to be applicable for electromagnetic computations. In this case, I expect this approach to produce the best results, but I have to admitt, that this has not been tested.

The *impedance model* is able to cope with the skin effect on relatively coarse meshes even for small skin depths because it automatically uses the right boundary condition, at least for comparatively 'flat' surfaces. The calculated current density in the interior of the conductors is, for the theoretical experiments that were made, in good agreement with the analytical solutions even for varying material parameters. Thus I expected this model would yield the best results in the simulation of inductive hardening, but unfortunately, the predicted temperatures are only close to the experimental data until the phase transition takes place at approximately 800^oC. Then the simulation becomes unstable. We were running out of time in the project, so we were not able to attend to the problem. However, it seems as if the boundary element part works well. The numerical experiments that were made indicate that the FEM part must be checked more carefully with focus on the special situation of heavily varying magnetic permeability.

If one is only interested in the electromagnetic fields for eddy current problems with moderately varying material parameters, each of the developed approaches can be applied. Depending on what the aim is, one has to choose the right approach. The magnetostatic approach is applicable if the skin depth is small, and if the solution at edges and corners is of minor importance. The impedance model can be used for a wide range of material parameters (except for high temperatures), and it provides a much better approximation at edges and corners compared with the magnetostatic approach. However, it must be pointed out that the impedance model needs much more storage than the magnetostatic approach, thus it should only be used for ’smaller’ problems. The eddy current approach can be applied if one is interested in the electromagnetic fields at edges and corners, but if the penetration depth is small, a lot of elements are needed to resolve the skin effect. The eddy current approach is the best choice if the items have edges and corners, and if the penetration depth is bigger than $3mm$.

A good idea for future simulations of the electromagnetic phenomena might be, to use the impedance model as an initial guess for the electric field and then apply the eddy current approach only as a correction, especially at edges and corners.

List of Notations

This is a fragmentary list of often used notations. Note that some symbols may occur several times like, for example, $\mathbf{B}$. However, everything except for very common signs, is defined locally in the text too. So mixing up different meanings is avoided.

$\langle \gamma', \gamma \rangle := L(\gamma\!\downarrow, \gamma')$

$[v]$:= Jump of v

$\bar{\lambda}$:= Complex conjugated λ

$|| \cdot ||$:= Euklidian norm of $\cdot$

$|| \cdot ||_V$:= Norm of $\cdot$ in V

$| \cdot |$:= Absolute value

$\gamma\!\downarrow$:= Submerged cycle γ

$\gamma_1 \not\simeq \gamma_2$ means γ_1 and γ_2 are homotopic

$\langle \mathbf{a}, \mathbf{b} \rangle_{\boldsymbol{\tau}} := \int\limits_{\Gamma} \mathbf{a}(\mathbf{x}) \cdot \overline{\mathbf{b}(\mathbf{x})}\, dS(\mathbf{x})$

$\mathbf{A}$:= Magnetic vector potential

arg z := Argument of $z = x + iy$, arg $z = \arctan(y/x)$

BEM-operators $\mathbf{E}_{\pm},\ \gamma_D^{\pm},\ \gamma_N^{\pm},\ \boldsymbol{\lambda}_{\pm},\ \mathbf{C},\ \mathbf{A},\ \mathbf{N},\ \mathbf{B}$ see page 19

$\mathbf{B}$:= Magnetic induction

$\mathbf{b}_{mk}$:= The basis functions of $\boldsymbol{\mathcal{N}}\boldsymbol{\mathcal{D}}_1(\Gamma_h)$

$\mathbb{C}$:= Complex numbers

$C(\Omega)$:= Continuous functions over Ω

$C^k(\Omega)$:= Functions with k-th derivative in $C(\Omega)$

c_p := Heat capacity

c := Speed of light

$curl_{\Gamma}\mathbf{v} := \mathbf{n} \cdot (\mathbf{curl}\, \mathbf{v})$

D^{α} := Differential operator $(\frac{\partial}{\partial x_1})^{\alpha_1}(\frac{\partial}{\partial x_2})^{\alpha_2} \cdots (\frac{\partial}{\partial x_n})^{\alpha_n}$

∂_y^α := Differential operator $(\frac{\partial}{\partial y_1})^{\alpha_1}(\frac{\partial}{\partial y_2})^{\alpha_2}\cdots(\frac{\partial}{\partial y_n})^{\alpha_n}$, with $|\alpha| := \alpha_1 + \alpha_2 + \cdots + \alpha_n$

δ := Penetration depth

$\mathbf{D}$:= Electric displacement

$diam$:= Diameter

$dist$:= Distance

$\mathrm{div}_\Gamma := \mathbf{grad}_\Gamma^*$

$\mathbf{E}$:= Electric field

$\epsilon = \epsilon_r \cdot \epsilon_0$:= dielectric constant

$$F(\mathbf{E},\,\mathbf{v}) := \begin{cases} q(\mathbf{E},\,\mathbf{v}) & \text{For the } \textit{eddy current approach} \\ \left\langle \frac{1}{\eta}\gamma_D\mathbf{E}, \gamma_D\mathbf{v}\right\rangle_{\boldsymbol{\tau}} & \text{For the } \textit{impedance model} \end{cases}$$

$f(T)$:= Temperature correction

Γ := Boundary of a region in $\mathbb{R}^3$

$G(\mathbf{x},\mathbf{y}) := \frac{1}{4\pi}\frac{1}{|\mathbf{x}-\mathbf{y}|}, \quad \mathbf{x},\,\mathbf{y} \in \mathbb{R}^3,\ \mathbf{x} \neq \mathbf{y}$

$\mathbf{grad}_\Gamma\,\phi := \mathbf{n} \times (\mathbf{grad}\,\phi \times \mathbf{n})$

h := Meshwidth

$\mathbf{H}_\perp^{-\frac{1}{2}}(\mathrm{curl}_\Gamma, \Gamma) := \{\mathbf{v} \in \mathbf{H}_\perp^{-\frac{1}{2}}(\Gamma),\, \mathrm{curl}_\Gamma\,\mathbf{v} \in H^{-\frac{1}{2}}(\Gamma)\}$

$\mathbf{H}_{||}^{-\frac{1}{2}}(\mathrm{div}_\Gamma, \Gamma) := \{\mathbf{v} \in \mathbf{H}_{||}^{-\frac{1}{2}}(\Gamma),\, \mathrm{div}_\Gamma\mathbf{v} \in H^{-\frac{1}{2}}(\Gamma)\}$

$\mathbf{H}_{||}^{-\frac{1}{2}}(\mathrm{div}_\Gamma 0, \Gamma) := \{\boldsymbol{\lambda} \in \mathbf{H}_{||}^{-\frac{1}{2}}(\mathrm{div}_\Gamma, \Gamma),\, \mathrm{div}_\Gamma\boldsymbol{\lambda} = 0\}$

$H^1(\Omega) := \{v \in L^1_{loc}(\Omega);\ D^\alpha v \in L^2(\Omega) \quad \forall\ |\alpha| \leq 1\}$

$\mathbf{H}(\mathbf{curl}, \Omega) := \{\mathbf{v} \in \mathbf{L}^2(\Omega);\ \mathbf{curl}\,\mathbf{v} \in \mathbf{L}^2(\Omega)\}$

$\mathbf{H}(\mathrm{div}, \Omega) := \{\mathbf{v} \in \mathbf{L}^2(\Omega);\ \mathrm{div}\,\mathbf{v} \in L^2(\Omega)\}$

$H_1(\Gamma_h, \mathbb{Z})$:= Homology group

H := Enthalpy

$\mathbf{H}$:= Magnetic field

$H_1^{(1)}$ and $H_1^{(2)}$ are Hankel functions

I_{exc} := Exciting current

Im, or $\Im[\cdot]$:= Imaginary part

J := Bessel functions

j := Spatial current density

κ := Heat conductivity

$\mathbf{k}$:= Surface current density

$\mathrm{Ker}(T)$:= Kernel of T

$L(\gamma, \gamma') := -\int\limits_{\gamma}\int\limits_{\gamma'} \mathbf{grad_y}\, G(\mathbf{x}, \mathbf{y}) \cdot (d\vec{s}(\mathbf{x}) \times d\vec{s}(\mathbf{y}))$

$L_t^\sigma(x_1))$:= Lagrange polynomial

$L^2(\Omega) := \left\{ v \,:\, \Omega \to \mathbb{R}\,, \|v\|_{L^2(\Omega)} := \left[\int_\Omega |v(\mathbf{x})|^2\, d\mathbf{x}\right]^{\frac{1}{2}} < \infty \right\}$,
$\mathbf{L}^2(\Omega) := L^2(\Omega)^3$

$\mathbb{N} \;:=\; \{1,\, 2,\, 3\ldots\}$

$\mathbb{N}_0 \;:=\; \{0,\, 1,\, 2,\, 3\ldots\}$

$\mathbf{n}$:= Outer normal

$\boldsymbol{\mathcal{N}\mathcal{D}}_1(\Gamma_h)$:= Space of linear surface edge functions

$O(\cdot)$:= Asymptotic behavior

ω := Angular frequency

Ω := Domain in $\mathbb{R}^3$

$\partial\Omega$:= Boundary of Ω

$\bar{\Omega}$:= Closure of Ω

$\overset{o}{\Omega}$:= Interior of Ω

ψ_i := Basis functions of $\mathcal{S}_1(\Gamma_h)$

$p_\iota^\sigma(\mathbf{x}) := L_t^\sigma(x_1) L_l^\sigma(x_2) L_m^\sigma(x_3)$ is a tensor product of Lagrange polynomials

P := Associated Legendre functions of the first kind

Q := Associated Legendre functions of the second kind

$\mathbb{R}$:= Real numbers

$\mathbb{R}_{>0}$:= Real numbers bigger than zero

Re, or $\Re[\cdot]$:= Real part

$\mathbf{R}_{\ldots}$:= Right hand side

Sobolev spaces $\gamma_D(H^1(\Omega)),\ H^{-\frac{1}{2}}(\partial\Omega),\ \mathbf{H}^{\frac{1}{2}}(\Gamma),\ \mathbf{H}^{-\frac{1}{2}}(\Gamma),\ \mathbf{H}_{||}^{\frac{1}{2}}(\Gamma),\ \mathbf{H}_{\perp}^{\frac{1}{2}}(\Gamma)$ see page 20

dS := Surface measure

$d\mathbf{S}$:= $\mathbf{n}dS$

σ := Electric conductivity

σ_0 := Stefan-Boltzmann constant

$\mathcal{S}_1(\Gamma_h)$:= Space of nodal hat functions

$\mathcal{S}_0 := \mathcal{V}_h, \mathcal{S}_1 := \mathcal{E}_h$, and $\mathcal{S}_2 := \mathcal{F}_h$ are the sets of vertices, edges, and faces

$d\vec{s}$:= Path measure

$S(\tau)$:= Set of sons of cluster τ

$sign(\mathbf{b})$:= sign (± 1) of the edge function $\mathbf{b}$ depending on the orientation

T := Temperature

T_m := Area of triangle m

$\mu = \mu_r \cdot \mu_0$:= Magnetic permeability

$\mu_r^{eff} := f \int\limits_0^{1/f} \mu_r\big(\|B_0\|\big)\, dt$

$d\mathbf{x}$:= Lesbesque measure

$\mathbf{X}(\mathbb{R}^3) := \mathbf{H}(\mathbf{curl}, \mathbb{R}^3) \cap \mathbf{H}(\mathrm{div}, \mathbb{R}^3)$

$\mathbb{Z}$:= All integer numbers

List of Figures

Bibliography

[ABN00] H. Ammari, A. Buffa, and J.-C. Nédélec. A justification of eddy currents model for the Maxwell equations. *SIAM J. Appl. Math.*, 60(5):1805–1823, 2000.

[AH01] K. Atkinson and W. Han. *Theoretical numerical analysis: a functional analysis framework*, volume 39 of *Texts in Applied Mathematics*. Springer, 2001.

[AI70] M. Abramowitz and I.Stegun. *Handbook of Mathematical Functions*. Dover Publications, New York, 1970.

[AR90] R. Albanese and G. Rubinacci. Fomulation of the eddy–current problem. *IEE Proc. A*, 137(1):16–22, 1990.

[BBHL99] A. Bonnet-BenDhia, C. Hazard, and S. Lohrengel. A singular field method for the solution of Maxwell's equations in polyhedral domains. *SIAM J. Appl. Math.*, 59(6):2028–2044, 1999.

[BC01] A. Buffa and P. Ciarlet. On traces for functional spaces related to Maxwell's equations. Part I: An integration by parts formula in Lipschitz polyhedra. *Math. Meth. Appl. Sci.*, 24(1):9–30, 2001.

[Ben90] G. Benkowsky. *Induktionserwärmung: Härten, Glühen, Schmelzen, Löten, Schweissen*. Verlag Technik GmbH, Berlin, 5 edition, 1990.

[BHHW00] R. Beck, R. Hiptmair, R.H.W. Hoppe, and B. Wohlmuth. Residual based a-posteriori error estimators for eddy current computation. $\mathrm{M}^2\mathrm{AN}$, 34(1):159–182, 2000.

[Bos91] A. Bossavit. The computation of eddy–currents in dimension 3 by using mixed finite elements and boundary elements in association. *Math. Comput. Modelling*, 15(3–5):33–42, 1991.

[Bos98] A. Bossavit. *Computational Electromagnetism. Variational Formulation, Complementarity, Edge Elements*, volume 2 of *Electromagnetism Series*. Academic Press, San Diego, CA, 1998.

[Bos99] A. Bossavit. On the Lorenz gauge. *COMPEL*, 18(3):323–336, 1999.

[BS89] I. Bronstein and K. Semendjajew. *Taschenbuch der Mathematik*. Verlag Nauka and B.G. Teubner Verlagsgesellschaft, Moskau and Leipzig, 24 edition, 1989.

[BS92] Bergmann and Schäfer. *Lehrbuch der Experimentalphysik*, volume 6 Festkörperphysik. Walter de Gruyter, 1992.

[CDN99] M. Costabel, M. Dauge, and S. Nicaise. Singularities of Maxwell interface problems. *M^2AN*, 33(3):627–649, 1999.

[CGC$^+$94] C. Chaboudez, R. Glardon, S. Clain, J. Rappaz, M. Swierkosz, and R. Touzani. Numerical modelling of induction heating of long workpieces. *IEEE Trans. Magnetics*, 30(6):5028–5036, 1994.

[DH91] P. Deuflhard and A. Hohmann. *Numerische Mathematik. Eine algorithmisch orientierte Einführung*. DeGruyter, Berlin, 1991.

[Dir96] H.K. Dirks. Quasi–stationary fields for microelectronic applications. *Electrical Engineering*, 79:145–155, 1996.

[DL90] R. Dautray and J.-L. Lions. *Mathematical Analysis and Numerical Methods for Science and Technology*, volume 4. Springer, Berlin, 1990.

[FK98] H. Fischer and H. Kaul. *Mathematik für Physiker*, volume 2. Teubner, 1998.

[GHZU95] L. Gong, R. Hagel, K. Zhang, and R. Unbehauen. A semi-analytical method for evaluation of the 3D inhomogeneous induction heating of a moving hollow cylinder. *COMPEL*, 14(4):257–260, 1995.

[Gie00] K. Gieberman. Multilevel representation of boundary integral operators. Technical Report 637, SFB 256, Universität Bonn, Bonn, Germany, 2000.

[Gri85] P. Grisvard. *Elliptic Problems in Nonsmooth Domains*. Pitman, Boston, 1985.

[Hac89] W. Hackbusch. *Integralgleichungen. Theorie und Numerik*, volume 68 of *Leitfäden der angewandten Mathematik und Mechanik*. Teubner-Verlag, Stuttgart, 1989.

[Hac91] W. Hackbusch. *Iterative Lösung großer linearer Gleichungssysteme*. B.G. Teubner–Verlag, Stuttgart, 1991.

[HB01] W. Hackbusch and S. Börm. $\mathcal{H}^2$-matrix approximation of integral operators by interpolation. Preprint 104/2001, MPI for Mathematics in the Sciences, Leipzig, Germany, December 2001.

[HGU94] R. Hagel, L. Gong, and R. Unbehauen. On the 3-D inhomogeneous induction heating of a shell. *IEEE Trans. Magnetics*, 30(5):3324–3327, 1994.

[Hip02] R. Hiptmair. Symmetric coupling for eddy current problems. *SIAM J. Numer. Anal.*, 40(1):41–65, 2002.

[HKS00] W. Hackbusch, B. Khoromskij, and S. Sauter. On $\mathcal{H}^2$-matrices. In H. Bungartz, R. Hoppe, and C. Zenger, editors, *Lectures on Applied Mathematics*, pages 9–29. 2000.

[HN89] W. Hackbusch and Z.P. Nowak. On the fast matrix multiplication in the boundary element method by panel clustering. *Numer. Math.*, 54:463–491, 1989.

[HO01] R. Hiptmair and J. Ostrowski. Generators of $H_1(\Gamma_h, \mathbb{Z})$ for triangulated surfaces: Construction and classification. Report 160, SFB 382, Universität Tübingen, Tübingen, Germany, 2001. To appear in SIAM J. Computing.

[HOQ00] R. Hiptmair, J. Ostrowski, and R. Quast. Modelling and simulation of induction heating. Technical Report 149, SFB 382, Universität Tübingen, Tübingen, Germany, March 2000.

[Hor79] E. Hornbogen. *Werkstoffe*. Springer-Verlag, 2nd edition, 1979.

[Jac75] J.D. Jackson. *Classical Electrodynamics*. Wiley, New York, 2nd edition, 1975.

[Jän01] K. Jänich. *Topologie*. Springer, 7 edition, 2001.

[Knö96] H. Knörrer. *Geometrie*. Vieweg, 1996.

[Kol02] O. Kolditz. *Computational Methods in Environmental Fluid Mechanics*. Springer, 2002.

[Kos94] Arnulf Kost. *Numerische Methoden in der Berechnung elektromagnetischer Felder*. Springer-Verlag, Berlin, 1994.

[LMTS96] R. Lewis, K. Morgan, H. Thomas, and K. Seetharamu. *The Finite Element Method in Heat Transfer Analysis*. John Wiley, 1996.

[LNA86] J. Luomi, A. Niemenmaa, and A. Arkkio. On the use of effective reluctivities in magnetic field analysis of induction motors fed from a sinusoidal voltage source. In *IECM'86*, volume 2, pages 706–709, September 1986.

[MML94] A. Muiznieks, A. Mühlbauer, and H.-J. Lessmann. Calculation of threedimensional electromagnetic fields during induction heating. *Archiv für Elektrotechnik*, 77(3):157–168, 1994.

[Mon92] P. Monk. Analysis of a finite element method for Maxwell's equations. *SIAM J. Numer. Anal.*, 29:714–729, 1992.

[Nol90] W. Nolting. *Grundkurs: Theoretische Physik, Elektrodynamik*, volume 3. Zimmermann-Neufang, 1990.

[Oev96] W. Oevel. *Einführung in die Numerische Mathematik*. Spektrum Akademischer Verlag, 1996.

[PBT00] K. Preis, O. Biró, and I. Ticar. Guaged current vector potential and reentrant corners and the FEM analysis of 3D eddy currents. *IEEE Trans. Magnetics*, 2000.

[PKU97] R. Przylucki, K. Kurek, and B. Ulrych. Induction heating as coupled or non-coupled electromagnetic and thermal problems. *Acta Technica CSAV*, 42(3):269–280, 1997.

[PS75] C. C. Paige and M. A. Saunders. Solution of sparse indefinite systems of linear equations. *SIAM J. Numer. Anal.*, 12(4):617–629, September 1975.

[Rei93] M. Reissel. On a transmission boundary-value problem for the time-harmonic Maxwell equations without displacement currents. *SIAM J. Math. Anal.*, 24(6):1440–1457, 1993.

[RS96] J. Rappaz and M. Swierkosz. Mathematical modelling and numerical simulation of induction heating processes. *Appl. Math. Comput. Sci.*, 6(2):207–221, 1996.

[Saa95] Y. Saad. *Iterative methods for sparse linear systems*. PWS Publishing Co., 1995.

[Sau99] S. Sauter. Variable order panel clustering (extended version). Technical Report 52, Max-Planck-Institut für Mathematik, Leipzig, Germany, 1999.

[Smy68] W.R. Smythe. *Static and Dynamic Electricity*. International Series in Pure and Applied Physics. McGraw-Hill, New York, 3rd edition, 1968.

[SR97] M. Swierkosz and J. Rappaz. Boundary-element method yields external vector potentials in complex industrial applications. *Computers in Physics*, 11(2):145–150, 1997.

[SS01] O. Sterz and C. Schwab. A scalar BEM for time harmonic eddy current problems with impedance boundary conditions. In U. van Rienen, M. Günther, and D. Hecht, editors, *Scientific Computing in Electrical Engineering*, volume 18 of *Lecture Notes in Computational Science and Engineering*, pages 129–136. Springer, Berlin, Germany, 2001.

[Sta88] G. Staudt. *Experimentalphysik*, volume 2. Attempto-Verlag, 4th edition, 1988.

[Stu62] W. Stuhlmann. In *Härterei - Technische Mitteilung Teil B*, volume 7. Organ des Instituts für Härterei-Technik und der Wissenschaftlich-Technischen Arbeitsgemeinschaft für Härterei-Technik und Wärmebehandlung e.V., Berlin-Dahlem, Pacalliallee 7, Juli 1962.

[vdV92] H. van der Vorst. BI-CGSTAB: A fast and smoothly converging variant of BI-CG for the solution of nonsymmetric linear systems. *SIAM J. Sci. Stat. Comput.*, 13(2):631–644, 1992.

[vR01] U. van Rienen. *Numerical Methods in Computational Electrodynamics. Linear Systems in Practical Applications*, volume 12 of *Lecture Notes in Computer Science and Engineering*. Springer–Verlag, Heidelberg, 2001.

[Wlo82] J. Wloka. *Partielle Differentialgleichungen*. Teubner–Verlag, Stuttgart, 1982.

List of Publications

R. Hiptmair und J.Ostrowski
Generators of $H_1(\Gamma_h, \mathbb{Z})$ *for Triangulated Surfaces: Construction and Classification*
Report No. 160, SFB 382, Universität Tübingen, März 2001
To appear in SIAM, Journal of Computing

R. Hiptmair und J.Ostrowski
Symmetric Coupling for Eddy Current Problems
Conference Proceedings, ECCM-2001 Krakau, Poland

R. Hiptmair, J. Ostrowski, und R. Quast
Modelling and Simulation of Induction Heating
Report Nr. 149, SFB 382, Universität Tübingen, März 2000

J.Ostrowski
Simulation des Schmelzaustriebs und der Verdampfung beim Laserbohren
Diplomarbeit, Sonderforschungsbereich 382, Universität Tübingen, 1998

Danksagung

Diese Arbeit entstand im Rahmen eines von der Deutschen Forschungsgemeinschaft geförderten Transferbereichs (TB26). Ihr sei deshalb zunächst für die Finanzierung gedankt.

Persönlich bedanken möchte ich mich an erster Stelle bei Herrn Prof. Dr. Ralf Hiptmair, von dem ich nicht nur in mathematischer Hinsicht sehr viel lernen durfte, sondern der mir in jedem Aspekt des beruflichen Lebens auch weiterhin ein Vorbild sein wird.

Herrn Prof. Dr. Hanns Ruder möchte ich für die jahrelange Unterstützung seit Beginn meiner Diplomarbeit danken. Er ermöglichte durch sein unbürokratisches Engagement erst das Zustandekommen dieser Arbeit.

Meinem Kollegen Dr. Wenqing Wang danke ich besonders für seine stets nachsichtige Haltung gegenüber meinem rohen europäischen Auftreten, vorallem aber für eine sehr gute und fruchtbare Zusammenarbeit.

Weiterhin gebührt den Herren Dr. Steffen Börm und Dr. Klaus Giebermann Dank für die Hilfe bei der Umsetzung der Kompressionstechnik, sowie Herrn Dr. Olaf Steinbach für die semi-analytische Integration einiger BEM-Operatoren.

Nicht unerwähnt bleiben sollen Tanja Bubeck und Dr. Vasile Gradinaru, Mitgliedern meiner Arbeitsgruppe, deren Numerik- und Mathe-Tips mir immer weiter halfen.

Desweiteren seien Stephanie Kaiser-Dauer und Frido Schefft für die sprachliche Durchsicht und geduldige Korrektur meiner Dissertation gedankt.

Im Andenken an meinen Vater
Oswald Ostrowski